Spectroscopic studies of electrochemical reactions and electrodeposition films

Wang, Rui Lin

Award date:
2000

Awarding institution:
University of Bath

SPECTROSCOPIC STUDIES OF ELECTROCHEMICAL REACTIONS AND ELECTRODEPOSITION FILMS

Submitted by Rui Lin Wang
for the degree of PhD
of the University of Bath
2000

COPYRIGHT

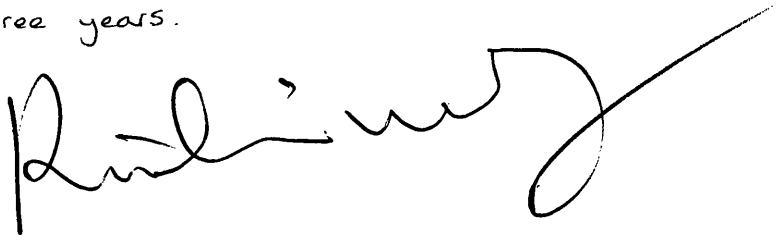

Rui Lin Wang

ProQuest LLC
789 East Eisenhower Parkway
P.O. Box 1346
Ann Arbor, MI 48106-1346

Abstract

Part one presents the development of a new methodology based on potential modulated reflectance spectroscopy (PMRS) which is used to study the electrode/electrolyte solution interfacial region where reactions take place. A thin layer flow cell has been employed to enable steady state mass transport conditions to be established. Numerical simulations have been performed to provide a quantitative description of the concentrations of species within the cell as a function of time and position. An FFT algorithm has been employed to derive the frequency response of the current/ spectroscopic signal when a modulated potential is applied to the electrode. The new methodology has been tested by using the oxidation of the tris (4-bromophenyl) amine in acetonitrile as an example of a simple reversible electron transfer reaction. The oxidation of ferrocyanide followed by the consequent oxidation of l-ascorbic acid by ferricyanide to regenerate ferrocyanide has been used as an example of a coupled chemical reaction. The good agreement between experimental and numerical simulations validates method.

In part two, CdTe thin films have been electrodeposited onto CdS-coated conducting glass substrates in stirred solution and in a channel flow cell. These thin films were characterised by capacitance voltage, photocurrent techniques and electrolyte electroreflectance/absorbance (EER/A). Film composition, structure and morphology were assessed by wavelength dispersive x-ray analysis (WDX), x-ray diffraction (XRD), atomic force microscopy (AFM) and scanning electron microscopy (SEM). A fast deposition technique has been developed that reduces the time for deposition of 2μm CdTe films from 2-3 h typical for deposition in stirred solution to 20 min. High quality films were obtained, and these were characterised by the techniques described above. The rapidly deposited films recrsytallised during thermal treatment, while films deposited in stirred solution do not recrsytallise. It appears that recrystallisation is important for the fabrication of efficient solar cells. Films have been fabricated into CdTe/CdS solar cells. The efficiency of a test cell under AM1.5 (G) illumination was 6%.

A two-side-fitting model for photocurrent spectra is proposed and used to characterise CdS-CdTe structures. Two key parameters, the width of the space charge region and the diffusion length of minority carrier, were obtained by using the model to fit experimental photocurrent spectra.

Acknowledgements

I wish to express my sincere thanks to my supervisor, Professor Laurence Peter, for his tireless supervision and constant encouragement over these three years.

My great thanks are also due to Dr. Adrian Fisher for his advice on part one of the thesis, and to Dr. Mike Bailes for his advice and support for electronic techniques.

I would also like to thank Noel, June, Siva, Qiu, Nia, Rachel, Shin and Upul for their great help and for providing a good time during my study. Thanks also to all the members of LMP research group.

My thanks are extended to Mr. Hugh Perrott of the Electron Optics Centre for help in obtaining the SEM images and WDX data. Thanks are also to Mr. Barry Chapman of Department of Physics for providing me XRD data.

I should particularly like to thank our glassblower to Mr. Mike Lock for his skilful work in making a range of glass cells.

Finally, but most importantly I would like to thank my wife Zhong Li and my daughter Wang Shiqi for all their love and tireless support.

The University of Bath is acknowledged for the award of a postgraduate scholarship.

PART ONE

POTENTIAL MODULATED REFLECTANCE SPECTROSCOPY STUDIES UNDER HYDRODYNAMIC CONDITIONS

PART TWO

ELECTRODEPOSITION AND CHARACTERISATION OF CdTe/CdS SOLAR CELLS

PART ONE

POTENTIAL MODULATED REFLECTANCE SPECTROSCOPY STUDIES UNDER HYDRODYNAMIC CONDITIONS

CHAPTER ONE

INTRODUCTION

1.1 PMRS

Studies of electrochemical systems are traditionally based on electrical measurements like cyclic voltammetry, ac voltammetry etc., but in recent years there has been increasing interest in the application of a wide range of *in situ* spectroscopic and structural techniques to characterise the interfacial region [1]. With the development of electrochemical measurements, in particular *in situ* techniques ranging from infrared (IR) spectroscopy to X-ray scattering, more detailed information about the chemical system can be obtained. Although a large number of spectroscopic methods have been utilised, UV- visible absorption spectroscopy has been one of the most extensively exploited. An important advantage of measuring the change in absorbance due to an electrode reaction, as opposed to measurement of the resulting current, is the additional selectivity provided by including wavelength as an experimental variable.

Alternating current techniques [2] have long been regarded as methods of choice for the quantitative characterisation of electrode processes. Bond et al. [3-4] used linear sweep cyclic ac voltammetry to show that the ac method can give more qualitative diagnostic information on the more popular technique of cyclic voltammetry.

The technique of potential modulated UV- vis reflectance spectroscopy (PMRS), based on the absorption spectroscopy and ac voltammetry methods, enables the electrode/electrolyte solution interfacial region to be monitored [5]. In this way reactions at the surface of the electrode can be observed *in situ*, and quantitative information about the charge transfer process can be obtained.

UV-visible absorption spectroelectrochemistry carried out in reflectance experiments at conventional solid planar electrodes [6-11] has been used for the spectroscopic characterisation of primary and secondary products of electrode reactions, and in mechanistic studies of homogeneous reactions coupled to an electrode reaction. Bancroft [12] has extended chronocoulometric theory to spectroscopic observation at optically transparent electrodes (OTEs) to build up a method for the determination of heterogeneous charge transfer parameters in which there is a particular advantage that impurities in the solvent or the redox species does not affect the spectroscopic determination of the electrochemical responses.

Pons et al. [13] first introduced the use of small sinusoidal perturbation modulated ac reflectance spectroscopy (SMACRS, later called PMRS). This method retains both the qualitative and quantitative utility of linear sweep ac voltammetry in conjunction with the advantages of spectroscopic observation, and it has been checked by using the ferro-ferricyanide model system. Martinez [14] used PMRS to investigate thin corrosion films on metals. Peter [1,15] used PMRS to investigate the characterisation of anodic oxide films on titanium and Fe(II)/Fe(III), Fe(III)/Fe(VI) couples on Fe within the range of wavelengths of interest. Gutierrez et al. [16-24] have used PMRS extensively to investigate a range of systems including chemisorption and electroadsorption of CO, methanol and ethanol using metals like Rh , Pt , Au, Ni, Pd, Fe as electrodes. Recently Fermin et al. [25] have studied the kinetics of methyl orange transfer across liquid-liquid interfaces by using PMRS and ac impedance. The rate constant of the electron transfer reaction and its transfer coefficient have been determined.

When a small amplitude sinusoidal perturbation is superimposed on a slowly varying cyclic potential ramp applied to an electrode in the PMRS experiment, an alternating current results from the alternate formation and removal of one form of a redox couple at the surface of the electrode. The intensity of a beam of light reflected from the surface of the electrode will vary in accordance with the alternation of the relative concentrations of the two forms of the redox couple, provided that they have different molar absorptivities at the wavelength used. A phase sensitive detector (PSD) or lock-in amplifier is used to monitor the variation in intensity of the modulated component of the reflected light beam. Generally the first harmonic ac signal is detected since it has the largest magnitude.

In the related technique of modulated specular reflectance spectroscopy (MSRS)[6-11], a large amplitude periodic square wave potential (typically 50mV peak to peak) is applied to the electrode such that first one and then the other form of a redox couple predominates periodically at the surface of an electrode. The method only provides qualitative information about reaction mechanisms at the surface or in the diffusion layer. In this thesis a new methodology for PMRS in hydrodynamic systems is developed. The method not only applies to the electrode process, but also to chemical reaction processes.

1.2 Electrode processes at solid electrodes

The electrode/solution system can be represented as shown in figure 1.1. Region I represents the Helmholtz double layer (typical thickness less than 10Å in concentrated solution [26]), where the main potential drop occurs and across which electron transfer process takes place. The concentrations of the oxidised and reduced

forms of the electroactive species in region I are a function of the potential difference across this region. Region III represents the bulk of the solution, throughout which the concentrations of the electroactive species are uniform. Region II, which represents the Gouy Chapman layer, is the space within which the electroactive species diffuse under the influence of the concentration gradient set up between region I and III, and the thickness depends on potential applied and electrolyte concentration. When the potential or current pulse is applied to a planar electrode in unstirred solution, the thickness of the diffusion layer increases as the square root of time, $\delta = (\pi Dt)^{1/2}$. D is the diffusion coefficient of the electroactive species, and t is the time after application of the potential or current pulse.

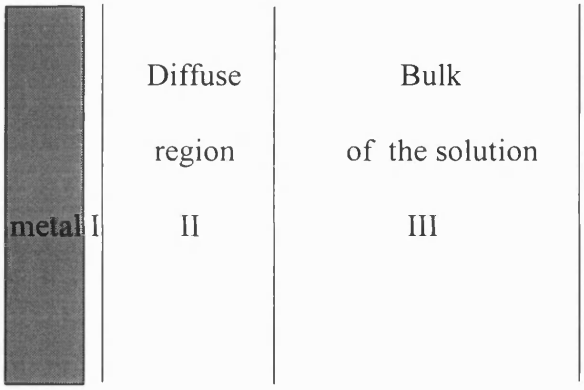

Figure 1.1, Schematic visualisation of the electrode / solution system

Consider a simple redox electrode reaction

$$Ox + n\,e^- \rightleftharpoons Red. \qquad (1.1)$$

The forward reaction involves the transfer of n electrons from the electrode to the oxidised form of the electroactive species and produces a cathodic current, which is designated as negative; the reverse reaction results in an anodic current which is defined as positive. The reaction involves a number of steps, which are summarised in figure 1.2.

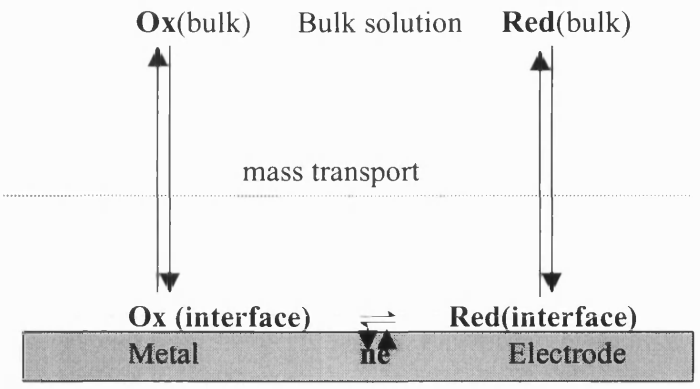

Figure 1.2 A schematic diagram of the mechanism of the electrochemical reaction of the electrode/ solution

According to the absolute rate equation [27], the current due to the forward reaction can be expressed as

$$i_f = -nFAk_f C_{Ox}^0 \tag{1.2}$$

where F is the Faraday constant, A the area of the electrode, C_{Ox}^0 the concentration of the oxidised form at the electrode and k_f the rate constant of the forward reaction. The current due to the reverse reaction is similarly given by

$$i_b = nFAk_b C_{\mathrm{Re}\,d}^0 \tag{1.3}$$

where $C_{\mathrm{Re}\,d}^0$ is the concentration of the reduced form at the electrode, and k_b the rate constant of the reverse reaction.

The net current flow through the interface is

$$i = nFAJ = nFA\left[k_b C_{\mathrm{Re}\,d}^0 - k_f C_{Ox}^0\right] \tag{1.4}$$

J is the net flux of the electroactive species of interest at the electrode. The rate constants k_f and k_b depend on the potential difference across the interface. Applying the absolute rate theory [27] to this system and combining the free energies of activation for oxidation and reduction with the Nernst relation [31], the Butler-Volmer equation [28-29] can be obtained

$$j = \frac{i}{A} = j_0 \left\{ \frac{C^0_{\mathrm{Re}\,d}}{C^{bulk}_{\mathrm{Re}\,d}} \exp\left(\frac{(1-\alpha) nF\eta}{RT} \right) - \frac{C^0_{Ox}}{C^{bulk}_{Ox}} \exp\left(\frac{-\alpha nF\eta}{RT} \right) \right\} \tag{1.5}$$

$$j_0 = \frac{i_0}{A} = nFk^0 \left(C^0_{Ox}\right)^{1-\alpha} \left(C^0_{\mathrm{Re}\,d}\right)^{\alpha} \tag{1.6}$$

where j is the current density, η is the overvoltage ($\eta = E - E_{eq}$), α the transfer coefficient, k^0 the standard heterogeneous rate constant of the electrochemical reaction at E_{eq}, and j_0 is the exchange current density at equilibrium. When the solution is well stirred or currents are kept so low that the surface concentrations do not differ appreciably from the bulk values, equation (1.5) becomes:

$$j = j_0 \left\{ \exp\left(\frac{(1-\alpha) nF\eta}{RT} \right) - \exp\left(\frac{-\alpha nF\eta}{RT} \right) \right\} \tag{1.7}$$

1.3 Mass transport to electrode interface

The thermodynamic properties of a system determine the cell voltage at open circuit, whereas interfacial kinetics, mass transport and conductivity determine the current. Mass transport of an electroactive species toward and away from an interface can occur by diffusion, convection and migration.

1.3.1 Diffusion

Diffusion is defined as the mass transport of a species across a concentration gradient within the solution. The flux of material, J (moles cm^{-2} s^{-1}) in one dimension x is proportional to the concentration gradient of the species (Fick's first law). It can be written for the species Ox as

$$J_{Ox} = -D_{Ox}\frac{dC_{Ox}}{dx} \tag{1.8}$$

Here D_{Ox} is the diffusion coefficient of the species Ox, and C_{Ox} is its concentration at distance x. Fick's second law is concerned with the time dependence of the concentration change, and it can be derived by considering the simplest case in which diffusion occurs along the x-direction in the situation referred to as planar diffusion that is illustrated in figure 1.3

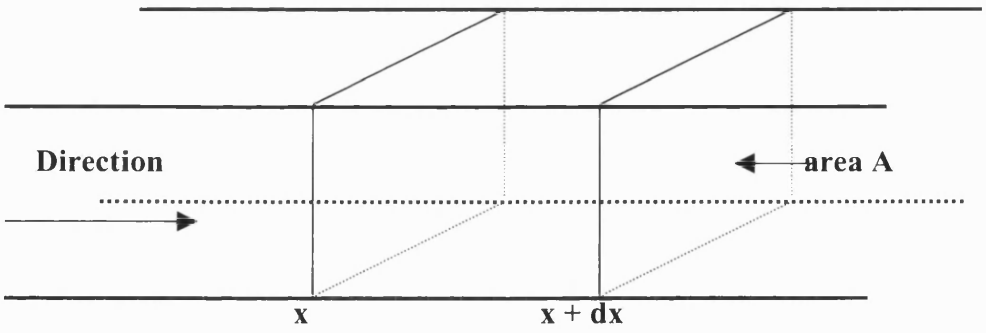

Figure 1.3 Planar diffusion in the x-direction

Considering the region of volume Adx and the concentration changes that occur in this region in the interval between t and t + dt.

Number of moles in region at time (t + dt) - Number of moles in region at time t

= Number of moles entering plane x - Number of moles leaving plane x + dx

$$C^{Ox}_{(x,t+dt)}Adx - C^{Ox}_{(x,t)}Adx = J^{Ox}_{(x,t)}Adt - J^{Ox}_{(x,t+dt)}Adt \qquad (1.9)$$

Substituting Fick's first law and rearranging leads to the following equation in the limit dx $\rightarrow$ 0:

$$\frac{\partial}{\partial t}C^{Ox}_{(x,t)} = D_{Ox}\frac{\partial^2}{\partial x^2}C^{Ox}_{(x,t)} \qquad (1.10)$$

This equation can be extended to three dimensions:

$$\frac{\partial}{\partial t}C^{Ox}_{(x,t)} = D_{Ox}\frac{\partial^2}{\partial x^2}C^{Ox}_{(x,t)} + D_{Ox}\frac{\partial^2}{\partial y^2}C^{Ox}_{(x,t)} + D_{Ox}\frac{\partial^2}{\partial z^2}C^{Ox}_{(x,t)} \qquad (1.11)$$

Note that one-dimensional diffusion, namely in y-direction, is only considered in this part of the thesis.

1.3.2 Convection

There are two forms of convection in solution, natural and forced. The first occurs spontaneously in any solution with a mechanical force arising from temperature and/or density gradients. Natural convection often affects electrochemical measurements in unstirred solution at a conventional electrode (approximately mm or larger) and tends to become a significant perturbation on the time-scale of 10-20 s or longer. It is generally undesirable since it is difficult to predict, and it can be made negligible by using forced convection such as a rotating disk or a channel electrode. The method used in the present work is described as 'hydrodynamic', which can be achieved by using a well-defined channel electrode. This enables a quantitative description of the flow in solution to be established and the pattern of mass transport to the electrode to be predicted rigorously. This has the function of swamping any contribution from

natural convection, so ensuring that reproducible experiments can be made over time-scales beyond the ten seconds limit.

The flux of species Ox due to forced convection in one dimension x, is given by

$$J_{ox} = C_{Ox}\, v_x \tag{1.12}$$

where v_x is the velocity of the solution in the direction x.

Combining the convection equation with Fick's first law gives for species Ox:

$$J_{Ox} = -D_{Ox}\frac{\partial C_{Ox}}{\partial x} + v_x C_{Ox} \tag{1.13}$$

which generalises to the three dimensional case:

$$J_{Ox} = -D_{Ox}\nabla C_{Ox} + C_{Ox} v \tag{1.14}$$

Here ∇ is the Laplacian operator

$$\nabla = \frac{\partial}{\partial x} + \frac{\partial}{\partial y} + \frac{\partial}{\partial z}, \qquad v = v_x + v_y + v_z$$

and v is the velocity vector of the solution.

The variation of the C_{Ox} with time is given by:

$$\frac{\partial C_{Ox}}{\partial t} = -\frac{\partial J_{Ox}}{\partial x} = D_{Ox}\nabla^2 C_{Ox} - v\nabla C_{Ox} \tag{1.15}$$

1.3.3 Migration

Migration is the result of an electrostatic force on the ions, and it occurs if there is a potential gradient. When the ion is in a fluid medium then the electrostatic force seeking to accelerate the ions is opposed by a viscous force. The electrostatic force, F_e, is given by

$$F_e = \frac{zF}{N_A}\frac{\partial \phi}{\partial x} \tag{1.16}$$

where ϕ is the local electric field, z is the charge on the ion, N_A is the Avogadro constant.

The external electric field ($d\phi/dx$) enables the movement of ions to or from the electrode by exerting an electrostatic force on charged species present in the interfacial region. These migration effects contribute to transport phenomena accompanying electrochemical reaction.

The migratory flux, J_m, is proportional to the concentration of the ion, C, the electric field, and the ionic mobility (μ)

$$J_m = \mu C \frac{\partial \phi}{\partial x} \tag{1.17}$$

The ionic mobility (μ) is dependent on the ionic charge and size, as well as on the solution viscosity.

The interaction of migration and electrolysis in any electrochemical reaction gives rise to a complex physical transport process that is hard to control or interpret. The consequence of this will be a change in the concentration on ionic species. Hence the electric field near the electrode is altered. This, in turn, causes a change in migratory fluxes (1.17) and the rate of mass transport of electroactive materials. This varying rate of mass transport makes interpretation of experimental data difficult.

To simplify this problem experiments are often carried out under conditions where migration can be neglected. This is made possible by means of a chemically and electrochemically inert supporting electrolyte added to the solution in high concentration, typical 0.1M. This can be understood by the transport number, t_i, which

is defined by the fraction of total current carried by one particular charge carrier. That is $t_i = \frac{|z_i|\mu_i c_i}{\sum_i |z_i|\mu_i c}$. Here $|z_i|$ is the absolute value of the charge number z_i, μ_i and c_i are the mobility and concentration of species i in solution, respectively. Consider, for example, that the concentration of the supporting electrolyte is 50 times higher than that of the electroactive species and assume that all species in solution has the same mobility, μ, and the same charge number, z. The transport number of the electroactive species is $t = \frac{|z|c\mu}{|z|50c\mu + |z|50c\mu + |z|2c\mu} = \frac{1}{102}$, so that the effect of migration is less than 1%. Calculations have shown that approximately 100 times the concentration of the supporting electrolyte relative to that of the reactant is required if the measured current is not to be perturbed significantly [30].

1.4 Cyclic voltammetry

Cyclic voltammetry is a powerful and widely used technique in electrochemistry. There are three basic kinds of cyclic voltammetry: conventional, ac modulated and steady state.

1.4.1 Conventional cyclic voltammetry

Potential sweep techniques have been widely used to investigate the mechanisms of electrochemical reactions over the past 30 years. A cyclic voltammogram indicating the potentials at which processes occur can be obtained, while homogeneous reactions can be identified, and other processes such as adsorption can be recognised. Consider the reaction Red $\rightleftharpoons$ Ox + ne^-. A potential waveform as depicted in figure 1.4 is applied to the electrode, and the corresponding cyclic voltammogram in which the cell

current is recorded as a function of the applied potential is shown in figure 1.5. The sweep rates used in the conventional experiment range up to a few hundred Vs^{-1}. Although rates up to a few thousand Vs^{-1} have been used, such high values give rise to considerable experimental difficulties that generally limit their application. Fortunately using a microelectrode can overcome this problem and gives high quality data at a very high scan rate due to minimising the charging currents and the effects of uncompensated resistance.

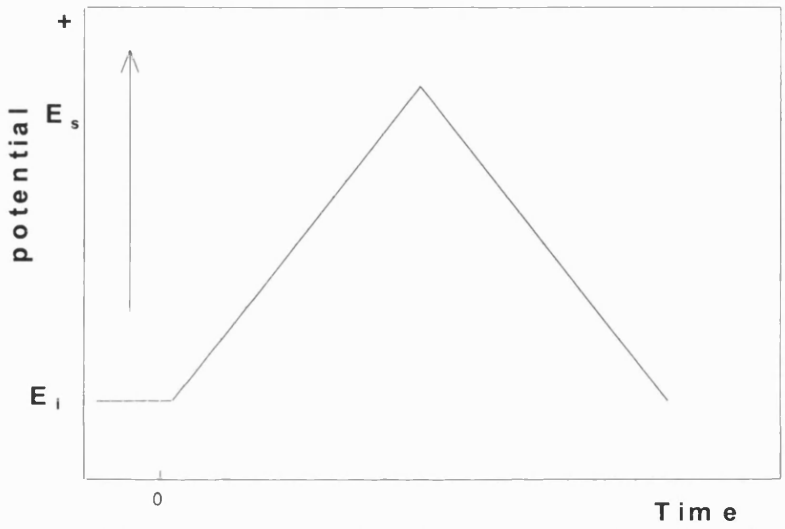

Figure 1.4 The potential waveform for conventional cyclic voltammetry

When studying an unknown system, it is usual to use cyclic voltammetry to carry out qualitative experiments in order to get information about the system. This is followed by semi-quantitave and finally quantitative analysis from which kinetic parameters may be obtained. Factors like scan rates, peak positions and the peak ratio of the forward and backward are important because from them the reversibility of the electron transfer reaction, coupled chemical reaction and adsorption can be obtained. The criteria [31,32] are as follows.

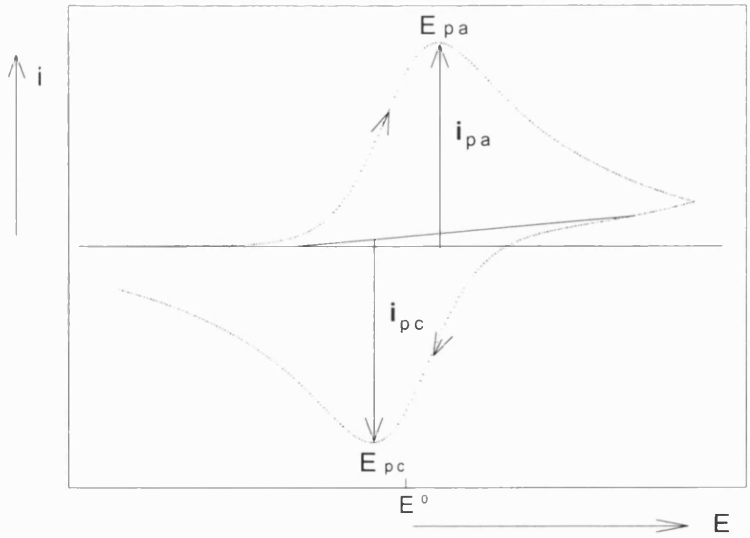

Figure 1.5 A cyclic voltammogram for the process Red $\rightleftharpoons$ Ox + ne$^-$

The criteria for a reversible system are as follows:

The peak potentials, E_{pa}, and E_{pc} are independent of scan rate, ν, but the peak currents, i_p, are proportional to the root of the scan rate. At potentials beyond E_p, $I^{-2} \propto$ time. The peak potential separation is

$$\Delta E_p = E_{pa} - E_{pc} = 2.218RT/nF = 58.5/n \text{ mV at } 25^0C$$

and the ratio of peak currents is

$$|i_{pa} / i_{pc}| = 1$$

Here the subscripts a and c represent the anodic and cathodic process, respectively.

The criteria for a quasi-reversible system are:

$|i_p|$ increases with the square root of the scan rate

$|i_{pa}/i_{pc}| = 1$ provided $\alpha_a = \alpha_c = 0.5$

ΔE_p is greater than 59 mV at 25^0C and increases with increasing scan rate

E_{pc} shifts negatively with increasing of the scan rate.

The criteria for the totally irreversible systems are:

There is no reverse peak, the i_{pa} is proportional to the square root of the scan rate, and also

$$\left|E_P - E_{p/2}\right| = \frac{1.857RT}{\alpha nF} = \frac{47.7}{\alpha n}\ mV\ at 25^0 C$$

$i_{pa}/i_{pc} \neq 1$

1.4.2 Cyclic ac voltammetry

Cyclic ac voltammetry is an extension of cyclic voltammetry. This technique is attractive because it combines the features of two powerful complementary methodologies. Conventional cyclic voltammetry is especially informative about the qualitative aspects of an electrode process. Cyclic ac voltammetry retains the diagnostic utility of conventional cyclic voltammetry, but it does so with an improved response function that permits qualitative analysis.

Consider the ac response at a planar electrode immersed in a stagnant solution containing initially only species Red of the Nernstian couple Red $\rightleftharpoons$ Ox + ne$^-$ (assuming a reversible system). The dc potential starts a value considerably more negative than $E^{0'}$, ($E^{0'} = E^0 + \frac{RT}{nF}\ln\frac{f_{Ox}}{f_{Red}}$, $E^{0'}$ is the standard formal potential, E^0 is the standard potential, f_{Ox} and f_{Red} are the activity coefficients of species Ox and Red, respectively), and is scanned slowly in a positive direction. Due to the slow scan rate, E_{dc} is effectively constant on the time scale of the ac modulation. The modulation amplitude is normally small so that the current – voltage relation can be linearised. The input response employed in cyclic ac voltammetry is shown in figure 1.6 (the amplitude of ac component is enlarged for the demonstration here).

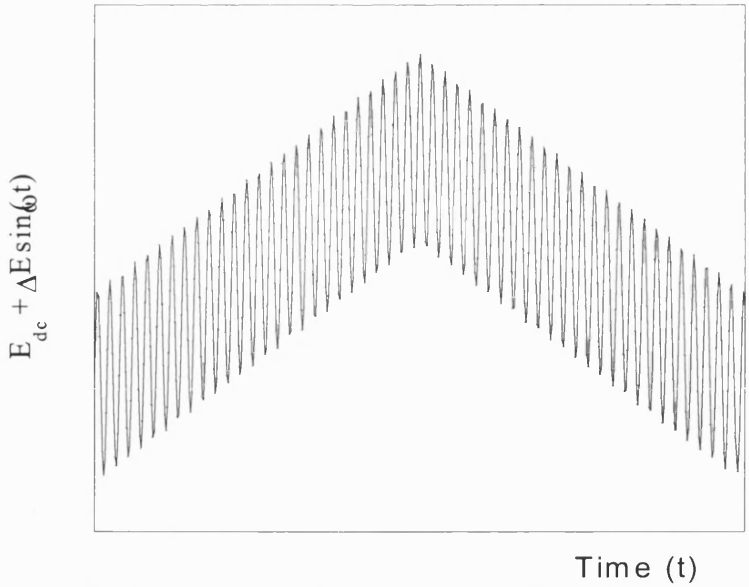

Figure 1.6 The input waveform employed in cyclic ac voltammetry

The output, ac current i_{revs}, can be expressed explicitly as [31]

$$i_{revs}(\omega t) = \frac{n^2 F^2 AC^*(\omega D_{Red})^{1/2}\Delta E}{4RT\cosh^2(\Phi/2)}\sin(\omega t + \frac{\pi}{4}) \qquad (1.18)$$

Where A is the electrode area, C* is the bulk concentration of species Red, D_{Red} is its diffusion coefficient, $\Phi = nF(E_{dc} - E^{0'})/RT$. The cyclic ac voltammogram is shown in figure 1.7.

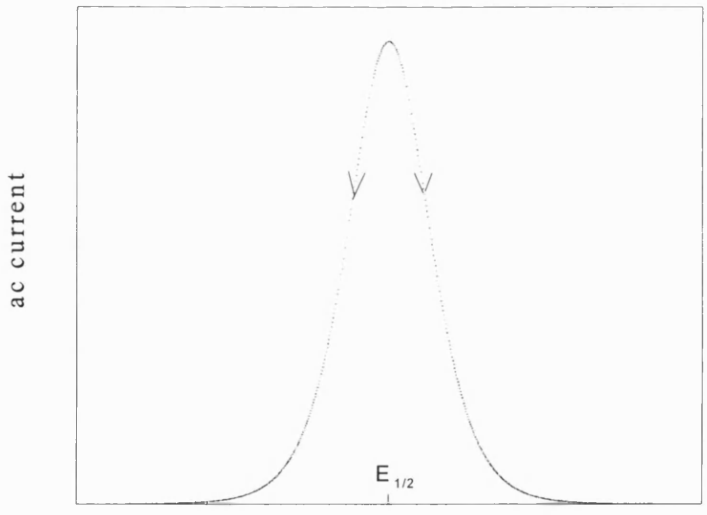

Figure 1.7 A cyclic ac voltammogram

The forward and backward scan are identical and symmetric about $E_{dc} = E_{1/2}$, where $E_{1/2}=E^0 -(RT/nF)\ln(f_{Red}D_{Ox}^{1/2}/f_{Ox}D_{Red}^{1/2})$. $E_{1/2}= E^{0'}$ when $D_{Ox} = D_{Red}$. The criteria for the totally reversible system are: phase angle 45^0 (ac current leads the voltage), peak half width, 90/n mV at 25^0C, and peak position and half width is independent under the low scan rate. Those formulas are modified for quasi – reversible systems where the dc process is reversible, but the ac process is not. The modified expression for the ac current is

$$i(\omega t) = i_{revs}(\omega t)F(t)G(\omega^{\frac{1}{2}}\lambda^{-1})\sin\left[\omega t + \cot^{-1}\left(1+\frac{(2\omega)^{\frac{1}{2}}}{\lambda}\right)\right] \qquad (1.18a)$$

Here

$$F(t) = 1 + \frac{(\alpha e^{-\Phi} - \beta)D^{\frac{1}{2}}\psi_0(t)}{ke^{-\alpha\Phi}} \qquad (1.18b)$$

$$G(\omega^{\frac{1}{2}}\lambda^{-1}) = \left\{\frac{2}{1+\left[1+\left((2\omega)^{\frac{1}{2}}/\lambda\right)\right]^2}\right\}^{\frac{1}{2}} \qquad (1.18c)$$

$$\psi_0(t) = \frac{k}{D^{\frac{1}{2}}}\left\{e^{-\alpha\Phi} - \left(e^{-\alpha\Phi} + e^{\beta\Phi}\right)\int \frac{\psi_0(t-\varsigma)d\varsigma}{(\pi\varsigma)^{\frac{1}{2}}}\right\} \qquad (1.18d)$$

Here

$$\lambda = \frac{k}{D^{\frac{1}{2}}}\left(e^{-\alpha\Phi} + e^{\beta\Phi}\right) \qquad (1.18e)$$

$$D = D_{Ox}^{\beta}D_{\mathrm{Re}\,d}^{\alpha} \qquad (1.18f)$$

$$\beta = 1 - \alpha \qquad (1.18g)$$

Here k is the rate constant of the electron transfer reaction at the electrode surface, and ω is the imposed ac angular frequency.

Generally speaking the frequency dependence of the ac current is non-linear except at low frequencies because F(t) and $G(\omega^{1/2}\lambda^{-1})$ are close to unity, and the peak potential varies with frequency, approaching $E_{1/2}$ at low frequencies. Details are given in the literature [33].

1.4.3 Voltammetry under steady state conditions

A steady state is a state in which in spite of the fact that none of the relevant properties of a system change, transport occurs between different regions of the system. Thus neither the potential or the concentrations of the electroactive species change with time when an electrode is in a steady state, the surface flux densities of Red and Ox and the current also have constant nonzero values. So steady-state voltammograms are simpler than the other two types discussed above. This simplicity enables us to predict the results of electrochemical experiments that would otherwise be too complicated to analyse. Microelectrodes, rotating-disk electrodes and channel electrodes are used to achieve reproducible steady states. A steady state voltammogram may be constructed in a point-by-point manner, but it is tedious. More conveniently, one may record the changing current that flows as the potential is changed continuously, provided that scan rate is slow enough that the electrode removes effectively in the steady state. The current-potential curves for the forward and backward sweeps overlap due to the unique feature of the steady state shown in figures 1.8a and 1.8c which represent conventional and ac voltammograms, respectively. If, however, the scan rate is too large, the forward and backward branches of the voltammograms will not overlap precisely, obtaining the results shown in figures 1.8c and 1.8d. If the scan rate is sufficiently large, the steady state conditions no longer

holds and the forward and backward branches of the voltammograms will be totally separate (not shown in the figures). Another feature of steady state voltammetry is the limiting currents that are independent of potential in conventional cyclic voltammetry, as can be seen in figures 1.8a. Note that the limiting currents also occur in transient voltammetry too due to limited transport. There are two factors, flow rate and scan rate, in a channel electrode in our experiments to be adjusted to achieve the steady state. Details will be discussed in the following chapters.

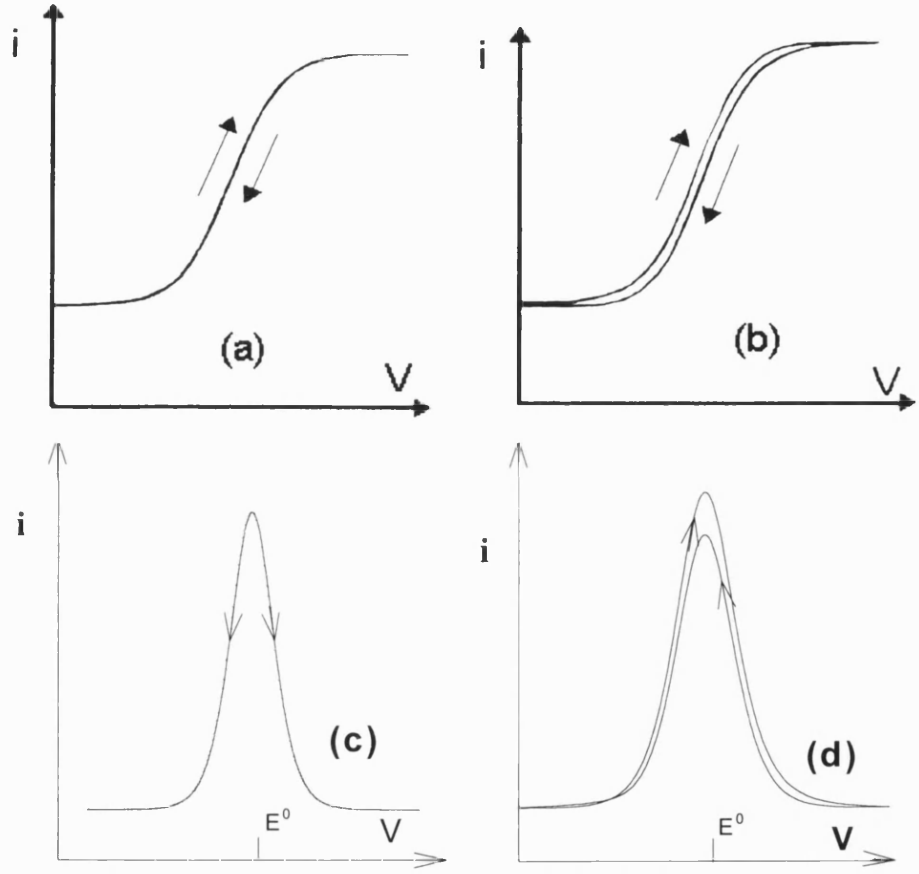

Figure 1.8 Cyclic voltammograms under the steady state conditions

(a) and (c) are ideal conventional cyclic and cyclic ac voltammograms under steady state, respectively.

(b) and (d) are conventional cyclic and cyclic voltammograms showing small deviation from true steady state conditions, respectively.

1.5 Hydrodynamic electrode methodology

1.5.1 The Channel Electrode

In this hydrodynamic system, solution moves over an electrode embedded in the wall of a channel [34] as depicted in figure 1.9. Consider a plug of solution [35-37] entering the channel in which frictional forces at the side of the channel ('edge' effects) can be considered to have negligible effect on the flow profile (h<<d). However, the effect of friction at the walls of the channel will be to slow down the flow in their vicinity, as shown in figure 1.10.

The Reynolds number, R_e, can be used to characterises the flow

$$R_e = 2h\frac{\rho v_0}{\mu} \tag{1.19}$$

where v_0 is the solution velocity of the centre of the channel and μ is the viscosity of the solution. ρ is the density of the solution, and the ratio, μ/ρ, is called kinematic viscosity. The flow is laminar if R_e is less than 2000 [34] after a lead in length l_e [38-39],

$$l_e = 0.022hR_e \tag{1.20}$$

Parabolic flow is established and

$$v_x = v_0\left(1-\frac{(h-y)^2}{h^2}\right) \tag{1.21}$$

Levich [33] first solved the convective diffusion equation for the channel electrode by invoking an approximation originally introduced by Leveque [40]

$$v_x = v_0\left(1 - \frac{(h-y)^2}{h^2}\right) = 2v_0\frac{y}{h} \tag{1.22}$$

which is valid at the electrode surface y ~ 0, i.e. in the vicinity of the channel walls, where the electrode is located. Furthermore the centre-line velocity is related to the volume flow rate, v_f, and the cross-section area, A, of the channel

$$v_f = \frac{2}{3}Av_0 = \frac{4v_0 dh}{3} \tag{1.23}$$

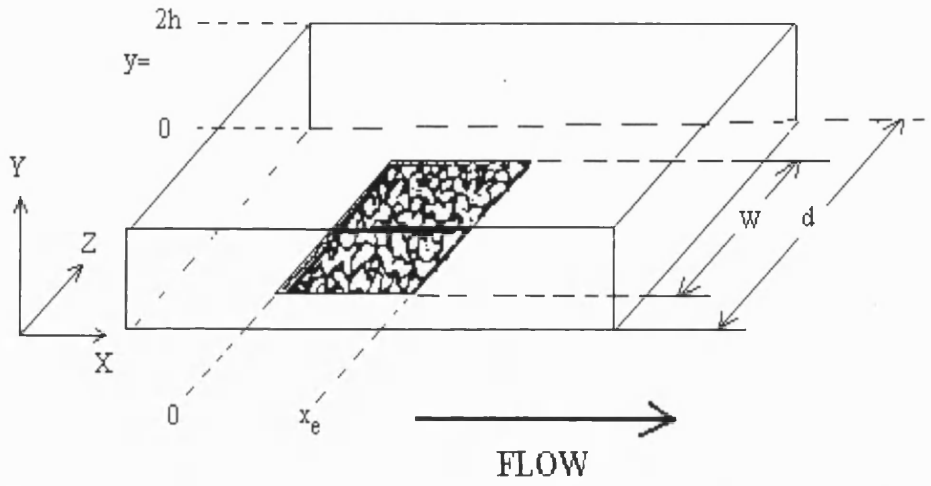

Figure 1.9 Coordinate system and dimensions of the channel flow-cell

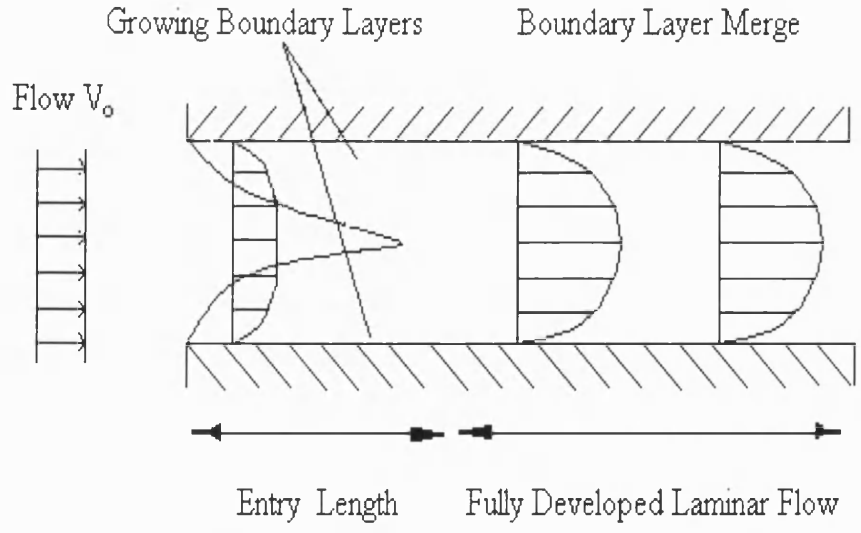

Figure 1.10 The solution velocity profile in the channel

The approximation replaces the parabolic velocity by a linear one near the electrode surface. It is satisfactory under conditions in which convection is efficient compared with diffusion because induced concentration changes are confined close to the electrode.

Assuming both diffusion in the direction of convective flow and diffusional edge effects to be negligible, it is considered that the species diffuses only in the y-direction (perpendicular to the electrode surface) and convects just in the x-direction (parallel to the electrode).

The convective diffusion equation with the Leveque approximation under steady state conditions becomes:

$$D_{\mathrm{Re}\,d}\frac{\partial^2 C_{\mathrm{Re}\,d}}{\partial y^2} = 2v_0\frac{y}{h}\frac{\partial C_{\mathrm{Re}\,d}}{\partial x} \tag{1.24}$$

The current is controlled solely by mass transport to the electrode surface if the concentration at the electrode surface is maintained close to zero by fast electrode kinetics.

Equation (1.24) can be solved subject to the boundary conditions

$$y = 0\,; \qquad C_{ox} \rightarrow 0$$

Now the total diffusional flux to the electrode may be calculated by integrating over the length, x_e:

$$J_{\mathrm{Re}\,d} = D_{\mathrm{Re}\,d}\int_0^{x_e}\left.\frac{\partial C_{\mathrm{Re}\,d}}{\partial y}\right|_{y=0} dx \tag{1.25}$$

There is a diffusion layer (thickness δ) formed under these conditions, which is given by:

$$\delta = D_{\mathrm{Re}d}\frac{C_{\mathrm{Re}d}^{bulk}}{J_{\mathrm{Re}d}} = \frac{1}{0.67}\left(\frac{D_{\mathrm{Re}d}hx_e}{v_0}\right)^{\frac{1}{3}} \qquad (1.26)$$

According to equation (1.4), the total mass transport limiting current to the electrode becomes:

$$i_{\mathrm{lim}} = nFAJ_{\mathrm{Re}d} = nFwx_eJ_{\mathrm{Re}d} = 0.925nwFC_{\mathrm{Re}d}^{bulk}\left(\frac{v_f D_{\mathrm{Re}d}^2 x_e}{h^2 d}\right)^{\frac{1}{3}} \qquad (1.27)$$

According to this equation, the channel height (2h) can be calibrated with a system with a known diffusion coefficient by plotting i_{lim} again $v_f^{1/3}$.

1.5.2 Homogeneous chemistry coupled to heterogeneous electron transfer

An application of hydrodynamic electrodes is the determination of the kinetics of electrochemical processes that involve heterogeneous electron transfers coupled to homeogeneous chemical steps. Some of mechanisms referred to in this thesis are listed below:

1) Simple electron transfer process

The electron transfer process is:

$$\mathrm{Red} \rightleftharpoons \mathrm{Ox} + \mathrm{ne}^-$$

where both Ox and Red are soluble species.

2) CE mechanism

This is defined by the following scheme,

$$\mathrm{Y} \rightleftharpoons \mathrm{Red}$$

$$\mathrm{Red} \rightleftharpoons \mathrm{Ox} + \mathrm{ne}^-$$

in which Y is electroinactive. The overall rate can be limited by the homogeneous chemical reaction if the electron transfer process which pulls chemical reaction to the right is very fast. When the electron transfer process is slow enough, it may become rate controlling.

3) EC′ mechanism

$$\text{Red} \rightleftharpoons \text{Ox} + ne^-$$

$$Ox + X \xrightarrow{k} \text{Re}d + P$$

Here X and P are electroinactive. an electrogenerated species Ox oxidises some other solution species (the substrate, X) with the regeneration of the original starting material which can thus undergo further electron transfer at the electrode surface.

1.6 Numerical solutions of the mass transfer equation and use of fast Fourier transform (FFT)

The basic philosophy of the numerical solution approach is to solve the differential equations describing the hydrodynamics and coupled chemical kinetics of a system and by adjusting parameters like rate constant, extinction coefficient etc. in the simulation, to obtain the best fit of the experimental data.

The most common simulation techniques are finite difference methods, and the most widely applied method is the explicit finite difference method for providing approximate solutions to partial differential equations, which was first introduced by Feldberg [41]. The basic principle behind all finite difference techniques for solving differential equations is to replace the derivatives by appropriate difference-quotient

approximations. The differential equations are thus replaced by a set of difference equations with the appropriate boundary and initial conditions, which can be solved.

Fast Fourier transform (FFT) techniques [42] are powerful and effective tools for solving partial differential equations, and they are used directly to filter signals in the frequency domain converted from the time domain for processing. The FFT algorithm, particularly the power- of-2 algorithm is a more effective one than Fourier transform (FT) [43-46], and it gives a complete set of complex values called real and imaginary components at any Fourier harmonics. This method is used in the present work to separate dc and ac signals.

1.6.1 The Backward Implicit Finite Difference Method (BIFD)

This section presents the backward implicit finite difference method for the numerical solution of mass transport equations for both the channel electrode and normal 3-electrode geometry. It is neither confined by the Leveque approximation, nor is it restricted in application to the case of first order coupled chemical kinetics. Rather, the method has been shown to be of general use in the generation of current-voltage curves for higher order mechanisms and importantly in the determination of kinetic parameters for experimental systems conforming to such electrochemical behaviour.

The details of the BIFD numerical solution of the convective - diffusion equations were developed by Anderson [47-48]. Whereas alternative methods involve matrix calculations based on a two-dimensional grid representing the (x, y) space, the BIFD method only involves vector calculations. The vectors describe concentrations in the y-direction for different values of x. The calculation proceeds downstream with each vector enabling the calculation of the next, starting from the vector defining

boundary and initial conditions specified for upstream of the electrode. The concentration profile of the reactants and products within the channel is calculated, and hence the flux to the electrode surface. The results of the simulation permit the steady-state current, the voltage, and current/time transient curves to be obtained [49], and the modified BIFD method allows chronoamperometric [50] and linear sweep voltammetric [51] measurements to be modelled.

There are many references in the literature extending the BIFD method to coupled chemical kinetics with heterogeneous electron transfer. In particular, kinetic parameters have been obtained for experimental systems which exhibit EC [52] or EC' [53-54], ECE [55], CE [56] electrochemical kinetics. Some of the investigations have employed the BIFD method to simulate the response obtained by *in situ* electrochemical spectroscopic techniques. If the finite difference grid is extended downstream of the electrode region, the absorption of radiation is simulated by integrating concentration profiles over the volume of the cell. All the investigations have been performed using only voltage-sweep methods either under transient or steady state conditions. In this work, the BIFD method was extended to PMRS studies based on the ac voltammetric technique. The full method is described in later chapters of this thesis.

1.6.2 The discrete Fourier transform method (DFT)

The development of an efficient algorithm for fast implementation of the discrete Fourier transform has led to a number of applications in such diverse disciplines as spectral analysis, medicine, thermograms, radar, sonar, acoustics, filtering, image processing, convolution and correlation studies, structural vibration, system design and analysis, and pattern recognition. Fast algorithms such as the fast Fourier transform

(FFT) lead to reduced computing time, reduced round - off error, and savings in storage requirements. The FFT based on the power-of-2 algorithm has been used to analysis PMRS signals in this thesis.

Let x(t) be a periodic time function. Applying the change in limits of integration to the integral for the Fourier series complex coefficient X(k) gives [42]

$$X(k) = \frac{1}{T}\int_0^T x(t)e^{-j2\pi kt/T}dt \tag{1.28}$$

Where T is the period in seconds and k is an integer.

The input to the DFT is a sequence of numbers rather than a continuous function of time x(t). The sequence of numbers usually results from periodically sampling the continuous signal x(t) at intervals of Δt s. The DFT is derived from x(t) using N samples taken at times t = 0, Δt, $2\Delta t$,..., (N-1) Δt. So t = $n\Delta t$, T = $N\Delta t$, therefore, we can use the simplified notation x(0), x(1), x(2),..., x(N-1) to mean samples of x(t) taken at times of 0, Δt, $2\Delta t$,..., $n\Delta t$,... (N-1) Δt, respectively. These N samples x(t) form the data sequence {x(0),x(1),...,x(n), ...,x(N-1)}, which we shall refer to as x(n), shown in Figure 1.11 for the 8-point samples.

Now we can express the relationship between the continuous and discrete-time values as

$$t \leftarrow \Delta t,\ dt \leftarrow n\Delta t,\ \ x(t) = x(n) \text{ at } t = n\Delta t \tag{1.29}$$

where n = 0, 1, 2, ... , N-1., Replacing the quantities in (1.28) according to (1.29) gives:

$$X(k) = \frac{1}{N}\sum_{n=0}^{N-1} x(n)e^{-j2\pi kn/N} \qquad k = 0,1,...,N-1 \tag{1.30}$$

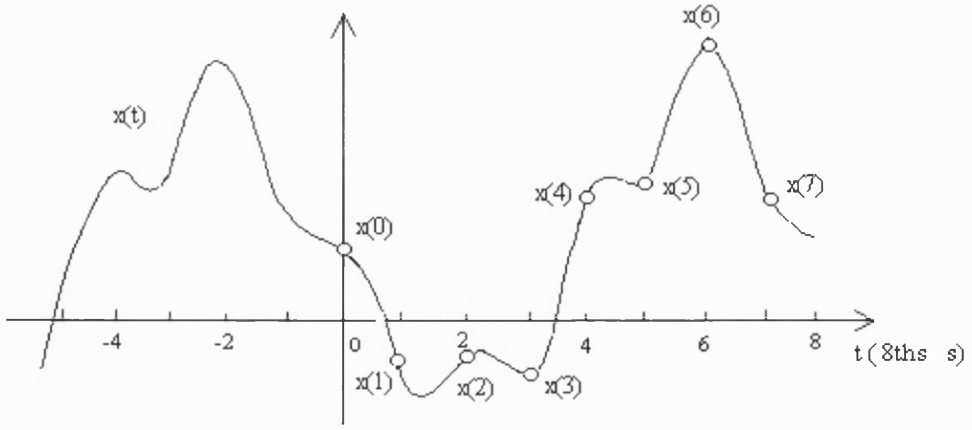

Figure 1.11 Periodic band-limited function x(t) and sampled values(dots)

The transform coefficient number k determines the number of cycles in Ts and identifies the frequency f as

$$f = k/T \quad Hz \tag{1.31}$$

Figure 1.12 illustrates the DFT coefficients for X(k). The sequence { X(0), X(1), ..., X(N-1) } is a transform sequence, which we shall call X(k).

If we define $W = e^{-j2\pi/N}$, equation (1.28) becomes

$$X(k) = \frac{1}{N}\sum_{n=0}^{N-1} x(n)W^{kn} \qquad k,n = 0,1,...,N-1 \tag{1.32}$$

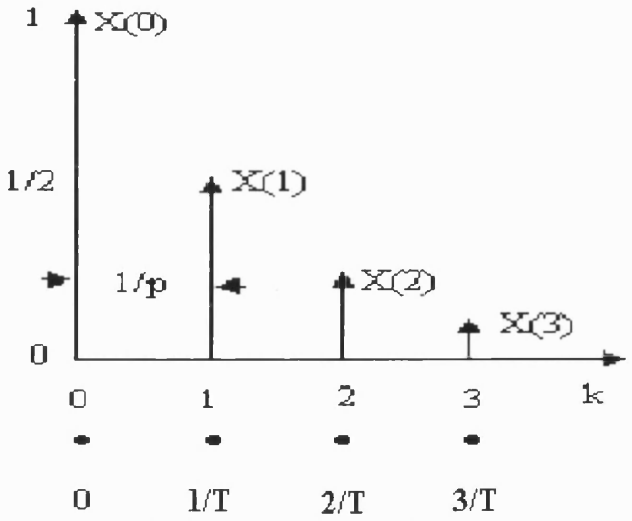

Figure 1.12 DFT coefficients versus transform sequence number and frequency

We can represent the DFT by a matrix. The input to the DFT is the data sequence contained in the vector x given by

$$x = [\, x(0), x(1), x(2), \ldots , x(N-1)]^T \tag{1.33}$$

where the superscript T denotes the transpose. The output of the DFT is the transform sequence contained in the vector X given by

$$X = [X(0), X(1), X(2), \ldots , X(N-1)\,]^T \tag{1.34}$$

The outputs are computed using the DFT definition (1.32), and given by

$$\begin{aligned} X(0) &= \frac{1}{N}\left(W^{0,0}W^{0,1}\cdots W^{0,N-1}\right)x \\ &\cdots\cdots\cdots\cdots\cdots\cdots\cdots\cdots \\ X(1) &= \frac{1}{N}\left(W^{1,0}W^{1,1}\cdots W^{1,N-1}\right)x \\ &\cdots\cdots\cdots\cdots\cdots\cdots\cdots\cdots \\ X(0) &= \frac{1}{N}\left(W^{N,0}W^{N,1}\cdots W^{N,N-1}\right)x \end{aligned} \tag{1.35}$$

All of the operations in the equations (1.35) can be combined into a matrix form given by

$$X = \frac{1}{N}W^E x \tag{1.36}$$

where

$$W^E = \begin{bmatrix} W^{0,0} & W^{0,1} & \cdots & W^{0,n} & \cdots & W^{0,N-1} \\ W^{1,0} & W^{1,1} & \cdots & W^{1,n} & \cdots & W^{1,N-1} \\ \vdots & \vdots & \vdots & \vdots & \vdots & \vdots \\ W^{n,0} & W^{n,1} & \cdots & W^{n,n} & \cdots & W^{n,N-1} \\ \vdots & \vdots & \vdots & \vdots & \vdots & \vdots \\ W^{N-1,0} & W^{N-1,1} & \cdots & W^{N-1,n} & \cdots & W^{N-1,N-1} \end{bmatrix} \tag{1.37}$$

The DFT matrix is a square matrix with N rows and N columns. Since the DFT has an N-point input and an N-point output, it is called an N-point DFT.

A quick and easy way to derive an FFT algorithm is to manipulate W^E into a product of matrices.

1.6.3 The power-of-2 FFT algorithm

The Fast Fourier transform uses a greatly reduced number of arithmetic operations in the computation of the DFT. An easy way to visualise the procedure for generating FFT algorithms results from matrix factorisation of the W^E. It is

$$W^E = W^{E_L} W^{E_{L-1}} \cdots W^{E_2} W^{E_1} \tag{1.38}$$

Here L is the number of integral factors of N. The easiest case is when $N = 2^L$. This case is called the power-of-2 FFT algorithm. Since N is a power of 2, N/2 is an integer, and samples separated by N/2 in the data sequence can be combined to yield:

$$X(k) = \frac{1}{N} \sum \left[x(n) + x(n + N/2) W^{kn/2} \right] W^{kn} \tag{1.39}$$

Equation (1.39) can be simplified because $W^{kn/2}$ takes only two values for integral values of k, as is seen from:

$$W^{kn/2} = e^{(-j2\pi/N)*(kn/2)} = e^{-j\pi k} = (-1)^k \tag{1.40}$$

First, let k be even, so that $W^{kn/2} = 1$. Also let

$k = 2l$, $l = 0, 1, 2, \ldots, N/2 - 1$

$$g(n) = x(n) + x(n+N/2) \tag{1.41}$$

Then the series for even - numbered DFT coefficients is given by

$$X(2l) = \frac{1}{N}\sum_{n=0}^{N/2-1} g(n)W^{2ln} = \frac{1}{2}\frac{1}{N/2}\sum_{n=0}^{N/2-1} g(n)\left(W^2\right)^{ln} \tag{1.42}$$

The right side of (1.42) is one -half times an (N/2)-point DFT because

$$W^2 = e^{-j2\pi/(N/2)}$$

and the input sequence is {g(0), g(1), g(2), ... , g(N/2 -1)}

Now let k be odd, so that $W^{kn/2} = -1$. Also let

$$k = 2l + 1,\ l = 0, 1, ..., N/2 - 1$$

$$h(n) = x(n) - x(n+N/2) \tag{1.43}$$

Then the series for odd-numbered DFT coefficients is given by

$$X(2l+1) = \frac{1}{N}\sum_{n=0}^{N/2-1} h(n)W^{(2l+1)n} = \frac{1}{2}\frac{1}{N/2}\sum_{n=0}^{N/2-1} h(n)W^{n}\left(W^2\right)^{ln} \tag{1.44}$$

The right side of (1.44) is one-half times an (N/2)-point DFT for the input sequence {h(0), h(1), h(2), ... , h(N/2 -1)}. It can be concluded that for values of both even and odd k we can reduce DFT inputs by a factor of 2 by letting g(n) = x(n) + x(n+N/2) and h(n) = x(n) - x(n+N/2), respectively, and use an (N/2)-point DFT to transform the sequence defined by g(n) and h(n), respectively.

Figure 1.13 shows the computer procedure for minimised multiplication for the 8-point FFT.

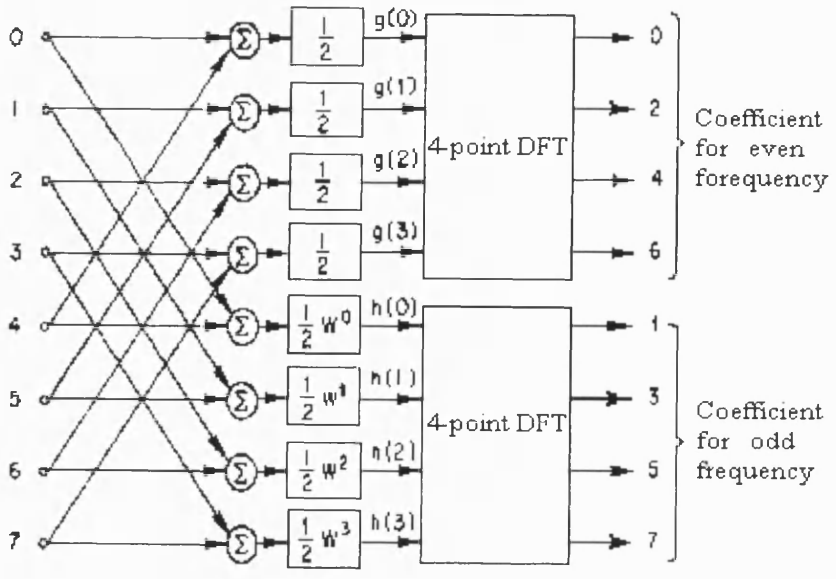

Figure 1.13 Reduction of an 8-point DFT to two 4-point DFT

A repetitive structure for the 8-point FFT can be seen in the FFT of Fig 1.14. The first stage on the left determines a matrix W^{E_1}, the second stage a matrix W^{E_2}, and the right stage a matrix W^{E_3} ($W^E = W^{E_1} W^{E_2} W^{E_3}$).

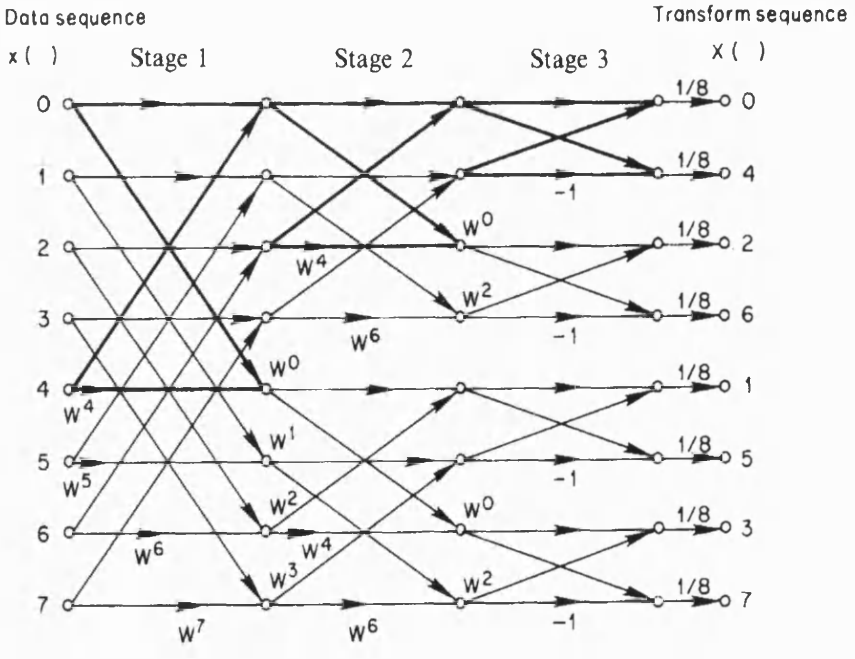

Figure 1.14 Flow diagram for an 8-point FFT

The operations can be extended to give a 16-point FFT, a 32-point FFT, and so forth. Generally speaking the input signals are complex, so the following definition must be used:

$$e^{-j\theta} = \cos\theta - j\sin\theta \tag{1.45}$$

and follows that

$$W = e^{-j2\pi/N} = \cos\left(\frac{2\pi}{N}\right) - \sin\left(\frac{2\pi}{N}\right) \tag{1.46}$$

Equations (1.42) and (1.44) become

$$X_{(2l)} = \mathrm{Re}\, X_{(2l)} - \mathrm{j}\ \mathrm{Im}\, X_{(2l)} \tag{1.47}$$

$$X_{(2l+1)} = \mathrm{Re}\, X_{(2l+1)} - \mathrm{j}\ \mathrm{Im}\, X_{(2l+1)} \tag{1.48}$$

where,

$$\mathrm{Re}_{(2l)} = \frac{1}{N}\sum_{n=0}^{N/2-1} g(n)\cos\frac{4\pi \ln}{N} \tag{1.49}$$

$$\mathrm{Im}\, X_{(2l)} = \frac{1}{N}\sum_{n=0}^{N/2-1} g(n)\sin\frac{4\pi \ln}{N} \tag{1.50}$$

$$\mathrm{Re}\, X_{(2l+1)} = \frac{1}{N}\sum_{n=0}^{N/2-1} h(n)\cos\frac{2\pi(2l+1)n}{N} \tag{1.51}$$

$$\mathrm{Im}\, X_{(2l+1)} = \frac{1}{N}\sum_{n=0}^{N/2-1} h(n)\sin\frac{2\pi(2l+1)n}{N} \tag{1.52}$$

Theoretically speaking, their magnitudes are not absolutely equal and depend on l, n, and N, but X(k) should be the same and stand for the Fourier transform coefficient at the frequency f = k/T. In our case, the real and imaginary components have specific meaning which is related to the properties of the double layer and the charge transfer

resistance. The outputs should be real ones since the inputs are real inputs. We are only interested in k = 0 (dc component) and k =1 (ac component) in the current research (PMRS studies) in this thesis.

References:

1. L.M. Peter, Phil. Trans. R Lond. A, **354**, 1613(1996).
2. D.E. Smith, Anal. Chem., **35**, 610 &1811(1963).
3. A.M. Bond, R.J. O'Halloran, I. Ruzic and D.E. Smith, Anal. Chem., **48**, 872(1976)
4. A.M. Bond, R.J. O'Halloran, I. Ruzic and D.E. Smith, Anal. Chem., **50**, 216(1978)
5. M.D. Ryan and G.S. Wilson, Anal. Chem. **54**, 20R(1982).
6. A.W. Aylmer-Kelly, A. Bewick, P.R. Cantrell and A.M. Tuxford, Discussion, Faraday Soc., **56**, 96(1973).
7. A. Bewick, J. Mellor and S. Pons, Electrochim. Acta., **23**, 77 (1978).
8. A. Bewick, A.M. Tuxford, J. Electroanal. Chem., **47**, 255(1973).
9. S. Pons and S.B. Khoo, Electrochim. Acta., **27**, 1161(1982).
10. S. Pons and S.B. Khoo, J.Am. Chem. Soc., **104**, 3845(1982).
11. A. Bewick, J. Mellor and S. Pons, Electrochim. Acta., **25**, 465(1980)
12. E.E. Bancroft, H.N. Blount and F.M. Hawkridge, Adv. Chem. Ser., **201**, 23(1982).
13. A. S. Hinman, J.F. McAleer and S. Pons, J. Electroanal. Chem., **154**, 45 (1983).
14. C. Gutierrez and M.A. Martinez, J. Electrochem. Soc., **131**, 1874 (1986).
15. D.J. Blackwood and L.M. Peter, Electochim. Acta., **35**, 1073(1990).
16. J.A. Caram and C. Gutierrez, J. Electroananl. Chem., **307**(1-2), 99(1991).
17. J.A. Caram and C. Gutierrez, J. Electroananl. Chem., **305**(2), 275(1991).
18. J.A. Caram and C. Gutierrez, J. Electroananl. Chem., **305**(2), 259(1991).

19. J.A. Caram and C. Gutierrez, J. Electroananl. Chem., **314**(1-2), 275(1991).

20. J.A. Caram and C. Gutierrez, J. Electroananl. Chem., **323**(1-2), 213(1992).

21. J.A. Caram and C. Gutierrez, J. Electroananl. Chem., **336**(1-2), 309(1992).

22. J.A. Caram and C. Gutierrez, J. Electroananl. Chem., **344**(1-2), 313(1993).

23. A. Cuesta and C. Gutierrez, J. Electroananl. Chem., **382**(1-2), 153(1995).

24. A. Kowal and C. Gutierrez, J. Electroananl. Chem., **395**(1-2), 243(1995).

25. D. J. Fermin, Z. Ding, P. F. Brevet and H. H. Girault, J. Electroanal. Chem., **447**(1-2), 125(1998).

26. E. Gileadi, Electrode Kinetics for Chemists, Chemical Engineers, and Materials Scientists, VCH, 1993

27. S. Glasstone, K.J. Laidler and H. Eyring, The Theory of Rate processes, McGraw Hill, New York, 575 (1941).

28. J.A.V. Butler, Trans. Faraday Soc., **19**, 734 (1924).

29. T. Erdey-Gruz, M.Z. Volmer, Phys. Chem., **150**A, 203(1930).

30. A. C. Fisher, Electrode Dynamics, Oxford University Press, 1996

31. A.J. Bard and L.R. Faulner, Electrochemical Methods, John Wiley & Sons, 1980

32. Southampton Electrochemistry Group, Instrumental Methods in Electrochemistry, John Wiley & Sons, 1985.

33. D. E. Smith in A.J. Bard (Ed), Electroanalytical Chemistry, Marcel Dekker, New York, **1**, 1(1966).

34. R.G. Compton and P.R. Unwin, in Comprehensive Chemical Kinetics, Eds. Hamnett, R.G. Compton, Amsterdam, Elsevier, **29**, Chapter 6 (1988).

35. V.G. Levich, Physicochemical Hydrodynamics, Prentice-Hall, Englewood Cliffs, NJ, (1962).

36. R.B. Bird, W.E. Stewart, E.N. Lightfoot, Transport Phenomena, Wiley, New York, (1960).

37. J.S. Newman, Electrochemical Systems, Prentice-Hall, Englewood Cliffs, (1973).

38. W.J. Albery, S. Bruckenstein, J. Electroanal. Chem., **144**, 105(1983).

39. B.A. Coles and R.G. Compton, J. Electroanal. Chem, **144**, 87(1983).

40. M.A. Leveque, Ann. Mines. Mem. Ser., **12**(13), 201(1928).

41. S. W. Feldberg and C. Auerbach, Anal. Chem., **36**, 505(1964).

42. D. F. Elliottand K. R. Rao, Fast Transform - Algorithm, Analysis,Applications, Academic press. INC.,(1982).

43. J. W. Cooley and J. W. Tukey, Math. Computation, **19**, 297(1965).

44. J.W. Cooley, P. A. W. Lewis and P. D. Welch, J. Sound Vib., **12**, 315(1970).

45. W. M. Gentleman and G. Sande, Fast Fourier transforms – for fun and profit. Proceedings of AFIPS Fall Joint Computer Conf., Washington D.C., Spartan, **29**, 563 (1996).

46. R.W. Hochney, The Potential Calculation and some Applications, Methods in Computational Physics 9, Academic Press, New York, 1970

47. S. Moldoveanu and J.L. Anderson, J. Electroanal. Chem., 175, 67(1984).

48. J.L. Andrerson and S. Moldoveanu, J. Electroanal. Chem., **179**, 107&119(1984).

49. R.G. Compton, M.B.G. Pilkington, J. Chem. Soc. Faraday Trans., **85**, 2255(1989).

50. R.G. Compton, A.C. Fisher, J. Phys. Chem., **95**, 3538(1991).

51. R.G. Compton and A.C. Fisher, J. Appl. Electrochem., **22**, 38(1992).

52. R.G. Compton, B.A. Coles, G.M. Stearn and A.M. Waller, J. Chem. Soc. Faraday. Trans. **85**, 761(1989).

53. R.G. Compton, A.M Waller and R.J. Northing, J. Chem. Soc. Faraday. Trans. **86**, 335 (1990).

54. R.G. Compton, J.C. Eklund and A.C. Fisher, J. Chem. Soc. Faraday. Trans., **86**, 2951 (1990).

55. R.G. Compton, J. Electoanal. Chem. , **322**, 183(1992).

56. R.H. Muller and R.L. Garman, Ind. Eng. Chem., **10**, 339(1938).

CHAPTER TWO

Studies on hydrodynamic potential modulated reflectance spectroscopy

2.1 Introduction

Potential modulated reflectance spectroscopy (PMRS) enables the electrode/electrolyte solution interfacial region to be monitored in the UV-visible region *in situ* [1]. PMRS is applied mainly to the study of semiconductors [2-4]. EER will be discussed in the second part in derived from electrolyte electroreflectance spectroscopy (EER) which was developed in the 1960s and this thesis. PMRS is generally used to study systems where electrochemistry occurs at the metal-solution interface. The technique of modulated specular reflectance spectroscopy has been used in the past to provide qualitative information about reaction mechanisms at the surface or in the diffusion layer. Bewick and Texford [5] was first used PMRS as a spectroelectrochemical technique in 1970 for the study of change in reflectivity of a platinum electrode. Here, electrochemical information about surface oxide layer formation and adsorption of hydrogen on the platinum was derived from the modulated reflectance response. Since then, this modulation technique has been increasingly used in electrochemical studies, most notably of the passivation of metal electrodes [6-10], the identification of intermediates in electrochemical reactions [11] and the studies of adsorption species at electrode surfaces [12-15]. In 1983 Hinman et al [16] introduced small sinusoidal perturbation modulated ac reflectance spectroscopy and gave some mathematical description of the processes. Blackwood and Peter [17-18] investigated the characterisation of anodic oxide films on titanium and Fe(II)/Fe(III), Fe(III)/Fe(IV) couples on Fe within the range of wavelengths of interest. Walker et al [19] used PMRS to study the anodic oxidation of ruthenium, which allowed identification of soluble RuO_4^{2-} and RuO_4^- species formed on the onset of oxygen evolution. Ding and Fermin et al. [20-22]

studied the kinetics of methyl orange transfer across liquid - liquid interfaces by using PMRS and ac impedance. The rate constant of the electron transfer and the transfer coefficient were determined. Huerta et al.[23] used PMRS to study adsorption on Pt (111) in different acidic and alkaline electrolytes. Here, the usual hydrogen adsorption-desorption region in both media corresponds to a zone in which PMRS signal is practically zero and does not change with the potential. However, in the anomalous region, an increase in PMRS signal was observed and electron density of the platinum surface has been used to explain phenomena in their paper. Recently Sagara et al [24] have characterised monolayers of thiol-functionalised viologens on a polycrystalline gold electrode by PMRS and cyclic voltammetry. The ratio of the binding constant to dication (V^{2+}) to radical cation ($V^{\bullet+}$) and the electron-transfer rate constant for the monolayers were estimated. Although there have been numerous qualitative applications of the method [17-23] due to its simplicity and convenience, there have been fewer examples of the quantitative application of PMRS.

Small synchronous changes in the optical properties of the electrode-solution interface that arise from the modulation of the electrode potential by a square or sine wave of known amplitude (AM) and frequency of modulation, can be measured as a function of wavelength λ, potential E, and frequency ω. These variables correspond to three kinds of measurements — PMRS, PMRS voltammetry and frequency resolved PMRS, respectively. The optical properties of the interface between electrode and solution are perturbed as an outcome of Faradaic processes provided the species involved absorb light in the selected wavelength region (PMRS). The optical properties of the interfacial region can also be changed by the

modulation of the optical dielectric constant of a semiconductor electrode by the applied electric field (electrolyte electroreflectance, details are present in next part in this thesis).

When an alternating Faradaic current flows at an electrode, it results in the alternate formation and removal of one form of the redox couple at the surface of the electrode. According to the Beer–Lambert law, the intensity of a light beam either transmitted through or reflected from the surface of the electrode at a given wavelength will vary in accordance with the changes of the concentrations of the related species of the redox couple in the interface. Since the change in absorbance due to Faradaic processes is proportional to the charge passed, the modulated reflectance signal attenuates with increasing frequency. In the present work, all parameters in the interface have been described quantitatively as a function of time and distance in PMRS voltammetry and solved by numerical simulation. The results are compared with experimental data for different reaction mechanisms including electron transfer processes with coupled chemical reaction.

It is clear that there is no dc stationary state in unstirred solution but when the scan rate is slow enough (a few mV/sec), the local concentrations are determined by the "dc" steady state. The ac perturbation results in a periodic steady state superimposed on the dc state. The analytical solution of a system with a simple electron transfer process for PMRS can be obtained for these conditions. In general, natural convection may interfere into with the experiment so that the well-defined mass transport [25] is needed. For this reason we need either rotating disk electrode (RDE) or a channel cell electrode (CCE) to achieve steady state. In the present work the channel cell was chose for that reason. In order to solve a range of problems including coupled chemical reaction, we have to have recourse to numerical simulation methods. This chapter deals with PMRS with a simple electron

transfer process occurred at the surface of the electrode. The analytical solution has been used to check the numerical simulation method in unstirred solution, and then simulation method is extended to the channel electrode under flow conditions. The analytical and simulation results not only match very well, but also are in good agreement with the experimental data. The Fast Fourier Transform (FFT) algorithm was used to derive the frequency response of the concentrations/spectroscopic signals at the electrode in this part of thesis. Chapter 3 deals PMRS with coupled chemical reactions.

2.2 Theory

The electrochemical studies have been performed under specific mass transport conditions using either unstirred solution and a linear potential sweep or a channel electrode system with a linear potential sweep to enable a quantitative description of mass transfer. Consider a simply reversible electron transfer reaction, carried out at a well-defined electrode, like a channel electrode or planar electrode, in unstirred solution. Both Ox and Red are soluble.

$$\text{Red} \rightleftharpoons \text{Ox} + \text{ne} \tag{2.1}$$

The potential is swept at a very slow scan rate with a superimposed small amplitude sinusoidal perturbation from an initial value, E_i, at which no reaction takes place, to one corresponding to the value of interest. The electrode potential, E(t), is therefore given by:

$$E(t) = E_{dc} + \Delta E \sin(\omega t) \tag{2.2}$$

$$E_{dc} = E_i \pm \upsilon t \tag{2.3}$$

Here, υ is the scan rate, and the sign (±) depends on the scan direction. ΔE is the amplitude of the sinusoidal voltage and ω is its angular frequency. The dc "term" is used here to indicate that the sweep rate is sufficiently low that the periodic response is not influenced by the scan.

2.2.1 Absorbance

Consider a beam of light with a certain wavelength that passes through solution to irradiate the electrode surface and is then reflected back without losses from the electrode as shown in figure 2.1.

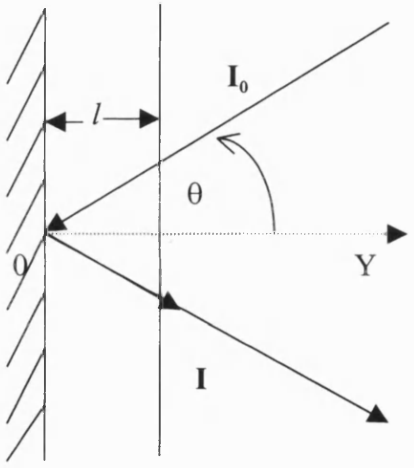

Figure 2.1 A diagram of the incident and reflected light

The reduction in intensity of the light beam, *dI*, is expressed by the Beer-Lambert law:

$$dI = -I_0\left[\alpha_{Ox}C^{Ox}_{(y,t)} + \alpha_{Red}C^{Red}_{(y,t)}\right]dy \qquad (2.4)$$

Here I_0 is the intensity of the incident light, I is the intensity of the reflective light, α_{Ox} and α_{Red} are molar extinction coefficients of species Ox and Red, respectively, $C^{Ox}_{(y,t)}$, and $C^{Red}_{(y,t)}$

are the concentrations of species OX and Red, respectively.

Integrating Equation (2.4) within the region l leads to:

$$\ln\frac{I}{I_0} = -\frac{2}{\cos\theta}\int_0^l [\alpha_{Ox}C_{(y,t)}^{Ox} + \alpha_{Red}C_{(y,t)}^{Red}]dy \tag{2.5}$$

Here the factor 2 indicates that the light passes through the solution twice, θ is the angle of the incident light, l is the length of the light passed through perpendicular to the electrode plane.

The absorbance, A(t), is given by

$$A(t) = \log\frac{I_0}{I} = \frac{2}{\cos\theta}\int_0^l (\varepsilon_{Ox}C_{(y,t)}^{Ox} + \varepsilon_{Red}C_{(y,t)}^{Red})dy \tag{2.6}$$

Here ε_{Ox} and ε_{Red} are the molar absorption coefficients of species Ox and Red, respectively, and have $\alpha_{Ox} = 2.303\varepsilon_{Ox}$, $\alpha_{Red} = 2.303\varepsilon_{Red}$. In some case the specific wavelength of the incident light can be chosen so that $\varepsilon_{Ox} = 0$ or $\varepsilon_{Red} = 0$, so the expression can be simplified as

$$A(t) = \frac{2\varepsilon}{\cos\theta}\int_0^l C(y,t)dy \tag{2.7}$$

Here ε stands for ε_{Ox} or ε_{Red}, C(y,t) represents $C_{(y,t)}^{Ox}$, or $C_{(y,t)}^{Red}$.

The number of moles of species Ox produced or Red consumed in reaction (2.1) at any given time must be equal to the number of moles of charge transferred in the interface as expressed by Faraday's law:

$$\int_0^l C(y,t)dy = \frac{1}{nFA}\int_0^t i_f(t)dt \tag{2.8}$$

Here $i_f(t)$ is the Faradaic current, A is the area of the electrode, t is time. Equation (2.7) can be rewritten as

$$A(t) = \frac{2\varepsilon}{\cos\theta}\int_0^t C(y,t)dy = \frac{2\varepsilon}{nFA\cos\theta}\int_0^t i_f(t)dt \qquad (2.9)$$

2.2.2 ΔR/R (PMRS signal)

In PMRS experiments, the electrode potential is modulated by a superimposed sinusoidal ac signal, which means that it is modulated between two values of potential V_1 and V_2 shown in figure 2.2a and centred on the mean value, dc potential $E_{dc}= (V_2+V_1)/2$. It is assumed that the modulation frequency is sufficiently high that the ac and dc components can be separated. After some time the periodic steady state is established. So the intensity of the reflective light will oscillate between two values I_1 and I_2 shown in figure 2.2b with the same frequency of the superimposed ac signal with the mean value, I_{dc} or I, corresponding to the intensity of the reflected light at the dc potential E_{dc}. The effective reading by a lock-in amplifier, ΔI, will be given in root mean square (RMS), that can be expressed as $\Delta I = \frac{|I_2 - I_1|}{2\sqrt{2}} = \frac{|I_2 - I|}{\sqrt{2}} = \frac{|I_1 - I|}{\sqrt{2}}$. Thus ΔI/I is measured by the ratio of the changes of the intensity, ΔI, to the intensity of the reflected light, I, obtained using a low - pass filter in the lock-in at the potential E_{dc}. It is

$$\frac{\Delta I}{I} = \left|\frac{I_2 - I}{I}\right| = \left|\frac{I_1 - I}{I}\right| \qquad (2.10)$$

Here $|I_2\text{-}I| = |I_1\text{-}I|$ in our case, It is assumed that $I_1 > I$ for convenience.

The reflectance, R, is defined as:

$$R = \frac{I}{I_0} \tag{2.11}$$

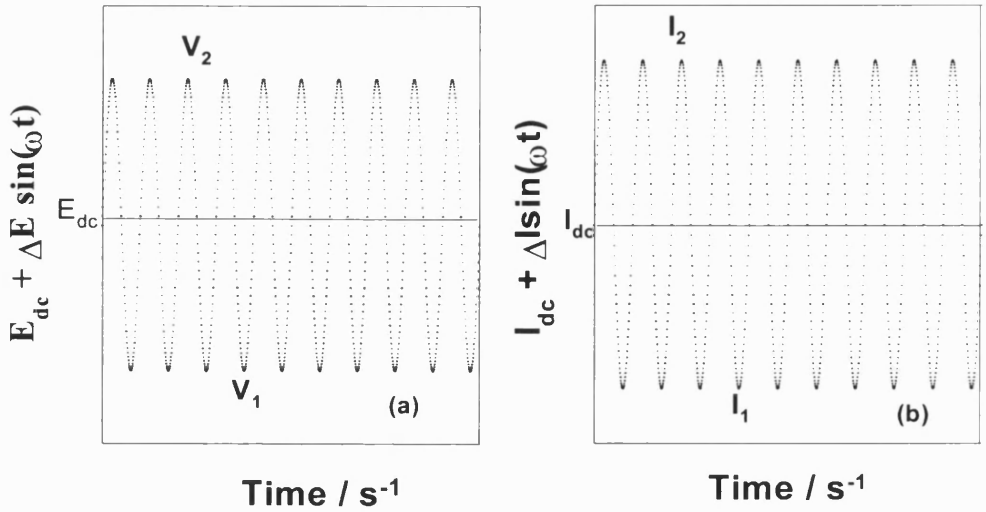

Figure 2.2 Wave forms of the potential applied and the intensity of the reflected light with same frequency ω and phase shift ϕ under the periodic steady state

a – Potential wave form applied to the electrode

b – Intensity of the reflected light at the electrode surface

So the equation (2.10) can be rewritten as

$$\frac{\Delta I}{I} = \frac{I_1 - I}{I} = \frac{I_1/I_0 - I/I_0}{I/I_0} = \frac{R_1 - R}{R} = \frac{\Delta R}{R} \tag{2.12}$$

$$\frac{\Delta R}{R} = \frac{I_1}{I} - 1 \tag{2.13}$$

Note that normalisation is necessary in order to compensate for the wavelength dependence of the incident lamp intensity and to allow for changes in surface reflectivity that may occur during the electrochemical process. It is also assumed that the concentration profiles and

surface concentrations of species in the interfacial region are determined almost entirely by the linear sweep. The ac component represents a small perturbation of these values based on the mean value. The dc concentration of species Ox or Red is $C_{(y,0)}$, called as the mean concentration, the ac concentration is $\Delta C_{(y)}\sin(\omega t+\phi)$, $\Delta C_{(y)}$ is the amplitude of the concentration wave, and ϕ is the phase angle. I_1 is the intensity of the reflected light after a certain time (greater than a few periods of the imposed ac signal to allow the periodic stationary state to be established) while the dc potential remains sufficiently constant where the concentration become $C_{(y,0)} + \Delta C_{(y)}\sin(\omega t+\phi)$. Note the time scales for the dc and ac responses are separated for convenience of the mathematical treatment [16, 26]. According to equation (2.5), if it is assumed that absorption of one species in solution can be neglected, one obtains:

$$R = \frac{I}{I_0} = e^{-\frac{2}{\cos\theta}\int_0^l \alpha C_{(y,0)}dy} \tag{2.14}$$

$$R_1 = \frac{I_1}{I_0} = e^{-\frac{2}{\cos\theta}\int_0^l \alpha (C_{(y,0)}+\Delta C(y)\sin(\omega t+\phi))dy} \tag{2.15}$$

So equation (2.13) becomes

$$\frac{\Delta R}{R} = e^{-\frac{2}{\cos\theta}\int_0^l \alpha \Delta C(y)\sin(\omega t+\phi))dy} - 1 \tag{2.16}$$

In experiments where both the amplitude of the imposed sine wave and the scan rate are small, and the frequency of the imposed sine wave is sufficiently high to satisfy, the condition, $2\pi\nu << \omega\Delta E$ [16, 26], the assumptions made above are approximately met.

Equation (2.16) can be simplified to become:

$$\frac{\Delta R}{R} = -\frac{4.606\varepsilon}{\cos\theta}\int_0^l \Delta C(y,t)dy \qquad (2.17)$$

Substituting equation (2.8) into equation (2.17) gives:

$$\frac{\Delta R}{R} = -\frac{4.606\varepsilon}{\cos\theta}\int_0^l \Delta C(y,t)dy = -\frac{4.606\varepsilon}{nFA\cos\theta}\int_0^t \Delta i_f(t)dt \qquad (2.18)$$

Here $\Delta C(y,t) = \Delta C_{(y)}\sin(\omega t+\phi)$, $\Delta i_f(t) = \Delta i \sin(\omega t+\psi)$, where ψ is the phase angle between the current and voltage, and Δi is the amplitude of the ac current. Note that $\Delta C(y,t)$ and $\Delta i_f(t)$ are the rms values.

It can be seen from equations (2.14) and (2.16) that both R and ΔR are functions of α, the incident angle, θ, and the concentration, $C_{(y,0)}$ which is related to the dc potential, E_{dc}. ΔR is also a function of the amplitude and frequency of the imposed sine wave. The ratio, $\Delta R/R$, is only a function of the ac concentration of species Ox or Red, which is linked to the amplitude and frequency of the imposed sine wave at a given dc potential. All those parameters are proportional to properties of the original electroactive materials such as the absorption, the concentration etc..

Equation (2.18) can be used to calculate the PMRS signal when ε and $\Delta C(y,t)$ or $\Delta i_f(t)$ are known.

2.2.3 Theoretical solution for stationary conditions

In the absence of migration effects, the general diffusion-convection equations describing the distribution of species Ox and Red for the reaction (2.1) in time (t) and space

(x, y, z) in three-dimension space are respectively:

$$\frac{\partial C_{Ox}}{\partial t} = D_{Ox}\frac{\partial^2 C_{Ox}}{\partial x^2} + D_{Ox}\frac{\partial^2 C_{Ox}}{\partial y^2} + D_{Ox}\frac{\partial^2 C_{Ox}}{\partial z^2} - v_x\frac{\partial C_{Ox}}{\partial x} - v_y\frac{\partial C_{Ox}}{\partial y} - v_z\frac{\partial C_{Ox}}{\partial z} \qquad (2.19)$$

$$\frac{\partial C_{Red}}{\partial t} = D_{Red}\frac{\partial^2 C_{Red}}{\partial x^2} + D_{Red}\frac{\partial^2 C_{Red}}{\partial y^2} + D_{Red}\frac{\partial^2 C_{Red}}{\partial z^2} - v_x\frac{\partial C_{Red}}{\partial x} - v_y\frac{\partial C_{Red}}{\partial y} - v_z\frac{\partial C_{Red}}{\partial z} \qquad (2.20)$$

The Cartesian co-ordinates x, y and z can be understood with reference to figure 2.2 which is a schematic diagram of a channel electrode (note the y direction is the direction normal to the electrode in stagnant solution). v_x, v_y, v_z are the solution velocity in the x-, y- and z-direction, respectively. In stagnant solution with the planar electrode with a size of great than 1mm×1mm, the convection is absent, and the "edge effect" can be neglected, so equations (2.19) and (2.20) can be reduced to:

$$\frac{\partial C_{Ox}}{\partial t} = D_{Ox}\frac{\partial^2 C_{Ox}}{\partial y^2} \qquad (2.21)$$

$$\frac{\partial C_{Red}}{\partial t} = D_{Red}\frac{\partial^2 C_{Red}}{\partial y^2} \qquad (2.22)$$

Here only one dimensional diffusion in y-direction is considered. The relevant boundary conditions for equations (2.21) and (2.22) are:

For $t = 0, y \geq 0$,

$$C_{Ox} = 0 \qquad C_{Red} = C_{Red}^{Bulk} \qquad (2.23)$$

For $t > 0, \quad y = 0$,

$$D_{Ox}\frac{\partial C_{Ox}}{\partial y}\Big|_{y=0} = -D_{Red}\frac{\partial C_{Red}}{\partial y}\Big|_{y=0} = \frac{i_f(t)}{nFA} \qquad (2.24)$$

$$\frac{C_{Ox}}{C_{\mathrm{Re}\,d}}\Big|_{y=0} = \left(\frac{D_{\mathrm{Re}\,d}}{D_{Ox}}\right)^{\frac{1}{2}} \exp(\Phi + \xi(t)) \tag{2.25}$$

For all t, y $\rightarrow \infty$,

$$D_{Ox}\frac{\partial C_{Ox}}{\partial y} = -D_{\mathrm{Re}\,d}\frac{\partial C_{\mathrm{Re}\,d}}{\partial y} = 0 \tag{2.26}$$

Here Φ, ξ(t) have the same meaning as before.

Equations (2.21) and (2.22) can be solved [16] by applying for Laplace transformation of equations (2.21) through (2.26). The surface concentrations can be expressed as:

$$C_{Ox|x=0} = \int_0^t \frac{i_F(t-\varsigma)d\varsigma}{nFA(D_{Ox}\pi\varsigma)^{1/2}} \tag{2.27}$$

$$C_{\mathrm{Re}\,d|x=0} = C^* - \int_0^t \frac{i_F(t-\varsigma)d\varsigma}{nFA(D_{\mathrm{Re}\,d}\pi\varsigma)^{1/2}} \tag{2.28}$$

Substituting equations (2.27) and (2.28) into equation (2.25) and applying the steady-state approximation [16] for the ac response

$$\int_0^t f(\varsigma)d\varsigma = \int_0^\infty f(\varsigma)d\varsigma \tag{2.29}$$

Here ς is the integration parameter. The steady-state approximation is valid if the scan rate is small and the frequency is sufficient high. Equations (2.21) and (2.22) can be solved, and the fundamental Faradaic ac current can be expressed explicitly as

$$\Delta i_f(t) = \frac{n^2F^2C_{\mathrm{Re}\,d}^{Bulk}(\omega D_{\mathrm{Re}\,d})^{\frac{1}{2}}\Delta E}{4RT\cosh^2(\Phi/2)}\sin\left(\omega t + \frac{\pi}{4}\right) \tag{2.30}$$

Equation (2.18) becomes

$$\frac{\Delta R}{R} = \frac{1.1515nFC_{\mathrm{Re}\,d}^{Bulk}\varepsilon\Delta E}{RT\cos\theta\cosh^2(\Phi/2)}\left(\frac{D_{\mathrm{Re}\,d}}{\omega}\right)^{\frac{1}{2}}\sin\left(\omega t-\frac{\pi}{4}\right) \tag{2.31}$$

This equation can be used directly to obtain the PMRS signal, which has a peak at the half-wave potential, $E_{1/2}$.

$$\left(\frac{\Delta R}{R}\right)_{Peak} = \frac{1.1515nFC_{\mathrm{Re}\,d}^{bulk}\varepsilon\Delta E}{RT\cos\theta}\left(\frac{D_{\mathrm{Re}\,d}}{\omega}\right)^{\frac{1}{2}} \tag{2.32}$$

It can been seen from equation (2.31) that the phase angle is 45^0, and that the voltage leads the PMRS signal. The PMRS signal decreases with the root of the angular frequency ($\omega^{1/2}$) and is proportional to ΔE. The width of the PMRS peak is 90/n mV at 25^0C. The theoretical solution can be used to predict the PMRS behaviour in the forward scan direction under zero convection conditions, but it fails for the backward scan because the boundary conditions are different. Numerical simulation is needed to provide a more general description of the PMRS response under these conditions.

2.2.4 Analytical solutions

Equations (2.19) and (2.20) are generally difficult to solve without some simplifications. In other words, three-dimension problems must be reduced two- or one-dimension ones using 'semi-infinite' planar electrodes with dimensions greater than the diffusion layer thickness or a channel electrode. In our case one-directional diffusion and one-directional convection problems are generally considered. A schematic diagram of a

channel electrode has shown in figure 2.3.

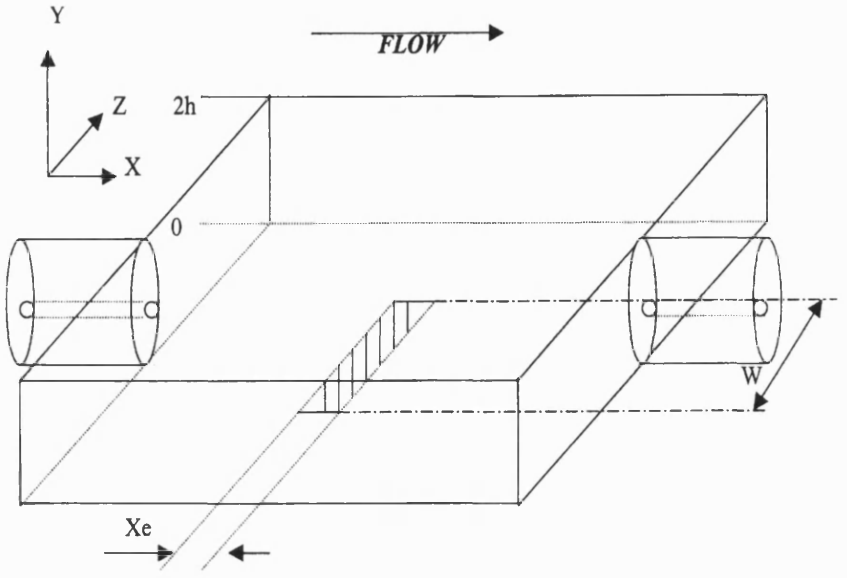

Figure 2.3 A schematic diagram of a channel electrode and the coordinate system.

Equations (2.19) and (2.20) become:

$$\frac{\partial C_{Ox}}{\partial t} = D_{Ox}\frac{\partial^2 C_{Ox}}{\partial y^2} - v_x\frac{\partial C_{Ox}}{\partial x} \tag{2.33}$$

$$\frac{\partial C_{\mathrm{Re}\,d}}{\partial t} = D_{\mathrm{Re}\,d}\frac{\partial^2 C_{\mathrm{Re}\,d}}{\partial y^2} - v_x\frac{\partial C_{\mathrm{Re}\,d}}{\partial x} \tag{2.34}$$

Here $v_y = v_z = 0$.

Under the full development of Poiseuille flow [19] v_x is parabolic, and can be expressed as:

$$v_x = v_0\left\{1-\left(\frac{h-y}{h}\right)^2\right\} \tag{2.35}$$

Here h is the half-height of the cell, and v_0 is the velocity of the flow at the centre of the channel. The volume velocity, v_f, is

$$v_f = \frac{4v_0hd}{3} \tag{2.36}$$

The boundary conditions are the same as equations (2.23) to (2.26). In order to indicate the time dependence the superscript t has been used. According to previous work [27,28], it is possible to assume $D_{Ox} \approx D_{Red}$ when their structures of Ox and Red are similar,

$${}^tC_{Ox}\big|_{y=0} + {}^tC_{Red}\big|_{y=0} = C_{Red}^{bulk} \tag{2.37}$$

Combining equation (2.25) with equation (2.37), the boundary conditions can be rewritten as:

$${}^tC_{Ox}\big|_{y=0} = C_{Red}^{bulk}\frac{1}{1+\exp(-\xi(t)-\Phi)} \tag{2.38}$$

$${}^tC_{Red}\big|_{y=0} = C_{Red}^{bulk}\frac{1}{1+\exp(\xi(t)+\Phi)} \tag{2.39}$$

Numerical methods, such as finite difference (FD) and finite element, have been used to solve these problems [29]. Details are given in literature [30].

The theory is now summarised for the case of the calculation of the concentration and the absorption for a simple reversible electron-transfer reaction in the channel electrode.

In order to apply the Backward Implicit Finite Difference (BIFD) method, the xy plane is covered with a two-dimensional finite difference grid shown in figure 2.4. Increments in the x-direction are Δx and in the y-direction, Δy.

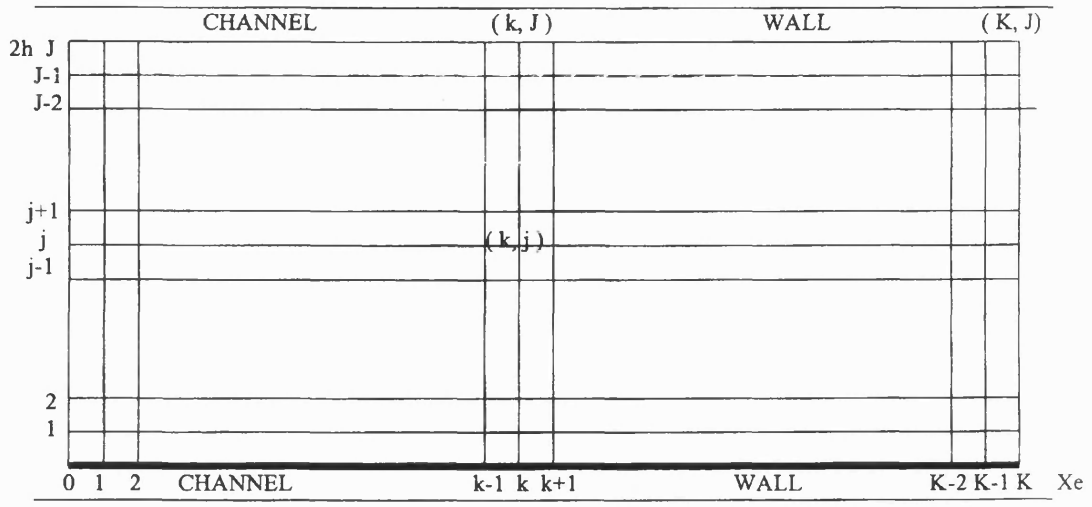

Figure 2.4 The two–dimensional grid representing the xy plane used in the BI method

The following definitions are used

$$y_j = j\Delta y \quad j = 0, 1, ..., J \quad \text{where } \Delta y = 2h/J \tag{2.40}$$

$$x_k = k\Delta x \quad k = 0, 1, ..., K \quad \text{where } \Delta x = x_e/K \tag{2.41}$$

Concentrations can be defined at a point (j,k) corresponding to $x = k\Delta x$, $y = j\Delta y$ and $^{t}a^{ox} = \frac{^{t}C_{ox}}{C_{ox}^{bulk}}$, $^{t}a^{Red} = \frac{^{t}C_{Red}}{C_{ox}^{bulk}}$. $^{t}a_{j,k}^{ox}$, $^{t}a_{j,k}^{Red}$ denote the normalised concentrations of Ox and Red at time(t), respectively at a point(j, k).

Equations (2.33) and (2.34) may be then cast into finite difference form by defining the dimensionless parameters:

$$\lambda_j^c = \frac{6v_f \Delta y \Delta t j(2h - j\Delta y)}{d(2h)^3 \Delta x} \tag{2.42}$$

and

$$\lambda^{y} = \frac{D\Delta t}{(\Delta y)^{2}} \tag{2.43}$$

Here Δt represents an increment of time. The notation ${}^{t}a_{j,k}^{ox}, {}^{t}a_{j,k}^{Red}$ is used to indicate the concentrations of Ox and Red, respectively at time tΔt. They have similar forms, so that is only necessary to solve the equation for the species Ox.

$$\frac{{}^{t+1}a_{j,k}^{ox} - {}^{t}a_{j,k}^{ox}}{\Delta t} = \frac{D_{ox}}{(\Delta y)^{2}}\left\{{}^{t+1}a_{j-1,k}^{ox} - 2{}^{t+1}a_{j,k}^{ox} + {}^{t+1}a_{j+1,k}^{ox}\right\} - v_{x}\frac{{}^{t+1}a_{j,k}^{Ox} - {}^{t+1}a_{j+1,k}^{Ox}}{\Delta x} \tag{2.44}$$

Substituting equations (2.42) and (2.43) into equation (2.44), and rearranging it

$${}^{t}a_{j,k}^{ox} + \lambda_{j}^{c}\left\{{}^{t+1}a_{j,k-1}^{ox}\right\} = -\lambda^{y}\left\{{}^{t+1}a_{j-1,k}^{ox}\right\} + \left(2\lambda^{y} + \lambda_{j}^{c} + 1\right)\left\{{}^{t+1}a_{j,k}^{Ox}\right\} - \lambda^{y}\left\{{}^{t+1}a_{j+1,k}^{Ox}\right\} \tag{2.45}$$

Application of the related boundary conditions (2.23) to (2.26) gives

$${}^{t}a_{1,k}^{ox} + \lambda_{1}^{c}\left\{{}^{t+1}a_{1,k-1}^{ox}\right\} + \frac{\lambda^{y}\exp(\xi(t)+\Phi)}{1+\exp(\xi(t)+\Phi)} = (2\lambda^{y} + \lambda_{1}^{c} + 1)\left\{{}^{t}a_{1,k}^{ox}\right\} - \lambda^{y}\left\{{}^{t+1}a_{2,k}^{ox}\right\} \tag{2.46}$$

and

$${}^{t}a_{J-1,k}^{ox} + \lambda_{J-1}^{c}\left\{{}^{t+1}a_{J-1,k-1}^{ox}\right\} = -\lambda^{y}\left\{{}^{t+1}a_{J-2,k}^{Ox}\right\}(2\lambda^{y} + \lambda_{J-1}^{c} + 1)\left\{{}^{t}a_{J-1,k}^{ox}\right\} - \lambda^{y}\left\{{}^{t+1}a_{J-1,,k}^{ox}\right\} \tag{2.47}$$

Systems of equations (2.33) and (2.34) may be expressed in the form of a (J-1) × (J-1) tridiagonal matrix described as

$$\{d\} = [T]\{u\} \tag{2.48}$$

Where

$$\begin{bmatrix} d_1 \\ d_2 \\ \cdot \\ \cdot \\ \cdot \\ d_j \\ \cdot \\ \cdot \\ \cdot \\ d_{J-2} \\ d_{J-1} \end{bmatrix} = \begin{bmatrix} b_1 & c_1 & 0 & & & & & & & \\ a_2 & b_2 & c_2 & 0 & & & & & & \\ & \cdot & \cdot & \cdot & & & & & & \\ & & \cdot & \cdot & \cdot & & & & & \\ & & & \cdot & \cdot & \cdot & & & & \\ & & & 0 & a_j & b_j & c_j & 0 & & \\ & & & & & \cdot & \cdot & \cdot & & \\ & & & & & & \cdot & \cdot & \cdot & \\ & & & & & & & \cdot & \cdot & \cdot \\ & & & & & & & 0 & a_{J-2} & b_{J-2} & c_{J-2} \\ & & & & & & & & 0 & a_{J-1} & b_{J-1} \end{bmatrix} \begin{bmatrix} u_1 \\ u_2 \\ \cdot \\ \cdot \\ \cdot \\ u_j \\ \cdot \\ \cdot \\ \cdot \\ u_{J-2} \\ u_{J-1} \end{bmatrix} \tag{2.49}$$

The matrix elements are given by:

For k =1,

$$d_1 = {}^t a_{1,1}^{ox} + \lambda_1^c \left\{ {}^{t+1} a_{1,0}^{Ox} \right\} + \frac{\lambda^y \exp(\Phi + \xi(t))}{1 + \exp(\Phi + \xi(t))} \tag{2.50}$$

$$d_j = {}^t a_{j,1}^{ox} + \lambda_j^c \left\{ {}^{t+1} a_{j,0}^{Ox} \right\} \qquad j = 2,3,\ldots,J-1 \tag{2.51}$$

For k > 1

$$d_1 = {}^t a_{1,1}^{ox} + \lambda_1^c \left\{ {}^{t+1} a_{1,0}^{ox} \right\} + \frac{\lambda^y \exp(\Phi + \xi(t))}{1 + \exp(\Phi + \xi(t))} \tag{2.52}$$

$$d_j = {}^t a_{j,k}^{ox} + \lambda_j^c \left\{ {}^{t+1} a_{j,k-1}^{ox} \right\} \qquad j = 2,3,\ldots,J-2 \tag{2.53}$$

$$b_j = 2\lambda^y + \lambda_j^c + 1, \qquad j = 1,2,\ldots,J-1 \tag{2.54}$$

$$u_j = {}^{t+1} a_{j,k}^{ox} \qquad j = 1,2,\ldots,J-1 \tag{2.55}$$

$$a_j = -\lambda^y \qquad j = 1, 2, ..., J-1 \tag{2.56}$$

$$c_j = -\lambda^y \qquad j = 1, 2, ..., J-1 \tag{2.57}$$

$$b_{j-1,k} = \lambda^y + \lambda^c_{j-1} + 1 \tag{2.58}$$

Note that the matrix equation (2.48) shows how the concentrations throughout the cell at time $(t+1)\Delta t$ may be calculated if those values at time $(t\Delta t)$ are known. To do this, we have to find the set of vectors $\{u\}$: for each k value has its own vector $\{u\}_k$. Since the matrix [T] is of tridiagonal form the Thomas algorithm [19] can be used to give $\{u\}_k$ from $\{d\}_k$. The initial conditions supply the vector $\{d\}_0$ from which $\{u\}_0$ is calculated. Then $\{d\}_{k+1} = \{u\}_k$, so $\{u\}$ is calculated from $\{d\}_1$, and on until $\{u\}_k$ is obtained. The calculation is then repeated. The same method can give all the concentrations of species Red.

In this way the Faradaic current, $i_f(t)$ and C(x, t) at the electrode at the instant time (t) may be evaluated as:

$$i_f(t) = nFwD_{\mathrm{Re}\,d} C^{bulk}_{\mathrm{Re}\,d} \left\{ \sum_{k=1}^{K} ({}^{t}a^{ox}_{1,k} - {}^{t}a^{ox}_{0,k}) \frac{\nabla x}{\nabla y} \right\} \tag{2.59}$$

$$C_i(x,t) = \frac{\sum_{0}^{X_e} \sum_{0}^{2h} W(j) W(k) {}^{t}a^{i}_{j,k} \Delta x \Delta y}{\sum_{0}^{X_e} \sum_{0}^{2h} W(j) W(k) \Delta x \Delta y} \tag{2.60}$$

where $C_i(y, t)$ is the concentrations of Ox or Red under the detected region, subscript *i* presents Ox or Red. W(j) and W(k) are the weighing functions for the space(j, k) and here are 1 for both. x_e, J, K can be seen in figure 3, $\Delta x = x_e/J$, $\Delta y = 2h/K$, J and K are the number of grid in casting into finite difference form within the interested area. So the PMRS signal,

$\Delta R/R$ can be derived from equation (2.18) when ε is known. Note that these equations (2.59) and (2.60) include all the harmonic components, but the fundamental harmonic PMRS signal can be separated by the FFT which maps the time domain to the frequency domain. Also note that when $v_x = 0$, equations (2.33) and (2.34) reduce to equations (2.21) and (2.22), so the theoretical solution can be used to check the correction of the simulation results.

2.3 Experimental

2.3.1 Chemical systems

The model system used to check the extension of PMRS studies in the channel cell was the oxidation of tris (4-bromophenyl) amine (TBPA). The concentration of the TBPA (Aldrich, 98%) was typically 2mM with 0.1M tetrabutylammonium perchloride (TBAP) (Fluka, > 99%) as supporting electrolyte in dried acetonitrile (Aldrich, 99%). A series of concentrations of tris (4-bromophenyl) aminium hexachloroantinate (Aldrich) were made from 0.02 to 0.12 mM in acetonitrile. All chemicals were used without further purification. Solutions were degassed thoroughly with argon for about 15 minutes prior to measurements. All experiments were conducted at 20^0C. The experimental arrangement is shown in figure 2.5. The outputs and readings of a lock-in amplifier give the values in root mean square (rms). The typical amplitude (Am) of the imposed ac modulation was 10mV(rms) at 9.8Hz, the scan rate was 3 mV/sec. $D_{TBPA} = D_{TBPA^{+\bullet}} = 1.64 \times 10^5$ cm^{2}s^{-1} [27].

$$\underset{\text{(colourless)}}{TBPA} \rightarrow \underset{\text{(blue)}}{TBPA^{+\bullet}} + e^-$$

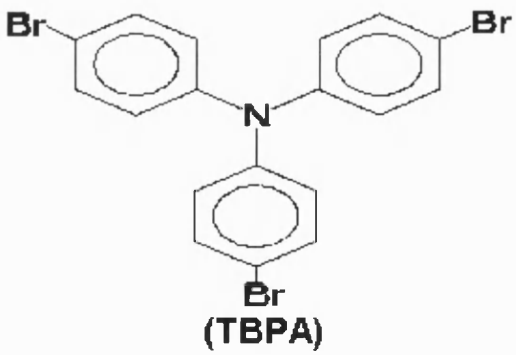

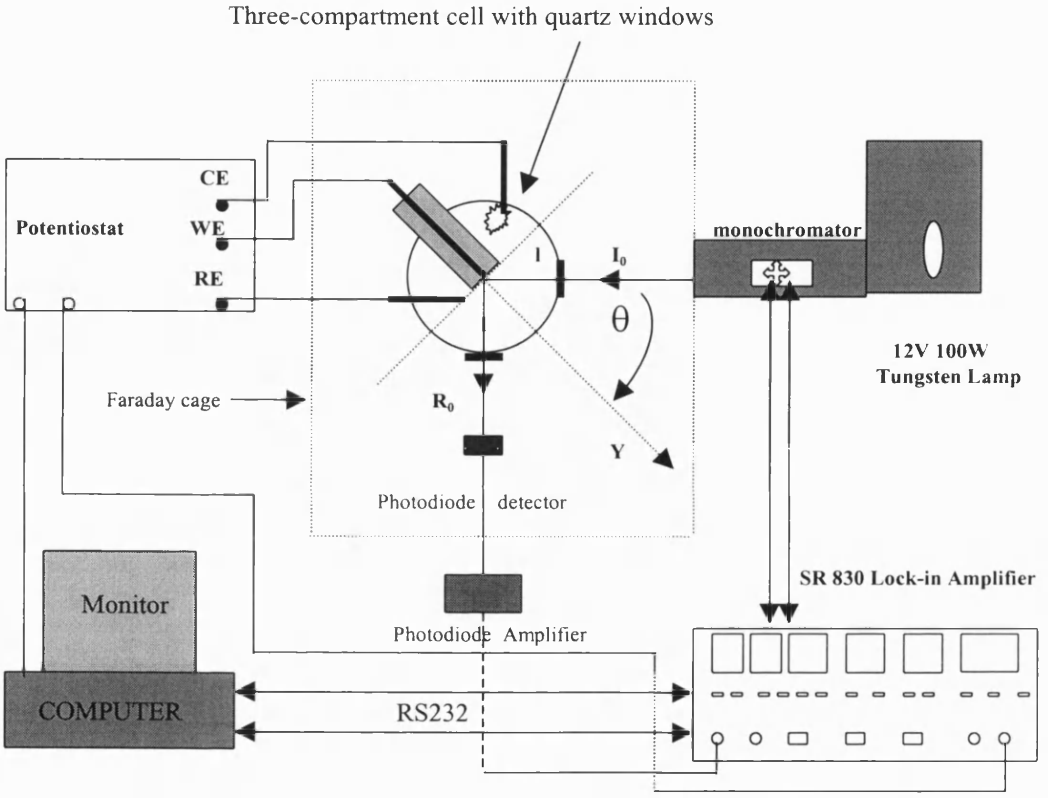

Figure 2.5 A schematic diagram of the PMRS setup

2.3.2 The Three-compartment Cell

A schematic diagram of the three-compartment cell is given in figure 2.6. The cell is designed to allow the incident and reflected light beams to pass through quartz windows. It comprises three compartments for three electrodes. The working electrode is a 3 × 2 mm

platinum foil sealed in glass. The dimensions were measured by a travelling microscope to ± 0.002 cm. The values obtained were 0.342 cm × 0.229 cm. The counter electrode is a large area platinum gauze. The saturated calomel electrode (SCE) electrode was situated in the reference compartment and connected to the solution by Luggin capillary which was positioned as close as possible to the working electrode to minimise the ohmic drop.

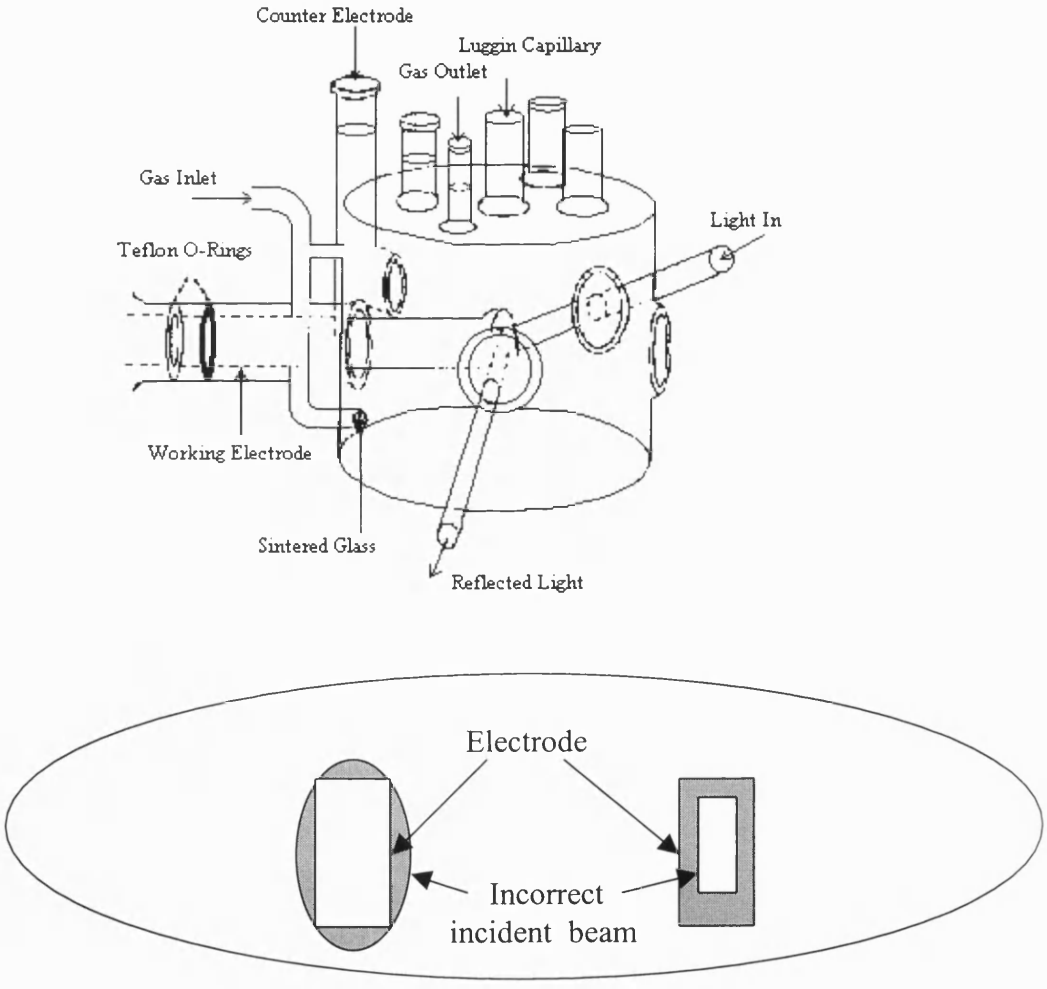

Figure 2.6 A schematic diagram of a three-compartment cell

2.3.3 The Channel Cell

The diagram of the channel cell is shown in figure 2.3. Its dimensions are about 5 cm long, 0.05cm deep and 1.0 cm wide. It was constructed in PTFE and closed by a thin cover plate of optical glass. The platinum working electrode (Goodfellows > 99.95%) with dimensions of approximately 4mm×4mm mounted flush to the wall surface. Solution was delivered in the range of 0 to 10^{-1} cm^3 s^{-1} using a gravity feed system in conjunction with pre-calibrated capillary tube as shown in figure 2.7. A large area platinum gauze counter electrode was placed downstream of the cell while the SCE was located upstream of the cell as the reference electrode. Typical values for the channel electrode were: x_e = 0.386 cm, w = 0.372 cm, d = 1.021 cm, the cell depth 2h (typically 2h = 0.044cm) was calibrated by a ferricyanide system with a well-known absorption coefficient.

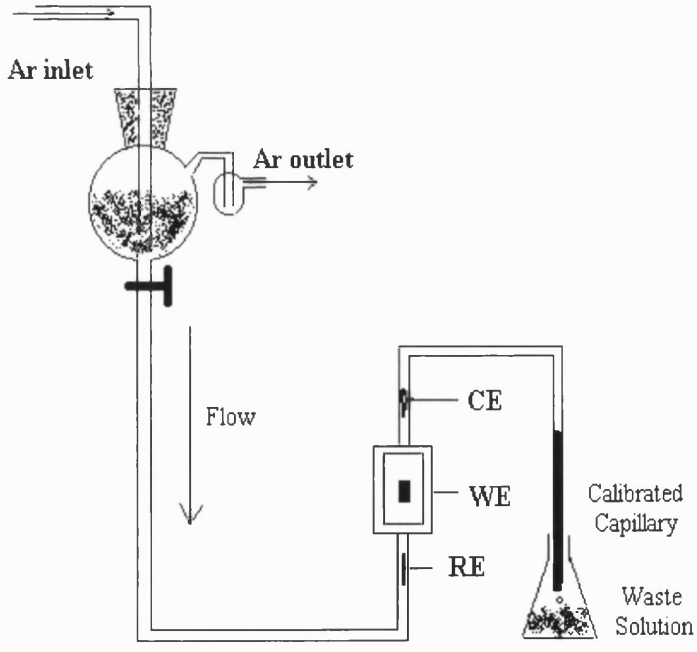

Figure 2.7 The gravity fed flow system for the channel electrode

2.3.4 Cyclic voltammetry and PMR spectroscopy

Cyclic voltammetry was first used to check the reversibility of the TBPA/TBPA$^{+\bullet}$ redox couple. A typical result is shown in figure 2.8.

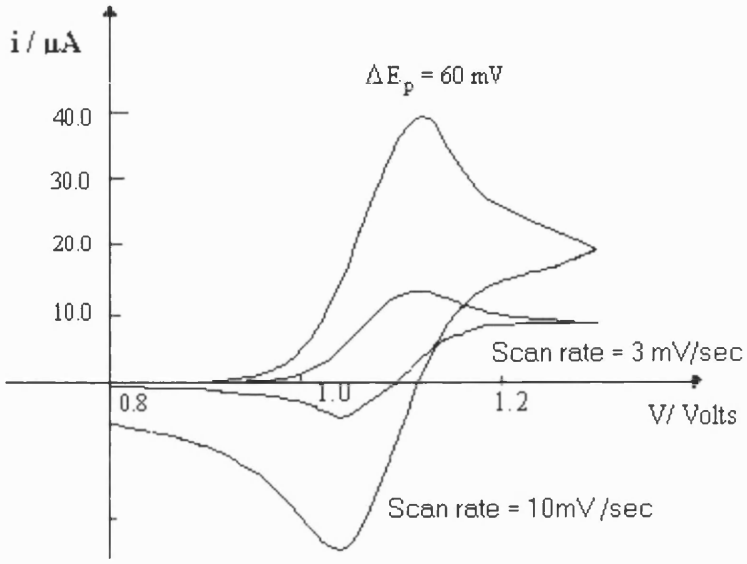

Figure 2.8 A cyclic voltammetry for 2 mM TBPA with 0.1 M TBAP in acetonitrile

It is apparent that ΔEpa - ΔEpc ≅ 60 mV, which indicates the system is electrochemically reversible, and $E_{1/2}$ is 1.05 V vs SCE. The absorption spectra of the species studied are important for PMRS studies because if the species of interest has no absorbance or the absorbance coefficient is too small, the system cannot be studied by PMRS. Usually a wavelength which gives maximum sensitivity for the variation of the concentration of the species of interest is selected for PMRS studies. Consequently absorption spectra were acquired using a Perkin-Elmer 'Lambda 10' UV/VIS spectrometer. The spectrum of the TBPA in acetonitrile is shown in figure 2.9, and that of the TBPA cation obtained by using 0.1 mM tris (4-bromophenyl) aminium hexachloroantinate

(TBPAHA) in acetonitrile as shown in figure 2.9.

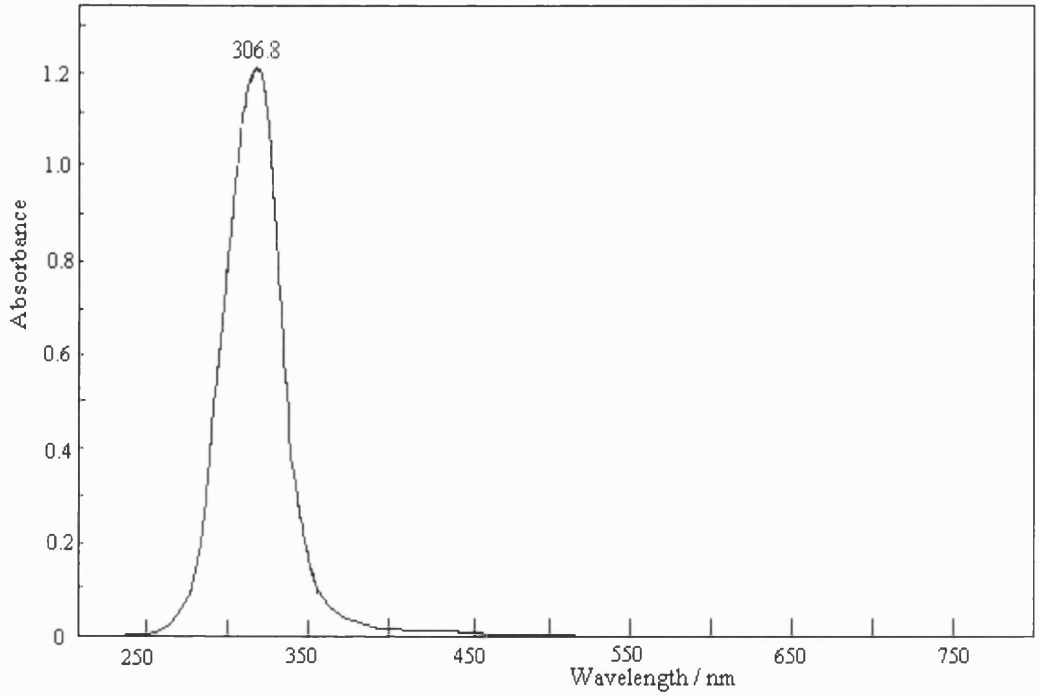

Figure 2.9 A absorption spectrum of 2 mM TBPA in acetonitrile.

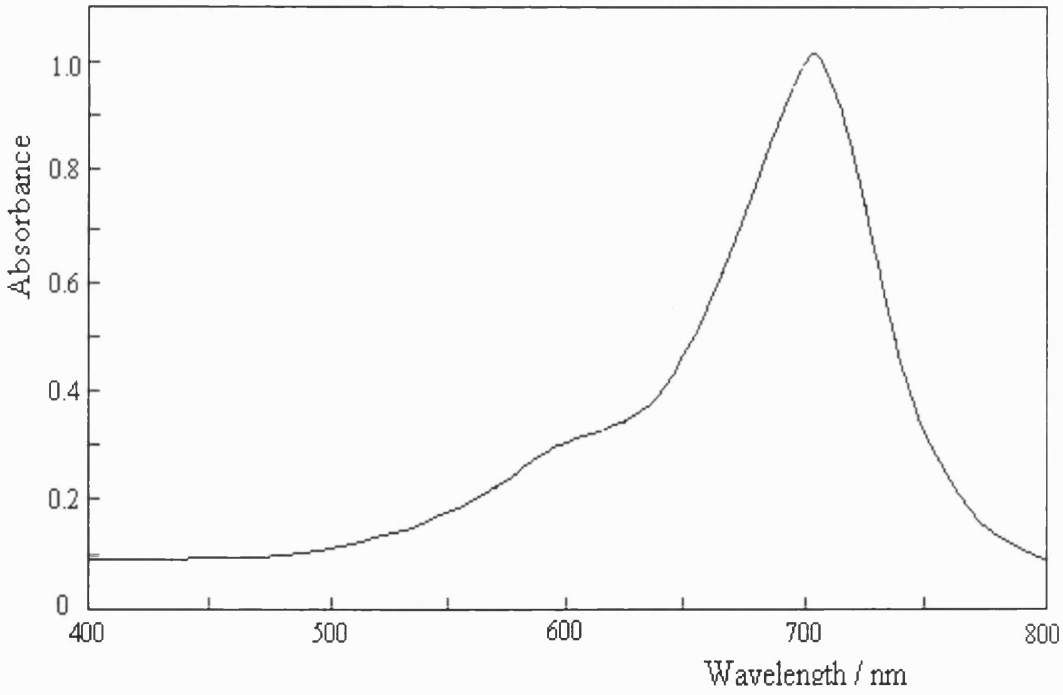

Figure 2.10 Absorption spectrum of TBPA radical cation

in 0.1mM TBPAHA in acetonitrile

The TBPA has absorption peak at λ = 306.8 nm, and does not absorb light for $\lambda > 550$ nm. The TBPA radical cation however has a peak at λ = 702 nm.

A typical PMR spectrum for the $TBPA^{+\bullet}$/TBPA redox couple is illustrated in figure 2.11. The spectrum was recorded at E_{dc}=1.044V, ac modulation 9.8 Hz, 10 mV rms. A peak is observed with a maximum at λ=702 nm, which is very good agreement with the difference spectrum. It was found that the absorption coefficient of TBPA radical at 702 nm in acetonitrile was 1.32×10^4 M^{-1} cm^{-1} , which is in good agreement with the reported peak maximum of 710 nm in acetonitrile within the range $1.3 - 3.4 \times 10^4$ M^{-1} cm^{-1} [32] .

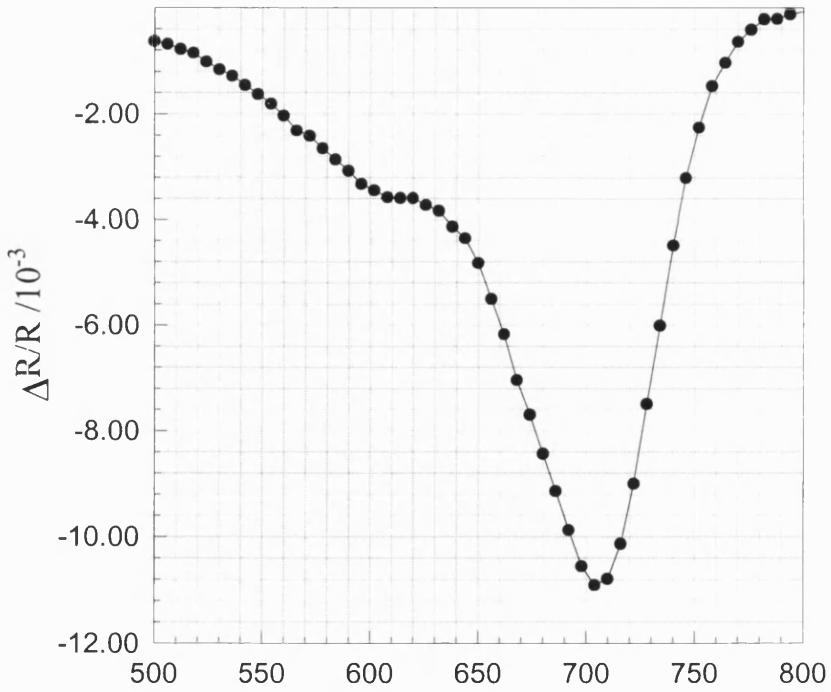

Figure 2.11 PMR spectrum of the $TBPA^{+\bullet}$/TBPA redox couple at E_{dc}=1.044V vs SCE, C_{TBPA}= 2mM, Am=10mV (rms), frequency=9.80 Hz, wavelength scan rate 3 nm/sec)

2.4 Results and discussion

Since an organic solvent was used, it was necessary to consider the uncompensated solution resistance in the channel cell. It was determined by impedance measurements under the same conditions, and found to vary from 88 to 100Ω, depending on what flow rate was used. The resistance was small in the three-compartment cell since the Luggin capillary placed close to the working electrode. The potentials used have been corrected for iR drop that will affect the phase angle that did not be concerned in this thesis. The half-wave potential for the TBPA in acetonitrile is 1.050 ± 0.005 V vs SCE, which is in good agreement with literature [31-33]. The absorption spectra of both the radical cation and parent of the TBPA are in good agreement with the literature [27,32]. Light with a wavelength of 702nm was used to irradiate the working electrode surface at an angle of 60^0, the ac and dc components of reflected light were measured with a photodiode and lock-in amplifier.

It can be seen from figure 2.12a that the simulation results in stagnant solution match the analytical solution very well on the forward scan. Further it can be seen in figure 2.12b that the predicted results by simulation in the backward scan is smaller than analytical solutions in the forward scan. That could be understood by those reasons: i) the diffusion processes and ii) the big scan rate that results in off steady state condition.

The simulation conditions are: Am = 10 mV (rms), K = 15, J = 600, sampling No = 8, x_e = 0.342 cm, w = 0.229 cm, frequency = 9.80 Hz, scan rate = 3mV/sec, $\varepsilon = 1.17\times10^4\ M^{-1}\ cm^{-1}$. The K (=15), J (= 600) and sampling No (=8) used for the simulation were guaranteed to obtain convergent results (error < 1%). They are shown in figure 2.13.

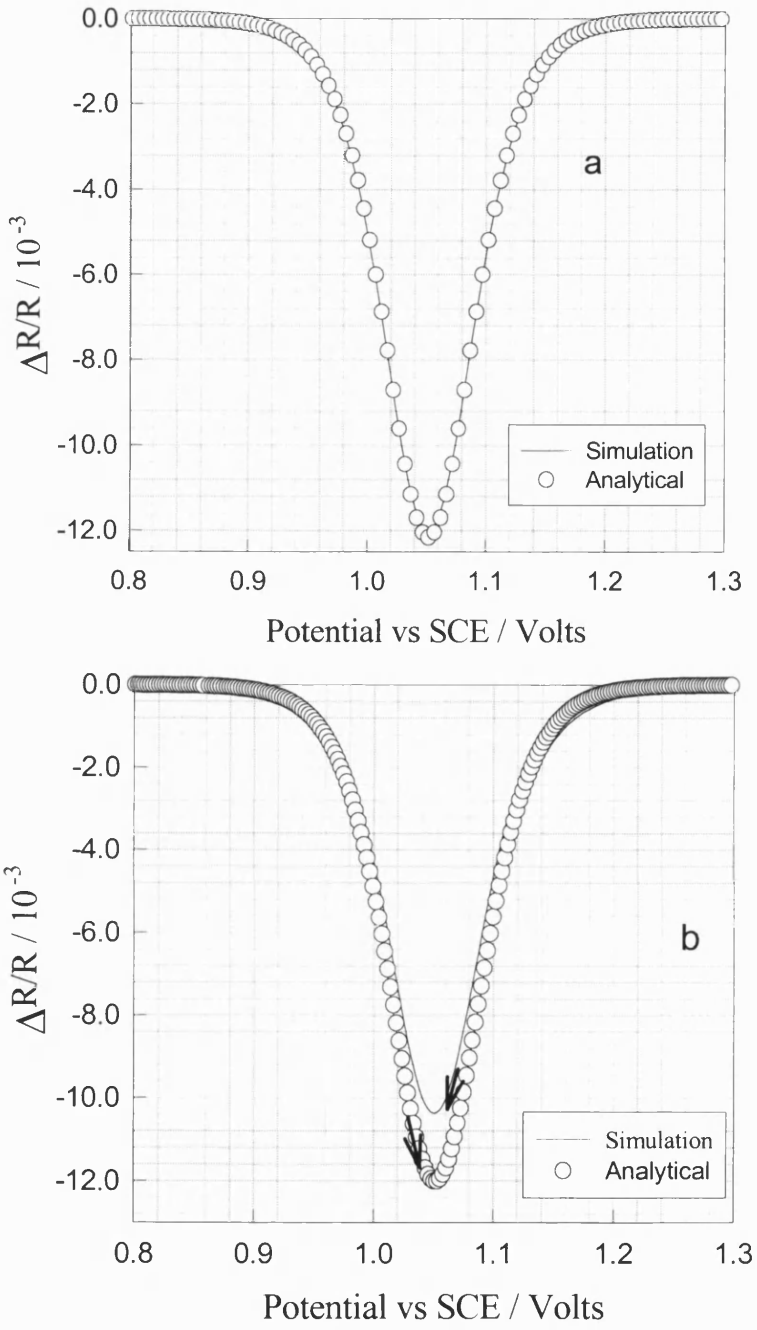

Figure 2.12 The analytical and simulation results of ΔR/R of 2mM TBPA

in stagnant solution . — Simulation, o Analytical.

a – only the forward scan, b – simulated reverse compared with analytical forward

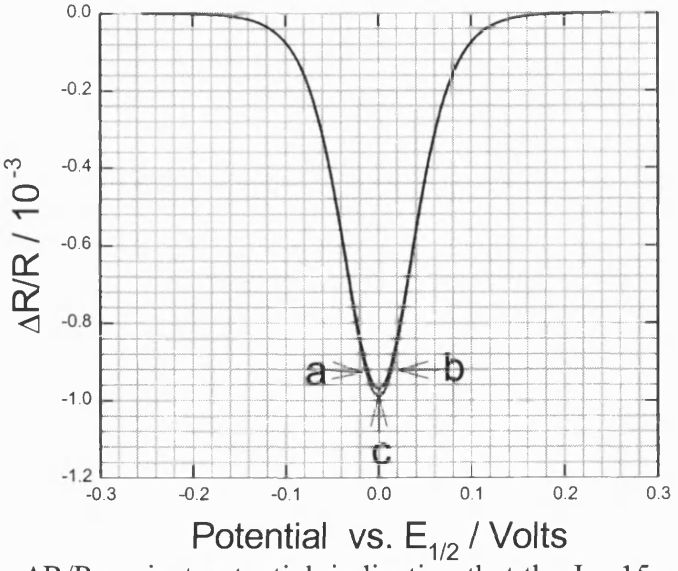

Figure 2.13 Simulation ΔR/R against potential, indicating that the J = 15 and K = 600 were sufficient for obtaining convergent results. $\varepsilon = 1.0 \times 10^3$ M^{-1} cm^{-1}, frequency = 9.8 Hz, scan rate = 3 mV/sec and sampling No = 8.

a) J = 15 and K = 600, b) J = 35 and K=600, c) J=15 and K=900

Furthermore the theoretical PMRS plots are in good agreements with the experimental ones shown in figures 2.14a and 2.14b. It can also be noted from figure 2.14 that the width of the experimental PMRS is larger than predicted by the analytical and simulation solution. This may be due to the uncompensated solution resistance.

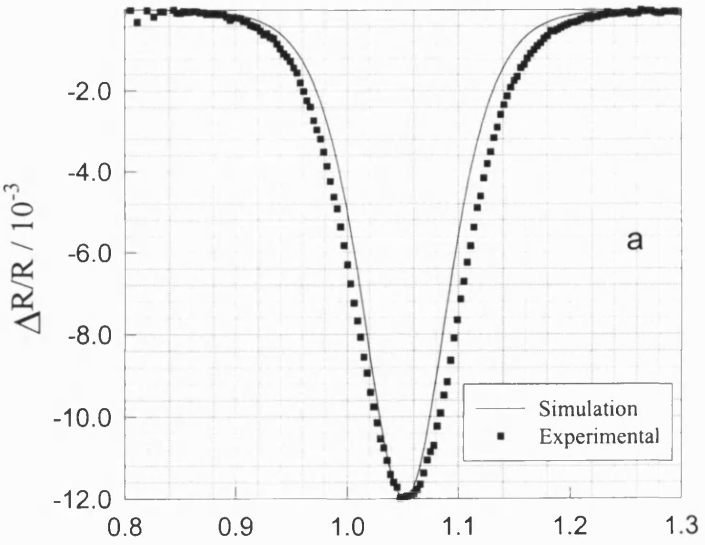

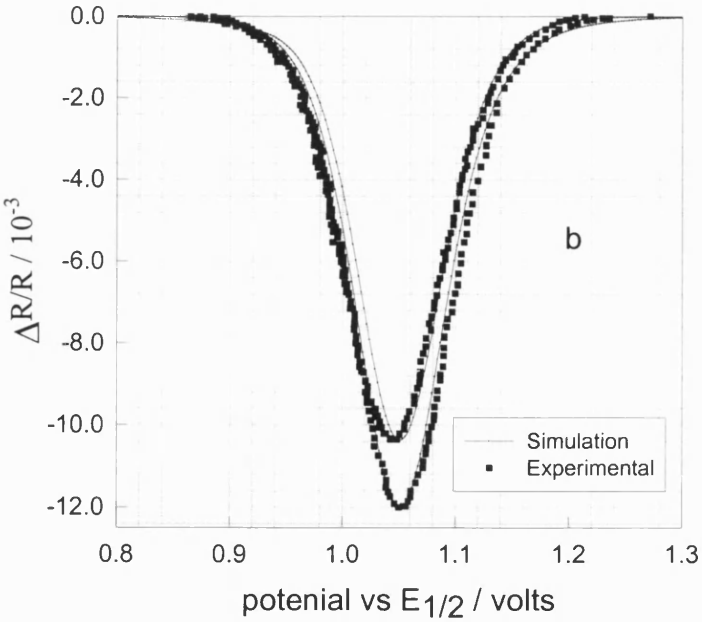

Figure 2.14 The experimental and simulation results of ΔR/R of 2mM TBPA in stagnant solution the conditions are same as the figure 2.12 — Simulation , ■ Experimental a –only the forward scan, b – the forward and reverse scan

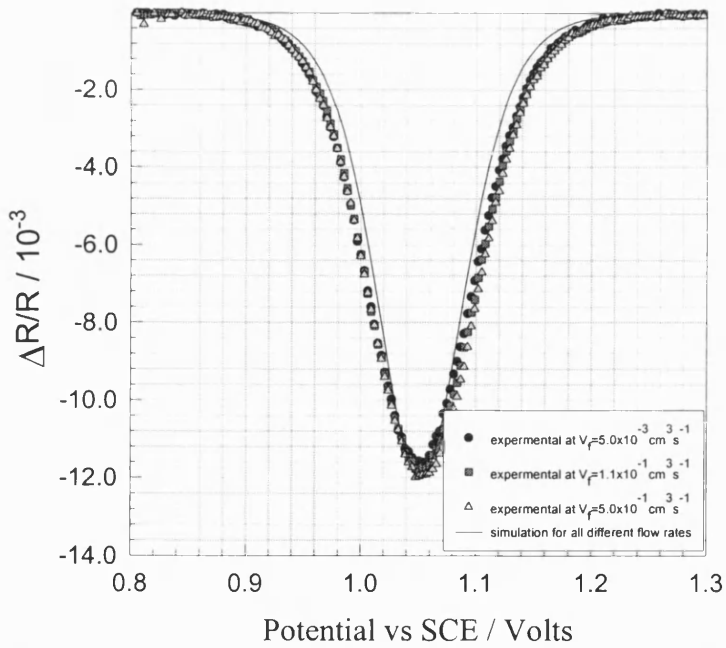

Figure 2.15 The experimental and simulation ΔR/R results under different flow rates ranging from 5.0×10^{-3} to 5.0×10^{-1} cm^3 s^{-1} (x_e= 0.382 cm, w = 0.376 cm, 2h = 0.044cm, Am = 10mV (rms), K = 15, J = 600, sampling No = 8, frequency = 9.80 Hz, scan rate = 3mV/sec, $\varepsilon = 1.17 \times 10^4 M^{-1}cm^{-1}$)

The important thing is that when the flowing solution was used, the forward and backward scans are identical since steady state conditions are achieved. It also can be seen from figure 2.15 that the spectrum of the PMRS in experiments remains unchanged when the flow rates increase up to 0.5 cm^3s^{-1}. This is probably due to fast diffusion process compared with the superimposed perturbation. It has been found from the simulation that the PMRS signal would not change when the flow rates are less than 10 cm^3s^{-1} under the present conditions (frequency = 9.8 Hz, 2h = 0.044 cm, d = 1 cm). This can be understood because there is a very thin diffusion layer under fast flow rates and would not change during the forward and reverse scan, so it can be concluded that the forced convection does not affect the studies of PMRS when the frequency is great than 1 Hz.

In order to achieve a better understanding, more simulations were undertaken, and the results are shown in figures 2.16 and 2.17. It can be seen that both R and ΔR vary with the flow rates by the same extent, so that the ratio, ΔR/R, keeps constant.

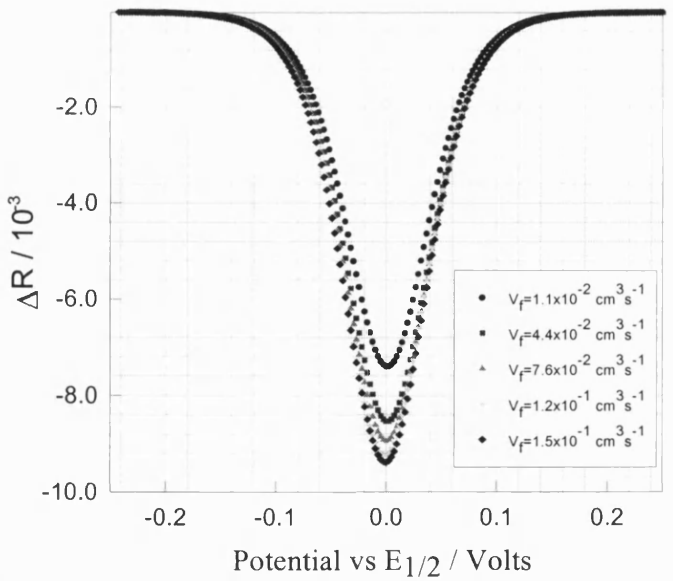

Figure 2.16 The simulation ΔR vs. v_f, the conditions are same as in figure 2.15.

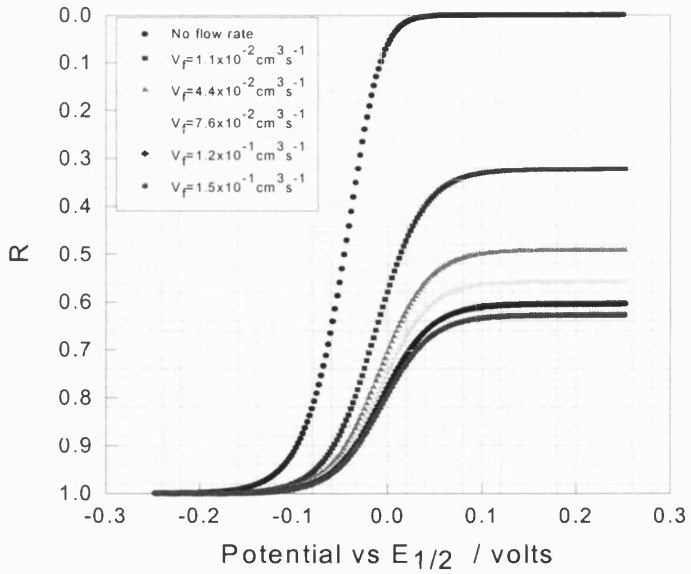

Figure 2.17 The simulation R against the flow rates, the conditions as for figure 2.15.

Figures 2.18 shows that the experimental results varied with amplitudes of the sinusoidal perturbation in stagnant and flowing solutions. At the same time the plot demonstrates that the flow rates do not affect the PMRS signal. The linearity and agreement between the analytical, simulated and the experimental results indicates the validity of equation (2.31).

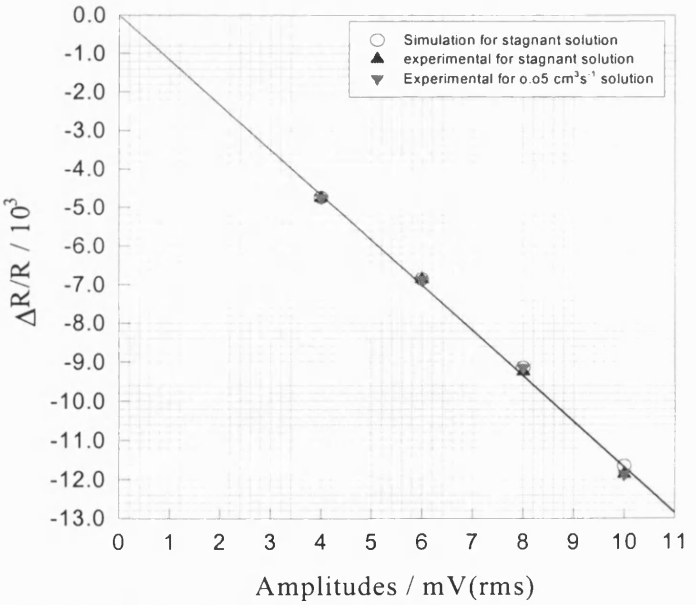

Figure 2.18 Experimental ΔR/R of 2mM TBPA in acetonitrile vs ac modulation amplitudes in stagnant and flowing solutions for E_{dc} = 1.05V vs SCE, ω = 61.57 s^{-1}.

The simulated and analytical solutions match, and they fit the experimental results. The key factor to fit the simulated and analytical results to the experimental ones by using equation (2.18) or (2.31) is the absorption coefficient of the radical of the TBPA, which is $(1.17 \pm 0.08) \times 10^4$ M^{-1} cm^{-1} average from the simulations and analytical solution. Tris (4-bromophenyl) aminium hexachloroantimonate was also used to obtain a reliable value of its absorption coefficient. It was found in acetonitrile that there is a maximum absorption at 702 nm. The absorption coefficient, ε_{702nm}, was found to be 1.35×10^4 M^{-1} cm^{-1}, which is in good agreement with the literature value [32] for 710 nm in acetonitrile within the range 1.3 – 3.4×10^4 M^{-1} cm^{-1}. It has been shown in literature [23,34] that the salt is stable in acetonitrile, but in the present experiments it was found that it gradually decomposed during absorption measurements, specifically in the dilute solution, as well as under illumination. This agrees with a report that [35] debromo dimerisation occurs in acetonitrile at 0^0 C. Also the type of the anion in the salt and solvent used will affect the peak position of absorptivity and the maximum absorption coefficient of the radical [35-37]. So the absorption coefficient of the TBPA radical will change with solvents and supporting electrolytes used.

2.5 Conclusions

Hydrodynamic PMRS has been simulated successfully using numerical methods. The new methodology has been checked by using the oxidation of TBPA as a model system. The simulation, experimental results and analytical solution matched very well.

References:

1. C. Gutierrez in "Spectroscopic and Diffraction Techniques in Interfacical Electrochemistry": Kluwer Academic Publishers, Amsterdam, 261 (1990).
2. Feinleib J., Phys. Rev. Lett., **16**(1966), 1200
3. B.O. Seraphin, Phys. Rev., **140**A,1716 (1965).
4. Koch D.F.A., Scaife D.E., J. Electrochem. Soc., **113**,302 (1966).
5. A. Bewick and A.M. Tuxford, Faraday Soc. Symp., **4**, 114 (1970).
6. W. Paatsch, Surface Science, **37**, 59 (1973).
7. N. Hara and K. Sugimoto, J. Electrochem. Soc., **126**(8), 1328 (1979)
8. J. Caram, C. Gutierrez, G. Pimenta and M.I. da Silva Pereira, J. Electroanal. Chem., **344**, 199 (1993)
9. C. Gutierrez and M.A. Martinez, J. Electrochem. Soc., **131**, 1873 (1986).
10. R. Adzic, B. Cahan and E.Yeager, J.Chem. Phys., **58**,1780(1973).
11. A.W.B. Aylmer-Kelly, A. Bewick, P.R. Cantrill and A.M. Tuxford, Discuss., Faraday Soc., **56**, 96 (1973)
12. A. Bewick and A.M. Tuxford, J. Electroanal. Chem., **47**, 255 (1973).
13. J.D.E. McIntyre and W.F. Peck, Jr., Faraday Discuss., Chem. Soc., **56**, 122 (1974)
14. J.A. Caram and C. Gutierrez, J. Electroanal. Chem., **291**, 289 (1990)
15. A. Kowal, C. Gutierrez, J. Electroanal. Chem., **395**(1-2), 243(1995).
16. S. Hinman, J.F. McAleer and S. Pons, J. Electroanal. Chem., **154**, 45(1983).
17. D. J. Blackwood, L.M. Peter, Electrochim. Acta, **35**, 1874(1990).
18. L.M. Peter, Phil. Trans. R Lond. A, **354**, 1613(1996).

19. R.C. Walker, M. Bailes and L.M. Peter, Electrochim. Acta, **44**, 1289 (1998).

20. D. J. Fermin, Z. Ding, P.F. Brevet and H.H. Girault, J. Electroanal. Chem., **447**(1-2), 125(1998).

21. Z.F. Ding, D.J. Fermin, P.F. Bervet and H.H. Girault, J. Electroanal. Chem., **458**, 139 (1998).

22. Z.F. Ding, F. Reymond, P. Baumgartner, D.J. Fermin, Bervet P.F., Carrupt P.A. and Girault H.H., Electrochimica Acta, **44**, 3 (1998).

23. F. Huert, E. Morallon, C. Quijada, J.L. Vazquez and L.E.A. Berlouis, J. Electroanal. Chem., **463**(1), 109 (1999).

24. T. Sagara, H. Maeda, Y. Yuan and N. Nakashima, Langmuir, **15**(11), 3823 (1999).

25. P. R. Unwin and R. G. Compton, in Comprehensive Chemical Kinetics, **29**, 173, Elsevier, Amsterdam, 1988,

26. D. E. Smith in A. J. Bard (Ed.), Electroanalytical Chemistry, **1**, Marcel Dekker, New York, 1(1966).

27. R. L. Wang, K. Y. Tam, R. G. Compton, J. Electroanal. Chem., **434**(1-2), 225(1997).

28. A. C. Fisher and R. G. Compton, J. Phys. Chem., **95**(19), 7538(1991).

29. D. F. Elliott, K. R. Rao, Fast Transform - Algorithm, Analysis, Applications, Academic press. INC., 1982

30. R. L. Wang, K. Y. Tam, R. G. Compton, Electroanalysis, **9**(4), 284(1997).

31. W. Schmidt and E. Steckhan, Chem. Ber., **113**, 577(1980).

32. R. I. Walter, J. Am. Chem. Soc., **88**(9), 1923(1966).

33. S. Dapperheld, E. Steckhan, K. H. Grosse Brinkhaus and T. Esch, Chem. Ber, **124**, 2557(1991).

34. E. T. Seo, R. F. Nelson, J. M. Fritsch, L. S. Marcoux, D. W. Leedy and R. N. Adams, J. Am. Chem. Soc., **88**, 3498 (1966).

35. L. Eberson, B. Larsson, Acta Chem. Scand., Ser. B, **40**, 210(1986).

36. D. H. R. Barton, F. Hayness, G. Leclerc, P. D. Magnus and F. Menzies, J. Chem. Soc. Perkin I, 2055(1975).

37. F. A. Bell, A. Ledwith and D. C. Sherrington, J. Chem. Soc. (C), 2719(1969).

CHAPTER THREE

PMRS STUDIES OF COUPLED CHEMICAL REACTIONS

3.1 Introduction

The previous chapter dealt with the PMRS technique for simple reversible electron transfer reactions using finite difference simulations. The good agreement between experimental and numerical simulations validates the new strategy. However, in many cases the electron transfer reaction is coupled to a homogeneous chemical reaction that involves species Ox or Red. For instance, Red may not be present initially but may be produced from another, nonelectroactive, species, or Ox may react with the solvent or supporting electrolyte species. Sometimes a substance that reacts with species Ox or Red is added intentionally so that the rate of the reaction can be determined by the electrochemical technique or so that a new product is produced. This chapter summarises the general classes of coupled homogeneous chemical reactions and describes the PMRS response under hydrodynamic conditions by numerical simulations. Some experimental results are presented.

3.2 Theory

3.2.1 CE Reaction (Preceding Reaction)

The derivation of PMRS equations for systems with coupled chemical reactions is accomplished for systems with first-order or pseudo-first-order reaction in essentially the same manner as the case treated in Chapter 2. The method of derivation will be outlined for the system with a preceding first-order chemical reaction designated by the scheme

$$Y \underset{k_b}{\overset{k_f}{\rightleftharpoons}} \text{Red} \qquad (3.1)$$

$$\text{Red} \rightleftharpoons \text{Ox} + ne^- \qquad (3.2)$$

Here the electroactive species Red is generated by a chemical reaction that precedes the electron transfer at the electrode. Ox is initially absent in solution. The system of partial-differential equations for one-dimensional diffusion and one-dimensional convection in a channel electrode is

$$\frac{\partial C_Y}{\partial t} = D_Y \frac{\partial^2 C_Y}{\partial y^2} - v_x \frac{\partial C_y}{\partial x} - k_f C_Y + k_b C_{\mathrm{Red}} \tag{3.3}$$

$$\frac{\partial C_{\mathrm{Red}}}{\partial t} = D_{\mathrm{Red}} \frac{\partial^2 C_{\mathrm{Red}}}{\partial y^2} - v_x \frac{\partial C_{REd}}{\partial x} + k_f C_Y - k_b C_{\mathrm{Red}} \tag{3.4}$$

$$\frac{\partial C_{Ox}}{\partial t} = D_{Ox} \frac{\partial^2 C_{Ox}}{\partial y^2} - v_x \frac{\partial C_{Ox}}{\partial x} \tag{3.5}$$

Here k_f is the rate constant of the forward direction of the equation (3.1), k_b is the rate constant of the backward direction. The equilibrium constant, $K_{eq} = k_f/k_b$.

The initial and boundary conditions for equations (3.3) to (3.5) are

For t = 0, any y,

$$C_{Ox} = 0, \qquad C_Y + C_{\mathrm{Red}} = C_Y^{Bulk} + C_{\mathrm{Red}}^{Bulk} = C_{total}^{Bulk} \tag{3.6}$$

$$\frac{C_{\mathrm{Red}}}{C_Y} = \frac{C_{\mathrm{Red}}^{bulk}}{C_Y^{bulk}} = \frac{k_f}{k_b} = K_{eq} \tag{3.7}$$

For t > 0, y → ∞,

$$C_Y + C_{\mathrm{Red}} = C_{total}^{bulk} \tag{3.8}$$

$$\frac{C_{\mathrm{Red}}}{C_Y} = K_{eq}, \qquad C_{Ox} \to 0 \tag{3.9}$$

For t > 0, y = 0,

$$-D_{Ox} \frac{\partial C_{Ox}}{\partial y} = D_{\mathrm{Red}} \frac{\partial C_{\mathrm{Red}}}{\partial y} = \frac{i(t)}{nFA} \tag{3.10}$$

$$\frac{C_{Ox}}{C_{\mathrm{Red}}}\bigg|_{y=0} = \left(\frac{D_{\mathrm{Red}}}{D_{Ox}}\right)^{\frac{1}{2}} \exp(\Phi + \xi(t)) \tag{3.11}$$

$$D_Y \frac{\partial C_Y}{\partial y} = 0 \tag{3.12}$$

Here

$$\Phi = \left(\frac{nF}{RT}\right)\left(E_{dc} - E_{1/2}\right) \tag{3.13}$$

$$\xi(t) = \frac{nF\Delta E}{RT}\sin(\omega t) \tag{3.14}$$

Here C_Y is the concentration of species Y, C_{total}^{bulk} is the total concentration of species Red and Y at equilibrium, D_Y is the diffusion coefficient of species Y. The other parameters are the same as in Chapter 2. The system of equations (3.3) to (3.5) can be solved by the numerical simulation method used in the Chapter 2 for the channel cell and may be expressed in the form of a (J-1) ×(J-1) tridiagonal matrix described as

$$\{d\} = [T]\{u\} \tag{3.15}$$

The matrix elements for species Red are given by:

For k =1,

$$d_1 = {}^{t}a_{1,1}^{Red} + \lambda_1^c\left\{{}^{t+1}a_{1,0}^{Red}\right\} + \frac{\lambda^y(D_{Ox}\,{}^{t}a_{1,1}^{Ox} + D_{Red}\,{}^{t}a_{1,1}^{Red})}{D_{Red} + \left(D_{Ox}D_{Red}\right)^{\frac{1}{2}}\exp\left(\Phi + \xi(t)\right)} + k_f\,{}^{t}a_{1,1}^{Y}\Delta t - k_b\,{}^{t}a_{1,1}^{Red}\Delta t \tag{3.16}$$

$$d_j = {}^{t}a_{j,1}^{Red} + \lambda_j^c\left\{{}^{t+1}a_{j,0}^{Red}\right\} + k_f a_{j,1}^{Y}\Delta t - k_b\,{}^{t}a_{j,1}^{Red}\Delta t \quad j = 2,3,\ldots,J-1 \tag{3.17}$$

For k > 1,

$$d_1 = {}^{t}a_{1,1}^{Red} + \lambda_1^c\left\{{}^{t+1}a_{1,k-1}^{Red}\right\} + \frac{\lambda^y(D_{Ox}\,{}^{t}a_{1,k}^{Ox} + D_{Red}\,{}^{t}a_{1,k}^{Red})}{D_{Red} + \left(D_{Ox}D_{Red}\right)^{\frac{1}{2}}\exp\left(\Phi + \xi(t)\right)} - k_f\,{}^{t}a_{1,k}^{Y}\Delta t + k_b\,{}^{t}a_{1,k}^{Red}\Delta t \tag{3.18}$$

$$d_j = {}^{t}a_{j,k}^{Red} + \lambda_j^c\left\{{}^{t+1}a_{j,k-1}^{Red}\right\} - k_f a_{j,k}^{Y}\Delta t + k_b\,{}^{t}a_{j,k}^{Red}\Delta t \qquad j = 2,3,\ldots,J-2 \tag{3.19}$$

All the terms and definitions are same as in the Chapter 2. One can obtain the concentrations of species Red in space (x, y) and time (t) at a given flow rate, then simply integrate them within the region at time t. The concentration profile of species Red can be obtained by the above method.

3.2.2 EC Reaction (Following Reaction)

In this case the product of the electrode reaction, Ox, reacts (e.g. with the solvent) to produce a species that is not electroactive at potentials where the oxidation of Red occurs.

$$\text{Red} \rightleftharpoons \text{Ox} + \text{ne}^- \tag{3.20}$$

Or

$$\text{Ox} \underset{k_b}{\overset{k_f}{\rightleftharpoons}} \text{X} \tag{3.21a}$$

$$\text{Ox} + \text{S} \underset{k_b}{\overset{k_f}{\rightleftharpoons}} \text{X}' \tag{3.21b}$$

Here S is the solvent, X and X′ are the electroinactive and stable product. The coupled chemical reactions can be divided into many types according to the reaction order, but only first-order or pseudo-first-order reactions are considered here. For example, The concentration of S can be made large so that [S]>>[Ox] and $k_f = k_f'[S]$ = constant. k_f is the rate constant of the first-order reaction (s^{-1}), k_f' is the rate constant of the second-order reaction ($M^{-1}\ s^{-1}$).

The general equations for one-dimensional diffusion and one-dimensional convection describing the distribution of species Ox, Red, and X for the reaction (3.20) and (3.21a) in time (t) and space (x, y) in three-dimension space are respectively:

$$\frac{\partial C_{Red}}{\partial t} = D_{Red}\frac{\partial^2 C_{Red}}{\partial y^2} - v_x\frac{\partial C_{Red}}{\partial x} \tag{3.22}$$

$$\frac{\partial C_{Ox}}{\partial t} = D_{Ox}\frac{\partial^2 C_{Ox}}{\partial y^2} - v_x\frac{\partial C_{Ox}}{\partial x} - k_f C_{Ox} + k_b C_X \tag{3.23}$$

$$\frac{\partial C_X}{\partial t} = D_X\frac{\partial^2 C_X}{\partial y^2} - v_x\frac{\partial C_X}{\partial x} + k_f C_{Ox} - k_b C_X \tag{3.24}$$

The boundary conditions are:

For t = 0, any y,

$$C_{Ox} = C_X = 0, \qquad C_{\mathrm{Re}d} = C_{\mathrm{Re}d}^{Bulk} \tag{3.25}$$

For t > 0, y → ∞,

$$\frac{C_X}{C_{Ox}} = \frac{k_f}{k_b} = K_{eq}, \qquad C_{\mathrm{Re}d} \rightarrow C_{\mathrm{Re}d}^{Bulk} \tag{3.26}$$

For t > 0, y = 0,

$$-D_{Ox}\frac{\partial C_{Ox}}{\partial y} = D_{\mathrm{Re}d}\frac{\partial C_{\mathrm{Re}d}}{\partial y} = \frac{i(t)}{nFA} \tag{3.27}$$

$$\frac{C_{Ox}}{C_{\mathrm{Re}d}}\Big|_{y=0} = \left(\frac{D_{\mathrm{Re}d}}{D_{Ox}}\right)^{\frac{1}{2}} \exp(\Phi + \xi(t)) \tag{3.28}$$

$$D_X\frac{\partial C_X}{\partial y} = 0 \tag{3.29}$$

All the parameters have the same meaning as before. The system of equations (3.22) to (3.24) combined with the equations (3.25) to (3.29) can be solved by the numerical method used in the Chapter 2 for the channel cell and may be expressed in the form of a (J-1) ×(J-1) tridiagonal matrix. The matrix elements for species Ox are given by:

For k =1,

$$d_1 = {}^{t}a_{1,1}^{Ox} + \lambda_1^c\left\{{}^{t+1}a_{1,0}^{Ox}\right\} + \frac{\lambda^y(D_{Ox}\,{}^{t}a_{1,1}^{Ox} + D_{\mathrm{Re}d}\,{}^{t}a_{1,1}^{\mathrm{Re}d})}{D_{\mathrm{Re}d} + (D_{Ox}D_{\mathrm{Re}d})^{\frac{1}{2}}\exp(-\Phi - \xi(t))} - k_f\,{}^{t}a_{1,1}^{X}\Delta t + k_b\,{}^{t}a_{1,1}^{Ox}\Delta t \tag{3.30}$$

$$d_j = {}^{t}a_{j,1}^{Ox} + \lambda_j^c\left\{{}^{t+1}a_{j,0}^{Ox}\right\} - k_f a_{j,1}^{X}\Delta t + k_b\,{}^{t}a_{j,1}^{Ox}\Delta t \qquad j = 2,3,\ldots,J-1 \tag{3.31}$$

For $k > 1$,

$$d_1 = {}^{t}a_{1,k}^{Ox} + \lambda_1^c\left\{{}^{t+1}a_{1,k-1}^{Ox}\right\} + \frac{\lambda^y\left(D_{Ox}\,{}^{t}a_{1,k}^{Ox} + D_{\mathrm{Red}}\,{}^{t}a_{1,k}^{\mathrm{Red}}\right)}{D_{\mathrm{Red}} + \left(D_{Ox}D_{\mathrm{Red}}\right)^{\frac{1}{2}}\exp\left(-\Phi - \xi(t)\right)} - k_f\,{}^{t}a_{1,k}^{X}\Delta t + k_b\,{}^{t}a_{1,k}^{Ox}\Delta t \qquad (3.32)$$

$$d_j = {}^{t}a_{j,k}^{Ox} + \lambda_j^c\left\{{}^{t+1}a_{j,k-1}^{Ox}\right\} - k_f\,{}^{t}a_{j,k}^{X}\Delta t + k_b\,{}^{t}a_{j,k}^{Ox}\Delta t \qquad j = 2,3,\ldots,J-2 \qquad (3.33)$$

Thus one can obtain the concentrations of species Ox in space (x, y) and at time (t) for a certain flow rate, and then simply integrate them within the region studied. The concentrations of species Red and X can also be obtained according to the same method as before.

3.2.3 Catalytic (EC') Reaction

An important type of electrode reaction is the so-called catalytic (EC') mechanism [1-10] in which an electrogenerated species oxidises or reduces some other solution species with the regeneration of the original electroactive material which undergo further electron transfer at the electrode. The process has significance both for synthesis [10] and for the kinetic characterisation of reaction intermediates [1-10]. In the simplest form, the mechanism is defined by the following kinetic scheme:

$$\mathrm{Red} \rightleftharpoons \mathrm{Ox} + \mathrm{ne}^- \qquad (3.34)$$

$$\mathrm{Ox} + \mathrm{S} \underset{k_b}{\overset{k_f}{\rightleftharpoons}} \mathrm{Red} + \mathrm{C} \qquad (3.35)$$

When C is the intermediate, then

$$\mathrm{C} \rightarrow \mathrm{product} \qquad (3.35a)$$

or

$$\mathrm{C} + \mathrm{S} \rightarrow \mathrm{Red} + \mathrm{product} \qquad (3.35b)$$

or

$$\mathrm{C} + \mathrm{S} \rightarrow \mathrm{Ox} + \mathrm{product} \qquad (3.35c)$$

Reaction (3.35a) is called EC′ (pre-eqm) mechanism [1-5,8-9,11] which involves a pre-equilibrium prior to an irreversible product-forming step. The equilibrium constant, K_{eq}, for reaction (3.35) is

$$K_{eq} = \frac{k_f}{k_b} = \frac{C_{Red} C_C}{C_{Ox} C_S} \tag{3.36}$$

Reaction (3.35b) is called the EC′ (disp Red) mechanism while reaction (3.35c) is called the EC′(disp Ox) mechanism. Here discussion is limited to the case in which C is stable.

The general equations for one-dimensional diffusion and one-dimensional convection that describe the distribution of species Ox, Red, and C for the reaction (3.34) and (3.34) at time (t) and space (x, y) in three-dimension space are respectively:

$$\frac{\partial C_{Red}}{\partial t} = D_{Red} \frac{\partial^2 C_{Red}}{\partial y^2} - v_x \frac{\partial C_{Red}}{\partial x} + k_f C_{Ox} C_S - k_b C_{Red} C_C \tag{3.37}$$

$$\frac{\partial C_{Ox}}{\partial t} = D_{Ox} \frac{\partial^2 C_{Ox}}{\partial y^2} - v_x \frac{\partial C_{Ox}}{\partial x} - k_f C_{Ox} C_S + k_b C_{Red} C_C \tag{3.38}$$

$$\frac{\partial C_S}{\partial t} = D_S \frac{\partial^2 C_S}{\partial y^2} - v_x \frac{\partial C_S}{\partial x} - k_f C_{Ox} C_S + k_b C_{Red} C_C \tag{3.39}$$

$$\frac{\partial C_C}{\partial t} = D_C \frac{\partial^2 C_C}{\partial y^2} - v_x \frac{\partial C_C}{\partial x} + k_f C_{Ox} C_S - k_b C_{Red} C_C \tag{3.40}$$

The boundary conditions are:

For t = 0, any y,

$$C_{Ox} = C_S = 0, \qquad C_{Red} = C_{Red}^{Bulk} \tag{3.41}$$

For t > 0, y → ∞,

$$\frac{C_{\mathrm{Re}d}C_C}{C_{Ox}C_S}=\frac{k_f}{k_b}=K_{eq}, \qquad C_{\mathrm{Re}d}\rightarrow C_{\mathrm{Re}d}^{Bulk} \tag{3.42}$$

For t > 0, y = 0,

$$-D_{Ox}\frac{\partial C_{Ox}}{\partial y}=D_{\mathrm{Re}d}\frac{\partial C_{\mathrm{Re}d}}{\partial y}=\frac{i(t)}{nFA} \tag{3.43}$$

$$\frac{C_{Ox}}{C_{\mathrm{Re}d}}\Big|_{y=0}=\left(\frac{D_{\mathrm{Re}d}}{D_{Ox}}\right)^{\frac{1}{2}}\exp(\Phi+\xi(t)) \tag{3.44}$$

$$D_X\frac{\partial C_X}{\partial y}=0 \tag{3.45}$$

Here k_f and k_b are the rate constants of the second-order reaction (M^{-1} s^{-1}). All the other parameters have the same meaning as before. The system of equations (3.37) to (3.40) with equations (3.41) to (3.45) can be solved by the numerical method used as before for the channel cell and may be expressed in the form of a (J-1) ×(J-1) tridiagonal matrix. The matrix elements for species Ox are given by:

For k =1,

$$d_1={}^{t}a_{1,1}^{Ox}+\lambda_1^c\left\{{}^{t+1}a_{1,0}^{x}\right\}-k_f\,{}^{t}a_{1,1}^{Ox}\,{}^{t}a_{1,1}^{S}\Delta t+k_b\,{}^{t}a_{1,1}^{\mathrm{Re}d}\,{}^{t}a_{1,1}^{C}\Delta t+\frac{\lambda^y(D_{Ox}\,{}^{t}a_{1,1}^{Ox}+D_{\mathrm{Re}d}\,{}^{t}a_{1,1}^{\mathrm{Re}d})}{D_{\mathrm{Re}d}+(D_{Ox}D_{\mathrm{Re}d})^{\frac{1}{2}}\exp(-\Phi-\xi(t))} \tag{3.46}$$

$$d_j={}^{t}a_{j,1}^{Ox}+\lambda_j^c\left\{{}^{t+1}a_{j,0}^{Ox}\right\}-k_f a_{j,1}^{Ox}a_{j,1}^{S}\Delta t+k_b\,{}^{t}a_{j,1}^{\mathrm{Re}d}\,{}^{t}a_{j,1}^{C}\Delta t \qquad j=2,3,\ldots,J-1 \tag{3.47}$$

For k > 1,

$$d_1={}^{t}a_{1,k}^{Ox}+\lambda_1^c\left\{{}^{t+1}a_{1,k-1}^{Ox}\right\}-k_f\,{}^{t}a_{1,k}^{Ox}a_{1,k}^{S}\Delta t+k_b\,{}^{t}a_{1,k}^{\mathrm{Re}d}\,{}^{t}a_{1,k}^{C}\Delta t+\frac{\lambda^y(D_{Ox}\,{}^{t}a_{1,k}^{Ox}+D_{\mathrm{Re}d}\,{}^{t}a_{1,k}^{\mathrm{Re}d})}{D_{\mathrm{Re}d}+(D_{Ox}D_{\mathrm{Re}d})^{\frac{1}{2}}\exp(-\Phi-\xi(t))} \tag{3.48}$$

$$d_j={}^{t}a_{j,k}^{Ox}+\lambda_j^c\left\{{}^{t+1}a_{j,k-1}^{Ox}\right\}-k_f\,{}^{t}a_{j,k}^{Ox}a_{j,k}^{S}\Delta t+k_b\,{}^{t}a_{j,k}^{\mathrm{Re}d}\,{}^{t}a_{j,k}^{C}\Delta t \qquad j=2,3,\ldots,J-2 \tag{3.49}$$

The superscripts represent species or time intervals, subscripts stand for space (j, k), Δt is the time difference. Once again we can get the concentrations of species Ox, Red, and S in space (x, y) and time (t) at a certain flow rate, then integrate them within the studied region.

In this way the forms common to all above cases for the Faradaic current, $i_f(t)$ and C(x, t) at the electrode at the instant time (t) may be expressed as:

$$i_f(t) = nFwD_{Red}\left\{\sum_{k=1}^{K}({}^{t}a_{1,k}^{ox} - {}^{t}a_{0,k}^{ox})\frac{\nabla x}{\nabla y}\right\} \tag{3.50}$$

$$C_i(x,t) = \frac{\sum_{0}^{X_e}\sum_{0}^{2h} W(j)W(k)\,{}^{t}a_{j,k}^{i}\Delta x\Delta y}{\sum_{0}^{X_e}\sum_{0}^{2h} W(j)W(k)\Delta x\Delta y} \tag{3.51}$$

where $C_i(x,t)$ is the concentrations of Ox or Red within the detection region, superscript i presents Ox or Red. W(j) and W(k) are the weighing functions for the space(j, k) and here are 1 for both. x_e, J, K can be seen in figure 2.3 in the Chapter 2, $\Delta x = x_e/J$, $\Delta y = 2h/K$, J and K are the number of the grid used in casting into finite difference form within the interested area. So the PMRS signal, $\Delta R/R$, can be derived from the equation (2.18) if ε is known. It should be noted that equations (3.50) and (3.51) include all harmonic components, but the PMRS signal can be separated by the FFT which maps the time domain onto the frequency domain. Also note that when $k_f = k_b = 0$, these problems reduce to the simple electron transfer case discussed in the Chapter 2.

3.3 Simulation Results

For the sake of simplicity, it has been assumed that all the species in the solution have a separate absorption region with maximum absorption coefficient of $1000M^{-1}cm^{-1}$. The following general conditions were used: species concentration, 2 mM, angles of the incident and reflected light, 60^0, amplitude (Am) of the superimposed perturbation 10 mV (rms), frequency 9.8 Hz. The potential scan rate was 3 mV/sec. The channel parameters are $x_e = 0.386$ cm, w = 0.372 cm, 2h = 0.044 cm, sampling number is 8, J = 15, K = 600 (unless stated).

3.3.1 CE Reaction

The initial total concentration of the species Y and Red was taken to be 2 mM in the solution at equilibrium with the equilibrium constant, K_{eq}. Both the forward and backward reactions are assumed to be first-order. D_Y is 2.0×10^{-5} cm^2 s^{-1}, $D_{Red} = D_{Ox} = 1.8 \times 10^{-5}$ cm^2 s^{-1}.

When K_{eq} and v_f are fixed, the concentrations of the species increase with increasing k_f as expected. So the PMRS signal will also increase with the increase of k_f as shown in figures 3.1and 3.2. It can been also seen that the PMRS signal is very sensitive to the rate constants.

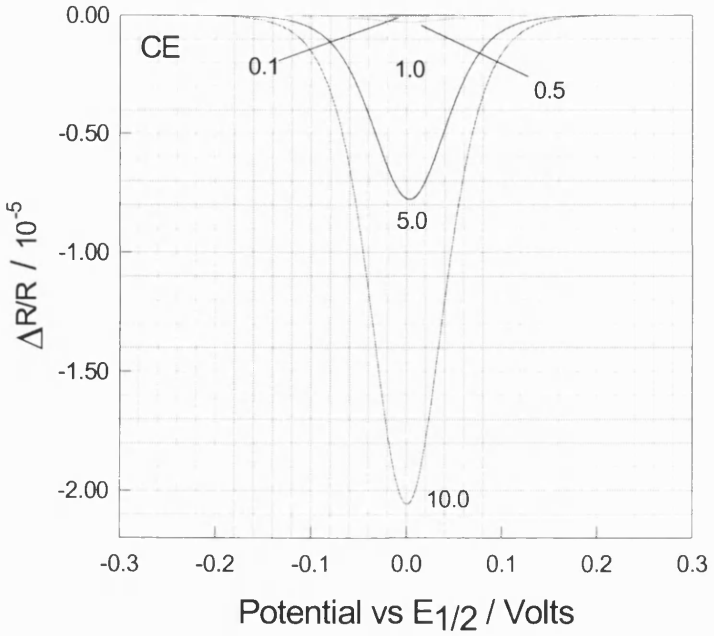

Figure 3.1 Calculated ΔR/R for CE mechanism as a function of k_f in s^{-1}: Y is the detected species, $C_{total}^{bulk} = 2\,mM$, $K_{eq} = 10$, $v_f = 5.0 \times 10^{-2}$ $cm^3\ s^{-1}$, $\varepsilon_Y = 1000$ $M^{-1}\ cm^{-1}$, $\varepsilon_{Red} = \varepsilon_{Ox} = 0$, frequency = 9.8 Hz, amplitude = 10 mV(rms), sampling number = 8, J = 15, K= 600.

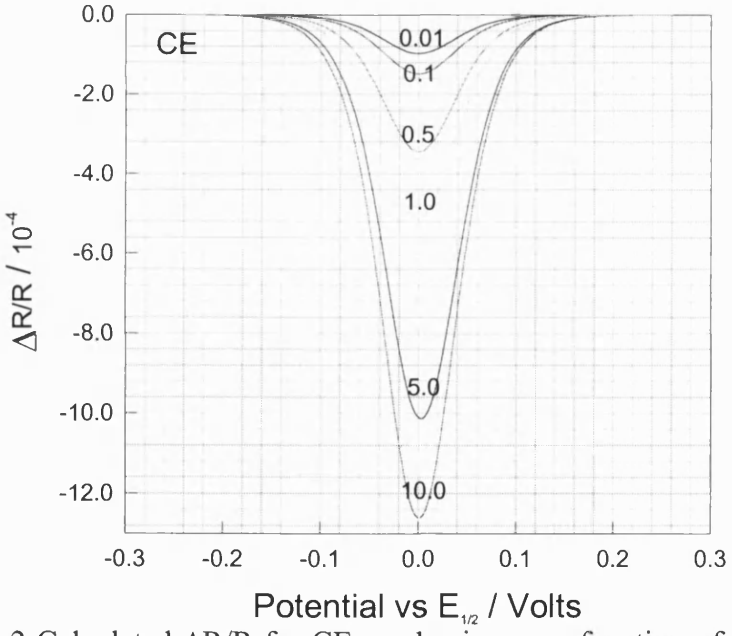

Figure 3.2 Calculated ΔR/R for CE mechanism as a function of k_f in s^{-1}: either Red or Ox is the detected species, $C_{total}^{bulk} = 2\,mM$, $K_{eq} = 10$, $v_f = 5.0 \times 10^{-2}$ $cm^3\ s^{-1}$, $\varepsilon_{Red} = \varepsilon_{Ox} = 1000$ $M^{-1}cm^{-1}$, $\varepsilon_Y = 0$, frequency = 9.8 Hz, amplitude = 10 mV (rms), sampling number = 8, J = 15, K= 600.

Furthermore the sensitivity of PMRS is very much dependent upon the species selected for detection in the solution. The sensitivity is higher when the species Y is selected than when Red or Ox is selected for detection. This is also true for the equilibrium constant that can be seen from figures 3.3 and 3.4. However, the PMRS signal will decrease with the increase of the equilibrium constant due to the decrease of the concentrations.

Since the thickness of the diffusion layer decreases with increasing flow rate under the fixed k_f and K_{eq}, the PMRS signals will decrease with increasing flow rate as shown in figures 3.5 and 3.6. It can be seen that the PMRS signals are very sensitive to the flow rate, and they are also relatively small when Y is the detected species.

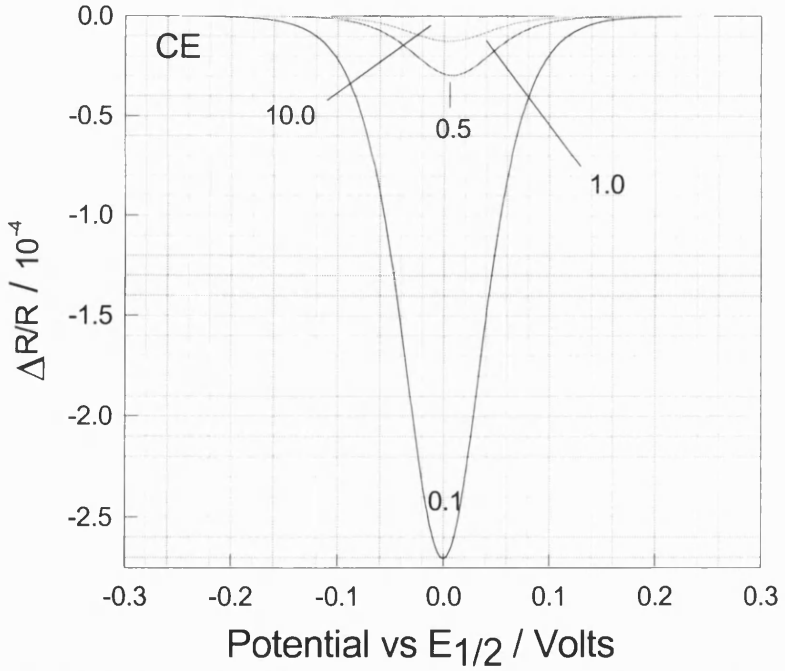

Figure 3.3 Calculated ΔR/R for EC mechanism varying with K_{eq}: Y is the detected species, $C_{total}^{bulk} = 2mM$, $k_f = 1.0\ s^{-1}$, $v_f = 5.0 \times 10^{-2}\ cm^3\ s^{-1}$, $\varepsilon_Y = 1000\ M^{-1}\ cm^{-1}$, $\varepsilon_{Red} = \varepsilon_{Ox} = 0$, frequency = 9.8 Hz, amplitude = 10 mV (rms), sampling number = 8, J = 15, K= 600.

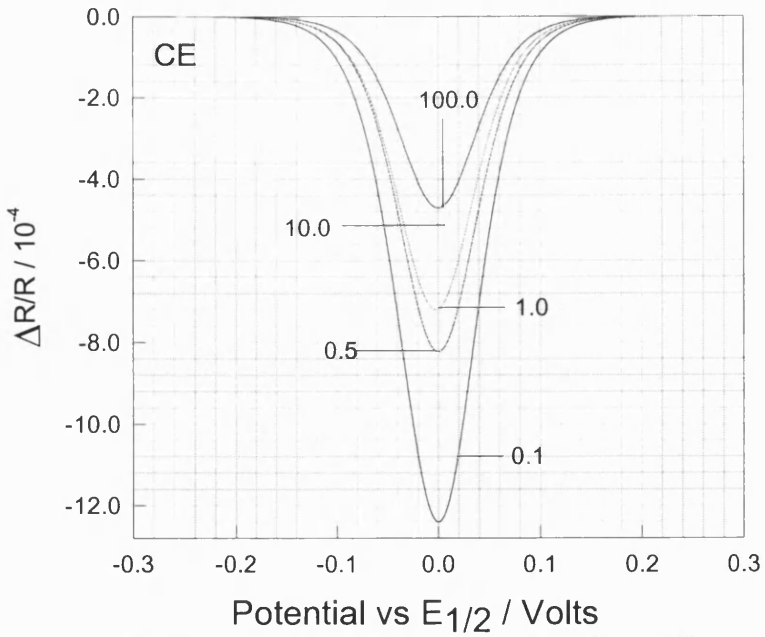

Figure 3.4 Calculated ΔR/R for CE mechanism as a function of K_{eq}: either Red or OX is the detected species, $C_{total}^{bulk} = 2mM$, k_f = 1.0 s^{-1}, v_f = 5.0 × 10^{-2} cm^3 s^{-1}, $\varepsilon_{Red} = \varepsilon_{Ox}$ =1000M^{-1} cm^{-1}, ε_Y = 0, frequency = 9.8 Hz, amplitude = 10 mV (rms), sampling number = 8, J = 15, K= 600.

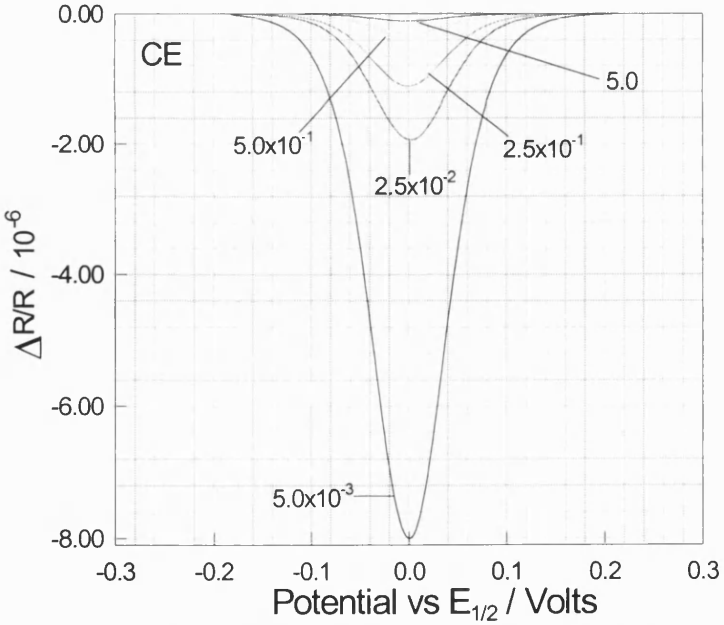

Figure 3.5 Calculated ΔR/R for CE mechanism under different flow rates, v_f, in cm^3s^{-1}: Y is the detected species, $C_{total}^{bulk} = 2mM$, k_f = 1.0 s^{-1}, K_{eq}= 10, ε_Y =1000M^{-1} cm^{-1}, $\varepsilon_{Red} = \varepsilon_{Ox}$ = 0, frequency = 9.8 Hz, amplitude = 10 mV (rms), sampling number = 8, J = 15, K= 600.

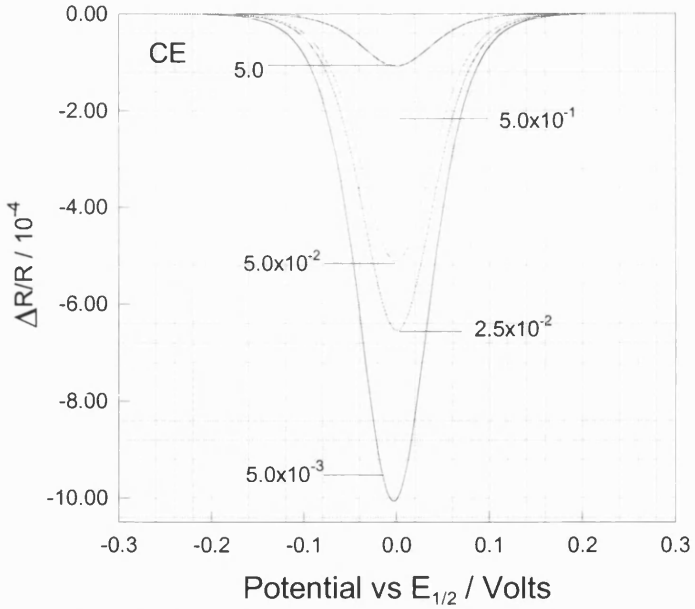

Figure 3.6 Calculated ΔR/R for CE mechansim under different flow rates, v_f: either Ox or Red is the detected species, $C_{total}^{bulk} = 2\,mM$, K_{eq} = 10.0, k_f = 1.0 s^{-1}, $\varepsilon_{Red} = \varepsilon_{Ox}$ =1000 M^{-1} cm^{-1}, ε_Y = 0, frequency = 9.8 Hz, amplitude = 10 mV (rms), sampling number = 8, J = 15, K= 600.

It has known from the Chapter 2 that the PMRS signal decreases with the increase of ω. Figure 3.7 only shows 3 significant frequencies at a constant k_f, K_{eq} and v_f.

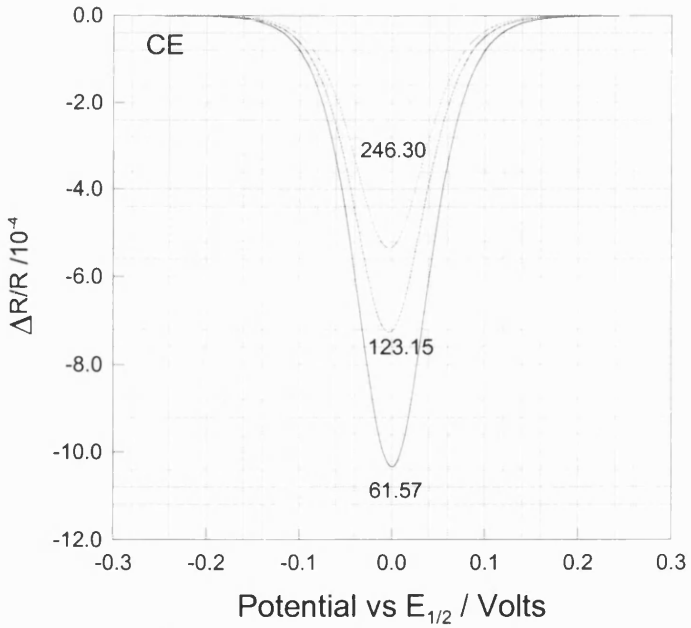

Figure 3.7 Calculated ΔR/R for CE mechanism as a function of ω in s^{-1}: Ox is the detected species, $C_{total}^{bulk} = 2\,mM$, v_f = 5.0 × 10^{-2} cm^3s^{-1}, k_f = 1.0 s^{-1}, K_{eq} = 10.0, ε_{Ox} = 1000 M^{-1} cm^{-1}, $\varepsilon_{Red} = \varepsilon_Y$ = 0, amplitude = 10 mV (rms), sampling number = 8, J = 15, K= 600.

In general the channel electrode PMRS technique can be used to study the CE mechanism quantitatively. All species involved in the mechanism can be detected by PMRS, but it is better to select the electroactive species if possible since the response is large.

3.3.2 EC Reaction

C_{Red} is taken to be 2 mM, and it is assumed that species Ox and X are initially absent from the solution. Both the forward and backward reactions in the coupled chemical reaction are first-order. D_X is 1.8×10^{-5} cm^2 s^{-1}, $D_{Red} = D_{Ox} = 2.0 \times 10^{-5}$ cm^2 s^{-1}. All other conditions and parameters are same as above except where stated.

When v_f and K_{eq} are fixed, the higher the rate constant of the forward reaction, the shorter the time required to reach equilibrium, and the higher the concentration of the species X. So the PMRS signal will increase with the increase of k_f as shown in figures 3.8 and 3.9. Both figures show that the PMRS signals are sensitive to the rate constant of the forward reaction.

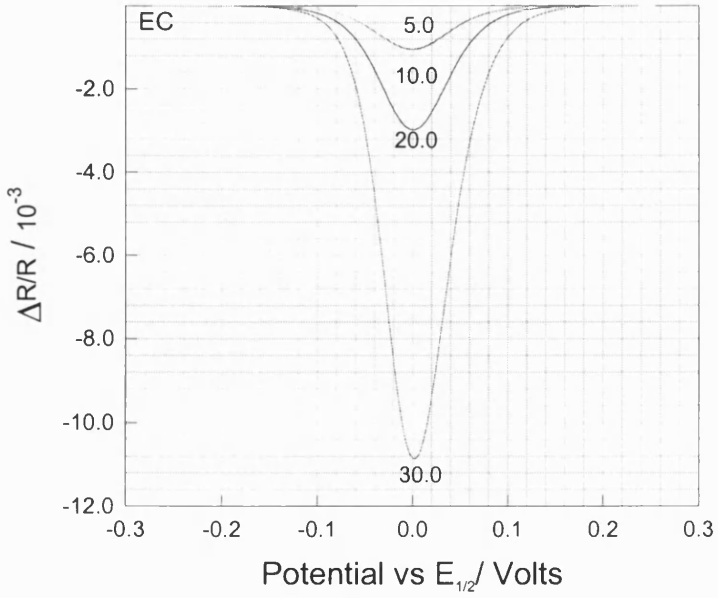

Figure 3.8 Calculated ΔR/R for EC mechanism as a function of k_f in s^{-1}: either Ox or Red is the detected species, C_{Red} = 2 mM, K_{eq} = 10.0, $v_f = 5.0\times10^{-2}cm^3\ s^{-1}$, ω = 61.57 s^{-1}, $\varepsilon_{Red} = \varepsilon_{Ox}$ = $1000M^{-1}\ cm^{-1}$, ε_Y = 0, amplitude = 10 mV (rms), sampling number = 8, J = 15, K= 600.

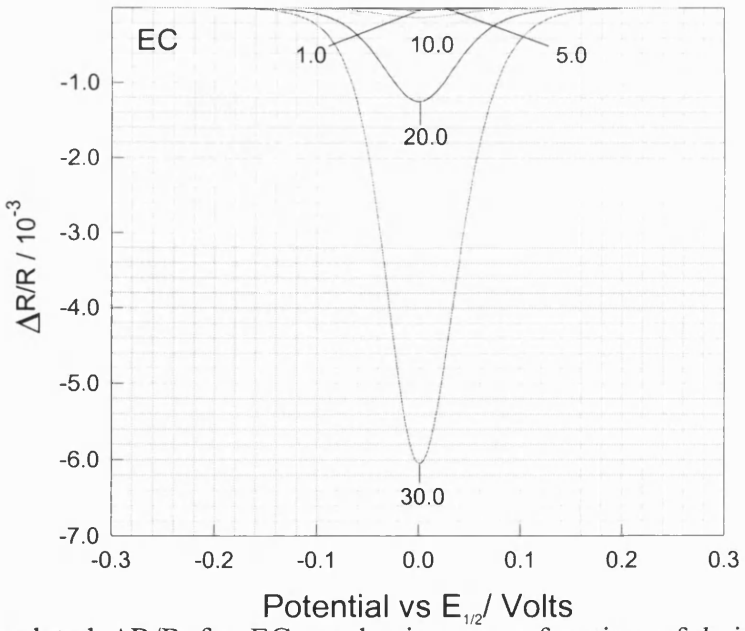

Figure 3.9 Calculated ΔR/R for EC mechanism as a function of k_f in s^{-1}: X is the detected species, C_{Red} = 2 mM, K_{eq} = 10.0, $v_f = 5.0\times10^{-2}cm^3\ s^{-1}$, ω = 61.57 s^{-1}, ε_X = $1000M^{-1}\ cm^{-1}$, $\varepsilon_{Red} = \varepsilon_{Ox}$ = 0, amplitude = 10 mV (rms), sampling number = 8, J = 15, K= 600.

When k_f and v_f are fixed, the larger the equilibrium constant, the longer the time to reach the equilibrium, so the concentration of species Ox is higher, and the PMRS signal will increase with increasing K_{eq} as shown in figures 3.10 and 3.11. It can be seen that the changes at lower equilibrium constants are distinguishable, while there are no differences at higher values. For example when k_f = 1.0 s^{-1}, there are no differences when the equilibrium constants are greater than 100, in which case the reverse reaction of the coupled chemical reaction can be ignored. Note that the maximum equilibrium constant studied by PMRS is related to the frequency of the superimposed perturbation and to the rate constants of both the forward and reverse chemical reaction.

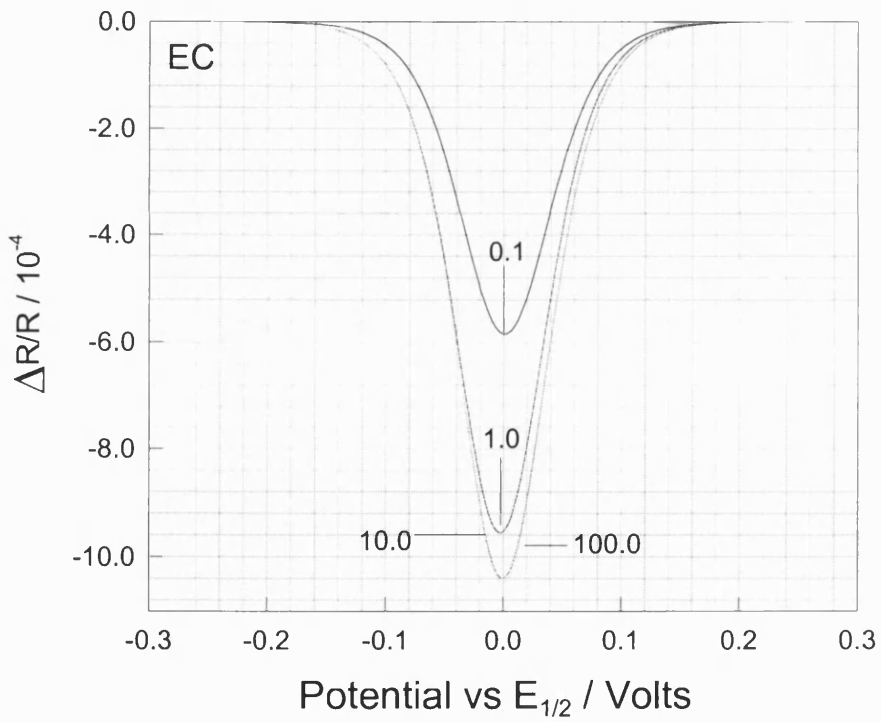

Figure 3.10 Calculated ΔR/R for EC mechanism as a function of K_{eq}: X is selected to be detected, C_{Red} = 2 mM, k_f = 1.0 s^{-1}, v_f =5.0×$10^{-2}$$cm^3$ s^{-1}, ε_X =1000 M^{-1} cm^{-1}, $\varepsilon_{Red} = \varepsilon_{Ox}$ = 0, amplitude = 10 mV (rms), sampling number = 8, J = 15, K= 600.

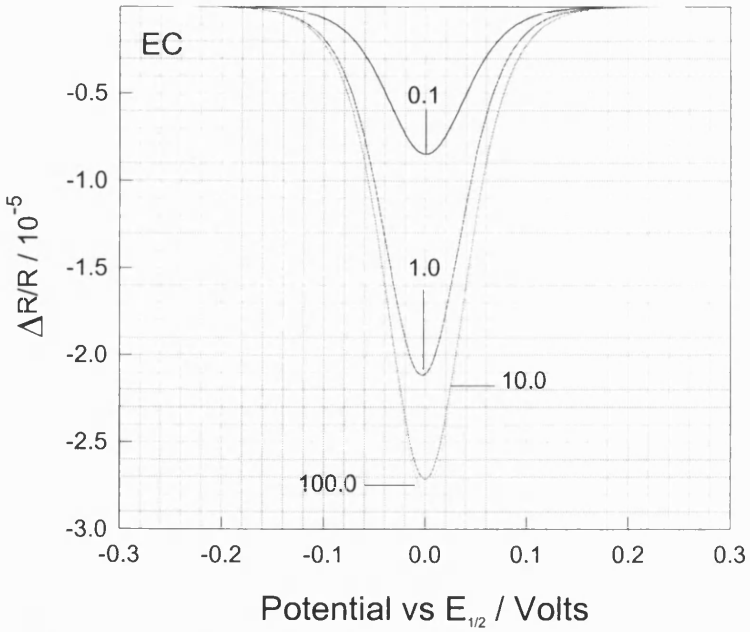

Figure 3.11 Calculated ΔR/R for EC mechanism as a function of K_{eq}: either Ox or Red is the detected species, C_{Red} = 2 mM, k_f = 1.0, v_f =5.0×10^{-2}cm^3 s^{-1}, ε_{Red} = ε_{Ox} = 1000M^{-1}cm^{-1}, ε_X = 0, amplitude = 10 mV(rms), sampling number = 8, J = 15, K= 600.

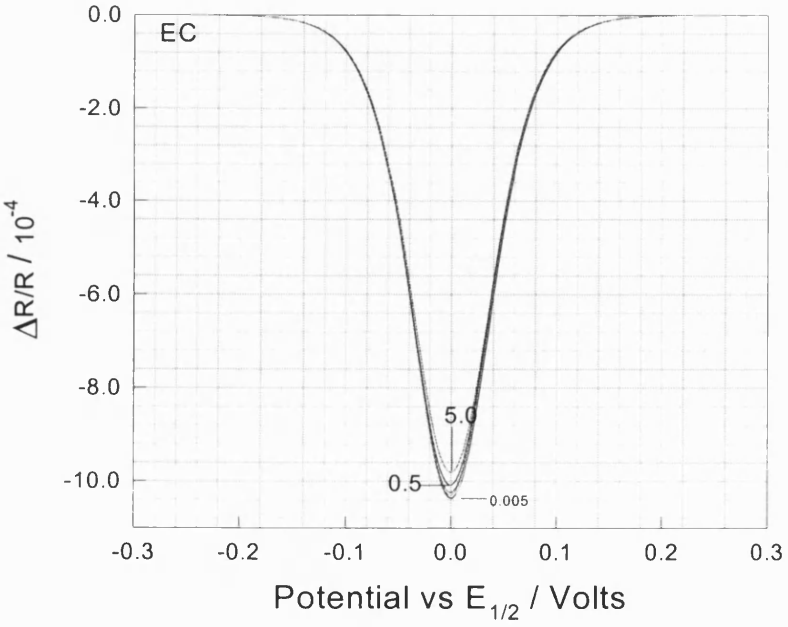

Figure 3.12 Calculated ΔR/R for EC mechanism varied v_f: either Ox or Red is the detected species, C_{Red} = 2 mM, K_{eq} = 10.0, k_f = 1.0 s^{-1}, ω = 61.57 s^{-1}, ε_{Red} = ε_{Ox} = 1000 M^{-1} cm^{-1}, ε_X = 0, amplitude = 10 mV (rms), sampling number = 8, J = 15, K= 600.

Figure 3.12 shows that the PMRS signals should not change much with flow rate when the species Ox or Red are detected. By contrast, the PMRS signals change significantly with flow rate when X is the detected species, as shown in figure 3.13.

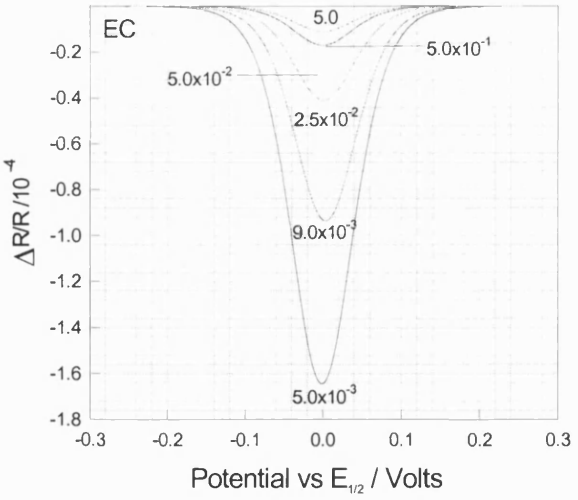

Figure 3.13 Calculated ΔR/R for EC mechanism under different v_f: the species X is detected, C_{Red} = 2 mM, k_f = 1.0 s^{-1}, K_{eq} = 10.0, ω = 61.57 s^{-1}, ε_X = 1000 M^{-1} cm^{-1}. ε_{Red} = ε_{Ox} = 0, amplitude = 10 mV (rms), sampling number = 8, J = 15, K= 600.

An important case occurs when the coupled chemical reaction is irreversible. ie k_b = 0. The following part discusses this case.

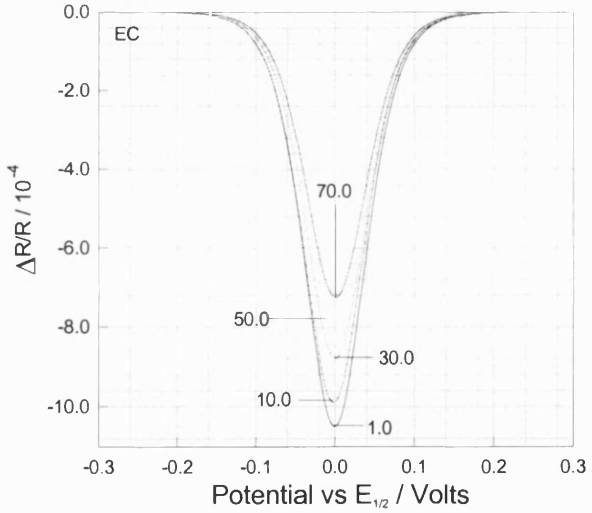

Figure 3.14 Calculated ΔR/R for EC mechanism as a function of k_f: either Ox or Red is the detected species, k_b = 0, C_{Red} = 2 mM, v_f = 5.0x$10^{-2}$$cm^3$ s^{-1}, ω = 61.57 s^{-1}, ε_{Red} = ε_{Ox} = 1000 M^{-1} cm^{-1}, ε_X = 0, amplitude = 10 mV (rms), sampling number = 8, J = 15, K= 600.

It can be seen from figure 3.14 that the PMRS signals decrease with increasing rate constants of the coupled chemical reaction when either Ox or Red are the detected species. By contrast, the PMRS signals increase with increase of the rate constants when the detected species is X, as shown in figure 3.15. The PMRS response is sensitive in both cases, but the latter is more sensitive and more distinguishable.

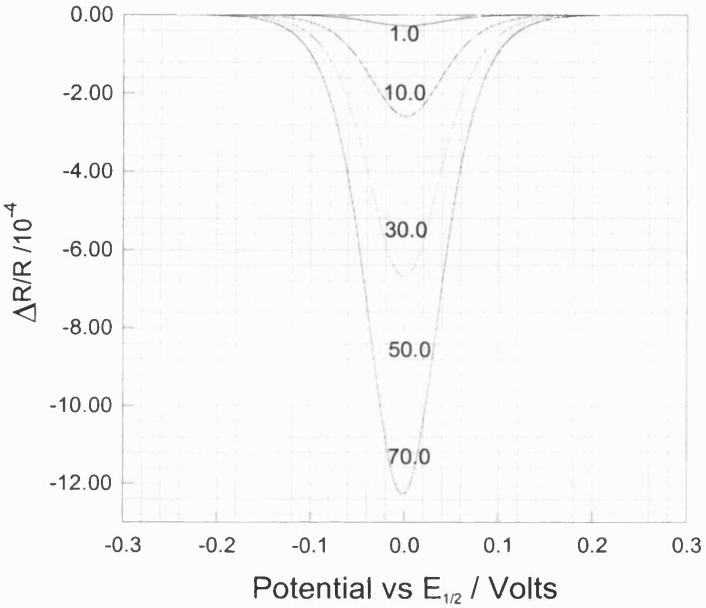

Figure 3.15 Calculated ΔR/R for EC mechanism varied k_f: X is the detected species, k_b = 0, C_{Red} = 2 mM, $v_f = 5.0\times10^{-2}$ cm^3 s^{-1}, ω = 61.57 s^{-1}, ε_X = 1000 M^{-1} cm^{-1}, $\varepsilon_{Red} = \varepsilon_{Ox}$ = 0, amplitude = 10 mV (rms), sampling number = 8, J = 15, K= 600.

Figures 3.16 shows that the PMRS signals vary with the flow rates when X is the detected species. It can be seen that the PMRS signal is sensitive and distinguishable. In marked contrast, figure 3.17 shows that the flow rate has a little effect on the PMRS signal when Ox or Red is the detected species. This is due to the fact that the modulation is too rapid for the coupled chemical reaction to be perturbed substantially. The half life of the coupled chemical reaction is given $t_{1/2} = ln2/k_f = 0.693$ s. By contrast, the period T of the modulation is given $T = 1/f = 0.1$ s.

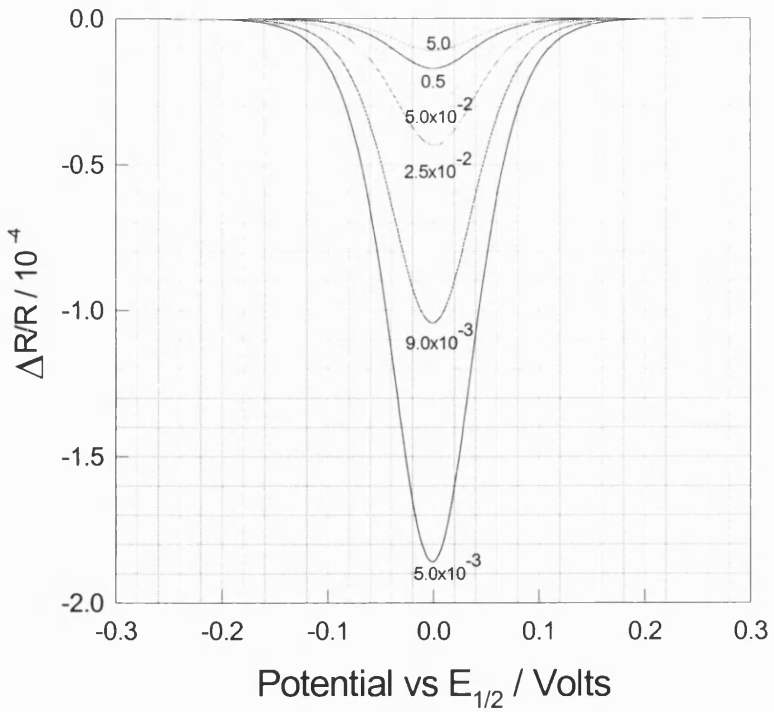

Figure 3.16 Calculated ΔR/R for EC mechanism as a function of v_f: X is the detected species, C_{Red} = 2 mM, k_f = 1.0 s^{-1}, k_b =0, ε_X = 1000 M^{-1} cm^{-1}, ω =61.57 s^{-1}, $\varepsilon_{Red} = \varepsilon_{Ox}$ = 0, amplitude = 10 mV (rms), sampling number = 8, J = 15, K= 600.

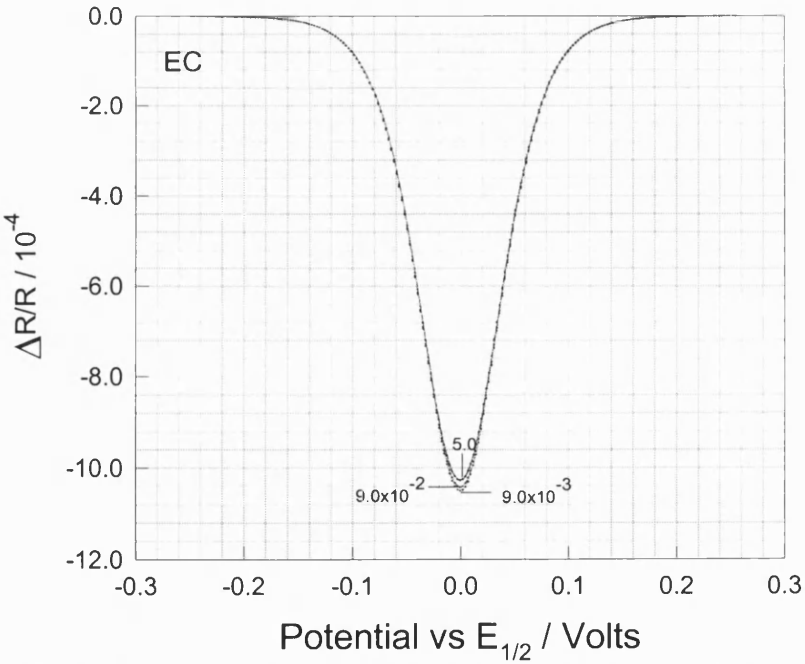

Figure 3.17 Calculated ΔR/R for EC mechanism as a fuction of v_f: either Ox or Red is the detected species, C_{Red} = 2 mM, k_f = 10.0 s^{-1}, k_b = 0, ε_X = 1000 M^{-1} cm^{-1}, ω = 61.57 s^{-1}, $\varepsilon_{Red} = \varepsilon_{Ox}$ = 0, amplitude = 10 mV (rms), sampling number = 8, J = 15, K= 600.

In general, the PMRS technique can be used to investigate the EC mechanism. If the coupled chemical reaction is reversible, the PMRS is very sensitive regardless of which of the species is detected. If the coupled chemical reaction is irreversible, PMRS is more sensitive when the species X is detected than when Ox or Red are the detected species.

3.3.3. EC′ Reaction

It is assumed that $C_{Red} = C_S = 2$ mM, and that C_{Ox} and C_C are initially zero in the solution. Both the forward and backward reactions in the coupled chemical reaction are second-order. $D_{Red} = 6.5 \times 10^{-6}$ cm^2 s^{-1}, $D_{Ox} = 7.6 \times 10^{-6}$ cm^2 s^{-1}, $D_S = D_C = 6.8 \times 10^{-6}$ cm^2 s^{-1}. All other conditions and parameters are same as above except where stated.

It can be seen from figure 3.18 that the PMRS signals do not change with the equilibrium constants when either species Red or Ox is detected. This can be understood because regeneration of the species Red keeps the concentrations of species Red and Ox unchanged. The PMRS response will change significantly `with the equilibrium constants when either species S or C is detected (similar as figure 3.19). However, in this case the PMRS signals are very small ($10^{-7}$to 10^{-8}) and probably impossible to observe reliably. The PMRS signals may be enhanced by reducing the frequency or by increasing the concentrations of the species S and Red.

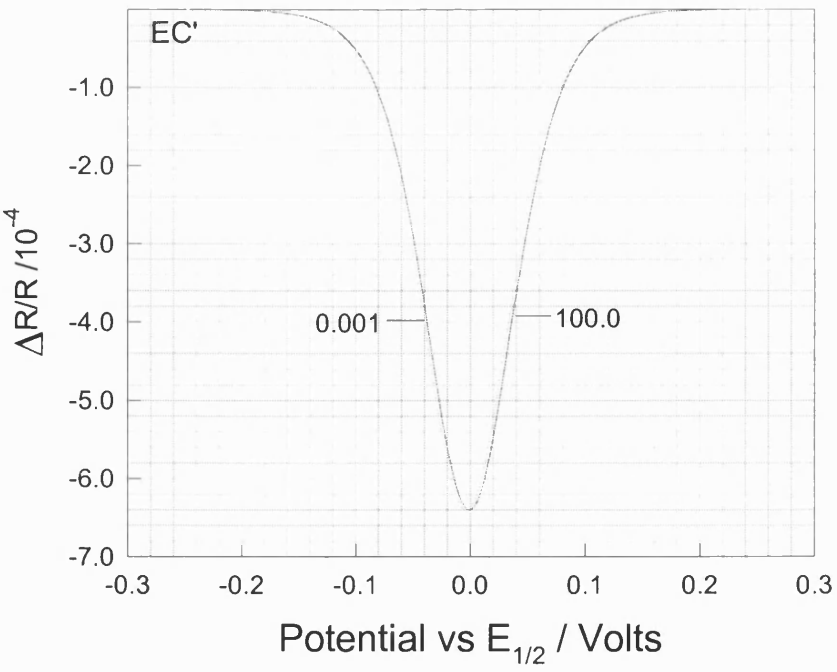

Figure 3.18 Calculated ΔR/R for EC′ mechanism as a function of K_{eq}: either Ox or Red is the detected species, $C_{Red} = C_S = 2$ mM, $k_f = 1.0$ M^{-1} s^{-1}, $\varepsilon_{Red} = \varepsilon_{Ox} = 1000$ M^{-1} cm^{-1}, $\omega = 61.57$ s^{-1}, $C_{Ox} = C_C = 0$, $\varepsilon_S = \varepsilon_C = 0$, amplitude = 10 mV (rms), sampling number = 8, J = 15, K= 600.

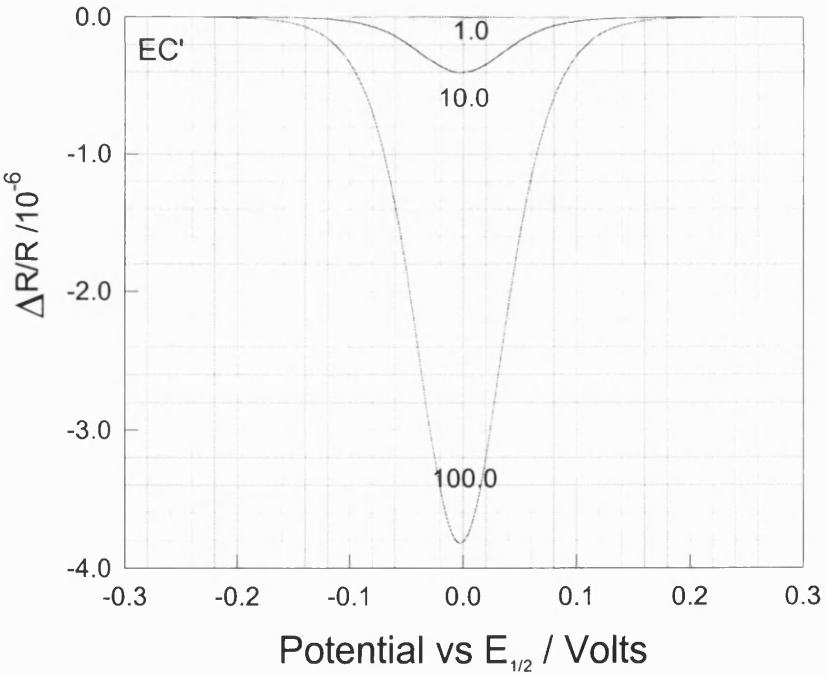

Figure 3.19 Calculated ΔR/R for EC′ mechanism as a function of k_f : either species S or C is detected, $C_{Red} = C_S = 2$ mM, $K_{eq} = 10.0$, $\varepsilon_S = \varepsilon_C = 1000$ M^{-1} cm^{-1}, $\omega = 61.57$ s^{-1}, $C_{Ox} = C_C = 0$, $\varepsilon_{Ox} = \varepsilon_{Red} = 0$, amplitude = 10 mV (rms), sampling number = 8, J = 15, K= 600.

The PMRS signals do not change with the change of the rate constants of the forward reaction when the flow rate and the equilibrium constant are fixed. The reason is that the concentrations of the species Ox and Red remain unchanged due to regeneration of the species Red when Ox or Red is the detected species (the response is similar to that shown in figure 3.18). However the PMRS signals change substantially when species S or C are detected, as shown in figure 3.19. Note that the PMRS signals are still very small relative to the usual resolution of a lock-in amplifier, but fortunately they can be improved by reducing the modulation frequency shown in figure 3.20, or by increasing the concentrations of the species Red and S as discussed later.

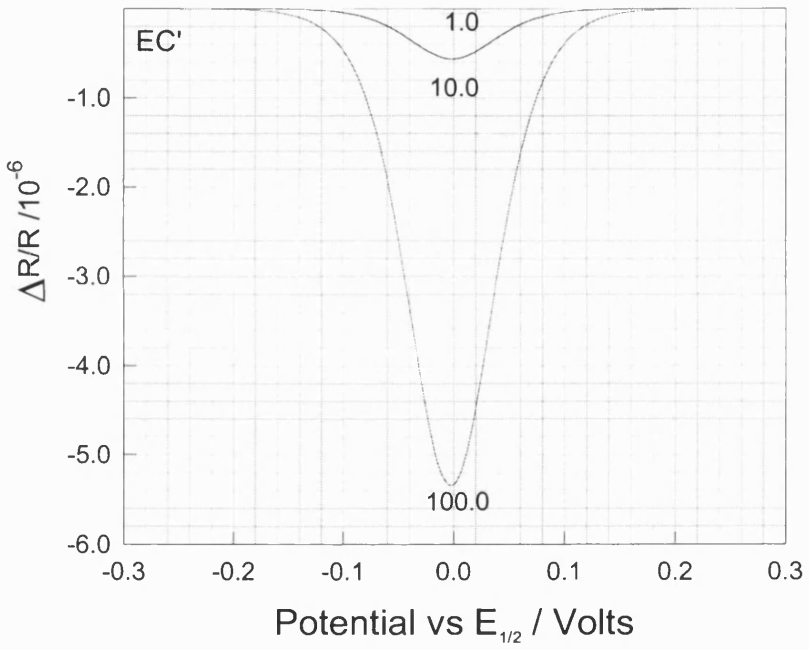

Figure 3.20 Calculated ΔR/R for EC′ mechanism as a function of k_f: either species S or C is detected, $C_{Red} = C_S = 2$ mM, $K_{eq} = 10.0$, $\varepsilon_S = \varepsilon_C = 1000\ M^{-1}\ cm^{-1}$, $\omega = 31.42\ s^{-1}$, $C_{Ox} = C_C = 0$, $\varepsilon_{Ox} = \varepsilon_{Red} = 0$, amplitude = 10 mV (rms), sampling number = 8, J = 15, K= 600.

As mentioned above, increasing the concentrations of the species Red or S can enhance the PMRS signals when species S or C is selected for detection. Figure 3.21

shows that the PMRS signals increase with the increase of the ratio of the concentration of the species S to Red, R_{sr}.

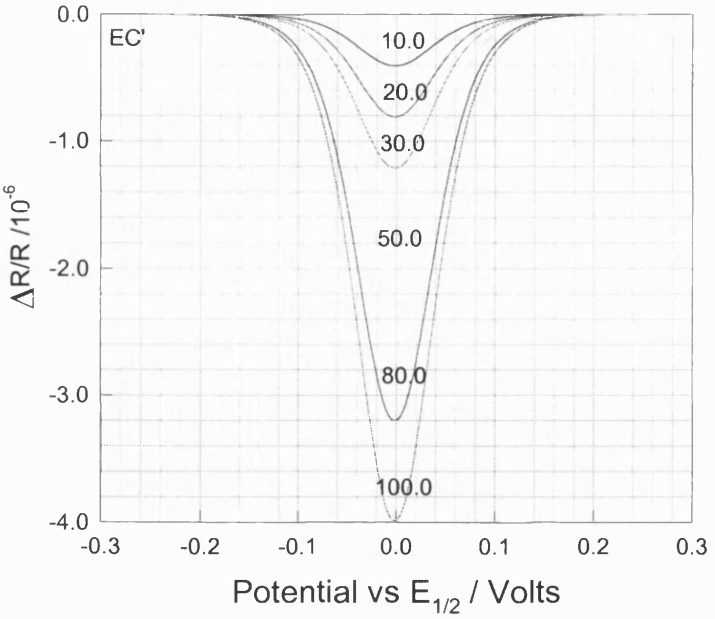

Figure 3.21 Calculated ΔR/R for EC′ mechanism varied R_s: either species S or C is detected, C_{Red} = 2 mM, K_{eq} = 10.0, k_f = 1.0 $M^{-1}s^{-1}$, $\varepsilon_S = \varepsilon_C$ = 1000 M^{-1} cm^{-1}, ω =61.57 s^{-1}, $C_{Ox} = C_C$ = 0, v_f= 5.0 x 10^{-2} cm^3 s^{-1}, $\varepsilon_{Ox} = \varepsilon_{Red}$ = 0, amplitude = 10 mV (rms), sampling number = 8, J = 15, K= 600.

The PMRS signal can be enhanced further by increasing the concentration of species Red, say, to 10 mM, 5 times higher, in which case the PMRS signal will be 10^{-5} which is within the resolution of the lock-in amplifier.

The above calculations were made for a fixed flow rate. Figure 3.22 shows that the PMRS signals vary with the flow rate when S or C are the detected species, the PMRS signal decreases with the increase of the flow rate. While the PMRS signal does not change with the change of the flow rate when Red or OX are the detected species (not shown in the figure).

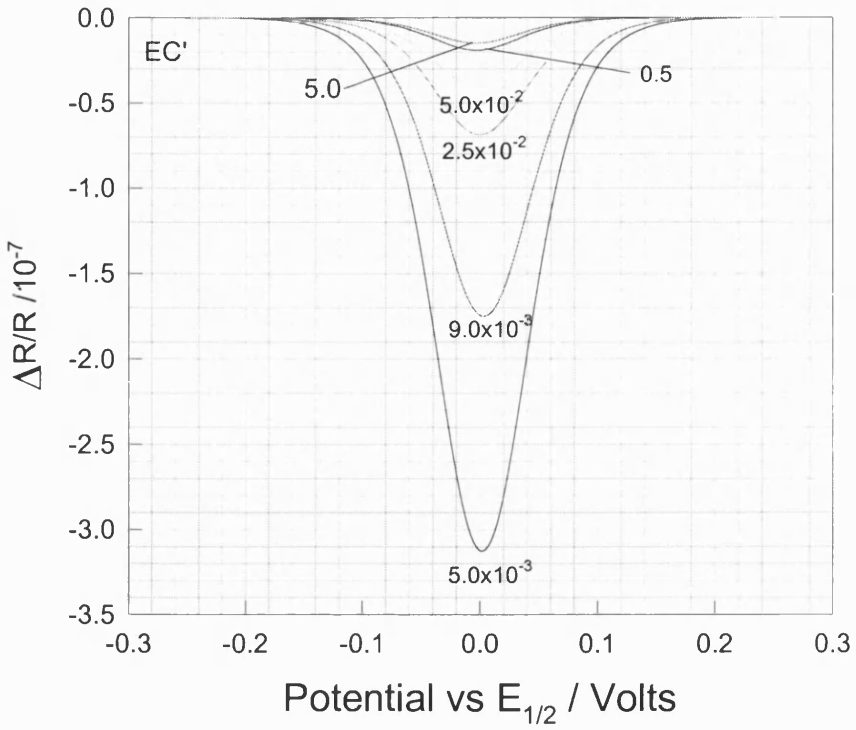

Figure 3.22 Calculated ΔR/R for EC′ mechanism as a function of v_f: either species S or C is detected, C_{Red} = 2 mM, K_{eq} = 10.0, k_f = 1.0 $M^{-1}s^{-1}$, $\varepsilon_S = \varepsilon_C$ =1000 M^{-1} cm^{-1}, ω =61.57 s^{-1}, $C_{Ox} = C_C = 0$, $\varepsilon_{Ox} = \varepsilon_{Red} = 0$, amplitude = 10 mV (rms), sampling number = 8, J = 15, K= 600.

It is very important to note that the PMRS signals in the EC′ mechanism do not change with the rate constant, the equilibrium constant, the concentration ratio, and the flow rate when Red or Ox is the detected species. The PMRS response does change when species S or C is detected, and the PMRS signals is very sensitive to parameters such the rate constant, the concentration ratio, and the flow rate and so on. However, in the later case the PMRS signal is normally much smaller, and it may be necessary to increase it by reducing the modulation frequency or by increasing the concentration of the original materials in the solution. When the coupled chemical reaction become

irreversible, these results discussed above are still valid. Details will be presented in the experimental part.

The above simulation results have shown that the PMRS is a powerful method for studies on the coupled chemical reactions and can provide quantitative support of the mechanisms of the system.

3.3.4 Effects of coupled chemical reactions

In general, coupled chemical reactions can affect the parameters of the forward reaction (e.g. the limiting or peak current in voltammetry) and the forward reaction characteristic potentials like E_p or $E_{1/2}$ used in the above discussion.

The manner in which the potential of the forward reaction is affected depends not only on the type of coupled reaction but also on the reversibility of the electron transfer reactions. For example, consider the EC case.

$$\text{Red} \rightleftharpoons \text{Ox} + \text{ne}^- \rightleftharpoons \text{X}$$

The potential of the electrode is given by the Nernst equation,

$$E = E^{0'} + \frac{RT}{nF}\ln\frac{C_{Ox}(x=0)}{C_X(x=0)}$$

Here

$$E^{0'} = E^0 + \frac{RT}{nF}\ln\frac{f_{Ox}K_{eq}}{f_X}$$

Here K_{eq} is the equilibrium constant of coupled chemical reaction, f_{Ox} and f_X are the activity coefficients of species Ox and X, respectively. $C_{Ox}(x=0)/C_X(x=0)$ is determined by the experimental conditions. The effect of the following reaction is to increase $C_X(x=0)$ and hence decrease $C_{Ox}(x=0)/C_X(x=0)$. Thus the half-wave potential, $E_{1/2}$, will be more negative in this case than in the case of the absence of the following reaction,

and the PMRS wave will shift toward negative. So it is important to note that $E_{1/2}$ depends not only on the type of coupled chemical reactions but also on individual conditions like the equilibrium constant, the rate constant of the forward reaction in the irreversible reaction, and the activity coefficients.

3.4 Experimental

The catalytic (EC′) reaction system has been investigated using the new method proposed above. In the system studied, the oxidation of ferrocyanide is followed by the consequent oxidation of *l*-ascorbic acid by ferricyanide to regenerate ferrocyanide [12]. The coupled chemical reaction is irreversible and second - order.

3.4.1 Chemical system

The scheme is:

$$Fe(CN)_6^{4-} \rightleftharpoons Fe(CN)_6^{3-} + e^-$$

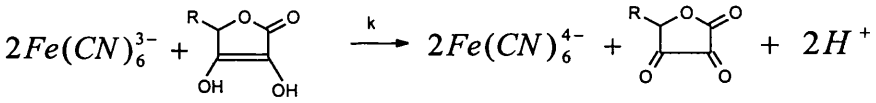

where R = $CH_2OHCHOH$. The ferricyanide is generated electrochemically from ferrocyanide and regenerated by the consequent oxidisation of ascorbic acid. Buffer solutions were made from 0.5M glycine and nitric acid as supporting electrolyte. The diffusion and extinction coefficients at 25°C are known [12-13]. $D_{Fe(CN)_6^{4-}} = 6.5\times10^{-5} cm^2 s^{-1}$, $D_{Fe(CN)_6^{3-}} = 7.63\times10^{-5} cm^2 s^{-1}$ [13], the diffusion coefficient of the ascorbic acid is $6.8\text{x}10^{-6}$ $cm^2 s^{-1}$ [14], $\varepsilon_{420\ nm}$ = 1020 M^{-1} cm^{-1} for $K_3Fe(CN)_6$ [12]. The second order rate constant for the oxidation of the ascorbic acid with $K_3Fe(CN)_6$ is reported to be 13.6 M^{-1} s^{-1}at 25°C [12].

3.4.2 Cyclic voltammetry

The channel cell was used for all experiments in this section, and the parameters were the same as in the Chapter 2. Solutions of 10 mM $K_4Fe(CN)_6$ were freshly made in glycine-nitric acid buffer solution (0.5 M glycine, pH = 2.2), and different concentrations of ascorbic acid were used in the different experiments. Cyclic voltammetric i - E curves of ferrocyanide and ascorbic acid at buffer solution (pH=2.2) are shown at a platinum electrode for zero flow rate in figure 3.23. It can be seen from the figure that no electron transfer process takes place for the ascorbic acid within the range in which the oxidation of ferrocyanide occurs.

The cyclic voltammograms of 10mM $K_4Fe(CN)_6$ with 100mM ascorbic acid (AH_2) (pH=2.2) is shown in figure 3.24. Comparing figure 3.23 with 3.24 it can be seen that the cyclic voltammogram at the higher concentration of the ascorbic acid was distorted. This is because the following coupled chemical reaction makes the electron transfer process appear irreversible. It can also be seen from figure 3.24b that the current has approached a limiting value that is dependent on the flow rate. Note that the current on the reverse scan is smaller due to the following coupled chemical reaction and diffusion process.

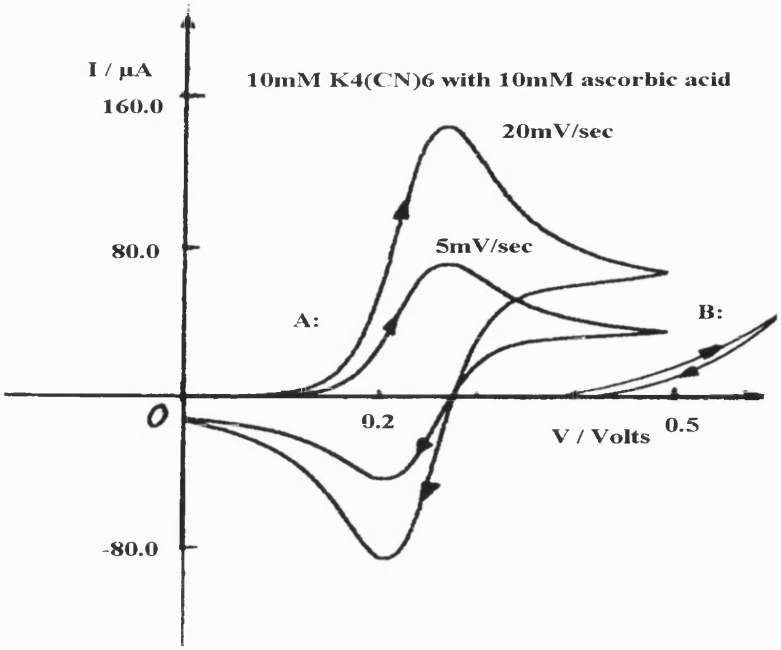

Figure 3.23 Cyclic voltammograms at a platinum electrode in a channel cell at pH=2.2 Zero flow rate

A: 10mM $K_4Fe(CN)_6$ at pH=2.2 , B: 100mM AH_2

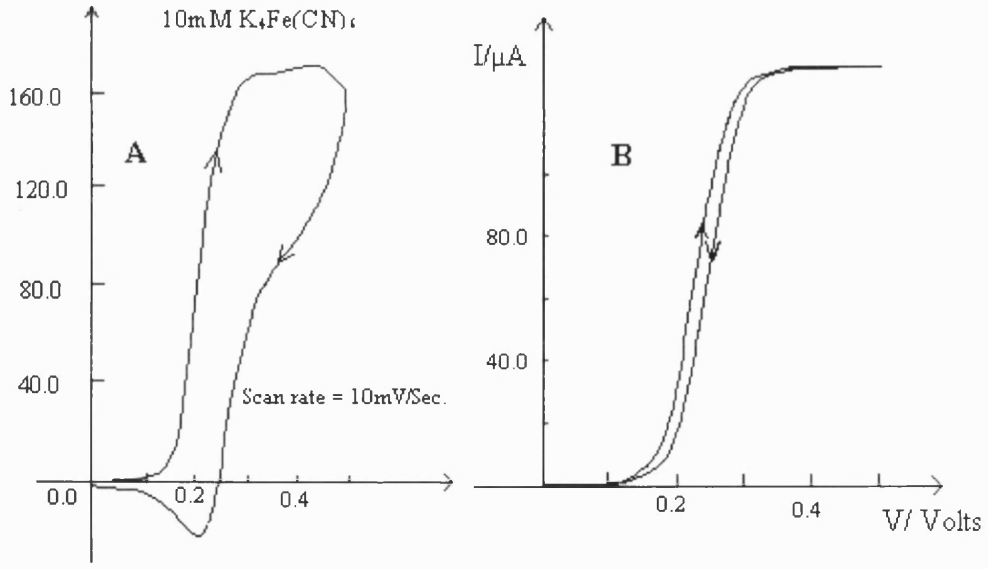

Figure 3.24 Cyclic voltammograms of 10mM $K_4Fe(CN)_6$ with 100mM ascorbic acid(pH=2.2)

A: Zero flow rate B: $v_f = 5.0 \times 10^{-3}$ cm^3 s^{-1}

3.4.3 Absorption and PMR spectra

All solutions were freshly made and degassed by argon prior to measuring spectra in the UV-visible spectrometer or the PMRS equipment. The results are shown in figures 3.25 and 3.26. It can be seen from figure 3.25 that illumination light with $\lambda > 350$ nm is convenient for the PMRS studies because there is no absorption for $K_4Fe(CN)_6$ within that region.

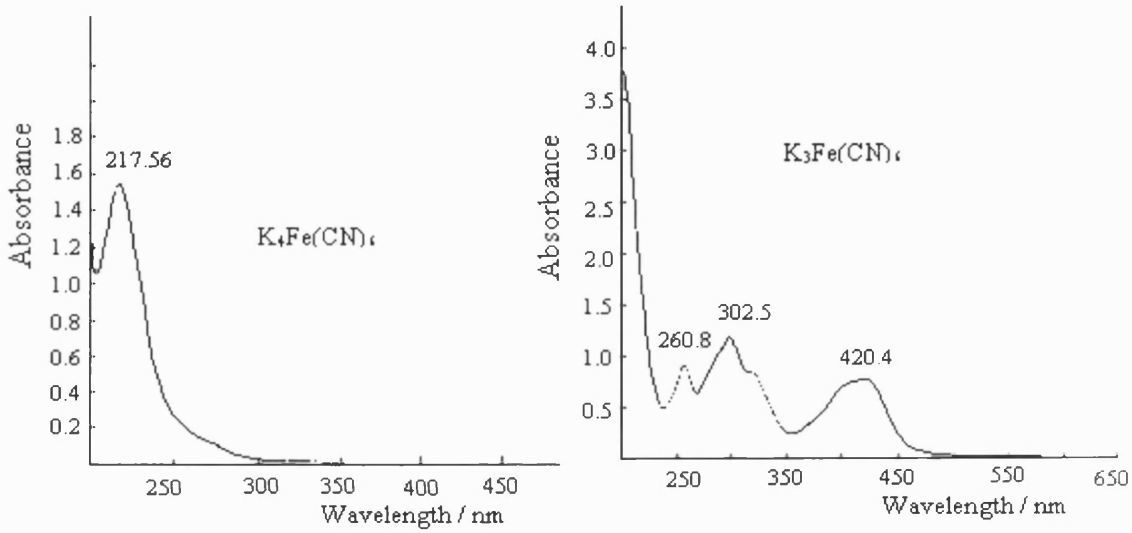

Figure 3.25 Absorbance spectra of 10mM ferricyanide and ferrocyanide at the buffer solution (pH=2.2) measured in UV/VIS spectrometer ----Lambda 40 (Perkin Elmer)

The ascorbic acid and its oxidation product have a maximum absorption around 254 nm with a very high absorption coefficient, 7934 $M^{-1}cm^{-1}$[15,16]. The absorption region overlaps with those of the $K_4Fe(CN)_6$ and $K_3Fe(CN)_6$, and is outside the region accessible to PMRS measurements.

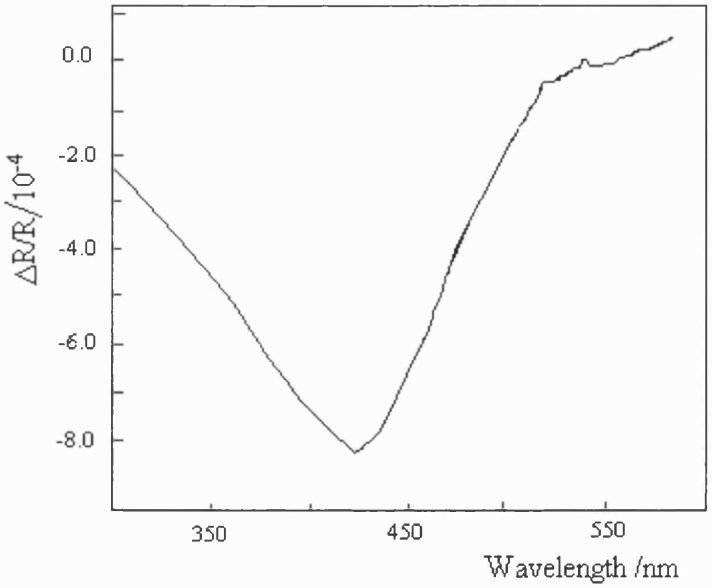

Figure 3.26 A PMR spectrum of 10mM ferricyanide and 10 mM AH_2 in the buffer solution (pH=2.2), E_{dc} = 0.24 V vs SCE, amplitude =10 mV (rms), frequency = 9.80Hz.

3.4.4 PMRS Setup

In order to follow changes in the concentration of ferricyanide, light with λ = 420 nm was used to irradiate the working electrode surface. The reflectance was measured using a photodiode and lock-in amplifier. All the parameters of the channel electrode were same as in the Chapter 2. The reference electrode was SCE.

3.5 Results and Discussion

As can be seen from the simulations in figure 3.27 and 3.28 the PMRS response is not expected to change with the rate constants and the flow rates if $K_3Fe(CN)_6$ is the species detected. The PMRS response should change significantly when the ascorbic acid or its product is detected as shown in figure 3.29.

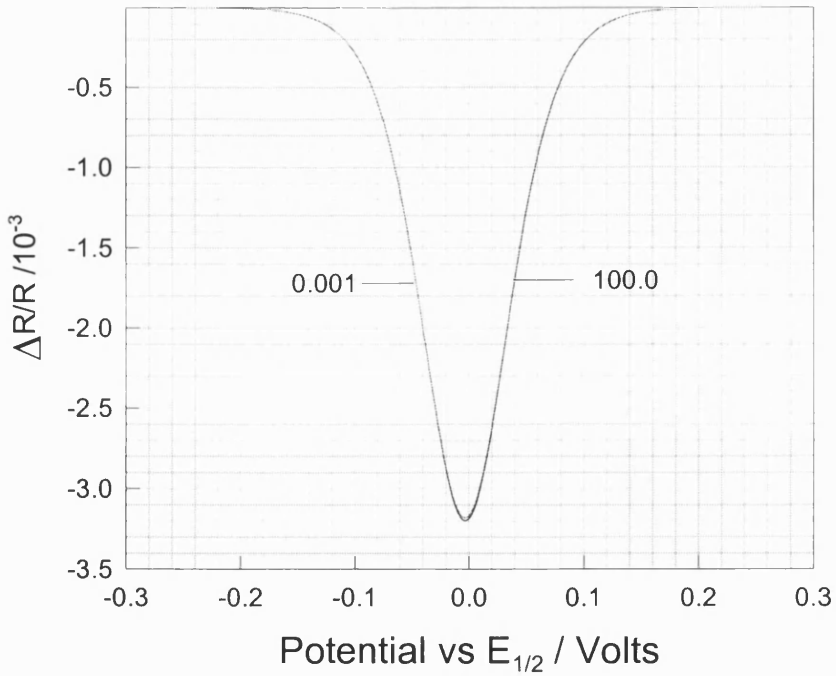

Figure 3.27 Calculated ΔR/R for different values k_f : species detected, $Fe(CN)_6^{3-}$,$C_{K4Fe(CN)6}$= C_{AH^2} = 10 mM, k_b = 0, ν_f= 5.0x10^{-2}cm^{3}s^{-1},$\varepsilon_{420\ nm}$ = 1020 M^{-1} cm^{-1}, ω =61.57 s^{-1}, J = 15, K = 600, Sampling No = 8, x_e = 0.382 cm, w = 0.372 cm, 2h = 0.044 cm.

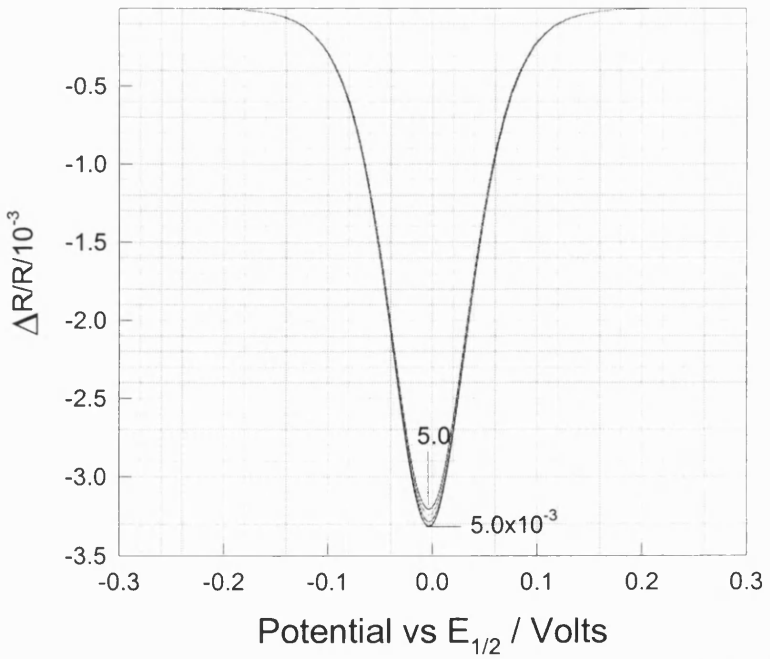

Figure 3.28 Calculated ΔR/R as a function of V_f : species detected, $Fe(CN)_6^{3-}$, $C_{K4Fe(CN)6}$= C_{AH^2} = 10 mM, k_f = 10.0 M^{-1} s^{-1}, J = 15, K = 600, ω = 61.57 s^{-1}, $\varepsilon_{420\ nm}$= 1020 M^{-1}cm^{-1}, Sampling No = 8, x_e = 0.382 cm, w=0.372 cm, 2h = 0.044 cm.

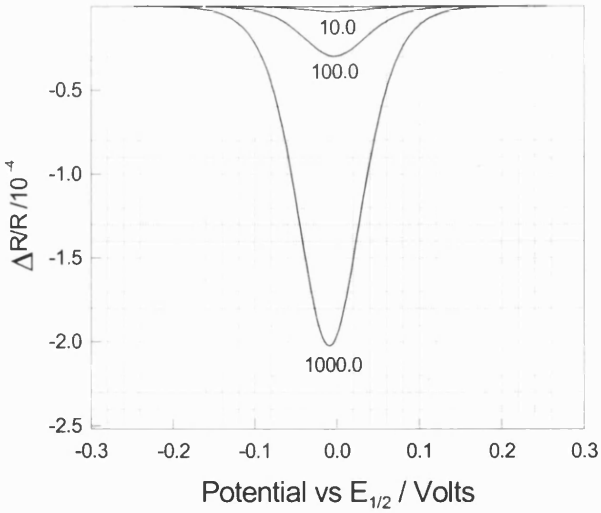

Figure 3.29 Calculated ΔR/R as a function of k_f: detected species is ascorbic acid, $C_{K4Fe(CN)6} = C_{AH2}$ =10 mM, k_b = 0, v_f= 5.0x10^{-2}cm^{3}s^{-1},$\varepsilon_{254\ nm}$ = 7943 M^{-1} cm^{-1}, ω =61.57 s^{-1}, J = 15, K = 600, Sampling No =8, xe=0.382 cm, w=0.372 cm, 2h = 0.044 cm.

Figure 3.30 compares the simulated and experimental PMRS responses. They fit very well. The experimental results show that the PMRS signals are not be affected by the ratio of the concentration of ascorbic acid to $K_4Fe(CN)_6$, nor do they depend on the flow rates up to 0.5 cm^3 s^{-1}.

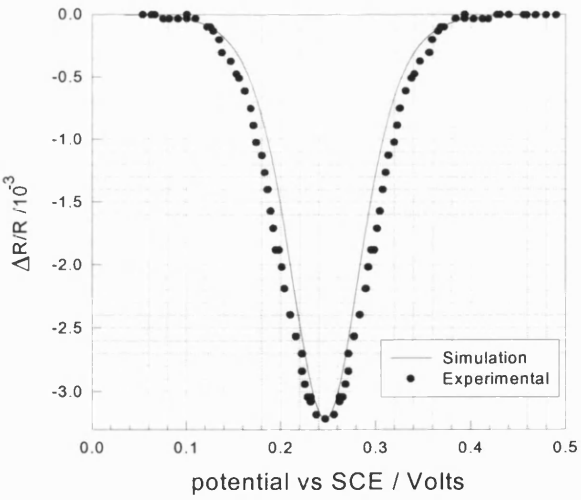

Figure 3.30 Calculated and experimental ΔR/R: detected species $Fe(CN)_6^{3-}$ (λ=420 nm), $C_{K4Fe(CN)6} = C_{AH2}$ = 10 mM, k_f = 10 M^{-1} s^{-1}, $\varepsilon_{420\ nm}$= 1020 M^{-1}cm^{-1}, ω = 61.57 s^{-1}, J = 15, K = 600, sampling No = 8, x_e = 0.382 cm, w = 0.372 cm, 2h = 0.044 cm.

Figure 3.31 shows that PMRS signals increase with decreasing frequencies, and the experimental and simulation results match very well.

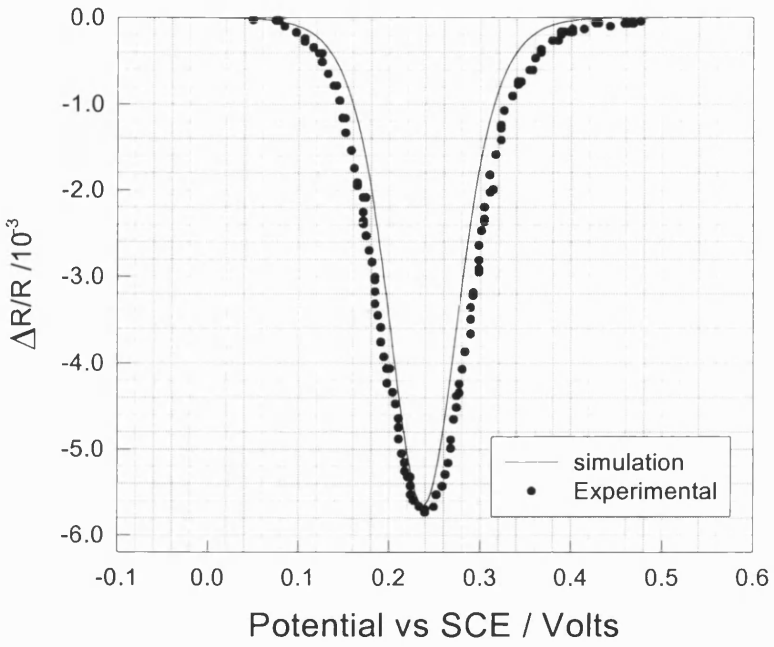

Figure 3.31 Comparison of the simulated and experimental PMR response: λ = 420 nm, $C_{K4Fe(CN)6} = C_{AH2}$ = 10 mM, Am = 10mV (rms), $\varepsilon_{420\ nm}$= 1050 $M^{-1}cm^{-1}$, ω =30.79 s^{-1}, J = 15, K = 600, Sampling No = 8, x_e = 0.382 cm, w=0.372 cm, 2h = 0.044 cm.

It can be seen from figure 3.32 that the PMRS signals increase with increasing amplitude of the superimposed perturbation, and the experimental and simulation results agree well. Comparison of the results in figures 3.30 to 3.32 with the relationship (2.34) given in the Chapter 2 confirms that the theoretical approach is valid, i.e. $\Delta R/R$ is proportional to ΔE as shown in figure 3.33 in which flow rate does not affect the results. The absorption coefficient $\varepsilon_{420\ nm}$ obtained from the best fitting to the PMRS response was 1040 $\pm$ 50 M^{-1} cm^{-1}, which is in good agreement with a value of 1020 M^{-1} $cm^{-1}$of ε_{420nm} in the literature [12]. The experimental curve is wider than predicted one probably due to uncompensated solution resistance.

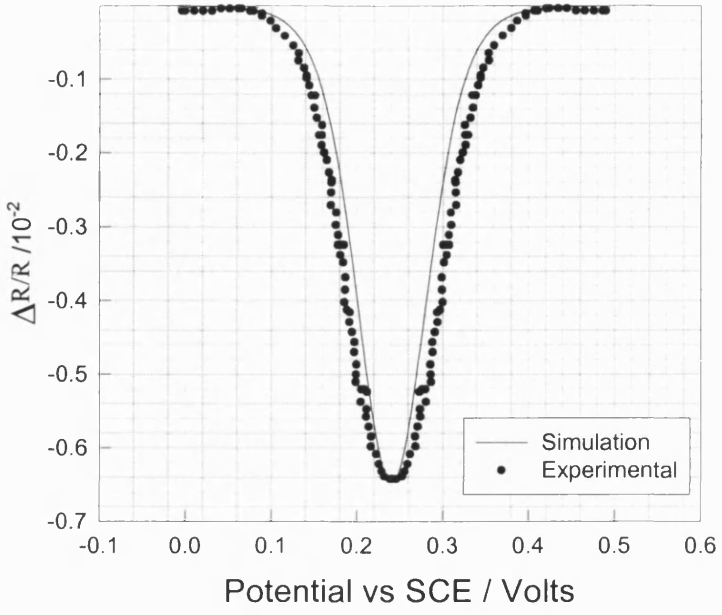

Figure 3.32 Comparison of simulation and experimental PMR response: at λ = 420 nm, $C_{K4Fe(CN)6}$= C_{AH2} = 10 mM, Am = 20mV (rms), $\varepsilon_{420\ nm}$= 1030 $M^{-1}cm^{-1}$, ω =61.57 s^{-1}, J = 15, K = 600, Sampling No = 8, xe = 0.382 cm, w=0.372 cm, 2h = 0.044 cm.

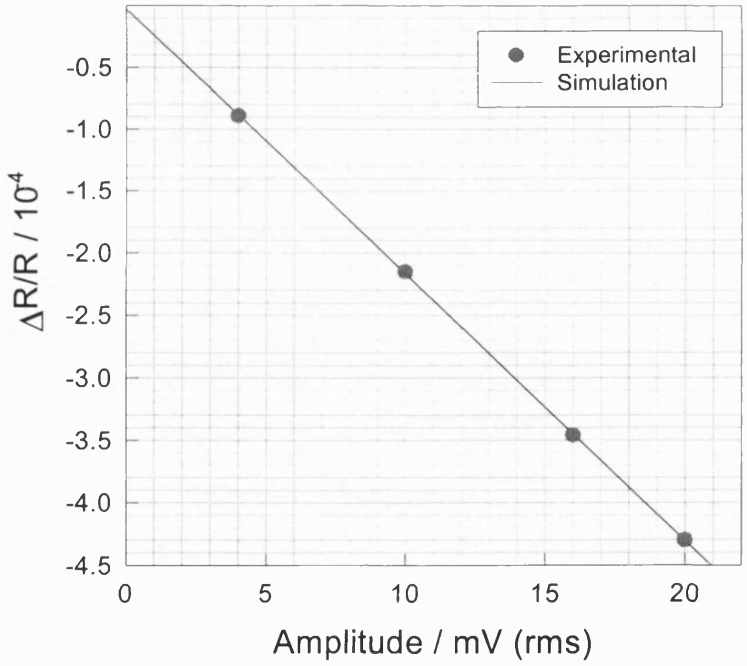

Figure 3.33 Simulation and experimental $\Delta R/R$ as a function of Am: at λ = 420 nm, $C_{K4Fe(CN)6}$= C_{AH2} = 10 mM, $\varepsilon_{420\ nm}$= 1030 $M^{-1}cm^{-1}$, ω =92.36 s^{-1}, J = 15, K = 600, Sampling No = 8, x_e = 0.382 cm, w=0.372 cm, 2h = 0.044 cm.

3.6 Conclusions

Simulation results have shown that PMRS can be successfully extended to study coupled chemical reactions, and the mechanisms proposed can be analysed quantitatively to provide the kinetic parameters. It is vital to select appropriate species for detection by PMRS. The comparison of simulated and experimental results has shown an excellent correlation, validating the new strategy.

REFERENCES:

1. D. S. Polcyn and I. Shain, Anal. Chem., 38, 370 (1966).
2. J. Heize, Angew Chemie Intl., 23, 831 (1984).
3. A. E. Kaiffer and A. J. Bard, J. Phys. Chem., 89, 4876 (1985).
4. M. Mohammad, Electrochim. Acta., 33, 417 (1988).
5. I. Ruzic, D. E. Smith and S. W. Feldberg, J. Electroanal. Chem., 52, 157(1974).
6. D. E. Richardson and H. Taube, Inorg. Chem., 20, 1278 (1981).
7. R. Guidelli, Anal. Chem., 43, 1715 (1971).
8. F. Magno and G. Bontepelli, Anal. Chem., 53, 599 (1981).
9. B. C. Bennion, J. J. Auborn and E. M. Eyring, J. Phys. Chem., 76, 701, (1972).
10. N. Winograd and T. Kuwana, J. Am. Chem. Soc., 93, 1353 (1971).
11. N. R. Armstrong and N. E. Vanderborgh, J. Phys. Chem., 80, 2740 (1976).
12. N. Winograd, H. N. Blount and T. Kuwana, J. Phys. Chem., 73, 3456 (1969).
13. W. Z. Wei, Q. J. Xie and S. Z. Yao, Electrochim. Acta, 40, 1057 (1995).
14. M. I. Manzanares, V. Solis and Rita H.de Rossi, J. Electroanal. Chem., 407, 141 (1996).

15. Handbook of Chemistry and Physics 55th edition, 1974-1975, CRC Press Inc., edited by R.Weast,

16. M. Surmeian, Drug Development and Industrial Pharmacy, 24(7), 691 (1998)

PART TWO

ELECTRODEPOSITION AND CHARACTERISATION OF

CdTe/CdS SOLAR CELLS

CHAPTER FOUR

INTRODUCTION

4.1 Introduction

Energy is vital to human life, and it has become a key factor that will limit economic growth of any nation, specifically a developing country. Currently used energy sources such as oil, natural gas, coal, and wood are limited. The supplies of all of these common energy sources are finite. The maximum period of the supplies estimated for coal, natural gas, and petroleum is 200 years [1]. Deforestation and climate change also confine the utilisation of wood. As current energy sources become depleted and new energy demands for population growth and industrialisation increase in many developing countries, an energy gap will develop, and enlarge. So humanity must turn to longer-term, permanent energy sources. Solar energy is the best choice and the world's most abundant permanent source of energy. The amount of solar energy received by the surface of the earth is about 1.73×10^{14} kW [2], an amount 5000 times greater than the sum of all other inputs including terrestrial nuclear, geothermal, and gravitational energies and lunar gravitational energy [3]. In fact it is equivalent to about ten thousand times the current annual world energy consumption [2], and 200,000 times of the total world electrical-generating capacity [1].

Although it is abundant, solar energy impinging on the earth's atmosphere is relatively dilute — approximately 1350 W/m^2. In traversing the earth's atmosphere, it will be further diluted by attenuation, local weather phenomena and air pollution. Moreover, solar energy is received only intermittently at any place on the earth due to its rotation. There are two forms of the solar energy that arrive on the surface of the earth: direct radiation and diffuse radiation. Direct radiation is collimated; diffuse

radiation is dispersed, or reflected, by the atmosphere and is not collimated. On the average, the radiation striking the earth's surface is in the range of 100 to 800 W/m^2.

There are several sources of energy excluding oil, coal and natural gas to be used at the present. They are:

A) Biomass: Biomass is mainly used in developing countries and provides about 15% of the present world energy supply [2]. The methods of conversion of biomass are summarised in Table 4.1. The simplest way to use biomass as an energy source is to burn it to provide heat. It is, however, often complicated and costly to pyrolyse and refine oil and tar from related fossil fuels.

Table 4.1 Biomass conversion for energy use

PROCESS	ENERGY FORM
Food	Muscle power (human, animal)
Combustion	Heat
Pyrolysis	Oil, char, and gas
Gasification	Gas
Fermentation	Gas(methane), liquid(ethanol)

B) Hydropower: Dating back to ancient times, the water wheel ranks with the windmill in importance as a source of power for simple industrial operations such as flour milling and later for sawmills and forges (it is still used in the poor countries nowadays). Building hydroelectric dams is being increasingly popular, especially in developing countries with poor energy infrastructures. Hydropower represents roughly 7% of the current world energy use [2].

C) Windpower: Wind and water were the most powerful sources of mechanical energy for humans before the invention of the steam engine. People have used

wind power to propel their ships since earliest times. But its utility is limited due to certain geographical locations and costly setup. Wave and tide powers are also expensive to develop for large-scale use.

D) Nuclear: Nuclear energy requires highly technical, political risks, and costly means for its safe and reliable utilisation and may have undesirable side effects. Specifically severe problems associated with the disposal of nuclear waste are still not sorted out.

On the one hand fossil fuel sources are limited and will be exhausted in the near future. On the other hand several problems have arisen from the increased use of energy, for example, oil spillage from extraction and transport and the release of carbon dioxide from the burning of fossil fuels. The latter is receiving great attention on a global scale since the level of this gas in the atmosphere could in the future exceed the natural level and may lead to climate change due to the green house effect. One of the more promising technologies which fulfil the demands of both cleanliness and future power generation requirements is to use solar energy. This tremendous unlimited supply of free energy has therefore presented an increasingly attractive source for meeting today's ever increasing power demand. The principal uses for solar energy are:

1. As a heat source, particularly for low temperature heat applications like domestic hot water or crop drying.
2. As high temperature heat to power heat engines, refrigerators and air conditioners.
3. To operate photovoltaic cells for direct electricity production.

Although not the only method, the direct conversion of solar energy to electricity by a photovoltaic technology has the number of technological and social advantages over other energy technologies. For example, in addition to the positive aspects of

using sunlight, photovoltaic system i) are quiet, ii) require little maintenance, iii) have no critical size and indeed the size can be matched to load with little loss in efficiency, iv) can be physically located near the load, and v) are environmentally friendly in operation. It is thus one of most attractive future technologies. The world's total production of solar cells in 1997 was 126.7MW. Of this, 53 MW came from the United States, 35 from Japan, 29.3 from Europe and 9.4 from the rest of the world [4]. Manufacturing capacity potential trends and estimates by country have been given in the literature [5] with developments of the technologies, the cost of solar cells has dropped dramatically since they were first invented by Bell Laboratories about 40 years ago. The price in US dollars for photovoltaic cells (PV) is given in Table 4.2.

Table 4.2 Price per Kilowatt/hour of Electricity from PV Cells [4]

Year 1970	Year 1975	Year 1980	Year 1985	Year 1990	Year 1995
$ 5.00	$ 2.50	$ 1.00	$ 0.50	$ 0.25	$ 0.25

4.2 Solar Intensity at the Earth's Surface

When solar radiation passes through the atmosphere, sunlight is attenuated by at least 30% [6]. Reasons for such attenuation are

1) Rayleigh scattering or scattering by molecules in the atmosphere. This mechanism attenuates sunlight at all wavelengths but is most effective at short wavelengths.
2) Scattering caused by aerosols and dust particles.
3) Absorption by the atmosphere and its constituent gases like O_2, O_3, CO_2 , and H_2O

A typical spectral distribution of sunlight reaching the earth's surface is shown by the lower curve of Figure 4.1. The surface temperature of the sun is around 6000 K and the radiation corresponding to this temperature can be roughly grouped into high frequency, visible and low frequency. The results are tabulated in Table 4.3 [2].

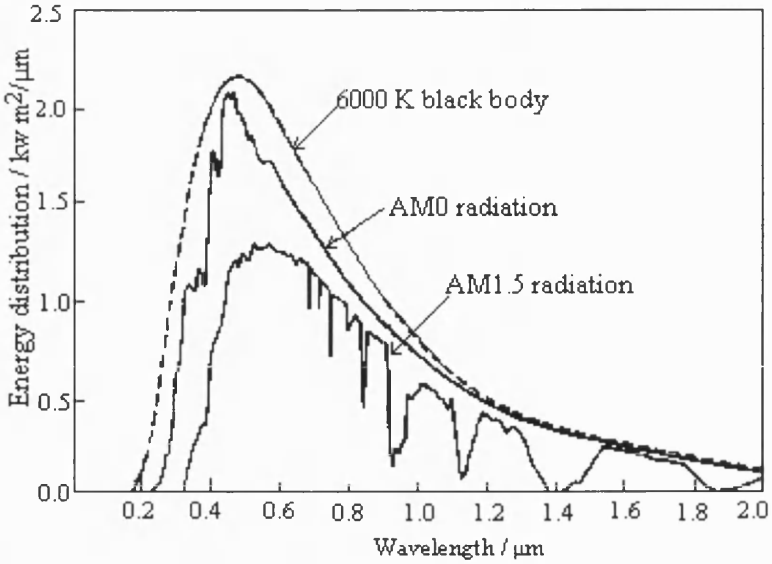

Figure 4.1 Spectral distribution of sunlight in space (AM0) and on earth (AM1.5)

Table 4.3 Fraction of Energy at the surface of the sun

Frequency	Radiation Type	Wavelength/ μm	Fraction of Energy
High Frequency	Ultra-violet	0.2 – 0.4	9%
Visible Frequency	Light	0.4 – 0.7	41%
Low Frequency	Infra-red	0.7 – 3.0	50%

The presently accepted value of the solar intensity outside the earth atmosphere, referred to as AM0, is 1.35kW/m^2as indicated by the two uppermost curves in Figure 4.1 in which the spectral distribution of AM0 radiation differs from that of an ideal black body. This is due to such effects as differing transmissivity of the sun's atmosphere at different wavelengths.

Due to the earth's rotation around the sun, the angle of incidence of the radiation changes, and as a result of the length of the light path changes, too. This length is shortest when the sun is directly overhead. The ratio of any actual path length, b, to this minimum value, l_{min}, is known as the optical air mass (AM). When the sun is

directly overhead, the optical air mass is unity, namely air mass one (AM1). The AM value is defined by [7] (γ can be seen in figure 4.2):

$$AM = b/l_{mix} = 1/\cos(\gamma)$$

As the international norm for the measurement of terrestrial solar cells, the value AM1.5 has generally been accepted. The correspondence between air mass values and maximum radiation intensity values is

Air mass values	AM0	AM1	AM1.5	AM2
Intensity / W/m^2	1350	925	844	691

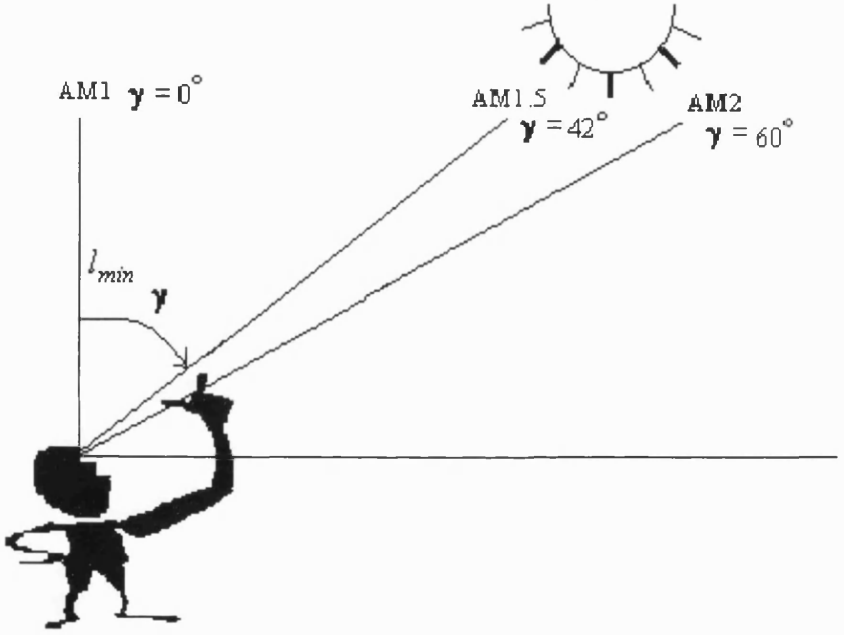

Figure 4.2 Air mass values against the angle of incident light

It is also noted that when a solar simulator with filters is used, the value of AM1.5 (G) under this condition is 1000 w/m^2 which is a standard introduced by the U.S. government in 1977 [8] and also close to the maximum received at the earth surface.

4.3 Efficient Conversion and Materials Requirements

Basically, there are three separate processes involved in photovoltaic conversion. They are: 1) the absorption of light with appropriate energy to create electron-hole

pairs in a semiconductor, 2) collection and separation of these carriers by an internal electric field, and then, 3) distribution to an external load. Absorption and carrier generation occur mainly for photons of energy greater than the band gap of materials. Obviously, the smaller the bandgap energy, the greater the carrier density generated and, consequently, the higher the photocurrent density. However, the open-circuit voltage is determined by the bandgap and is, for optimally designed devices, about half the bandgap [9]. Thus, for high-efficiency solar cells with high photocurrent and high open-circuit voltage, the semiconductor bandgap has to be matched to the solar spectrum shown in figure 4.1, and it can be shown that the optimum bandgap is in the range of 1.1 to 1.5 eV. The important thing is that the material should have a high absorption coefficient to ensure capture of all available photons. Since high absorbance is often found in limited wavelength regions for any one material, if we want to use the full solar spectrum, it is essential to have a series of solar cells of varying and/or graded bandgaps arranged in cascade or acting in tandem or constructed in an integrated, multilayer, tandem structure. Alternatively, the solar spectrum can be split into different spectral regions by filter mirrors and each of the split beams is directed to individual solar cells with response and bandgap matched to that particular region. The theoretical calculation indicates that by appropriate combinations of as many as 36 cells, theoretical efficiencies as high as 72% are expected [10]. The materials with an appropriate bandgap, absorption coefficient α, minority carrier lifetime τ, or minority carrier diffusion length L_D, and surface recombination velocity S_r can be used to make efficient thin film solar cells such as Si, GaAs, InP, CdTe and $CuInSe_2$ etc.

4.4 Growth methods of Thin Films

A deposition technique and its associated processes have a characteristic effect on the nucleation- and growth-dominated microstructure of a thin film and thereby on its physical properties. Materials with thicknesses ranging from angstroms to hundreds of micrometers can be prepared by many of so-called thin film and thick film techniques.

Any thin film deposition process involves three main steps: (i) creation of atomic/molecular/ionic species, (ii) the transport to the substrate through a medium, and (iii) condensation on the substrate, either directly or via a chemical and/or electrochemical reaction, to form a solid deposit. The deposition techniques may be classified into vapour deposition, solution deposition, and thick film deposition techniques that were reviewed extensively in the literature [11-16]. Here a very brief review is given about the techniques most relevant to films for solar cell applications.

4.4.1 Vapour Deposition Techniques

Vapour deposition techniques can be divided into two categories: (1) physical vapour deposition, and (2) chemical vapour deposition.

4.4.1.1 Physical Vapour deposition (PVD)

4.4.1.1.1 Vacuum Evaporation

Vacuum evaporation is one of the most broadly used deposition techniques. The technique consists of vaporisation of the solid material by heating it to sufficiently high temperatures and condensing it onto a cooler substrate to form a film. Heating of the material can be carried out directly or indirectly (via a support) by a variety of methods.

According to the Langmuir-Dushman theory of the kinetics of evaporation, the rate of free evaporation of atoms or molecules from a clean surface of unit area in atoms or molecules $cm^{-2}s^{-1}$ in vacuum is given by

$$N_e = 3.513 \times 10^{22} p_e (1/MT)^{1/2}$$

where p_e is the equilibrium vapour pressure (in Torr; 1 Torr =1 mm Hg) of the evaporant under saturated vapour conditions at a temperature T, M is the atomic or molecular weight of the vapour species. The rate of condensation of the vapours (or the deposition rate) depends not only on the evaporation rate but also on the source geometry, its position related to the substrate, and condensation coefficient. Note that a very important variation of vacuum evaporation is molecular beam epitaxy (MBE) [17-18]. MBE is basically a slow and well-controlled evaporation technique and makes it possible to obtain multilayer structures of different materials in a predetermined sequence with layer thicknesses ranging from 10 Å to several microns, enabling the formation of quantum-well structures, heterojunctions and graded composition/property structures. But it is a very expensive process.

4.4.1.1.2 Sputtering

Besides thermal evaporation, vapour species may also be created by mechanically pulling out the atoms or molecules from the surface of a solid material by bombarding it with energetic, nonreactive ions. The ejection process, known as sputtering, occurs as a result of momentum transfer between the impinging ions and the atoms of the target bombarded. There are two types of sputtering. One is called Glow-Discharge Sputtering, produced a cheap and simple means of producing ions, which occurs when an electric field is applied between two electrodes in a gas at low pressure (~ 10^{-2} Torr). Another is Ion-Beam Sputtering by producing ions in a high-vacuum (~10^{-4} –

10^{-5} Torr) chamber and then extracting them into a differentially pumped vacuum chamber through suitable apertures with the help of suitable electron and ion optics. The sputter-deposition rates generally depend on the material and individual operation conditions.

4.4.1.2 Chemical Vapour Depsoition (CVD)

It is the foremost characteristic of a CVD technique [19-20] to involve a heterogeneous chemical reaction at the surface of a substrate without requiring vacuum as an essential condition for deposition.

The chemical reactions utilised in CVD processes can be classified as: (1) decomposition reactions, (2) reduction reactions, (3) chemical transport reactions, and (4) polymerisation.

The major advantages of the CVD techniques are: (1) in general, a relatively simple setup and fast recycling due to low vacuum; (2) high (~1 μm /min) deposition rates with possibility to deposit compounds with easily controlled amount stoichiometry; (4) relatively easy to dope the deposits with controlled amounts of impurities; (5) epitaxial layers of high perfection and low impurity content. However, the technique also has some drawbacks: (1) generally poor understanding about complex thermodynamics; (2) in most cases, highly toxic and explosive gases used for deposition and the volatile reaction products form; (3) the corrosive vapours which may attack the substrate, the deposited film, and the materials of the deposition setup; (4) the volatile products generated during the deposition process which may lead to incorporation of impurities in the film; (5) difficult to control the uniformity of the deposit.

In general the PVD and CVD setups are complicated and expensive, it is not suitable for large-scale deposition.

4.4.2 Solution Deposition Techniques

In these techniques, the materials to be deposited are dispersed or dissolved in a liquid medium (generally aqueous) and are almost present in ionic form. Solution deposition techniques therefore inherently involve chemical and/or electrochemical reactions for the formation of the deposit material. They may be broadly classified into two categories: (1) chemical solution deposition (CSD) and (2) electrochemical deposition (ECD). Reactions such as precipitation, displacement, or reduction may be utilised in CSD techniques. By contrast, ECD techniques involve electrochemical reaction, i.e. chemical reactions necessarily involving interaction with an external source of electric current. The general advantages are: (1) experimental setups are much less sophisticated compared to those in vapour deposition techniques; (2) no expensive equipment such as vacuum systems is required for deposition; (3) deposition is carried out at much lower temperatures (<100°C). Specifically electrodeposition technique can easily control the compound stoichiometry by the deposition potential with large-scale area. This is one of promising techniques to make lower cost solar cells like CdTe/CdS [21-30] and $CuIn_{1-x}Ga_xSe_2$ [31-34].

4.4.2.1 Chemical Solution Deposition (CSD)

Chemical solution deposition techniques are generally immersion techniques in which they involve simply dipping of the substrate into the reaction mixture for some time depending on the thickness required. The CSD techniques have the following advantages: (1) deposits are formed more uniformly even on complex parts without

any excessive buildup on projections and edges; (2) deposits can be grew directly on insulators; and (3) no power supplies and contacts are needed.

The CSD techniques may involve those processes: 1) autocatalytic reduction/electroless plating; 2) homogeneous precipitation and solution growth such as chemical bath deposition (CBD); 3) spray pyrolysis; 4) displacement deposition, chemiplating, or immersion plating; and 5) conversion coating.

Of the CSD techniques, chemical bath deposition has been used to deposit CdS window material for solar cell applications, which provides a cost-effective route to produce uniform, adherent and large area layers for CdTe/CdS [35-36] or $CuInSe_2$ [37-38] solar cells.

4.4.2.2 Electrochemical Deposition (ECD)

All ECD techniques require an external source of current for deposition. Obviously, they also require electrically conducting substrates. It consists of electrophoretic deposition and electrodeposition.

4.4.2.2.1 Electrophoretic Deposition

Electrophoretic deposition is a process in which electrically charged particles suspended in a liquid are deposited onto an electrode under an electric field. This technique can be used to deposit metals, alloys, oxides, refractory compounds, polymers, and mixtures of various components. In contrast to electrodeposition, electrophoretic deposits are usually loosely adherent coatings of power required further treatment to produce adherent, compact, and mechanically strong coatings.

4.4.2.2.2 Electrodeposition

The occurrence of chemical changes due to the passage of electric current through an electrolyte is termed electrolysis, and the deposition of any substance on an electrode as a consequence of electrolysis is called electrodeposition. This technique has been extensively used to deposit Group II – VI compound semiconductors such as CdS [38-40], CdSe [41], ZnO [42-43] and CdTe [20,44-47] and Copper indium diselenide (CIS) [48-51] and copper indium gallium diselenide (CIGS) [30,51-52] recent years. These materials are important in a wide range of optoelectronic applications ranging from solar cells to IR windows and quantum dot structures [53-56]. In the past films of these materials were mainly synthesised by a range of techniques like vacuum deposition [57-58], spray pyrolysis [59] chemical vapour deposition [60], slurry painting [61], molecular beam deposition [62-63], closed-space sublimation [64-65], and screen printing [66]. Electrodeposition provides a simple and viable alternative to these cost intensive routes [67-68]. Electrodeposition technique has successively applied to CdTe/CdS solar cell in the commercial BP "Apollo^{TM}". Here CdTe is electrodeposited onto CdS substrates deposited by CBD. CdTe/CdS solar cells give conversion efficiencies of up to 10% under AM 1.5 illumination [69].

The advantages of electrodeposition are as follows:

i) Large area [70]: Large scale and complex area substrates can be used to electrodeposit. In the BP "Apollo ^{TM}" cells [69], 30 cm square CdTe module has been electrodeposited with excellent stoichiometry and uniformity.

ii) Low cost [71]: Besides the much lower-price equipment compared with vacuum deposition apparatus, the most obvious advantage is to save energy due to the operation at 80^{o} C or lower temperature. Deposition solutions can

also be used for very long periods. In the case of CdTe deposition, only small amounts of tellurium need to be added to the solution to maintain the deposition conditions unchanged.

iii) Controlling the electrode potential according to the requirements can control components in the deposits.

iv) Low toxicity: Electrodeposition involves the use of easily handled stable precursors in the condensed phase like liquid at low temperature. While chemical vapour deposition techniques essentially involve the thermal decomposition of highly toxic organometallic precursors.

There are two processes in electrodeposition. They are cathodic and anodic processes. In a cathodic process a solution species is reduced by the transfer of electrons from the cathode, for example

$$Cd^{2+} + HTeO_2^{+} + 3H^{+} + 6e^{-} \rightarrow CdTe + 2H_2O$$

Conversely charge transfer may be an anodic process where a metal electrode (anode) is oxidised by the removal of electrons. For instance, anodic growth of CdS

$$Cd\ (s) + HS^{-} \rightarrow CdS\ (s) + H^{+} + 2e^{-}$$

This process involves the anode dissolution.

The electrodeposition rates normally depend on the following factors:

1) The properties of the deposit materials themselves;
2) Mass transport of the deposition materials between electrode surface and the bulk solution;
3) The concentrations of the deposition species and the solution temperature.

4.4.3 Thick Film Deposition Techniques

Thick film deposition techniques are of considerable technical interest in the development of thin film devices. They are liquid-phase epitaxy (LPE), screen printing, melt spinning, and dip coating, spinning and solution casting. Those techniques can provide fast and effective ways to grow thick thin films. Details are in literature [11-15].

4.5 Classes and Performance of Thin Film Solar Cells

The earliest recorded photopotentials were not derived from silicon nor were they solid-state [72]. They were electrochemical in nature, studied by Becquerel in France in 1839 [72]. In 1876 Adams and Day in England were pioneers on studying solid-state photopotentials using a selenium device. In the following 70 years, various materials were studied as photovoltaics, including copper-cuprous oxide, selenium, thallous sulfide, and silicon, but their conversion efficiencies were not greater than 1%. The following is a brief description of progress on different kinds of solar cells.

4.5.1 Silicon Solar Cells

A wide range of technologies for silicon solar cells has developed including thin film, amorphous, tandem cells that are based on a variety of materials for use in space and terrestrials application. Solar energy conversion efficiencies to electricity in excess of 30% have been reported, and a range of large-scale surface area modules is being developed. As shown in figure 4.2 the solar to electricity conversion efficiency improved dramatically in the 1950s, and from approximately 15% in the 1960s to 24% in 1994 [73] and to 24.4% in 1998 [74]. The film thickness of silicon solar cells

also decreased significantly from 400 μm to 47 μm, and it only resulted in a 10% drop in short circuit current.

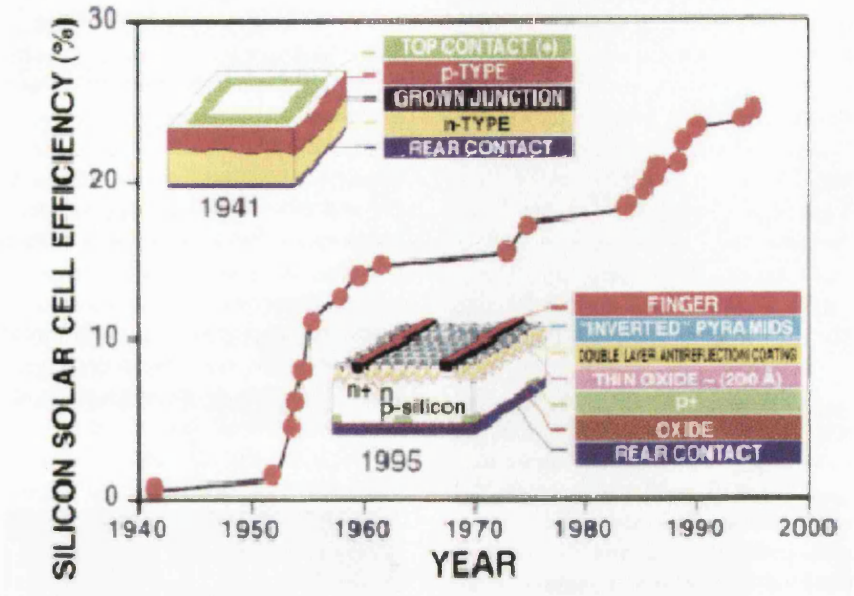

Figure 4.3 Performance of silicon solar cells taken from [72]

4.5.2 III-Photovoltaics

In principle, several Group III-V materials, including GaAs, offer significant advantages compared with silicon. First they have high absorption coefficient, required only a few micrometers thickness to absorb most of light, and secondly they normally have a bandgap around 1.4 eV, a better match than the silicon 1.1 eV bandgap to a the solar spectrum. Both InP and GaAs are a direct bandgap material and exhibit better radiation and high temperature tolerance than silicon. The solar-to-electricity conversion efficiencies for GaAs has reached 27.3% [75] in the laboratory, 21% efficiency cells are commercially available for satelites.

4.5.3 Polycrystalline Thin Film Solar Cells

Cadmium telluride (CdTe) and copper indium diselenide (CIS) or copper indium gallium diselenide (CIGS) are promising candidates for thin film photovoltaic solar

cells and have been investigated since the 1970s. CdTe has a nearly ideal bandgap of 1.5eV and very high absorption coefficient, CIS or CIGS can be made a bandgap from 1.3 eV to 1.5 eV, and it has a high absorption coefficient, too. These are direct bandgap materials. The solar-to-electricity conversion efficiency of a CdTe/CdS solar cell was 15.8% in 1992 [76-77], and 16% in 1997 [78]. A 0.4 cm^2 CIGS device with 17.7% conversion efficiency was reported in 1996 [79]. The improvement of polycrystalline CIS and CdTe thin film solar cells is shown in figure 4.4 [79-80]. In comparison with silicon solar cells, substantial recombination losses can occur at the grain boundaries of these polycrystalline devices, which diminishes cell performance.

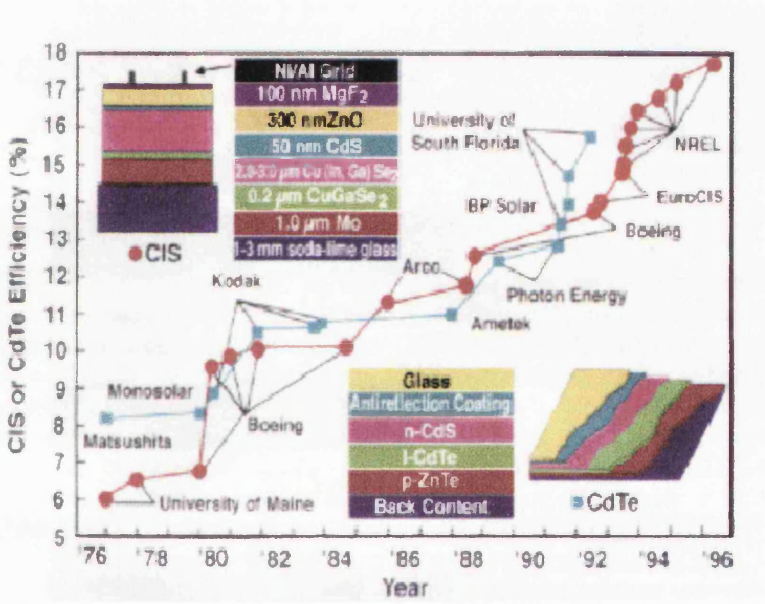

Figure 4.4 Improvement of polycrystalline CIS and CdTe thin film solar cells taken from the literature [72]

4.5.4 Dye-Sensitised Solar Cells

The solar cells described above which convert light into electricity by exploiting the photovoltaic effect existing at semiconductor junctions are termed "conventional solar cells". They can be regarded as photodiodes. The solar cells perform two processes simultaneously: 1) absorption of light, and as a consequence of that 2) the

generation and separation of the electric charges (electrons and holes). Recombination of holes and electrons may occur in those devices. In order to prevent recombination, the semiconductors employed must be highly pure and defect-free. In contrast, the solar cells developed by Graetzel [81-82] work on a different principle, whereby the processes of light absorption and charge separation are differentiated. The principle of operation of the dye-sensitised solar cell is depicted in figure 4.5.

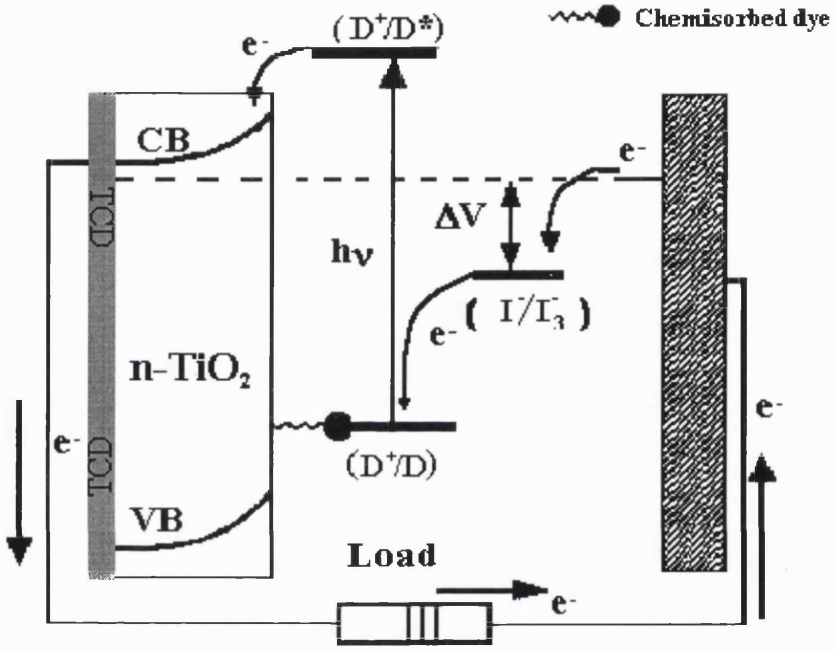

Figure 4.5 A schematic of dye sensitised solar cell

Light is absorbed by a monolayer of dye (D) chemisorbed at the semiconductor surface. The excited (D*) dye is able to eject an electron to the conduction band of the semiconductor (normally n-type TiO_2). The gradient of electrochemical potential inside the bulk material allows extraction of the electrons. Positive charge is transferred from the dye (D^+) to a redox couple, I^-/I_3^-, present within the cell, and hence to the counter electrode to recombine with the electrons. By this last electron transfer, in which the mediator is returned to its reduced state, the circuit is closed. The theoretical maximum voltage that such a device could deliver corresponds to the difference between the redox potential of I^-/I_3^- and the Fermi level of the

semiconductor as shown in the figure 4.5. The highest solar-to-electricity conversion efficiency was 10.4% in 1998 [82]. The solar cell efficiencies depend mainly on the dye used.

4.6 Research Aims and Approaches

Cadmium telluride-based thin-film solar cells are promising photovoltaic devices because of the high absorption coefficient (>10^4 cm^{-1}) and optimum bandgap (1.45eV) [83,84] of CdTe which is the best for the solar spectrum as seen in figure 4.1. CdTe/CdS solar cells have intensively been studied in the last decade [76-79,85-91]. Electrodeposition has has already been established as a low-cost technique for preparing CdTe thin films [20,85-92]. CdS deposited by CBD has been accepted for a window material for solar cell application [34-37]. Although there is a lattice mismatch of ~11% [43] in the CdTe/CdS solar cells, the highest efficiency achieved so far was 16% [78]. This is due, on the one hand, to post-deposition treatments in which dipping in $CdCl_2$ and annealing result in grain growth, reduction in the defect density, and formation of the interfacial $CdTe_{1-x}Te_x$ layer, which is regarded to reduce the interfacial stress caused by the lattice mismatch between CdTe and CdS [83,93-96]. On the other hand, due to improvements of back contacts [97-99]. Advances have slowed in recent years, and the main reason behind this is the lack of understanding of the materials and complex interfaces used in this device structure [99-100]. Electrodeposition processes used so far for solar cell application are too slow, for example, deposition times for the 2μm CdTe film are 2-3 hours. The recrystallisation of the CdTe polycrystalline thin-film is regarded play an important role in high efficiency cells. Although electrodeposition can control the components deposited, the same Cd:Te ratio as in the single crystal does not necessarily lead to recrystallisation during the thermal treatment. What ratio of Cd to Te or what kind of

processes can result in the recrystallisation is still not clear so far. So the aims in this work were as follows:

1) Investigation of the feasibility of using a flow cell to control the rate of mass transport of $HTeO_2^+$ and to achieve a substantial reduction of the deposition time.
2) Modification of the Gärtner model for thin-film solar cells to find out the minority carrier diffusion length and width of space charge region.
3) Examination of the properties of the CdTe films by *ex-situ* and *in-situ* techniques
4) Comparison of the properties of the CdTe films deposited in stirred solution with those deposited in the flow cell
5) Correlation of the minority carrier diffusion length, recrstallisation and grain size to the deposition processes to find out the best ones for solar cell applications.

In order to achieve the above aims, the following approaches were used:

1) A well-defined flow cell technique [101] was used to deposit the smooth and uniform CdTe films;
2) A potentiostat was used to control the electrode potential to ensure the right Cd:Te ratio;
3) The films were characterised by *Ex-situ* techniques such as X-ray diffraction (XRD) to determine the crystallographic properties, wavelength-dispersive X-ray analysis (WDX) to examine the components, scanning electron microscopy (SEM) and atomic force microscopy (AFM) to reveal the morphology of the films;
4) *In-situ* methods used to obtain bandgaps, doping level, flat band potential, stacking faults were electrolyte electroreflectance/absorbance (EER/EEA), photocurrent spectroscopy and capacity measurements;

5) Two-side fitting of photocurrent spectra based on modification of Gärtner model was used to obtain the minority carrier diffusion length and the width of space charge region.

References:

1. Comptons Interactive Encyclopedia for Windows on PC CD-ROM, Comptons New Media, 1995.
2. P. D. Dunn, Renewable Energies: source, conversion and application, ed by M. Barak and D.T. Swift-Hook, Peter Peregrinus Ltd, 1986.
3. J. F. Kreider, C. J. Hoogendorn and F. Kreith, Solar Design: components, system, Economics, Hemishere Publishing Corp., 1989.
4. http://www.fortunecity.com/bally/balleydehob/118/solar.html
5. J. E. Rannels, Renewable Energy, **19,** 75(2000)
6. M. A. Green, Solar Cells: Operating Principles, Technology, and System Applications, ed by N. Holonyak, Prentice-Hall, Inc., 1982
7. http://umwelt.ew.ph-erfurt.de/projekte/energie/ILSE/solar/
8. Terrestrial Photovoltaic Measurement Procedures, Report ERDA/NASA/1022-77/16, June 1977.
9. K. L. Chopra and S. R. Das, Thin Film Solar Cells, Plenum Press, New York, 1983
10. C. H. Henry, J. Appl. Phys., **51,** 4494 (1980).
11. L. Holland, Vacuum Deposition of Thin Films, John Wiley and Sons, Inc., New York (1961).
12. K. L. Chopra, Thin Film Phenomena, McGraw-Hill Book Company, New York (1969).

13. L. I. Maissel and R. Glang (Eds.), Handbook of Thin Film Technology, McGraw-Hill Book Company (1970).

14. G. V. Planer and L.S. Phillips, Thick Film Circuits, Butterworths and Company, London (1972).

15. T. J. Coutts (Ed.), Active and Passive Thin Film Devices, Acdamic Press, London (1978).

16. J. L. Vossen and W. Kern (Eds.), Thin Film Processes, Academic Press, New York (1978).

17. L. Esaki and C. L. Chang, Thin Solid Films, **36**, 285 (1976).

18. D. R. Arthur, J.Vac. Sci. Technol., **16**, 273 (1979).

19. C. F. Powell, in Vapour Deposition, C. F. Powell, J. H. Oxley, and J. M. Blocher, Jr., eds., Wiley, New York (1966), p.249.

20. W. M. Feist, S. R. Steele, and D. W. Readey, in Physics of Thin Films, **5**, G. Hass and R. E. Thun, eds., Academic Press, New York (1969), p. 237

21. S. R. Das, G. C. Morris, Solar Energy Mater. Solar Cells, **30**,107 (1993).

22. Y. Guo and X. Deng, Solar Energy Mater. Solar Cells, **29**,115 (1993).

23. P. Loaeza, and O. Solorza, J.Mater. Sci. Lett., **9,** 11 (1990).

24. G. Mausin, O. Solorza and H. Takenovti, J. Electroanal. Chem., **202**, 323 (1986).

25. P. K. Pandey, G.Razzini, L. Bicelli, Solar Energy Mater. Solar Cells, **26**, 285(1992).

26. F. A. Kroger, J. Electrochem. Soc., **125,** 2028 (1978).

27. A. C. Rastogi, K.S. Balakrishnan, Solar Energy Mater. Solar Cells, **36**, 121(1995).

28. C. L. Kolyer and M. Cocivera, J. Electrochem. Soc., **139**, 406 (1992).

29. K. D. Rogers, J. D. Painter, M. J. Healy, D. W. Lane and M. E. Ozsan, Thin Solid Films, **339**, 299 (1999).

30. A. K. Turner, J. M. Woodcock, M. E. Ozsan and J. G. Summers, Proc. 10th E.C. photovoltaic Solar energy Conf., Lisboa, 1991, p 791.

31. R. N. Bhattachcharya, W. Batchelor, H. Wiesner, F. Hasoon, J. E. Granata, K. Ramanathan, J. Alleman, J. Keane, A. Mason. R. J. Matson and R. N. Noufi, J. Electrochem. Soc., **10**, 3435 (1998).

32. M. E. Calixto, R. N. Bhattachcharya, P. J. Sebastian, A. M. Fernandez, S. A. Gamboa and R. N. Noufi, Solar Energy Mater. Solar Cells, **55**(1-2), 23(1998).

33. B. Dimmler and H. W. Schock, Progress in Photovoltaics, **6**(3), 193 (1998).

34. O. Savadogo, Solar Energy Mater. Solar Cells, **52**(3-4), 361(1998).

35. M. E. Ozsan, D. R. Johnson, M. Sadeghi, D. Sivapathasundaram, D. Lincot, B. Mokili, M. Froment, J. Vedel, L.M. Peter, G. Goodlet and R.C. Walker, 13th European Photovoltaic Solar Energy Conference, Nice, France, 1995, p2115.

36. M. E. Ozsan, D. R. Johnson, M. Sadeghi, D. Sivapathasundaram, G. Goodlet, M. J. Furlong, L. M. Peter, A. A. Shingleton and M. Bailes, J. Mater. Sci: Materials in Electronics, **7**, 119(1996).

37. A. M. Hermann, R. Westfall and R. Wind, Solar Energy Mater. Solar Cells, **52**,355(1998).

38. R. P. Raffaelle, H. Forsell, E. M. Potdevin, R. Friendfeld, J. G. Mantovani, S. G. Bailey, S. M Hubbard, E. M. Gordon and A. F. Hepp, Solar Energy Mater. Solar Cells, **57**(2),167 (1999).

39. O. A. Ileperuma, C. Vithana, K. Premaratne, S. N. Akuranthilaka, S. M. McGregor and I. M. Dharmadasa, J. Materials Science-Materials in Electronics, **9**(5), 367(1998).

40. D. Lincot and R. Ortega Borges, J. Electrochem. Soc., **139**, 1880 (1992).

41. R. K. Pandey, S. R. Kumar, A. J. N. Rooz, and S. Chandra, Thin Solid Films, **200**, 1 (1991).

42. K. Keis, L. Vayssieres, S. E. Lindquist and A. Hagfeldt, Nanostructured Materials, **12**(1-4), 487(1999).

43. S. Peulon and D Lincot, Advanced Materials, **8**(2), 166(1996).

44. K. D. Rogers, J. D. Painter, M. J. Healy, D. W. Lane and M. E. Ozsan, Thin Solid Films, **339**(1-2), 299(1999).

45. J. Touskova, D. Kindl and J. Tousek, Thin Solid Films, **293**(1-2), 272(1997).

46. S. Dennison, J. Materials Chemistry, **5**(11), 1885(1995).

47. A. K. Turner, J. M. Woodcock, M. E. Ozsan, J. G. Summers, J. Barker, S. Binns, K. Buchanan, C. Chai, S. Dennison, R. Hart, D. Johnson, R. Marshall, S. Oktik, M. Patterson, R. Perks, S. Roberts, M. Sadeghi, J. Sherbone, J.Szubert and S. Webster, Solar Energy Materials, **23**(2-4), 388(1991).

48. L. Thouin, S. Massaccesi, S. Sanchez and J. Vedel, J. Electroanal. Chem., **374** (1-2), 81(1994).

49. J. F. Guillemoles, A. Lusson, P. Cowache, S. Massaccesi and J. Vedel, Advanced Materials, **6**(5), 376(1994).

50. R. Jeyakumar, S. Ramamurthy, M. Jayachandran and M. J. Chockalingam, Materials Research Bulletin, **29**(2), 195(1994).

51. P.J. Sebastian, M. E. Calixto, R. N. Bhattachcharya and R. N. Noufi, J. Electrochem. Soc., **145** (10), 3613 (1998).

52. R. N. Bhattachcharya, W. Batchelor, J. E. Granata, F. Hasoon, H. Wiesner, K. Ramanathan, J. Keane and R. N. Noufi, Solar Energy Mater. Solar Cells, **55**(1-2), 83(1998).

53. G. Hodes, Y. Golan, L. Margulis and I. Rubenstein, Langmuir, **8**(3), 749 (1992).

54. M. Tomkiewicz, I. Ling and W.S. Parsons, J. Electrochem. Soc., **129**(9), 2016 (1982).

55. G. A. Ozin, Adv. Mater., **4**(10), 612 (1992).

56. G. Hodes, Nature, **285**, 29 (1980).

57. W. M. Yim and E. J. Stofko, J. Electrochem. Soc., **121**, 965 (1974).

58. H. Uda, S. Ikegami and H. Sonmura, Jpn. J. Appl. Phys., **36**, 5549(1997).

59. C. Liu and T. H. Wang, Appl. Phys. Lett., **36**, 852 (1980).

60. T. M. Ratcheva-Stambolieva, Y. D. Tchistyakov, G. A. Krasulin and H. D. Djoglev., Phys. Status Solid A, **16**,315 (1973).

61. G.Hodes, D. Cahen, J. Manassen and M. David, J. Electrochem. Soc., **127**, 2252 (1980).

62. M. Hyugaji and T. Miura, Jpn. J. Appl. Phys., **24**, 1575 (1985).

63. A. Nouhi, R. J. Stirn, P. V. Meyers and C. H. Liu, J. Vacu. Sci. & Techno. A-Vacuum Surfaces and Films, **7**(3), 833 (1989).

64. T. H. Myers, S. W. Edwards and J. F. Schetzina, J. Appl. Phys., **52**(6), 4231 (1981).

65. Y. S. Tyan and E. A. Perez-Albuerene, Proc. 16th IEEE Photovoltaic Specialists' Conf., San Diego, CA, 1982, IEEE, New York, 1982, p794.

66. H. Uda, H. Matsumoto, Y. Komatsu, A. Nakano and S. Ikegami, Proc. 16th IEEE Photovoltaic Specialists' Conf., San Diego, CA, 1982, IEEE, New York, 1982, p801.

67. C. D. Lokhande and S. H. Pawar, Phys. Stat. Sol. (a), **111**,17 (1989).

68. K. Rajeshwar, Adv. Mater., **4**(1), 23 (1992).

69. M. E. Ozsan, Int. Jnl. Solar Energy, **12**, 79 (1992).

70. B. M. Basol, Solar Cells, **23**, 69 (1988).

71. M. P. R. Panicker, M. Knaster and F. A. Kroger, J. Electrochem. Soc., **125**, 566(1978).

72. S. Licht, Interface, Vol.6, No. **3**, 34 (1997).

73. http://www.pv.unsw.edu.au/achiev.html

74. S. R. Wenham and M. A. Green, Progr. Photovolt., **4**,3 (1996).

75. http://www.entityconnect.com.au/~doranje/Efficiency.html

76. T. L. Chu, S. S. Chu, C. Ferekides, C. Q. Wu, J. Britt and C. Wang, J. Appl. Phys., **70**, 7608(1991).

77. J. Britt and C. Ferekides, Appl. Phys. Lett. **62**(22), 2851(1993).

78. T. Aramoto, S. Kumazawa, H. Higuchi, T. Arita, S. Shibutani, T. Nishio, J. Nakajima, M. Tsuji, A. Hanafusa, T. Hibino, K. Omura, H. Ohyama and M. Murozono, Jpn. J. Appl. Phys., **36**, 6304(1997).

79. R. F. Service, Science, **272**, 1744(1996).

80. J. R. Tuttle, M. A. Contreras, T. J.Gillespie, K. R. Ramanathan, A. L. Tennant, J. Keane, A. M. Gabor and R. Noufi, Progr. Photovolt., **3**, 235 (1995).

81. http://dcwww.epfl.ch/icp/ICP-2/solarcellE.html

82. K. Kalyanasundaram and M. Graetzel, Coord. Chem. Rev., **77**, 347(1998).

83. L. R. Cruz, L. L. Kazmerski, H. R. Moutinho, F. Hasoon, R. G. Dhere and R. de. Avillez, Thin Solid Films, **350**, 44(1999).

84. J. Sarlund, M. Ritala, M. Leskela, E. Siponmaa and R. Zilliacus, Solar Energy Mat. Solar Cells, **44**, 177(1996).

85. N. W. Duffy, D. Lane, M. E. Ozsan, L. M. Peter, K. D. Rogers and R. L. Wang, Thin Solid Films, in press.

86. L. M. Peter and R. L. Wang, Electrochemistry Communications, **1**,554 (1999).

87. G. C. Morris and R. J. Vandeveen, Solar Energy Mat. Solar Cells, **30**, 339(1993).

88. G. C. Morris, S. K. Das and P. G. Tanner, J. Crystal. Growth, **117**, 929(1991).

89. B. M. Basol, J. Appl. Phys., **55**, 601(1984).

90. B. W. Han, S. C. Park, J. H. Ahn and B. T. Ahn, Solar Energy, 64(1-3), 49(1998).

91. D. P. Halliday, J. M. Eggleston, K. Durose, J. Cryst. Growth, 186, 543(1998).

92. M. P. R. Panicker, M. Knaster and F. A. Kroger, J. Electrochem. Soc., **125**,566(1978).

93. K. D. Rogers, J. D. Painter, M. J. Healy, D. W. Lane, J. Electronic Mat., **28**, 112(1999).

94. Z. C. Feng, H. C. Chou, A. Rohatgi, G. K. Lim, A.T. S. Wee and K. L. Tan, J. Appl. Phys., **79**, 2151(1996).

95. P. V. Meyers and R. W. Birkmire, Prog. Photovolt., **3**, 393(1995).

96. D. H. Levi, H. R. Moutinbo, F. S. Hasoon, B. M. Keyes, R. K. Ahrenkiel, M. Al-Jassim, L. L. Kazmerski, R. W. Birkmire, Solar Energy Mat. Solar Cells, **41/42**,381(1996).

97. I. M. Dharmadasa, Prog. Crystal Growth and Charact., **36**(4), 249(1998).

98. H. Uda, S. Ikegami, H. Sonomura, Solar Energy Mat. Solar Cells, **50**, 141(1998).

99. H. C. Chou, A. Rohatgi, N. M. Jokerst, S. Kamra, S. R. Stock, S. L. Lowrie, R. K. Ahrenkiel and D. H. Levi, Materials Chemistry and Physics, **43**, 178(1996).

100. S. M. McGregor,I. M. Dharmadasa, I. Wadsworth and C. M. Care, Optical Materials, **6**,75(1996).

101. P. R. Unwin and R. G. Compton in *Comprehensive Chemical Kinetics* Vol 29, p 173 Elsevier, Amsterdam (1989).

CHAPTER FIVE

SOLID-STATE THEORY

5.1 CRYSTAL STRUCTURE AND ORIENTATION

5.1.1 Crystal Structure

Group II and VI elements prefer to take the sp^3-hybridisation to form the II-VI compounds. The sp^3-hybridised bonding mechanism leads to tetrahedral lattice sites provided there is a tendency towards sharing rather than the transfer of electrons between atoms. A tetrahedral lattice site in a compound, for example, CdTe, is a site in which each atom Cd is surrounded symmetrically by four nearest neighbouring Te atoms. The combination of the tetrahedral sites leads to two possible forms as shown in figure 5.1. These two combinations lead to the two crystal structures, wurtzite and zinc blende [2]. They are two interpenetrating close packed lattices.

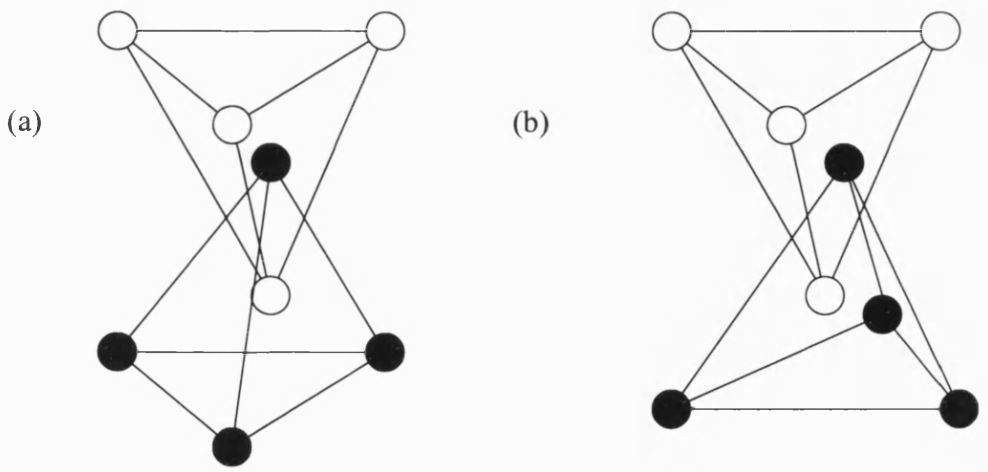

Figure 5.1 Tetrahedral sites for the II-VI compounds where bases of tetrahedra are parallel. (a) in line vertically (b) rotated by 60^0

Figure 5.2 shows the crystal structures of ZnS. The wurtzite or hexagonal crystal structure of ZnS is shown in figure 5.2a. The zinc blende or cubic crystal structure is depicted in figure 5.2b which has the combination of tetrahedral sites illustrated in figure 5.1b.

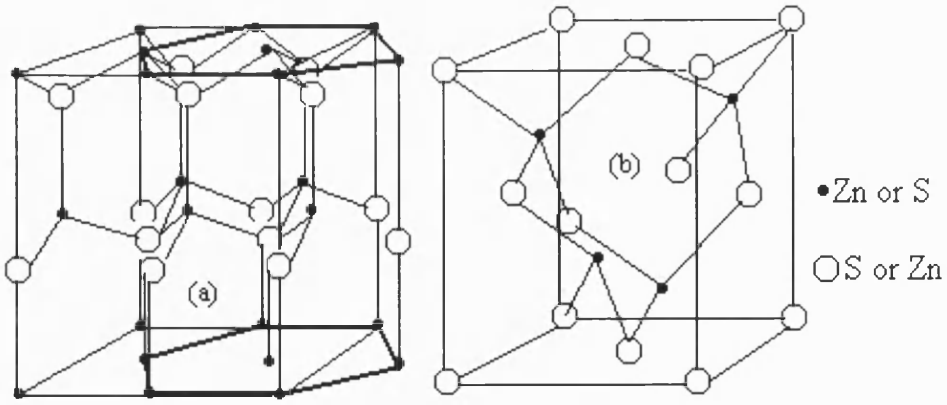

Figure 5.2 Crystal structures of ZnS (a) wurtzite and (b) zinc blende lattices.

The Table 5.1 lists properties of most of the II-VI compounds that may be used as photovoltaic materials. It includes the crystal structure, the bandgap, colour and conductivity of the materials and the mobility of the electrons or holes. In addition the properties of typical conducting substrates are listed.

Table 5.1 Properties of the II-VI compounds and the conducting substrates

Compound	Eg / eV	$\mu/cm^2V^{-1}s^{-1}$	ρ / Ω cm	Structure	Colour
SnO_2	~4.63[2-4]	10-50(e)	0.1– 0.0001	Rutile	Transparent
In_2O_3	~3.85[5-8]	15-70(e)	0.0002-0.01	Cubic	Transparent
ZnO	3.3[9]	15(e)	0.0008[10]	W[1]	White
ZnS	3.56-3.76 [11-12]	~600(e)[13] ~15(h)[13]		W or ZB	White
CdS	2.41-2.52 [14-15]	~330(e)[16] ~50(h)[17]	10^7-10^9[18] 1(annealed)	W	Yellow or Orange
ZnSe	2.33-2.83 [19-20]	~600(e)[21] 28[22]		W or ZB	Yellow or Orange
CdSe	1.74[23]	~900(e)[25] 50 (h)[24]	10^8-10^9[26] 10(annealed)	W or ZB	Yellow or Orange
ZnTe	2.35[27]	330[28]		ZB	Yellow
CdTe	1.43-1.50 [23,29]	~1050(e) ~100(h)[17]	10-10^8	ZB	Black

W = wurtzite, ZB = zinc blende, h = holes, e = electron.

5.1.2 Orientations

An ideal crystalline material is characterised by an orderly, repeated arrangement of the atoms of which it is composed. In such an orderly arrangement the entire crystal structure may be built up by repeatedly stacking a small subsection. The smallest section is known as a primitive cell. These primitive cells contain all the information required to reconstruct the locations of atoms in the crystal but frequently have awkward shapes. So it is sometimes more convenient to have a larger unit cell that also contains the information but has a simpler shape. For example, figure 5.3a shows the unit cell for the faced-centred-cubic (fcc) lattice and figure 5.3b depicts the corresponding primitive cell. The length of the edge of the unit cell is known as the lattice constant.

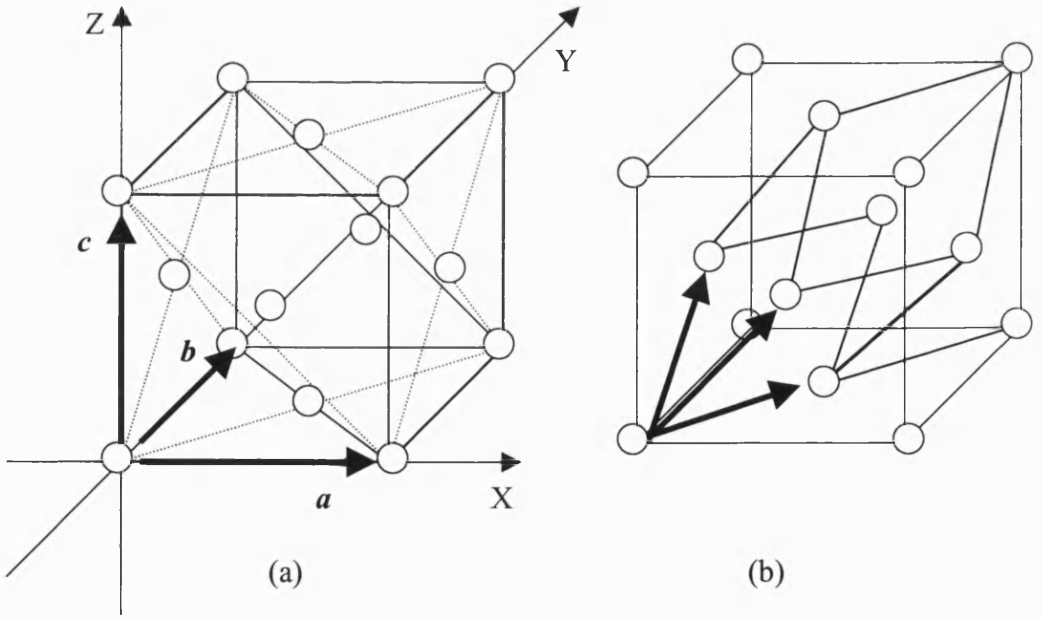

Figure 5.3 (a) Unit cell for the fcc lattice. The ***a***, ***b*** and ***c*** are unit vectors in each of these directions. (b) The corresponding primitive cell.

Crystals are often anisotropic, so that properties such as electrical resistivity, magnetic susceptibility are different when measured in different crystallographic directions. The less symmetry the crystal possesses, the more these properties differ. The orientation of planes within the crystal can be expressed in terms of the unit cell structure using a system termed "Miller indices". The basis of a coordinate system with the vectors defining the outline of the unit cell is shown in figure 5.3a. The Miller indices for planes in three-dimensional lattices are given by *hkl*, where *h*, *k*, *l* are the indices for the x, y and z axis, respectively. A plane is indexed *hkl* when it makes intercepts a/*h*, b/*k*, and c/*l* with the unit cell edges a, b, and c. An example is shown in figure 5.4. The intercepts in this case along each of the axes are 2, 1, and 4 atoms from the origin. Taking inverses gives ½, 1, and ¼. The smallest integrals with the same ratio are 2, 4 and 1. This plane is then expressed in Miller indices as the (241) plane. Negative intercepts are indicated by a bar over the top of the corresponding index, for example $(\bar{3})$

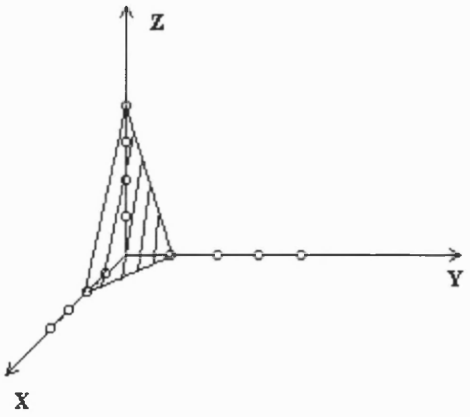

Figure 5.4 Sketch of a plane in a crystal described by the Miller indices (241)

Note that there are planes within the crystal structure that are equivalent. For example, for the fcc lattice, the difference between the (100), (010), and (001) planes depends only on the choice of origin.

5.2 The Band Model of Solids

The best way to understand electron transfer in solids is by using the concepts of the band model. There are continuous levels of energy for an electron in free space. However, the situation in a solid can be quite different. In a finite solid, there can only be a finite number of energy levels. An orbital corresponds to an energy level that may be described quantitatively by the wave functions. The orbitals occupied by the valence electrons form the "valence band" of the solid which is a few electron volts broad. The band associated with the first excited state, normally unoccupied by electrons, is called the "conduction band" of the solid. This band is normally much broader than the valence band as a result of the greater overlap of the orbital wave functions. The valence and conduction bands may be separated by a bandgap, Eg.

The electron occupancy of the bands determines the nature of the conductivity of a solid. There are three kinds of solids – metal, semiconductor and insulator. Figure 5.5 shows schematically the electron occupancy for different classes of solids.

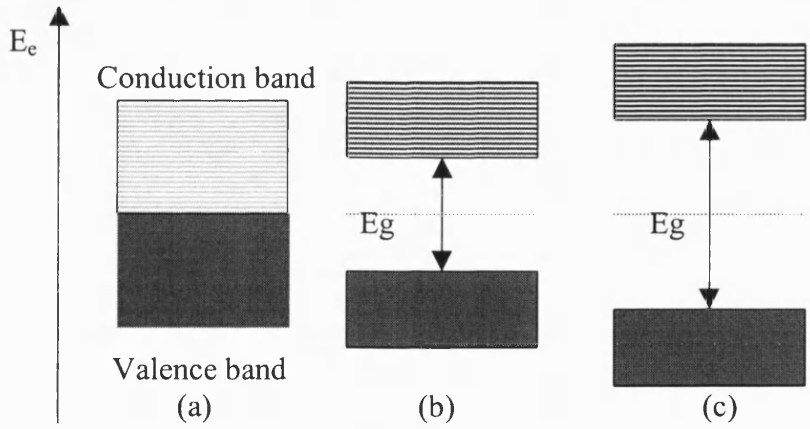

Figure 5.5 The electron occupancy in solids classified by (a) metals, (b) semiconductors and (c) insulators

In metals, there is no discontinuity between the valence and conduction bands. This means that some of the bands may overlap, and so electrons can be very easily

excited into the conductance bands by thermal energy (kT) at room temperature. This results in highly electrical conductivity.

In pure semiconductors, an electron can jump from the valence to the conduction band when the electron gains energy greater than the bandgap from heat or light. The excitation of the electron leaves a hole in the valence band. Both the electron and hole become the mobile electrical carriers but in opposite directions. A semiconducting material in which the electrons and holes originate not from an impurity but from thermal excitation across the bandgap is called an intrinsic semiconductor. Normally intrinsic material has a small bandgap (< 1eV). If a semiconducting material contains some impurities which act as the sources of the electrons or holes, it is called as extrinsic semiconductor. The process in which some impurities are added to a semiconductor to increase the electron or hole density is referred to as doping. If an added impurity or dopant contributes electrons to the conduction band of the semiconductor, the impurity is called a donor, and the doped semiconductor is called n-type. If the dopant injects holes into the valence band, the dopant is called an acceptor, and the doped semiconductor is termed p-type. Insulators have a fully occupied valence band and a large bandgap (4 eV) [31], so that the conduction band is essentially empty at room temperatures.

The lowest energy level for an excited electron is at the bottom of the conduction band, whereas that for a hole is at the top of the valence band. Mobile electrons in the conduction band and holes in the valence band normally carry electrical current in the solid.

5.3 The Fermi Level

The Fermi level or energy is defined thermodynamically as the electrochemical potential of the electron in the solid [30]. An equivalent definition arises from the distribution of electrons among energy levels in a solid: the probability of an energy level being occupied by an electron is exactly ½ at the Fermi energy, E_F. In general, probability of occupation of any level is determined by the Fermi function, f(E), given by the Fermi-Dirac distribution function

$$f(E) = \frac{1}{(1+\exp((E-E_F)/k_BT)} \tag{5.1}$$

where k_B is the boltzmann constant, and T the temperature (Kelvin). The probability f(E) decreases rapidly for levels above E_F, and increases rapidly for levels below E_F. For semiconductors the Fermi level is located in the bandgap region. For an intrinsic semiconductor the Fermi level is situated approximately midway between the conduction band edge, E_C, and the valence band edge, E_V, as seen in figure 5.5. For n-type doping, the Fermi level shifts towards the conduction band edge, while p-type doping shifts it towards the valence band edge. The position of the Fermi level is related to the doping level (the concentration of charge carriers). For example, when semiconductors are highly doped to charge carrier concentrations of 10^{18} –10^{19} cm^{-3}, the Fermi level shifts to a position within 0.1eV of a band edge [30].

5.4 Electrons and Holes in Semiconductors

5.4.1 Intrinsic Semiconductors

In this case, the Fermi level is deep in the bandgap, Eqn. 5.1 can be simplified [31-32] as:

$$f(E_C) = \frac{n}{N_C} \approx \exp((E_F - E_C)/k_B T) \tag{5.2}$$

and

$$f(E_V) = \frac{p}{N_V} \approx \exp((E_F - E_V)/k_B T) \tag{5.3}$$

where n is the density of electrons in the conduction band, p the density of holes in the valence band. N_C is the effective density of energy levels in this region of the conduction band, and N_V is the effective density of energy levels in the region of the valence band. They are given by [33]

$$N_C = 2\left(\frac{m_e^* k_B T}{2\pi\hbar^2}\right)^{\frac{3}{2}} \tag{5.4}$$

and

$$N_V = 2\left(\frac{m_h^* k_B T}{2\pi\hbar^2}\right)^{\frac{3}{2}} \tag{5.5}$$

where m_e^* and m_h^* are the effective masses of electrons and holes at the band edge, respectively.

An inportant result is obtained by multiplying together Eqs. 5.2 and 5.3 and inserting Eqns. 5.4 and 5.5:

$$np = 4(k_B T / 2\pi\hbar^2)^3 (m_e^* m_h^*) \exp(-Eg/k_B T) \tag{5.6}$$

where n = p in the intrinsic case because each electron thermally excited into the conduction band creates a hole in the valence band. The intrinsic carrier concentrations in silicon and germanium at room temperature are 2×10^{10} and 2×10^{13} cm^{-3} respectively [34]. The Fermi level, E_F, of intrinsic semiconductors is obtained from Eqn. 5.6 as:

$$E_F = \frac{1}{2} Eg + \frac{3}{4} k_B T \ln(m_h^* / m_e^*) \tag{5.7}$$

If $m_e^* = m_h^*$, then E_F = Eg/2 and the Fermi level is exactly in the centre of the band gap. If as is usual in semiconductors, m_h^* is larger than m_e^*, the Fermi lies slightly above the centre of the bandgap.

5.4.2 Extrinsic Semiconductors

Semiconductors are normally doped n-type, and p-type to form, for example, p-n junctions. Figures 5.6 and 5.7 show the density of states and energies of electrons and holes in n- and p-type semiconductors (extrinsic semiconductors), respectively.

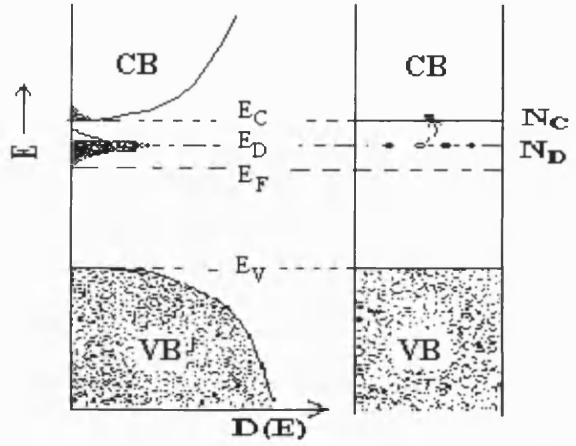

Figure 5.6 Electron energy and density of states in n-type semiconductor

E_D is the donor level,N_D is the donor density

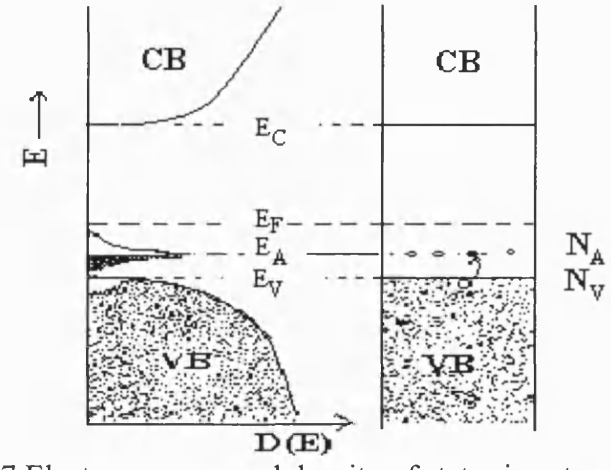

Figure 5.7 Electron energy and density of states in p-type semiconductor

E_A is the acceptor level, N_A is the acceptor density

The localised donor levels are close to the conduction band in n-type semiconductors as seen in figure 5.6, while the localised acceptor levels in p-type semiconductors are close to the valence band as shown in figure 5.7. The ionisation of donors and acceptors injects electrons into the conduction band and holes into the valence band, respectively. The densities of electrons, n, and holes, p, are still given by Eqns. 5.2 and 5.3, respectively. The density of ionised donors, N_{D^+}, and acceptors, N_{A^-}, are derived using the Fermi function approximated by the Boltzmann function, respectively as:

$$N_{D^+} = N_D \exp((E_D - E_F)/k_B T) \tag{5.8}$$

$$N_{A^-} = N_A \exp((E_F - E_A)/k_B T) \tag{5.9}$$

where N_D and N_A are the densities of donors and acceptors, respectively.

To satisfy the condition of electroneutrality, there is a requirement, $n = N_{D^+} + p$, for n-type semiconductors, but it may be approximated by $n \approx N_{D^+}$ since that p is much less n. Then one has

$$n = N_C \exp((E_F - E_C)/k_B T) = N_{D^+} = N_D \exp((E_D - E_F)/k_B T) \tag{5.10}$$

The density of electrons, n, and the Fermi level, E_F, can be obtained as

$$n = \sqrt{N_C N_D} \exp((E_D - E_C)/k_B T)) \tag{5.11}$$

$$E_F = \frac{E_C + E_D}{2} - \frac{k_B T}{2} \ln \frac{N_C}{N_D} \tag{5.12}$$

Similar equations can be obtained for p-type semiconductors as follows:

$$p = \sqrt{N_V N_A} \exp((E_V - E_A)/k_B T)) \tag{5.13}$$

$$E_F = \frac{E_V + E_A}{2} + \frac{k_B T}{2} \ln \frac{N_V}{N_A} \qquad (5.14)$$

It is clear from Eqns. 5.12 and 5.14 that the Fermi level is dependent on the energy level and density of the dopant in extrinsic semiconductors.

The density of electrons, n, in the conduction band is different from the density of holes, p, in the valence band in extrinsic semiconductors due to the doping. Both electrons and holes are mobile charge carriers in semiconductors. In n-type semiconductors, electrons dominate and are called majority carriers, and holes are called minority carriers. By contrast in p-type semiconductors, holes are the majority carriers and electrons are the minority carriers. The product of the densities of majority and minority carriers in a semiconductor of extrinsic type equals the square of the concentration of electron-hole pairs, n_i, in the same semiconductor of intrinsic type. This means that Eqn. 5.6 is still valid. The value of this product is characteristic of individual semiconductors. For example np is 4.2×10^{21} cm^{-6} for silicon, and 6×10^{26} cm^{-6} for germanium at 298K [33].

So far the Fermi level has been defined for conditions of thermodynamic equilibrium. However, semiconductors for solar cell applications are subjected to illumination. When a semiconductor is illuminated, the photoexcited electron-hole pairs are relatively long lived, so that the thermal equilibrium is established between phonons and electrons in the conduction band as well as between phonons and holes in the valence band. The electrochemical potential for the photoexcited electrons and holes is called the quasi-Fermi level of electrons, ${}_nE_F^*$, and the quasi-Fermi level of holes, ${}_pE_F^*$ [35-37].

In the dark, the quasi-Fermi Levels of electrons and holes equal the original Fermi level of the semiconductor (${}_nE_F^* = {}_pE_F^* = E_F$) due to thermal equilibrium between

electrons in the conduction band and holes in the valence band. However under the illumination, the quasi-Fermi level of electrons is higher and the quasi-Fermi level of holes is lower than the original Fermi level of the semiconductor (${}_nE_F^* > E_F > {}_pE_F^*$). A schematic diagram showing the splitting of the Fermi level into quasi-Fermi levels under illumination is given in figure 5.8.

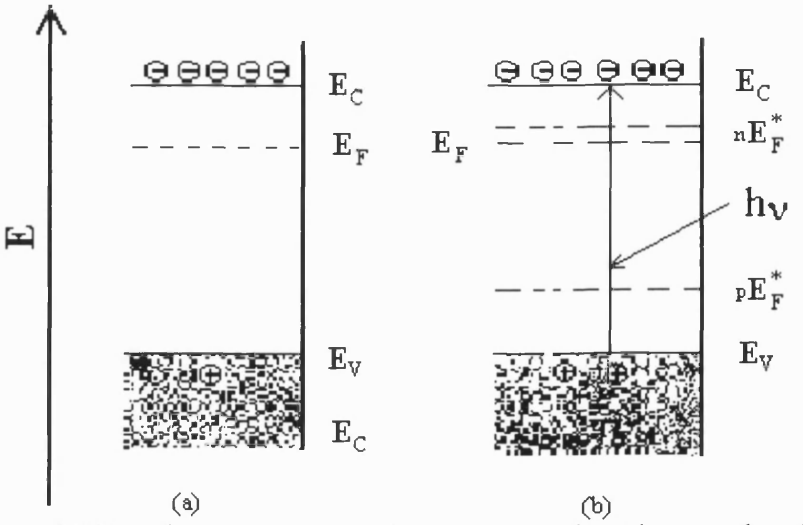

Figure 5.8 Fermi energy diagram for n-type semiconductors showing (a) in the dark and (b) under illumination

Under illumination, the electron and hole densities become:

$$p^* = p + \Delta p \tag{5.15}$$

$$n^* = n + \Delta n \tag{5.16}$$

where n and p are the electron and hole densities in the dark, and Δn and Δp are the changes in the electron and hole densities under illumination ($\Delta n = \Delta p$), respectively. In the case of an n-type semiconductor, the majority carrier density is not significantly increased by the illumination, so the position of the quasi-Fermi level of electrons, ${}_nE_F^*$, is remains close to E_F, and $n >> \Delta n$. by contrast, the density of minority carriers, holes, is dramatically increased so the quasi-Fermi level of holes is much lower than

E_F. As described in section 5.4.1, the Fermi levels of n-type and p-type semiconductors are obtained, respectively, as:

$$E_F = E_C - k_B T \ln\left(N_C / n\right) \tag{5.17}$$

$$E_F = E_V + k_B T \ln\left(N_V / p\right) \tag{5.18}$$

Inserting Eqns 5.15 and 5.16 into Eqns 5.17 and 5,18, the quasi-Fermi levels of electrons and holes obtain, respectively:

$${}_n E_F^* = E_C - k_B T \ln\left(\frac{N_C}{n^*}\right) = E_F + k_B T \ln\left(\frac{n+\Delta n}{n}\right) \tag{5.19}$$

$${}_p E_F^* = E_V + k_B T \ln\left(\frac{N_V}{p^*}\right) = E_F - k_B T \ln\left(\frac{p+\Delta p}{p}\right) \tag{5.20}$$

In general, under illumination, the quasi-Fermi level of the majority carriers will remain close to the original Fermi level, whereas the quasi-Fermi level of the minority carriers will shift away from the original Fermi level.

5.5 Defects, Traps and Recombination Centres

Defects play a very important role in the properties of semiconductors. Solids generally contain vacancies, interstitials, dislocations and grain boundaries and so on.

A vacancy is a missing atom in the crystal, and such a site can be electrically active. It has been shown that cation vacancies are acceptors, anion vacancies are donors. An interstitial atom is one that is squeezed between the atoms of the normal crystal. Either a host atom or a foreign atom can be located interstitially in the lattice. If such an interstitial atom tends to give up electrons, it will be an active donor. If it tends to accept electrons, in principle, it can be an active acceptor. Movement of

vacancies and interstitials is of importance in the doping of solids by diffusion and corrosion. For example, in the CdTe crystal, Cd vacancies lead to n-type behaviour, while Te vacancies result in p-type behaviour.

Dislocations and grain boundaries are also bulk defects that are of great importance both in the behaviour of the solution/solid interface and in polycrystalline photovoltaic devices. Both may provide energy levels in the gap [38] and may allow current flow along these energy levels. Dislocations arise mainly in two ways. First, they arise from mechanical damage to a crystal. For example, mechanical abrasion (polishing or lapping) of a crystal surface will generate dislocations. The second origin of dislocations is their formation during crystal growth (mainly due to dislocations at the surface of the seed crystal). Grain boundaries act in many ways as an accumulation of dislocations.

The term "trap" is used to describe energy levels deep in the band gap caused by defects such as two described above or arising from impurities that capture electrons or holes. The trapped carrier may be thermally reemitted, or it may return to the band from where it came.

A recombination centre is a site that can capture carriers readily from either band. Thus, if an electron is optically excited from the valence band to the conduction band, creating an electron-hole pair, the pair will often become deexcited through a recombination centre. Normally the centre first captures the minority carrier and then is reoccupied by the majority carrier and so that the electron and hole recombine. The lifetime [39-40] of the minority carrier, τ, is the average time before recombining with the majority carrier after generation. The lifetime of a carrier in given semiconductor will depend on the kinetics of recombination, either by direct recombination, or by recombination via an intermediate state or trap.

5.6 Band Structure at the Semiconductor Surface

So far the existence of a surface on the crystal has been ignored. When considering semiconductor devices like solar cell applications, surfaces are very important. The basic ideas of the physics of semiconductor surfaces are in the literature [40-42].

5.6.1 Surface States

Intrinsic surface states are due to the presence of the surface itself. There is generally one such surface state per surface atom, resulting in a surface state density of the order of 10^{15} cm^{-2} [42]. There are two kinds of surface states: fast and slow surface states. The fast surface states associated with the semiconductor surface itself are due to the fact that the transition times between such states and the semiconductor bulk are short, of the order of 1 μsec or less [43]. The slow surface states are often linked to the formation of an oxide layer, or other adsorbed species, generally found on semiconductor surfaces [44]. The transition times with the bulk semiconductor are long (of the order of seconds).

5.6.2 Band Structure at the Semiconductor Surface

At the solid/gas or solid/liquid surface, the interaction of surface states with the electron energy levels of a bulk semiconductor can lead to the band bending at the surface. Consider a p-type semiconductor with a number of donor surface states. These donor surface states are neutral when empty and are positively charged when filled. It is assumed that all of donor states are ionised. Electrons from surface states flow into the empty acceptors in the bulk semiconductor, producing a positive surface charge and leaving behind uncompensated positively charged ionised donors. This results in the creation of a region of fixed positive space charge at the semiconductor surface and of negative space charge in the bulk of the semiconductor. There is, at

equilibrium, an electric field $\underline{E}$ in the space charge region, as shown in figure 5.9a. The electric field corresponds to a gradient of electrostatic potential V(x) in the space charge region. Since $\underline{E}$ is directed opposite the surface, V(x) must decrease in the direction away from surface, also as shown schematically in figure 5.9b. The potential V is thus higher at the surface than in the bulk of the semiconductor by an amount indicated by Φ_s. The quantity Φ_s is called the surface potential. The electron energy in the bulk is higher by an amount $q\Phi_s$ than at the surface. The energy bands in the p-type semiconductor are thus "bent" downward at the surface due to the existence of surface donor states.

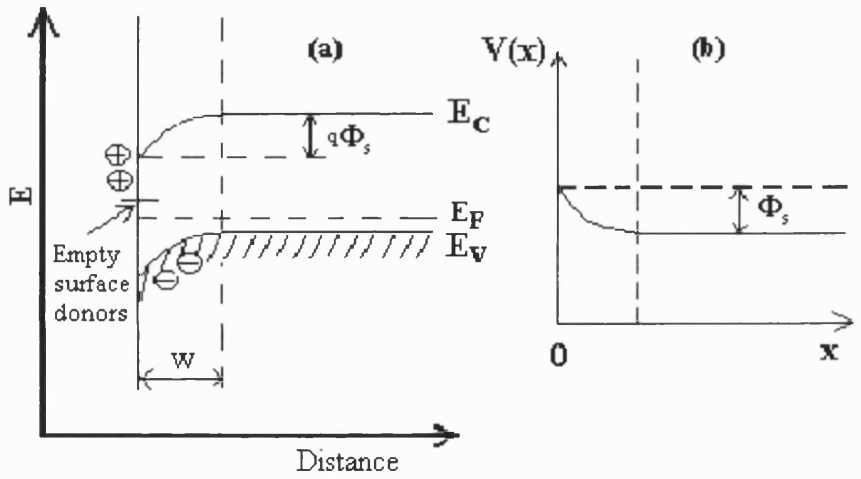

Figure 5.9 Band diagram and potential distribution of a p-type semiconductor with donor surface states, W is the width of space charge region

(a) band diagram at equilibrium (b) electrostatic potential V(x) as a function of distance x (x=0 at the surface)

In the same manner, the surface band structure of an n-type semiconductor with acceptor surface states can be examined [45-46].

In case in which the number of surface states is very large, not all of them are ionised. Consider an n-type semiconductor with acceptor surface states, all of which lie at roughly the same energy E_s as shown in figure 5.10. Electrons flow from the bulk semiconductor into the surface acceptors only until the Fermi level at the surface coincides with the surface acceptor energy. This means that some of the surface acceptors will remain empty. The Fermi level position at the surface is determined only by the surface acceptor energy E_s , and is independent of the doping in the n-type bulk. In this case the surface Fermi level is "stabilised" or "pinned" [47-48] at the energy E_s, relative to the valence band (Fermi level pining).

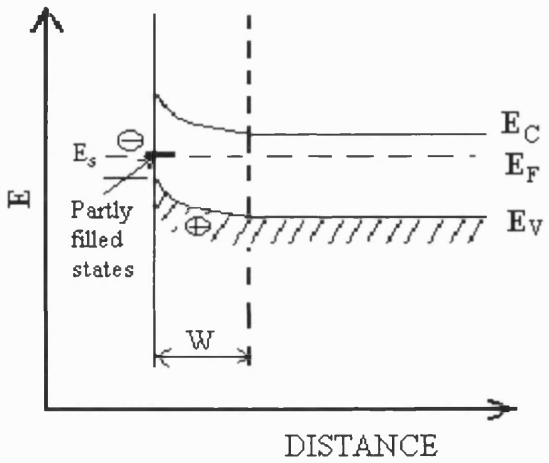

Figure 5.10 Band diagram, at equilibrium, of an n-type semiconductor with a sufficiently larger number of surface acceptors, so that the acceptors are partly filled (Fermi level pining).

5.6.3 The Amount of Band Bending

As mentioned above, the amount ($q\Phi_s$) of band bending is determined by the situation shown in figure 5.9. It is assumed that the bulk acceptor density is N_A, and the density of surface donors is n_s, the others are shown in figure 5.9. Then the space charge density, ρ, in the bulk is given by

$$\rho = -qN_A \tag{5.21}$$

where q is an electron charge, and Poisson's equation for the electrostatic potential V(x) is

$$\frac{d^2V}{dx^2} = \frac{-\rho}{\varepsilon\varepsilon_0} = \frac{qN_A}{\varepsilon\varepsilon_0} \tag{5.22}$$

where ε is the relative dielectric constant of the semiconductor, and ε_0 is the permittivity of free space.

Integrating Eqn. 5.22 once gives:

$$\frac{dV}{dx} = \frac{qN_A}{\varepsilon\varepsilon_0}x + C \tag{5.23}$$

The space charge region in the semiconductor can be regarded as a capacitor filled with a solid of dielectric constant ε and since the electric field $\underline{E}$ is given by Gauss's law, its magnitude at the surface is

$$\left.\frac{dV}{dx}\right|_{x=0} = \frac{qn_s}{\varepsilon\varepsilon_0} \tag{5.24}$$

The boundary conditions are

$$\left.\frac{dV}{dx}\right|_{x=W} = 0, \tag{5.25}$$

$$V(0) = \Phi_s \; and \; V(W) = 0 \tag{5.26}$$

The solutions are given

$$W = n_s/N_A \tag{5.27}$$

$$\Phi_s = \frac{qN_A W^2}{2\varepsilon\varepsilon_0} = \frac{qn_s^{\,2}}{\varepsilon\varepsilon_0 N_A} \tag{5.28}$$

The amount of band bending in a p-type semiconductor is obtained as

$$q\Phi_s = \frac{q^2 N_A W^2}{2\varepsilon\varepsilon_0} = \frac{q^2 n_s^{\,2}}{\varepsilon\varepsilon_0 N_A} \tag{5.29}$$

In a similar way the amount of band bending in an n-type semiconductor is

$$q\Phi_s = \frac{q^2 N_D W^2}{2\varepsilon\varepsilon_0} = \frac{q^2 n_s^{\,2}}{\varepsilon\varepsilon_0 N_D} \tag{5.30}$$

Here n_s is the density of surface acceptors, and N_D is the bulk donor density.

5.7 The Semiconductor/electrolyte Interface

The semiconductor electrolyte interface plays a key role in studies of photoelectrochemistry. A number of textbooks have been published that deal with this area [30,33,49-52].

When a semiconductor contacts an electrolyte, most of the applied potential is distributed in the space charge region within the semiconductor, the rest is across the double layers on the electrolyte side. A schematic diagram of the various regions and potential profile across them in the semiconductor electrolyte junction is depicted in figure 5.11a. They are three distinct layers: 1) a mobile diffuse charge layer in the ionic solution; 2) a compact layer of adsorbed solvent molecules, and 3) a fixed diffuse charge layer in the semiconductor. These layers are called the diffuse layer or the Gouy region, Helmholtz layer (introduced in part I), and the space charge layer, respectively. These charged layers also form three capacitities: the space charge layer

capacitance C_{SC} on the solid side, the Helmholtz capacitance C_H at the interface, and the diffuse layer capacitance C_d in the solution as shown in figure 5.11b.

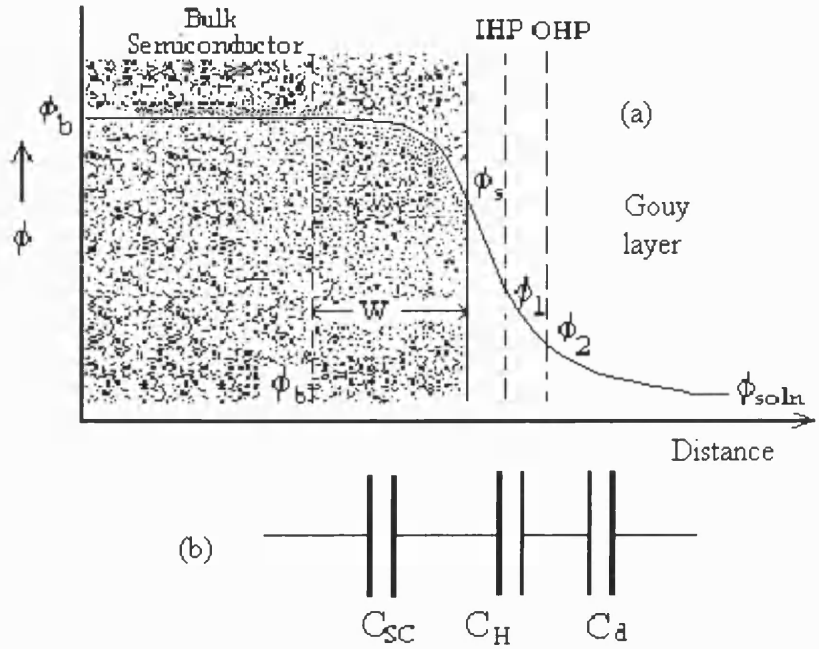

Figure 5.11 A schematic diagram of an interfacial double layer model:

ϕ = inner potential, IHP = inner Helmholtz plane, OHP = out Helmholtz plane

The ohmic drop in the bulk semiconductor is neglected here (lengths not to scale).

5.7.1 Double Layers

5.7.1.1 Gouy Double Layer

The Gouy-Chapman theory describes a region in the solution near the electrode where there is a space charge due to an excess of free ions of one sign. The ions attracted to the OHP do not suffice to compensate all the charges on the electrode, and form a charged Gouy double layer. The thickness of the Gouy double layer is about 10 to 100 nm in solution of low ionic strength [33], but when the concentration of ions in the electrolyte is the order of 0.1 mol dm^{-3}, the Gouy double layer is hardly distingushable from Helmholtz layer [50].

5.7.1.2 The Helmholtz Double Layer

The Helmholtz double layer is considered to be formed between two planes of charge. The thickness of the Helmholtz double layer is nearly constant and independent of the nature of the semiconductor, being 1.5 to 2 times the thickness of the mono-molecular water [33]; a typical value is 5 Å [50]. The capacity of the layer is quite large. Typically, at a metal electrode the measured Helmholtz capacity, is 100 $\mu F /cm^2$ [50], and at a semiconductor it is of the order of 20 $\mu F/cm^2$ [52].

5.7.1.3 The Space Charge Layer

The amount of charge in the space charge region of the semiconductor depends on the nature of different contacts. When a semiconductor is put into contact with the electrolyte, the charge in the space charge region may change due to i) the interaction between the surface states and the solution, ii) injection or extraction electrons from the semiconductor by ions with the appropriate energy levels in the solution, and iii) application of an external potential. Normally the voltage across the space charge region will change by an amount equal to a change in external voltage, because the capacitance C_{SC} is much smaller than C_H [53]. Eqns. 5.29 or 5.30 can be used to calculate the capacity of the space charge layer, depending on the type of the semiconductor.

The double layer capacity is defined by

$$C = \frac{dQ}{dV} = \frac{\varepsilon\varepsilon_0}{AW} \tag{5.31}$$

Here A is the area of the semiconductor in cm^2, dQ is a differential increase in the charge, dV is the differential voltage change across the double layer, and W is its width.

The total capacity is represented by a series connection of three capacities.

$$\frac{1}{C}=\frac{1}{C_{SC}}+\frac{1}{C_H}+\frac{1}{C_d} \tag{5.32}$$

The smallest capacity predominates in determining the overall capacity, and usually, the space charge layer capacity is the smallest so that $C \approx C_{SC}$..

5.7.2 The Effects of Applied Potential

For any given semiconductor and electrolyte, there exists a unique potential for which the potential drop between the surface and the bulk of the electrode is zero, and no net charge exists within the space charge layer. This potential is called the flatband potential (V_{fb}) (due to no band bending) or point of zero charge which is shown in figure 5.13.

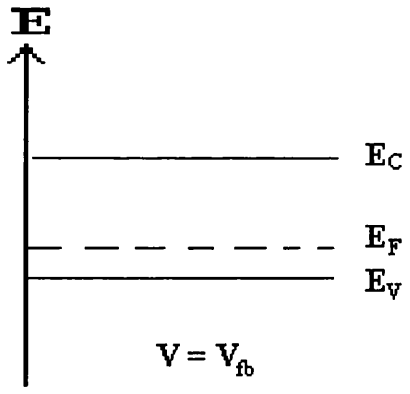

Figure 5.13 Band bending for a p-type semiconductor at $V = V_{fb}$

An externally applied potential controls the Fermi level of the semiconductor electrode relative to the Fermi level of a reference electrode, and the band bending can be classified into three types in terms of the applied potential. Take an n-type

semiconductor as an example. At potentials more negative than V_{fb}, the majority carrier (electrons) in the conduction band flow into the surface to form an accumulation layer as shown in figure 5.14a. When the applied potential is made more positive than V_{fb}, a depletion layer is formed as shown in figure 5.14b. Finally, when the applied potential become much more positive than V_{fb}, the Fermi level at the surface is closer to the minority carrier band (here the valence band) than the majority carrier band (here is the conduction band). This is shown in figure 5.14c. Thus the surface is inverted from an n-type bulk to a p-type surface at equilibrium because that the concentration of holes exceeds that of electrons obtained by Eqns. 5.2 and 5.3. This is termed the "inversion layer". For wide bandgap semiconductors the thermal excitation of electrons is so slow that an inversion lay may not form – in this case the situation is referred to as deep depletion.

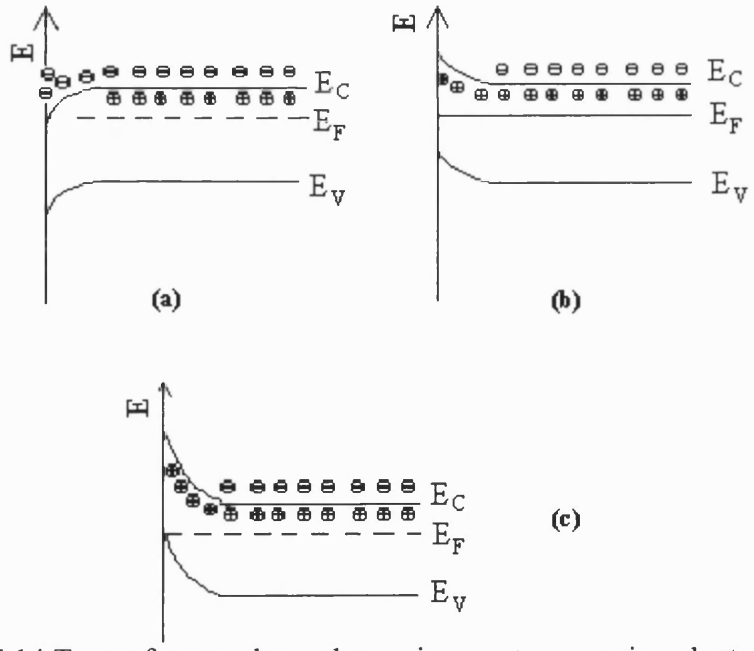

Figure 5.14 Type of space charge layers in an n-type semiconductor

(a) accumulation layer (b) depletion layer (c) inversion layer

5.7.3 Mott-Schottky Relationship

As discussed above, an external potentials applied to a semiconductor electrode will lead to band bending. The flatband potential, V_{fb}, and the density of charge in the space charge region, n_s, are very important parameters that can be obtained from the capacitance - voltage measurements. The well-known Mott-Schottky equation [54-55] can be obtained directly from Eqns. 5.29 or 5.30 for different type of semiconductors. The relationship for n-type semiconductors is

$$C_{SC}^{-2} = (2/q\varepsilon\varepsilon_0 N_D)(V - V_{fb} - k_B T/q) \tag{5.33}$$

which at 298°K becomes

$$C_{SC}^{-2} = \left[\frac{1.41\times10^{20}}{\varepsilon N_D}\right](V - V_{fb} - 0.0257) \tag{5.34}$$

Here C is in μFcm^{-2}, N_D in cm^{-3}, V in volts. For a p-type semiconductor N_A replaces N_D, and the other terms are unchanged.

This equation is valid only when changes in the applied potential appear mainly across the space charge region. This means $C_{SC} \approx C$ in Eqn 5.32. Surface states [51], redox couple in solution [30], and deep levels [56] will affect the capacitance behaviour.

The flatband potential of semiconductor electrodes is characteristic of the materials and is determined by the potential difference across the Helmholtz double layer at the electrode interface. However, for some semiconductor electrodes, illumination changes the potential difference across the potential difference across the Helmholtz layer on the electrode, and hence shifts the flatband potential of the electrode [33]. The photo-induced shift of the flatband potential, V_{fb}^{ph} – V_{fb}, equals to

the change in the potential, ΔV_{fb}, of the Helmholtz layer due to the photoexcitation as defined as:

$$\Delta V_{fb} = V_{fb}^{ph} - V_{fb} \tag{5.35}$$

Figure 5.15 shows Mott-Schottky plots of an n-type molybdenum selenide electrode in the dark and under illumination [57]. This is due to a dissolution reaction involving the transfer of ions of the semiconductor electrode.

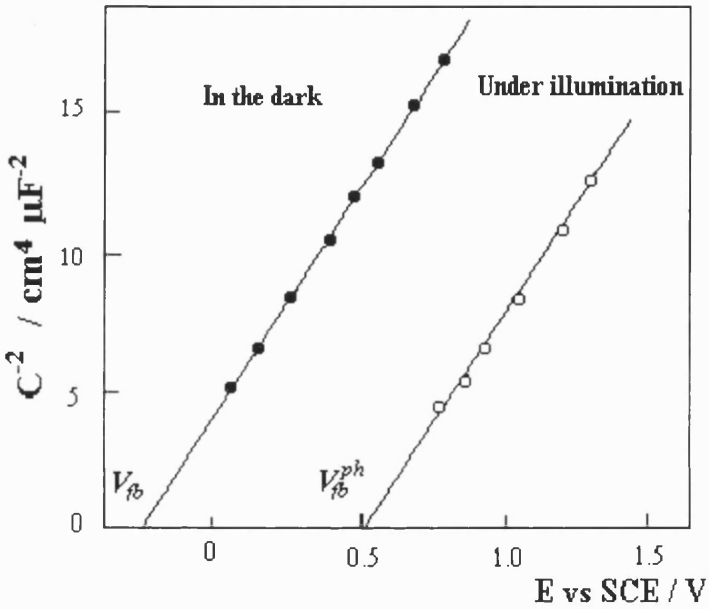

Figure 5.15 Mott-schottky plots of $MoSe_2$ electrode in 2M HCl in the dark and under illumination in the acidic solution from ref. [57]

5.8 Electron Transfer Processes at Semiconductor/Electrolyte Interface

When a metal or semiconductor electrode is immersed in solution containing a redox couple with two forms – the oxidised (Ox) and reduced (Red), electrons flow across the interface until their energies are equal. The rate of charge transfer processes is mainly dependent on the metal or semiconductors itself and the redox couple. Generally the rate is much faster for a metal electrode than for a semiconductor.

5.8.1 The Relation between the Hydrogen and the Vacuum Scale of Energy

There are two scales used for energy in the chemical physics of surfaces. In the gas/solid interface, the Fermi energies are defined relative to the energy of an electron in the vacuum. The energy of an electron at infinity, E^e, is defined as zero. In electrochemistry, the potential scale is defined relative to the standard hydrogen electrode (SHE). The two scales are related by the theoretical value for the Fermi level of SHE [58]:

$$qV = -4.5 - E \tag{5.36}$$

Here V is the potential in SHE scale, E is the corresponding energy. The potential scale decreases as the energy increases; electrons spontaneously flow from more negative (higher level of energy) to more positive potential (lower energy). The relation between two scales is shown in figure 5.16.

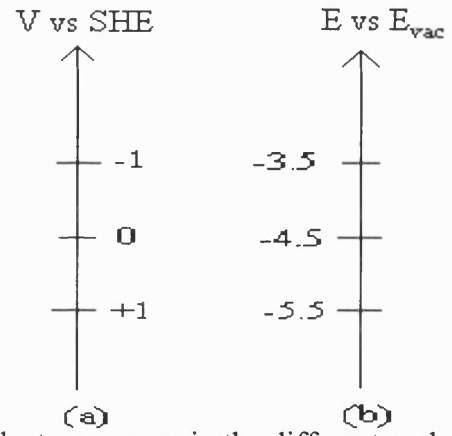

Figure 5.16 The electron energy in the different scales

(a) electrochemical potential scale (b) vacuum scale

5.8.2 The Fermi Level of Redox Electrons

The localised electron levels of hydrated redox species (oxidised and reduced form) in aqueous solutions fluctuate due to the thermal motion of the molecules in the

solution. This concept was introduced first by Marcus [58-59] and is described by Morrison [50]. The probability density of electron energy fluctuation, Q(E), is given by a Gaussian distribution

$$Q(E)=Q_0 \exp(-(E-E_0)^2/Q_0^2) \tag{5.37}$$

where Q_0 is a normalising factor that is given by $1/\sqrt{4\lambda kT}$, where λ is the reorganisation energy due to the rotation and vibration of the particles in the solution, and E_0 is the most probable electron level of hydrated particles. The donor level of the reduced species fluctuates around its most probable level, E_{Red}, and the acceptor energy of the oxidised species fluctuates around the most probable level, E_{Ox}. The total probability density of the donor and acceptor levels, $Q_{RedOx}(E)$, is

$$Q_{RedOx}(E)=Q_{Red}(E)+Q_{Ox}(E) \tag{5.38}$$

where $Q_{Red}(E)$ and $Q_{Ox}(E)$ are the probability densities of the donor level in the reduced and the acceptor level in the oxidised, respectively. So the electron state densities $D_{Red}(E)$ and $D_{Ox}(E)$ in the donor and acceptor bands of hydrated redox species are given by

$$D_{Red}(E)=Q_{Red}(E)C_{Red} = C_{Red}Q_0 \exp(-(E-E_{Red})^2/Q_0^2) \tag{5.39}$$

$$D_{Ox}(E)=Q_{Ox}(E)C_{Ox} = C_{Ox}Q_0 \exp(-(E-E_{Ox})^2/Q_0^2) \tag{5.40}$$

where C_{Red} and C_{Ox} are the concentrations of the reduced and the oxidised in the solution, respectively. The total state density $D_{RedOx}(E)$ is the sum of $D_{Red}(E)$ and $D_{Ox}(E)$, This can be expressed as

$$D_{RedOx}(E)=D_{Red}(E)+D_{Ox}(E)= Q_{Red}(E)C_{Red}+Q_{Ox}(E)C_{Ox} \tag{5.41}$$

Figure 5.17 shows the state density distribution for two different ratios of the concentrations of the redox couple i) $C_{Red} = C_{Ox}$, and ii) $C_{Red} > C_{Ox}$.

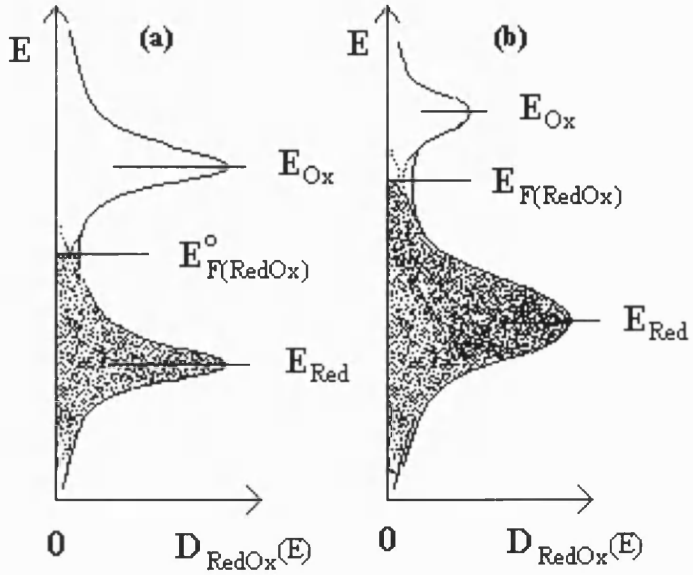

Figure 5.17 The electron state density of the redox couple in solution. $E^{o}_{F(RedOx)}$ is the standard Fermi level of the redox electron, $E_{F(RedOx)}$ is the redox electron Fermi level. (a) $C_{Red} = C_{Ox}$ and (b) $C_{Red} > C_{Ox}$

In the fluctuation model, the reduced species forms a donor band and the oxidised species forms an acceptor band. When the donor state density equals the acceptor state density, the redox electron Fermi level, $E_{F(RedOx)}$, obtained from Eqns. 5.39 and 5.40 is given by

$$E_{F(RedOx)} = E^{o}_{F(RedOx)} + k_B T \ln \frac{C_{Red}}{C_{Ox}} \qquad (5.42)$$

Here $E^{o}_{F(RedOx)} = \frac{1}{2}(E_{Ox} + E_{Red})$ is called the standard Fermi level of the redox electron.

5.8.3 Electron Transfer Reactions between Semiconductor/Electrolyte Interface

As mentioned previously, electrons will flow across the interface between the semiconductor and electrolyte until their Fermi energies are equal. Now we can use the Fermi levels to describe the electron transfer processes across the interface. Gerischer [60-61] first developed the theory for semiconductor electrodes. There are two conditions to ensure that electron transfer takes place: first it can only occur at energies above the conduction band edge or below the valence band edge and secondly the electron levels of the redox couple must overlap appreciably with one of the semiconductor band. This is illustrated in figure 5.18.

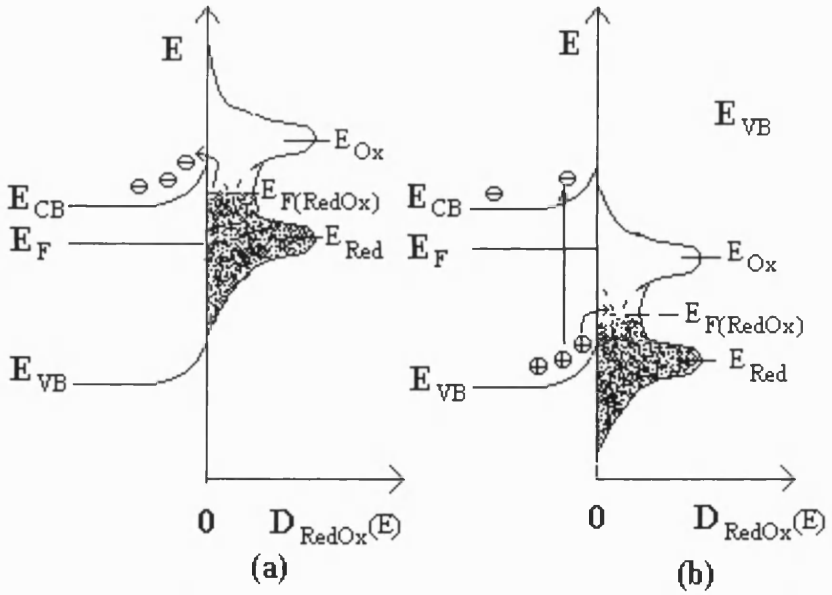

Figure 5.18 Energy band diagrams for an n-type semiconductor electrode in the solution with redox couple: (a) injection electrons into the conduction band of the semiconductor and (b) injection holes into the donor band of the redox couple.

Electron transfer can be driven by an external electric field or by photoexcitation. When surface states are present, the electron transfer processes can take place by tunnelling at energies within the bandgap.

5.9 Electrolyte Electroreflectance/Electroabsorbance Spectroscopy (EER/EEA)

Modulation spectroscopies are powerful techniques used for the characterisation of semiconductors, single crystals and polycrystalline thin films materials. The techniques are based on superimposing a small periodic perturbation on a constant value of some physical variable and then measuring the normalised change in the optical response of the material using a phase sensitive detector or a lock-in amplifier. The perturbations include electric field, heat pulse, stress and magnetic field. The corresponding techniques are called electroreflectance [62-64], thermoreflectance [65-67], piezoreflectance [68-70] and magnetoreflectance [71-74]. There is a large volume of work published on this topic [75-80]. Pollak et al [81] have recently provided an excellent and comprehensive review of modulation spectroscopy.

The normalised changes in the optical constant brought about by the perturbation are very small ($\sim 10^{-5}$). They can be derived theoretically from the optical properties of the solid. There are several obvious advantages of modulation spectroscopy. It suppresses background effects such as light source fluctuations and possible unintentional sample changes during measurements, and it yields lineshape optical spectra related directly to interband transitions. Modulation spectroscopy using a potential perturbation has played an important role in studies of properties of semiconductors and semiconductor alloys in the past decades. Discussions in this thesis will be limited to electroreflectance/absorbance and to the case where an electrolyte is used as a contact with semiconductors. This is electrolyte electroreflectance or electroabsorbance (EER/EEA) spectroscopy.

The origin of the modulated spectra lies in the correlation between optical absorption and the dielectric function.

A monochromatic flux of photons entering an absorbing material in a plane at x = 0 with intensity I_0 is reduced to I_t after penetrating to the plane at x = d, according to

$$\ln\frac{I_0}{I_t}=\alpha\cdot d \tag{5.43}$$

And,

$$\alpha=\frac{\omega}{n\cdot c}\cdot\varepsilon_2(\omega) \tag{5.44}$$

where α is the absorption coefficient of the medium, c is velocity of light in vacuum, ω is the frequency of monochromatic light, and ε_2 is the imaginary part of the complex dielectric function $\varepsilon(\omega)$, which is expressed as

$$\varepsilon(\omega)=\varepsilon_1(\omega)+i\cdot\varepsilon_2(\omega) \tag{5.45}$$

and describes the optical properties of the medium at all photon energies $E = h\omega/2\pi$. The optical constants n and k can be used to express the dielectric function

$$\varepsilon_1^2(\omega)=n^2-k^2;\quad \varepsilon_2(\omega)=2nk \tag{5.46}$$

Since the definition of the absorption coefficient excludes all reflection and scattering losses, absorption measurements are the most direct way to determine $\varepsilon_2(\omega)$. Consequently, the effect of the perturbation on the properties must appear as a change in the real and imaginary parts of the dielectric function. For simplicity, a cubic symmetric lattice semiconductor is considered. So $\varepsilon(\omega)$ is a scalar. The Fresnel equation expresses the reflectance at normal incidence in terms of ε_1 and ε_2 as:

$$R=\left|\frac{n-n_a}{n+n_a}\right|^2,\ n^2=\varepsilon,\ and\ n_a^{\ 2}=\varepsilon_a \tag{5.47}$$

where the subscript a means the real part of the parameter. Perturbation induced changes ΔR or ΔT in the reflectance R or transmittance T of a medium produce a change in the intensity reflected or transmitted by the medium, so that

$$\Delta I/I = \Delta R/R \text{ or } \Delta T/T \tag{5.48}$$

Further

$$\frac{\Delta R}{R} = \mathrm{Re}\left[\frac{2n_a}{n(\varepsilon - \varepsilon_a)}\Delta\varepsilon\right] = \mathrm{Re}\left[(\alpha - i\beta)\Delta\varepsilon\right] = \alpha\Delta\varepsilon_1 + \beta\Delta\varepsilon_2 \tag{5.49}$$

where $\Delta\varepsilon = \Delta\varepsilon_1 + \Delta\varepsilon_2$ is the perturbation-induced change in ε, and α and β are the Seraphin coefficients [82]. In general, α and β are non-zero quantities but near the bandgap of the solid, $\beta \approx 0$. According to the type of external modulation used, modulation spectroscopy can be classified two categories. The first case is where the

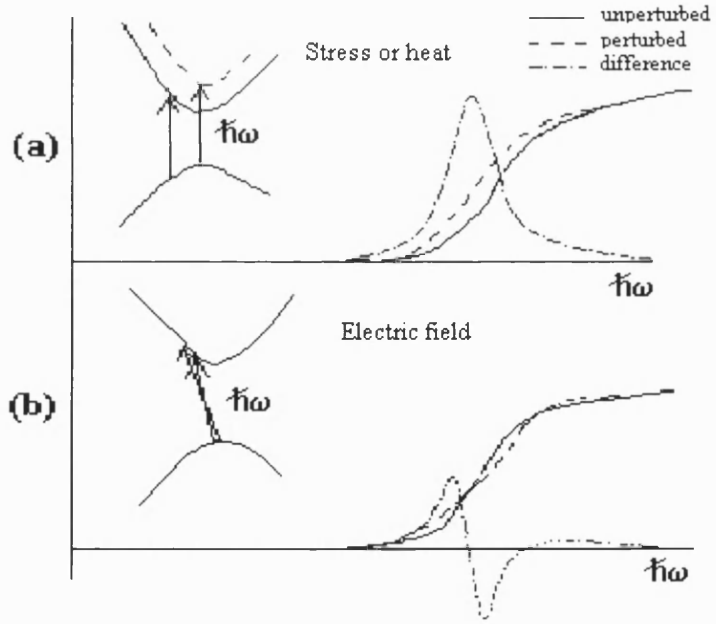

Figure 5.19 A schematic diagram showing the effects of changes on the imaginary dielectric constant, ε_2, for different types of modulation: (a) piezo- or thermomodulation and (b) electromodulation. The effect of the perturbation on the energy band structure and optical transition is also shown at the left side in each case.

Perturbation does not destroy the translation symmetry of the lattice and electrons are not accelerated under the field. Examples of this case are thermo- and piezomodulation. The second case is where the translation symmetry of the material is removed by the perturbation, and charge carriers are accelerated. In this case the lineshape is the third derivative of the unperturbed dielectric function. These cases are depicted in figure 5.19.

The existence of the strong electric field in the dipole layer adjacent to a semiconductor/electrolyte interface was first exploited in electro-optical work by Williams [83]. Shaklee adapted the configuration to electroreflectance [84], and Aspnes and Cardona [85] changed that configuration slightly by using the normalisation to avoid a drift of the point of operation. The potential distribution in the interface has been discussed early this chapter. The Helmholtz layer is less 10 nm thick, and the width of the space charge region is less 100 nm, so that either external potential differences of a few volts can cause large changes in field strength and reflectance. This technique is called EER or EEA, and it requires a modulated electric field that leads to the changes on the imaginary dielectric constant, ε_2 and yields a derivative spectrum. Normally EER/EEA belongs to the low field modulation limit [75] where a third-derivative spectrum is produced. The spectrum can be fitted by the generalised lineshape function introduced by Aspnes [75]

$$\frac{\Delta R}{R} = \mathrm{Re}\left[Ce^{i\theta}(E - E_g + i\Gamma)^{-n}\right] \tag{5.50}$$

Here C and θ are amplitude and phase factors that vary slowly with E, and $n \geq 2$. The amplitude and phase factors determine the amplitude and asymmetry of the lineshape, respectively, and the bandgap, Eg, and broadening parameter, Γ, determine the energy location and width of the structure. n is the lineshape factor. For simple parabolic

critical points model: n = 3 for two-dimensional critical points, n=5/2 for three-dimensional critical points, n=2 for excitonic critical points. Those parameters can be obtained directly by fitting the experimental lineshape to Eqn. 5.50 or by using a third derivative fitting function, sometimes called the three-point fitting method developed by Aspnes et al [86]. This fitting is based on three points – baseline zero ($\Delta R/R=0$), the lower energy extremum A, with a point ($\Delta R/R$, E_A), and the higher energy extremum B, with another point ($\Delta R/R$, E_B). One variable, ρ, called the asymmetry parameter, is defined as

$$\rho = -(\Delta R/R_B)/(\Delta R/R_A) > 0 \tag{5.51}$$

Then the bandgap, E_g, and broadening parameter, Γ are given by

$$E_g = E_A + (E_B - E_A) f(\rho) \tag{5.52}$$

$$\Gamma = (E_B - E_A) g(\rho) \tag{5.53}$$

The function $f(\rho)$ and $g(\rho)$ are shown in figure 5.20. Note that E_g is nearly independent of n, although the value of Γ depends ±20% on the model assumed for the critical point.

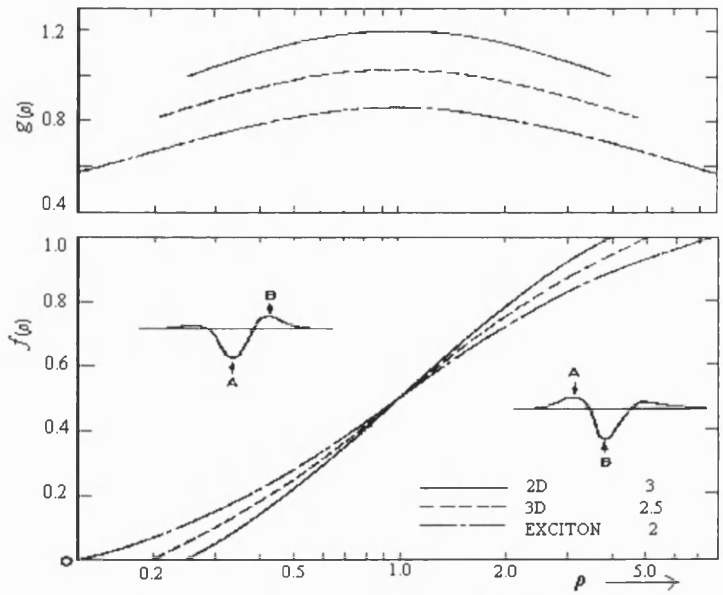

Figure 5.20 The function $f(\rho)$ and $g(\rho)$ for the critical point lineshape fitting (taken from ref. [86])

In general, this third derivative fitting function is found to fit experimental spectra very well. However, there are number of problems in applying that theory if, for example, the lineshape depends on the applied dc bias [87-89], or if the spectra are inverted [90]. These effects may arise from excitonic broadening [91-92] and field inhomogeneities [93-94].

5.10 Electrodeposition

Electrodeposition plays a very important role on the preparation of the II-VI compounds for solar applications. It offers a low-cost and large-area route to deposit thin-film devices. It has been used extensively to deposit those semiconductors like CdSe [95], CdS [96-98], CdTe [99-102] and $CuInSe_2$ [103-106] that have been used for solar cells for a few decades.

As mentioned in Chapter 4, electrodeposition can be classified into cathodic and anodic processes. But cathodic processes are more popular in use due to the convenience. Our discussion will be limited to cathodic deposition processes of CdTe onto CdS substrates here.

5.10.1 Deposition Mechanism and Deposition Conditions

There are a few steps involved in the electrodeposition of CdTe [107]. There is a soluble equilibrium reaction for TeO_2 in the acidic solution.

$$TeO_2(s) + H^+ \rightleftharpoons HTeO_2^+ \tag{5.54}$$

The first step is the four electron reduction of $HTeO_2^+$ to Te at a site s,

$$HTeO_2^+ + 3H^+ + 4e^- \rightarrow Te,s + 2H_2O \tag{5.55}$$

Then Cd^{2+} is reduced Cd at the Te site

$$Cd^{2+} + Te,s + 2e^- \rightarrow CdTe \tag{5.56}$$

The above total reaction can be written as

$$3H^+ + Cd^{2+} + HTeO_2^+ + 6e^- = CdTe + 2H_2O \qquad (5.57)$$

There are five major deposition parameters: i) the concentration of TeO_2; ii) the concentration of Cd^{2+} ion; iii) the solution pH; iv) the deposition potential or deposition current density; v) the temperature of the deposition solution. The TeO_2 concentration is limited by its solubility which is related to the solution pH [108]. Low pH will give a higher concentration of TeO_2 in solution. But a low pH will dissolve the CdS substrates, so a commonly used pH is ~1.4. The concentration of Cd^2 ion must be very high, at least a few hundred times higher than that of TeO_2 [109]. The rate of electrodeposition is therefore controlled by diffusion of the $HTeO_2^+$ to the electrode surface. The deposition potential, a key factor to control the deposit composition, is a few tens mV positive of the Cd reference electrode [110]. The best deposition temperature is ~85°C [109]. It takes about 3 hours to deposit a 2 μm thick film in stirred solution.

5.10.2 Fast Deposition Under a Channel Cell

Since the low concentration of $HTeO_2^+$ limits the deposition rate of CdTe, it also limits the speed with which thin-film devices can be prepared. Rapid deposition would be desirable for large area solar cell applications. There are two ways to achieve fast electrodeposition. One is to use the rotating disc electrode (RDE), but the method is not suitable for the preparation of the substrates for solar cells. The other is to use a channel flow cell to control the rate of mass transport of $HTeO_2^+$ and to achieve a substantial reduction of the deposition time.

The well-defined channel electrode has been developed by Compton [111], and it has been widely used to study electron transfer reactions [112-113] and coupled chemical reactions [114-115]. In the present case, the deposition current density, j_L, in mA/cm^{-2} in the channel cell [111] can be expressed as:

$$j_L = 92.5nFC\left(\frac{v_f D^2}{h^2 x_e d}\right)^{1/3} \qquad (5.58)$$

Here n is the number of electrons transferred in the reaction 5.57, (n = 6), F is the Faraday constant, v_f is the volume flow rate ($cm^3\ s^{-1}$), C is the bulk concentration of the $HTeO_2^+$ (mol cm^{-3}), D is the diffusion coefficient of $HTeO_2^+$ ($cm^2\ s^{-1}$), h is the half height of the channel (cm), d (cm) is the channel width and x_e is the length of the electrode (cm). Further details are in part I of this thesis.

Figure 5.21 illustrates the calculated dependence of j_L on volume flow rate and the corresponding deposition time for a 2 micron CdTe film. It should clearly be possible to reduce the deposition time to 25 minutes at a volume flow rate of 10 $cm^3\ s^{-1}$. The calculated conditions are: C = 5.0×10^{-4} mol dm^{-3}, $D_{HTeO_2^+} = 1.13 \times 10^{-5}$ $cm^2 s^{-1}$ at 85°C [107], h = 0.07 cm, x_e = 1.0 cm and d = 1.0 cm.

In theory, the technique will give a smooth and uniform CdTe film when the counter electrode with a large area is placed on the opposite side of the substrates in parallel. Details are discussed in the next chapter.

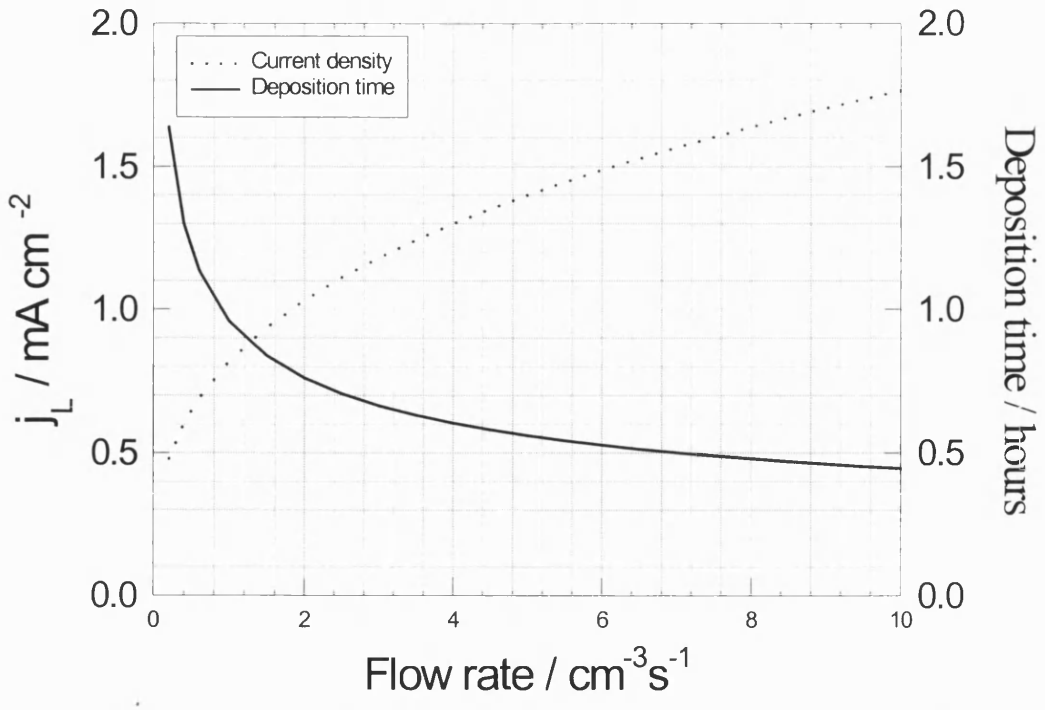

Figure 5.21 Limiting current density and time required to grow a 2μm CdTe film in the channel flow cell. Calculated from Eqn. 5.58 for h=0.07cm, $D_{HTeO_2^+} = 1.13\times10^{-5}$ at 85°C.

5.11 Absorption of Light

This is an essential process of absorption of light for photovoltaic cells. The semiconductors can be divided into two types in accordance with the absorption manner of light. They are direct-band-gap and indirect-band-gap. The II-IV semiconductors like CdS, CdTe are direct-band-gap materials, while silicon is an indirect-band-gap material. Absorption coefficients are very high for the direct process, typically 10^5 cm^{-1}, and low for the indirect process, typically 10^3 cm^{-3} [116]. The energy-momentum plot for a direct-band-gap semiconductor is shown in figure 5.22a. The form of the absorption process for an indirect material is depicted in figure 5.22b. It can be seen that transitions can occur at lower energies involving a phonon.

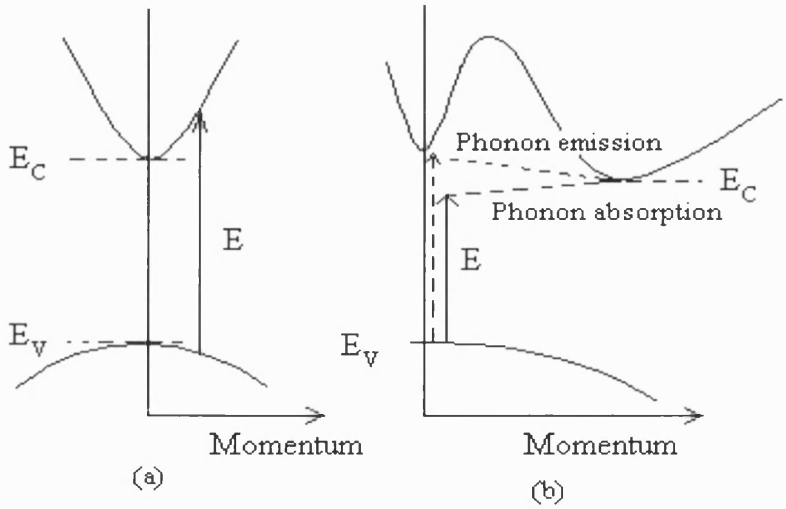

Figure 5.22 Energy-momentum diagrams for absorption processes

(a) a direct process (b) an indirect absorption process

There is a relationship between the absorption coefficient, α(E), and the photon energy, E, for a direct absorption process [117] and can be expressed as

$$\alpha(E) = A(E - Eg)^{1/2} \tag{5.59}$$

Also there is an expression for an indirect absorption process, and one has

$$\alpha(E) = B(E - Eg)^{2} \tag{5.60}$$

where A and B are constant. The band gap of the semiconductor is determined by a plot of the absorption coefficient against the photon energy from equation 5.59 or 5.60 that depends on which semiconductor material is used.

5.12 Photocurrent Spectroscopy

5.12.1 Background and Theories

Illumination of a semiconductor gives rise to the electron-hole pairs. When the circuit is under the short circuit conditions, photocurrent flows in an external circuit. While the circuit is open, a photovoltage develops is across the junction. The earliest

studies theoretically on the photocurrent produced under illumination is by Gärtner [118] in 1959 for the Schottky junction (metal/semiconductor). The theory, which is termed as the Gärtner theory described the flux of minority carriers, *J*, in the space charge region is given by

$$J = I_0(1 - \frac{\exp(-\alpha W)}{1 + \alpha L}) \qquad (5.61)$$

where I_0 is the incident intensity, W is the width of the space charge region, L is the minority carrier diffusion length and is given by $L=(D\tau)^{1/2}$. They can be seen in figure 5.23.

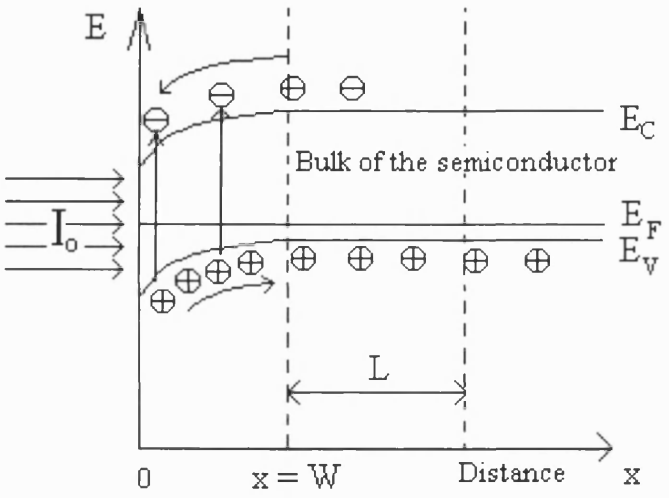

Figure 5.23 Schematic diagram for a p-type semiconductor under illumination

Equation 5.61 can be rewritten as

$$IPCE = \frac{J}{I_0} = (1 - \frac{\exp(-\alpha W)}{1 + \alpha L}) \qquad (5.62)$$

Here IPEC is the Incident-Photon-to-Current-Efficiency, also termed photocurrent conversion efficiency, Φ.

Figure 5.24 shows calculated photocurrent spectra of p-type CdTe. The absorption coefficients were taken from literature [126]. Figure 5.24a shows a variety

of the minority carrier diffusion length while figure 5.24b shows a change of the width of the space charge region.

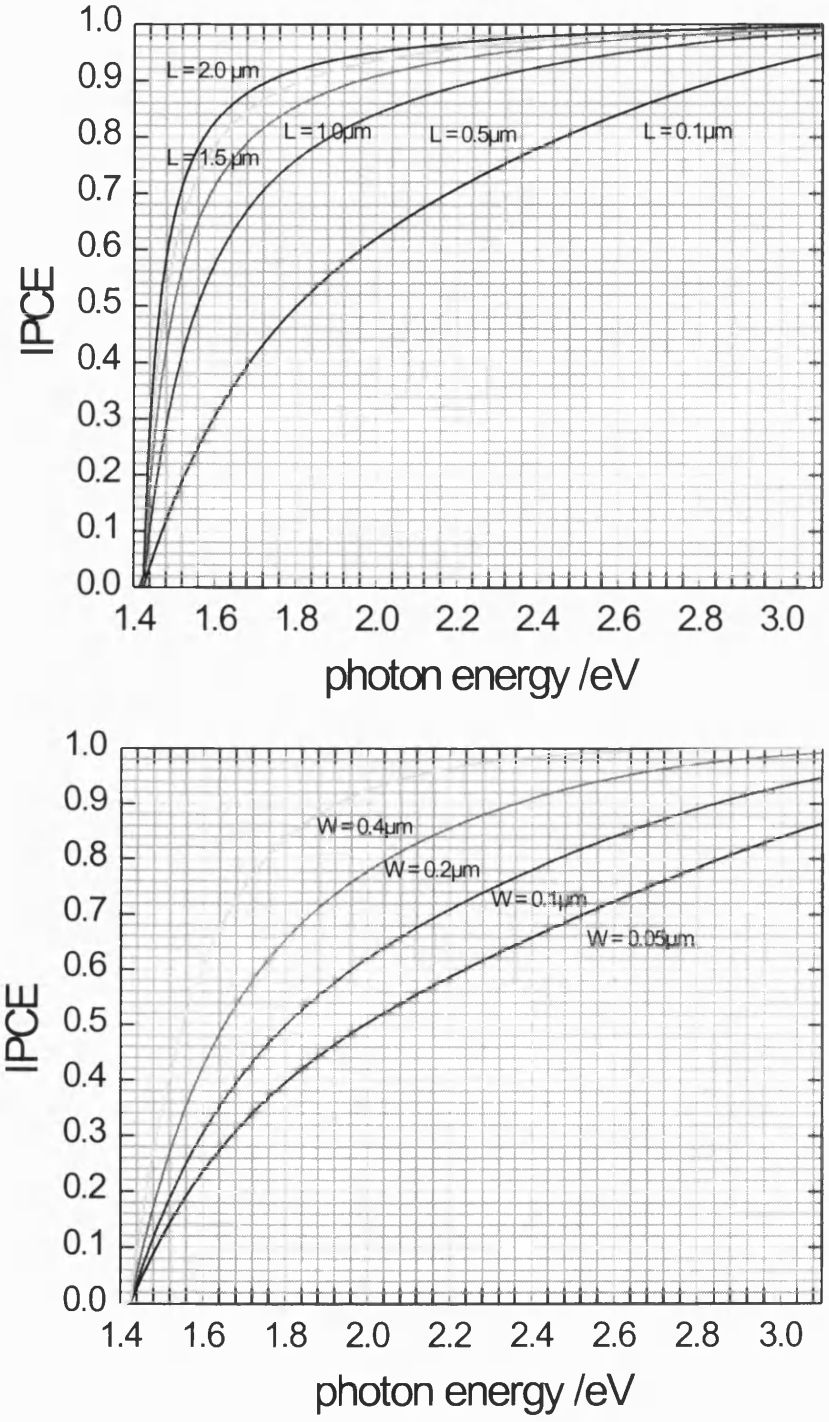

Figure 5.24 IPCE spectra of p–type CdTe calculated from equation 5.62

(a) W = 0.1μm (b) L= 0.1μm

Butler [119] extended equation 5.62 to the semiconductor/electrolyte junction. This equation is valid under the following assumptions: 1) no losses of minority carriers within the space charge region; 2) surface recombination rate is zero; 3) recombination rate at the back contact is infinity due to ohmic contact; 4) one-dimensional diffusion for carriers. This equation has been subsequently improved by Reichman [120-121], El Guibaly et al [122-123] and by Albery et al [124]. The recombination within the space charge region had been taken into account in their consideration. Those considerations lead to Quasi-equilibrium theories of space-charge recombination and the Albery theory. Details for those theories are reviewed by Peter [125].

In general, if the film or crystal is thick, its thickness, d, is greater than all other characteristic lengths like W and L. Equation 5.62 can be directly used to obtain information about the width of the space charge region and the minority carrier length (normally combining with other methods like the capacity measurements). However, if the thickness of the film or crystal is less than the space charge layer, there is no contribution from diffusion and so equation 5.62 becomes

$$IPCE = 1-\exp(-\alpha d) \tag{5.63}$$

The earlier measurements of photocurrent were also used to obtain value of the flat-band potential [119-120]. This is based on the assumptions: $\alpha W \ll 1$ and $aL \ll \alpha W$. So equation 5.61 becomes

$$J = I_0\left(\frac{\alpha(L+W)}{1+\alpha L}\right) \tag{5.64}$$

further

$$J = I_0 \alpha W \tag{5.65}$$

Combining with equations 5.31 and 5.33, one has

$$J = I_0 \alpha \left(\frac{2\varepsilon\varepsilon_0}{qN} (V - V_{fb} - kT/q) \right)^{1/2} \tag{5.66}$$

So the intercept in a plot of photocurrent against potential is the flatband potential. Unfortunately this case, aL <<αW, hardly exists in fact [127]. By contrast, equation 5.64 is more useful, since the intercept and slope can be used to calculate W and L for n-type semiconductor as shown by Etcheberry et al [128]. Note that reflection loss is not considered in the above equations and must be taken into account for the practical uses. Although many researchers [129-130] have made efforts to obtain characteristic parameters such as W and L from the photocurrent spectroscopy, less detailed quantitative research work has published. An effort is made in this thesis to develop models appropriate for thin film system.

5.12.2 A Model for Two-Side Illumination

With applications of thin-film solar cells, there is a new demand for fast non-destructive technology to check the properties of thin films. Of those properties, the width of the space charge region and the diffusion length of the minority carrier are very important parameters. Both of them will determine the performance of a solar cell to a certain extent. Normally several methods are combined to obtain these parameters. This makes it difficult to eliminate errors due to different measuring conditions and methods, and also it takes a long time to perform all the necessary measurements. A model for two-side illumination is proposed in this thesis when an electrolyte is used for a contact rather than a metal.

Consider an n-type semiconductor deposited on conducting glass and then insert into a concentrated solution. Incident light can irradiate both sides of the

semiconductor and lead to photocurrent when the circuit is reverse-biased. Assume that the contact at the conducting glass side is ohmic, no recombination occurs within the space charge region, while recombination takes place at the surface of the semiconductor with the first-order rate constant, k_r. One dimensional diffusion for charged carriers is considered. The losses due to reflection and absorption of the conducting glass are ignored for simplicity. The processes are shown in figure 5.25.

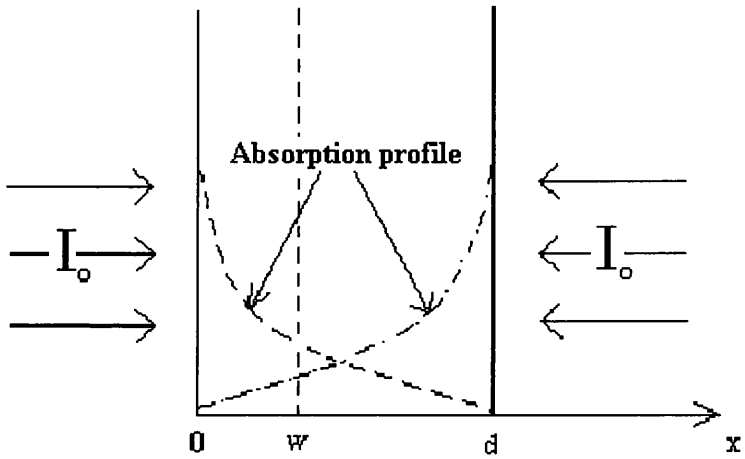

Figure 5.25 Schematic diagram of an n-type semiconductor under double side Illumination and an electrolyte as a contact. The thickness of the film is d. I_0 is the total incident photon flux.

5.12.2.1 Illumination from the Junction Side of the Semiconductor

The continuity equation for minority carriers (holes here) under illumination is given by

$$\frac{d\rho}{dt} + \frac{d}{dx} j_{photo} = G(x) - \frac{qp}{\tau} \qquad (5.67)$$

where ρ is the minority charge carrier density, ρ =qp, p is the time- and space-dependent density of holes. $G(x) = q\alpha I_0 \exp(-\alpha x)$ is the rate of generation, τ is the hole lifetime, j_{photo} is the current density and is sum of the diffusion and drift current

densities, but the drift current density out side of the space charge region is negligible [131]. One has

$$j_{photo} = -qD_p \frac{dp}{dx} \tag{5.68}$$

So equation 5.67 becomes

$$p\frac{dp}{dt} - pD_p \frac{d^2p}{dx^2} = q\alpha I_o \exp(-\alpha x) - \frac{qp}{\tau} \tag{5.69}$$

Rearranging equation 5.69 gives

$$\frac{dp}{dt} = D_p \frac{d^2p}{dx^2} - \frac{p}{\tau} + \alpha I_o \exp(-\alpha x) \tag{5.70}$$

Under steady state conditions,

$$\frac{dp}{dt} = D_p \frac{d^2p}{dx^2} - \frac{p}{\tau} + \alpha I_o \exp(-\alpha x) = 0 \tag{5.71}$$

Defining

$$L^2 = D_p \tau \tag{5.72}$$

$$y = x/L \tag{5.73}$$

and substituting equations 5.72 and 5.73 into equation 5.71 and rearranging gives

$$\frac{d^2p}{dy^2} - p + a\exp(-\alpha L y) = 0 \tag{5.74}$$

Here

$$a = \frac{\alpha I_o L^2}{D_p} \tag{5.75}$$

The general solution for equation 5.74 is given by

$$p = A\cosh y + B\sinh y + C\exp(-\alpha L y) \tag{5.76}$$

Here

$$C = \frac{a}{1-(\alpha L)^2} = \frac{\alpha I_o L^2}{D_p\left(1-(\alpha L)^2\right)} \tag{5.77}$$

where A and B are integral constants.

The boundary conditions are

$$p(y = W/L) = 0 \tag{5.78}$$

$$j_{photo} = -qD_p \frac{dp}{Ldy}\Big|_{y=d/L} = qk_r p \tag{5.79}$$

So a set of equations is obtained by substituting equations 5.78 and 5.79 into 5.76

$$A\cosh\frac{W}{L} + B\sinh\frac{W}{L} = -C\exp(-\alpha W) \tag{5.80}$$

$$A(k_r\cosh\frac{d}{L} + \frac{D_p}{L}\sinh\frac{d}{L}) + B(k_r\sinh\frac{d}{L} + \frac{D_p}{L}\cosh\frac{d}{L}) = C(D_p\alpha - k_r)\exp(-\alpha d) \tag{5.81}$$

Hence A and B can be obtained as

$$A = -\frac{Ce^{-\alpha W}\left(k_r\sinh\frac{d}{L} + \frac{D_p}{L}\cosh\frac{d}{L}\right) + Ce^{-\alpha d}\left(\alpha D_p - k_r\right)\sinh\frac{W}{L}}{k_r\sinh\frac{d-W}{L} + \frac{D_p}{L}\cosh\frac{d-W}{L}} \tag{5.82}$$

$$B = \frac{Ce^{-\alpha W}\left(k_r\cosh\frac{d}{L} + \frac{D_p}{L}\sinh\frac{d}{L}\right) + Ce^{-\alpha d}\left(\alpha D_p - k_r\right)\cosh\frac{W}{L}}{k_r\sinh\frac{d-W}{L} + \frac{D_p}{L}\cosh\frac{d-W}{L}} \tag{5.83}$$

Now finally the solution for equation 5.67 under those boundary conditions is

$$p(x) = C\frac{e^{-\alpha d}\left(\alpha D_p - k_r\right)\sinh\frac{x-W}{L} - e^{-\alpha W}\left(k_r\sinh\frac{d-x}{L} + \frac{D_p}{L}\cosh\frac{d-x}{L}\right)}{k_r\sinh\frac{d-W}{L} + \frac{D_p}{L}\cosh\frac{d-W}{L}} + Ce^{-\alpha x} \tag{5.84}$$

The total current density through the reverse-biased depletion layer is given by

$$j_{Total} = j_W + j_{diff}\big|_{x=W} \tag{5.85}$$

where j_W is the drift current density due to carriers generated inside the depletion layer, and j_{diff} is the diffusion current density of minority carriers generated outside

the space charge region in the bulk of the semiconductor that are collected at the space charge region.

$$j_W = -\int_0^W g(x)dx = -\int_0^W q\alpha I_o e^{-\alpha x}dx = qI_o(1-e^{-\alpha W}) \tag{5.86}$$

where the minus means that photogenerated electrons drift to the space charge surface (x=W).

$$j_{diff|x=W} = -qD_p \frac{dp(x)}{dx}\Big|_{x=W}$$
$$= \frac{qD_pC}{L}\left(\frac{e^{-\alpha d}\left(\alpha D_p - k_r\right) + e^{-\alpha W}\left(k_r \cosh\frac{d-W}{L} + \frac{D_p}{L}\sinh\frac{d-W}{L}\right)}{k_r \sinh\frac{d-W}{L} + \frac{D_p}{L}\cosh\frac{d-W}{L}} - \alpha L e^{-\alpha W}\right) \tag{5.87}$$

Substituting equations 5.86 and 5.87 into 5.85, and rearranging gives

$$j_{total} = qI_o\left(1 - \frac{1}{1-(\alpha L)^2}\left(e^{-\alpha W} - \frac{\alpha L\left(e^{-\alpha d}\left(\alpha D_p - k_r\right) + e^{-\alpha W}\left(k_r \cosh\frac{d-W}{L} + \frac{D_p}{L}\sinh\frac{d-W}{L}\right)\right)}{k_r \sinh\frac{d-W}{L} + \frac{D_p}{L}\cosh\frac{d-W}{L}}\right)\right) \tag{5.88}$$

$$IPCE = 1 - \frac{e^{-\alpha W}}{1-(\alpha L)^2} + \frac{\alpha L}{1-(\alpha L)^2}\frac{e^{-\alpha d}\left(\alpha D_p - k_r\right) + e^{-\alpha W}\left(k_r \cosh\frac{d-W}{L} + \frac{D_p}{L}\sinh\frac{d-W}{L}\right)}{k_r \sinh\frac{d-W}{L} + \frac{D_p}{L}\cosh\frac{d-W}{L}} \tag{5.89}$$

5.12.2.2 Illumination from the Substrate Side of the Semiconductor

Equation 5.70 is still valid to describe the problem shown in figure 5.25 if the coordinate system is redefined by shifting the coordinate axis.

$$x' = d - x \tag{5.90}$$

so equation 5.70 becomes

$$\frac{dp}{dt} = D_p \frac{d^2p}{dx'^2} - \frac{p}{\tau} + \alpha I_o \exp(-\alpha(d-x')) \tag{5.91}$$

For $x' = x$, equation 5.91 becomes

$$\frac{dp}{dt} = D_p \frac{d^2 p}{dx^2} - \frac{p}{\tau} + \alpha I_o \exp(-\alpha(d-x)) \tag{5.92}$$

For steady state conditions, using definitions 5.72 and 5.73,

$$\frac{d^2 p}{dy^2} - p + a\exp(-\alpha(d - Ly)) = 0 \tag{5.93}$$

Here a is the same as equation 5.75. The general solution is

$$p = A'\cosh y + B'\sinh y + C\exp(-\alpha(d - Ly)) \tag{5.94}$$

where A′, B′ and C are integration constants, C is the same as in equation 5.77.

The boundary conditions are the same as equations 5.78 and 5.79 for equation 5.94. The method used above is repeated here, and the solution is given by

$$p(x) = C\left(e^{-\alpha(d-x)} - \frac{(\alpha D_p + k_r)\sinh\frac{x-W}{L} + e^{-\alpha(d-W)}\left(k_r \sinh\frac{d-x}{L} + \frac{D_p}{L}\cosh\frac{d-x}{L}\right)}{k_r \sinh\frac{d-W}{L} + \frac{D_p}{L}\cosh\frac{d-W}{L}} \right) \tag{5.95}$$

In the same manner as used above, the IPCE is obtained:

$$IPCE = \left(\frac{e^{\alpha W}}{1-(\alpha L)^2} - 1\right)e^{-\alpha d} + \frac{\alpha L}{1-(\alpha L)^2}\frac{e^{-\alpha(d-W)}\left(k_r \cosh\frac{d-W}{L} + \frac{D_p}{L}\sinh\frac{d-W}{L}\right) - (\alpha D_p + k_r)}{k_r \sinh\frac{d-W}{L} + \frac{D_p}{L}\cosh\frac{d-W}{L}} \tag{5.96}$$

It is important to note that when the thickness of the semiconductor tends to infinity, equation 5.89 returns to the Gärtner equation 5.62 and equation 5.96 approaches to zero as expected. The reason is that all light is absorbed within a few micrometers and the photogenerated carriers can not diffuse to the space charge region to be collected.

Now two important deductions can be easily obtained by taking a limit to equations 5.89 and 5.96. They are as follows:

1) $k_r \rightarrow \infty$ that means p(x=d) = 0, so that the equations for illumination from the junction side of the semiconductor become

$$p(x) = C\left(e^{-\alpha x} + \frac{e^{-\alpha d}\sinh\frac{W-x}{L} + e^{-\alpha W}\sinh\frac{x-d}{L}}{\sinh\frac{d-W}{L}}\right) \tag{5.97}$$

$$IPCE = 1 - \frac{e^{-\alpha W}}{1-(\alpha L)^2} + \frac{\alpha L}{1-(\alpha L)^2}\frac{e^{-\alpha W}\cosh\frac{d-W}{L} - e^{-\alpha d}}{\sinh\frac{d-W}{L}} \tag{5.98}$$

Equations for illumination from the substrate side are

$$p(x) = C\left(e^{-\alpha(d-x)} + \frac{\sinh\frac{W-x}{L} - e^{-\alpha(d-W)}\sinh\frac{d-x}{L}}{\sinh\frac{d-W}{L}}\right) \tag{5.99}$$

$$IPCE = \left(\frac{e^{\alpha W}}{1-(\alpha L)^2} - 1\right)e^{-\alpha d} + \frac{\alpha L}{1-(\alpha L)^2}\frac{e^{-\alpha(d-W)}\cosh\frac{d-W}{L} - 1}{\sinh\frac{d-W}{L}} \tag{5.100}$$

2) $k_r \rightarrow 0$, that means no recombination to occur at the surface. That is $j = -qD_p\left.\frac{dp}{dx}\right|_{x=d} = 0$. Hence those equations can be expressed as

a) Illumination from the junction side

$$p(x) = C\left(e^{-\alpha x} + \frac{\alpha L e^{-\alpha d}\sinh\frac{x-W}{L} - e^{-\alpha W}\cosh\frac{d-x}{L}}{\cosh\frac{d-W}{L}}\right) \tag{5.10}$$

$$IPCE = 1 - \frac{e^{-\alpha W}}{1-(\alpha L)^2} + \frac{\alpha L}{1-(\alpha L)^2}\frac{e^{-\alpha W}\sinh\frac{d-W}{L} + \alpha L e^{-\alpha d}}{\cosh\frac{d-W}{L}} \tag{5.102}$$

b) Illumination from the substrate side of the semiconductor

$$p(x) = C\left(e^{-\alpha(d-x)} + \frac{\alpha L\sinh\frac{W-x}{L} - e^{-\alpha(d-W)}\cosh\frac{d-x}{L}}{\cosh\frac{d-W}{L}}\right) \tag{5.103}$$

$$IPCE = \left(\frac{e^{-\alpha W}}{1-(\alpha L)^2} - 1\right) e^{-\alpha d} + \frac{\alpha L}{1-(\alpha L)^2} \frac{e^{-\alpha(d-W)} \sinh \frac{d-W}{L} - \alpha L}{\cosh \frac{d-W}{L}} \qquad (5.104)$$

Figures 5.26 and 5.27 show the hole density profiles against the distance for different rates of the recombination or diffusion lengths for p-type semiconductor under illumination conditions.

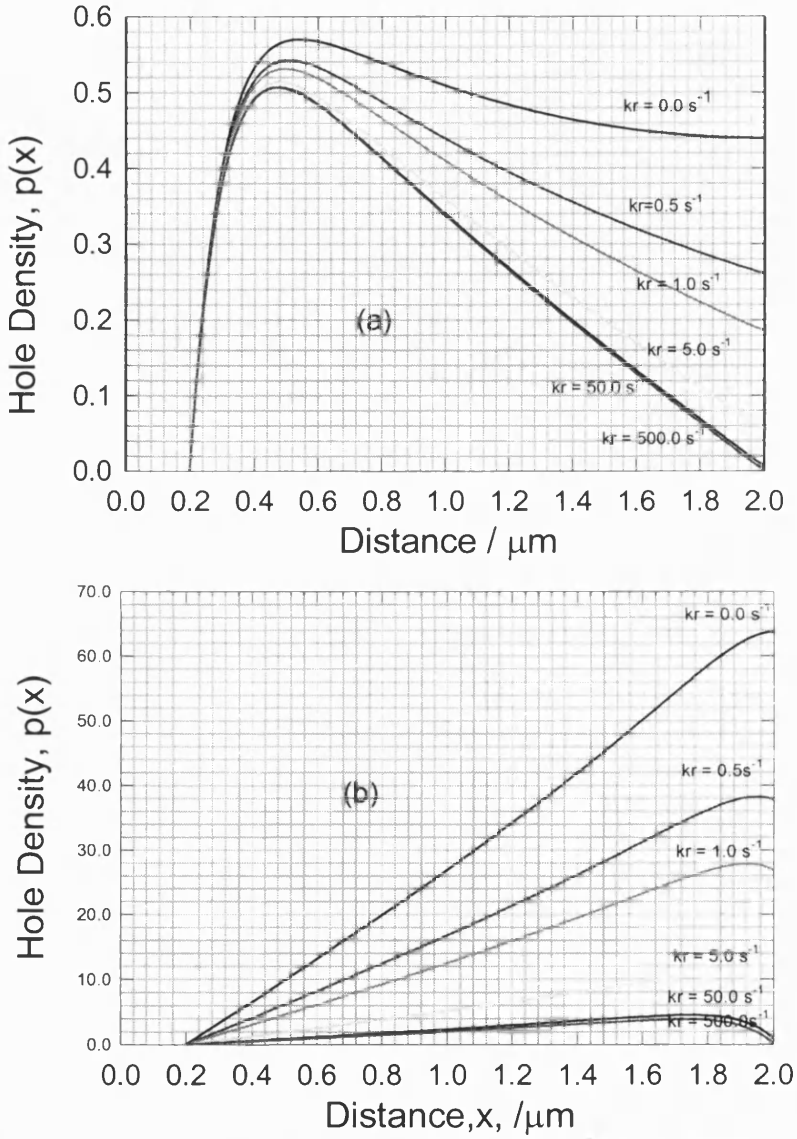

Figure 5.26 Calculated hole densities under illumination from both sides from equations 5.84 and 5.95 for different rates of the recombination. Calculation conditions are: I_o= 50 photons cm^{-2}, D=10^{-4} cm^2s^{-1}, L=1.8μm, d = 2.0μm, w = 0.2 μm, α=10^5 cm^{-1}. a) Illumination from the junction side b) Illumination from the substrate side

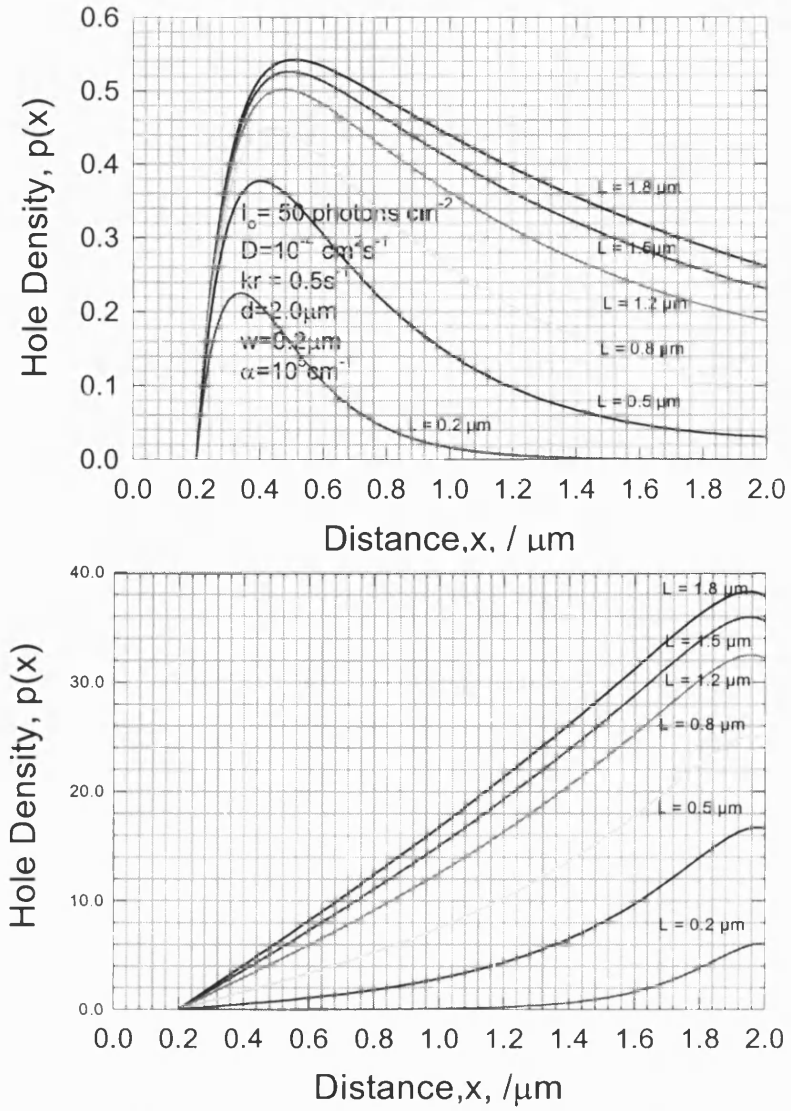

Figure 5.27 Calculation of the hole densities under illumination from both sides from equations 5.84 and 5.95 with different diffusion lengths. Calculation conditions are: I_o= 50 photons cm^{-2}, D=10^{-4} cm^2s^{-1}, *k*r=0.5 s^{-1}, d = 2.0μm, w = 0.2 μm, α=10^5 cm^{-1}.

a) Illumination from the junction side b) Illumination from the bulk side

It can be seen from figure 5.26 and 5.27 that the hole densities are higher near the space charge region when light is incident from the junction side, and are relatively low due to high absorption in the space charge region. So the drift currents predominate and a high IPCE is expected. On the other hand, the hole densities are lower close to the space charge region when the illumination is from the substrate side of the semiconductor, and the current is dominated by the diffusion of the holes and is

small, so that the IPCE is small as well. Figure 2.28 shows the effects of the diffusion coefficients on the hole densities. The bigger the diffusion coefficients, the lower the hole density near the space charge region.

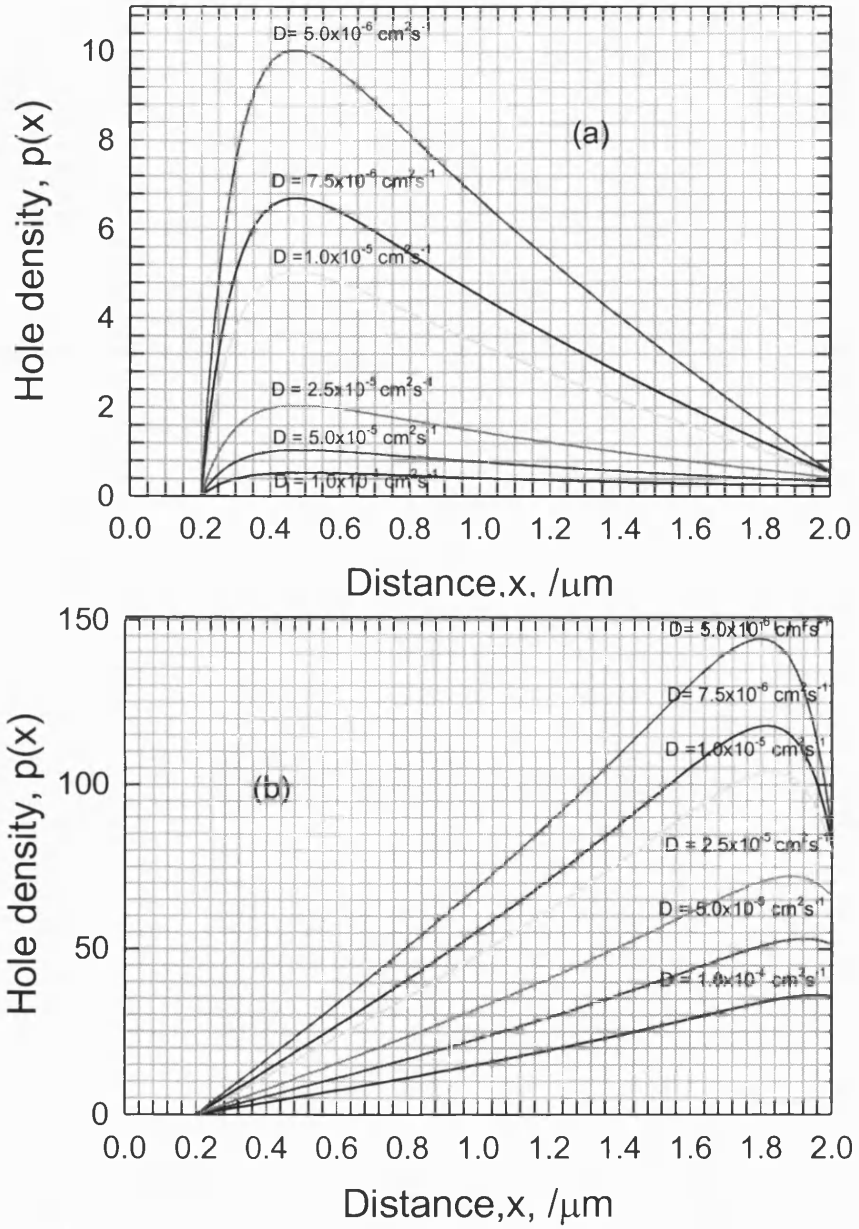

Figure 5.28 Calculated hole densities under illumination from both sides from equations 5.84 and 5.95 with different diffusion coefficients. Calculation conditions are: I_o= 50 photons cm^{-2}, L=1.5μm, *k*r = 0.5 s^{-1}, d = 2.0μm, w = 0.2 μm, $\alpha=10^5$ cm^{-1}.

a) Illumination from the junction side b) Illumination from the substrate side

Figure 5.29 shows the influence of the absorption coefficients on the hole densities under two-side illumination conditions. The absorption means that light can penetrate deeper into the semiconductor, and the electron-hole pairs can be generated and diffuse into the space charge region to be collected, which can be seen in the figure. Note that there is a maximum in the hole density under these conditions.

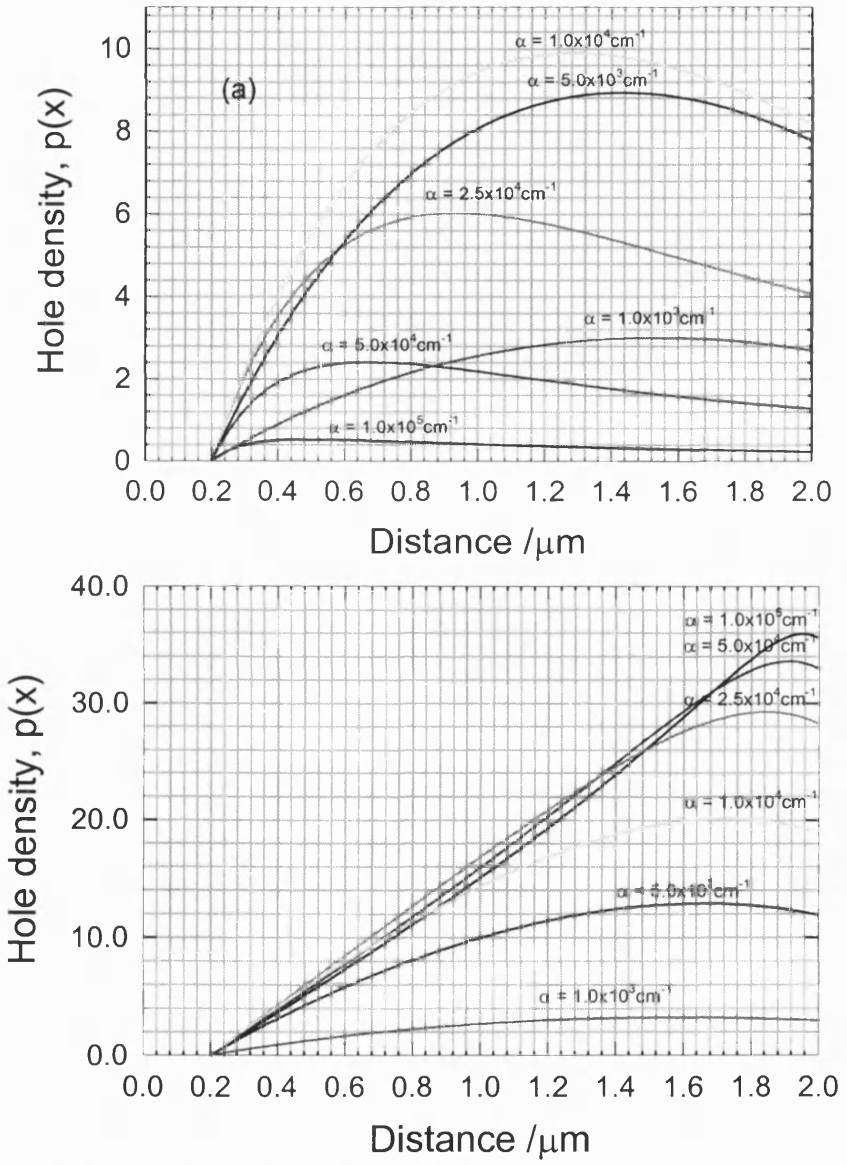

Figure 5.29 Calculated hole densities under illumination from both sides from equations 5.84 and 5.95 with various absorption coefficients. Calculation conditions are: I_o= 50 photons cm^{-2}, L=1.5μm, *k*r = 0.5 s^{-1}, d = 2.0μm, w = 0.2 μm, D=10^{-4} cm^2 s^{-1}. a) Illumination from the junction side b) Illumination from the bulk side

Figures 5.30 and 5.31 show the IPCE varies with the diffusion length and the width of the space charge region in a case in which the rate of the recombination is infinity, which often happens in reality due to surface damages or high doping. P-type CdTe is used as an example in figures 5.30 and 5.31. The absorption coefficients were taken from literature [126]. The reflection losses have been corrected. Increasing the diffusion length improves the IPCE for both illumination geometries in the lower energy region, which is clear to see in figure 5.30.

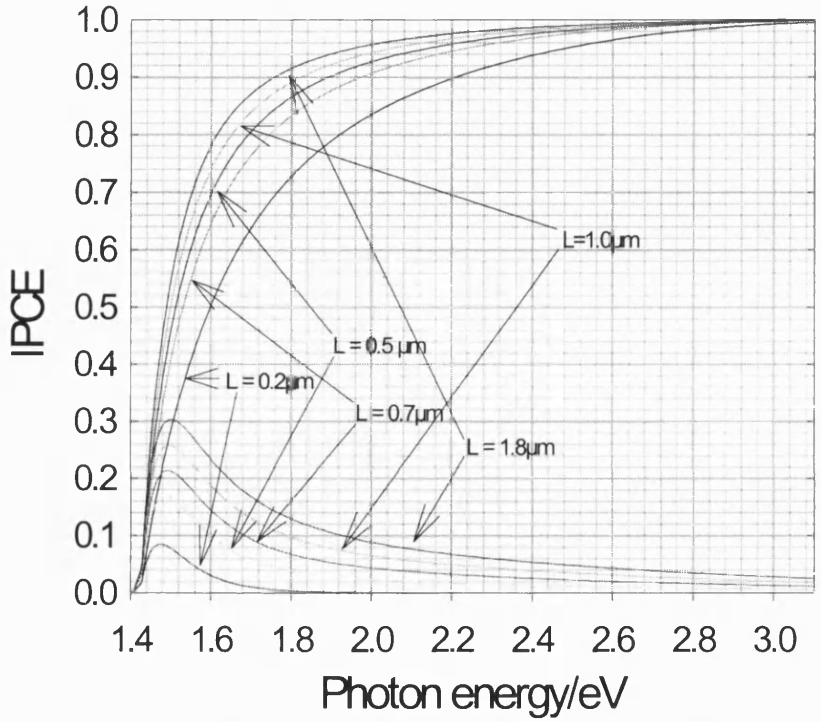

Figure 5.30 Calculated IPCE for p-type CdTe for both illumination geometries from equations 5.98 and 5.100 with various diffusion lengths. Calculation conditions are: d = 2.0μm, w = 0.2 μm.

Increasing the width of space charge region also improves the IPCE in both illumination geometries in the lower energy region, which is shown in figure 5.31. Both the diffusion length and width of the space charge region are characteristic

parameters for a semiconductor, which are determined by processes of the film growth and subsequent treatments.

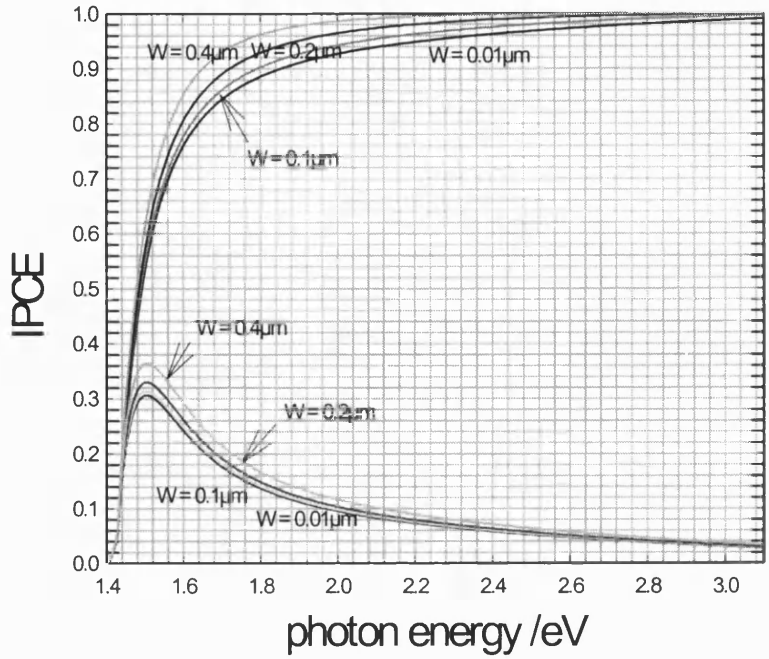

Figure 5.31 Calculation of the IPCE for p-type CdTe for both illumination geometries from equations 5.98 and 5.100 with a range of widths of the space charge region. Calculation conditions are: d = 2.0μm, L = 1.0 μm.

More details are discussed in the following chapters.

5.13 The Semiconductor p-n Junction

The most common solar cells in use are very large area p-n junction diodes. So it is essential to understand the properties of the p-n junction.

5.13.1 The p-n Junction in Equilibrium

If the two kinds of semiconductors are brought together, a p-n junction forms between the p- and n-type regions as shown in figure 5.32. Since the n-type has an excess of electrons relative to the p-type side, electrons transfer into the p-type to recombine with the holes in the p-type region. So a region in the n-type side near the

junction becomes deficient of free electrons. That means there is an excess of positively charged ionised donor particles ($n=N_D$) and a region of positive space charge is created in the n-type region near the junction. In the same manner, electrons diffusing from the n-type region into the p-type region create a region with negative charge ($p=N_A$) in the p-type region near the junction. These two regions combine together near the junction to the space charge region or the depletion layer due to electron-hole recombination. Figure 5.32 shows a p-n junction formed with different materials like n-type CdS with p-type CdTe (a heterojunction).

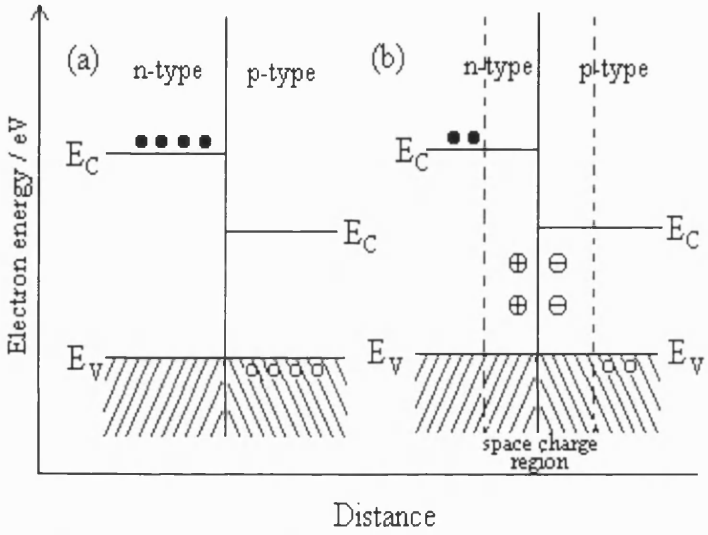

Figure 5.32 Schematic band diagram showing contact formation between n- and p-type semiconductors. Filled circles ● indicate free electrons, and circles ❍ represent free holes. (a) at the moment of contact and (b) at equilibrium after contact

The creation of the two regions of the space charge with opposite signs produces an electric field ***E*** which is called the built-in electric field. The field ***E*** is directed from the n-type to the p-type space charge region as can be seen in figure 5.33a. At equilibrium, the diffusion current density of electrons j_{n1} from n to p equals the drift current density of electrons j_{n2} from p to n due to the built-in electric field in

magnitude and in opposite direction, so the net electron current density vanishes. Similarly, the diffusion current density of holes j_{p1} is equal in magnitude and opposite in direction to the drift or generation current density of holes j_{p2}, so the net hole current density is zero. They are expressed by

$$j_{n1} + j_{n2} = 0 \tag{5.105}$$

$$j_{p1} + j_{p2} = 0 \tag{5.106}$$

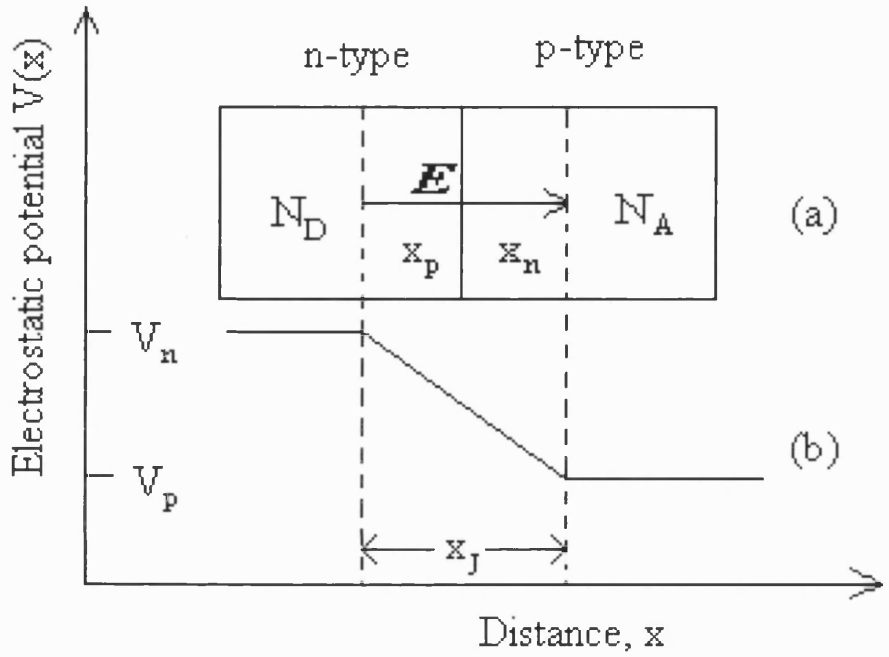

Figure 5.33 Electrostatic potential V(x) against distance in an ideal abrupt p-n junction. The direction of the built-in electric field ***E*** in the space charge region is shown in (a).

The magnitude of thebuilt-in electric field ***E*** is equal to a gradient dV/dx of the electrostatic potential V(x), where V(x) is a function of distance in the semiconductor. The existence of the built-in electric field as shown in figure 5.33b increases the electrostatic potential of an electron in the neutral n-type semiconductor of the junction by an amount

$$V_n - V_p = V_o \tag{5.107}$$

where V_n and V_p are the constant electrostatic potentials in the neutral n and p regions, V_o is called the contact or diffusion potential. So the energy of the electrons in the neutral p region is higher than that in the neutral n region by qV_o. Now the band diagram can be drawn in figure 5.34 at equilibrium.

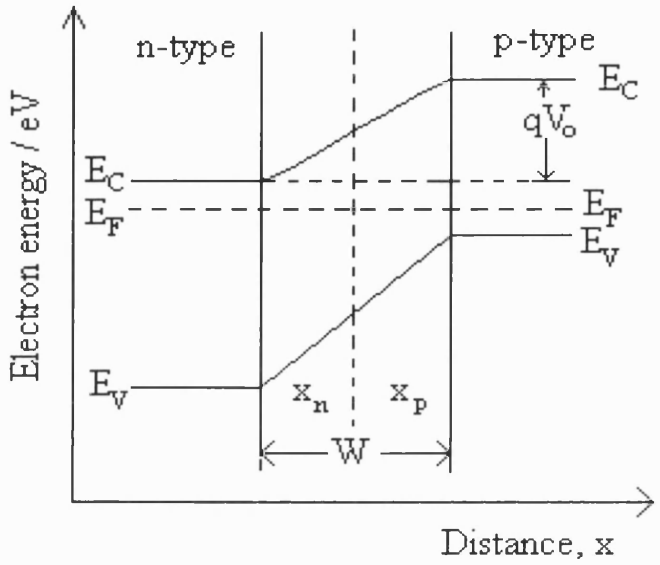

Figure 5.34 Band diagram for the p-n junction at equilibrium ($W = x_p + x_n$).

The relationship between V_o and the width of the space charge region W can be obtained from equations 5.105, 5.106 and 5.107. The details were given in literature [41].

$$W = \left[\frac{2\varepsilon\varepsilon_0}{q} \left(\frac{N_A + N_D}{N_A N_D} \right) V_o \right]^{1/2} \tag{5.108}$$

Due to requirement of the electrical neutrality in the space charge region,

$$N_A x_p = N_D x_n \tag{5.109}$$

Note that it has been assumed that $N_A = N_D$, so $x_p = x_n$. In applications of solar cells, one side of the p-n junction is usually heavily doped so that $N_D >> N_A$. For example,

in CdTe/CdS solar cells, $N_D \approx 10^{18}$ cm^{-3}, while $N_A = 10^{15}$ cm^{-3}, so $x_p >> x_n$, equation 5.108 can be simplified as

$$W = \left[\frac{2\varepsilon\varepsilon_0}{q}\frac{V_o}{N_A}\right]^{1/2} \qquad (5.110)$$

5.13.2 The p-n Junction under an Applied Potential

There is a standard terminology for the application of a potential difference to the p-n junction. If the n-type region is biased negatively, it is called forward bias. If the n-type is biased positively, it is termed reverse bias.

Consider a potential V_a is applied to the above p-n junction. Under an forward bias, the magnitude of the electric field in the space charge region decreases to $\boldsymbol{E-E_a}$. That means that the forward bias decreases the width of the space charge region. On the contrary, the reverse bias increases the width of the space charge region. At high reverse bias, inversion may occur (see section 5.7.2).

The junction capacitance C can be expressed as

$$C = \frac{\varepsilon\varepsilon_0}{W} \qquad (5.111)$$

Substituting $V_o - V_a$ for V_o in equation 5.108, then combining with equation 5.111 gives

$$C^{-2} = \frac{2}{q\varepsilon\varepsilon_0}\left(\frac{N_A + N_D}{N_A N_D}\right)(V_o - V_a) \qquad (5.112)$$

When one side of the p-n junction is heavily doped, all equations used for single semiconductor are valid for the p-n junction diode.

5.13.3 Solar Cell Output Parameters

The short-circuit current, I_{sc}, the open-circuit voltage, V_{oc}, and the fill factor, FF, are three common parameters to be used for characterisation of solar cells. They are shown in figure 5.35. The short circuit current, I_{sc}, is the current output when there is no external load and the circuit is closed. The open-circuit voltage, V_{oc}, is the output voltage when the external load is much much greater than the internal load. The fill factor, FF, is defined as

$$FF = \frac{V_{mp} I_{mp}}{V_{oc} I_{sc}} \tag{5.113}$$

where V_{mp} and I_{mp} are the voltage and current at the maximum power output, respectively. Recombination in the depletion region can reduce the fill factor.

There is a relationship between I_{sc} and V_{oc}. It can be expressed as [132-133]

$$V_{oc} = m \frac{kT}{q} \ln\left(\frac{I_{sc}}{I_o} + 1\right) \tag{5.114}$$

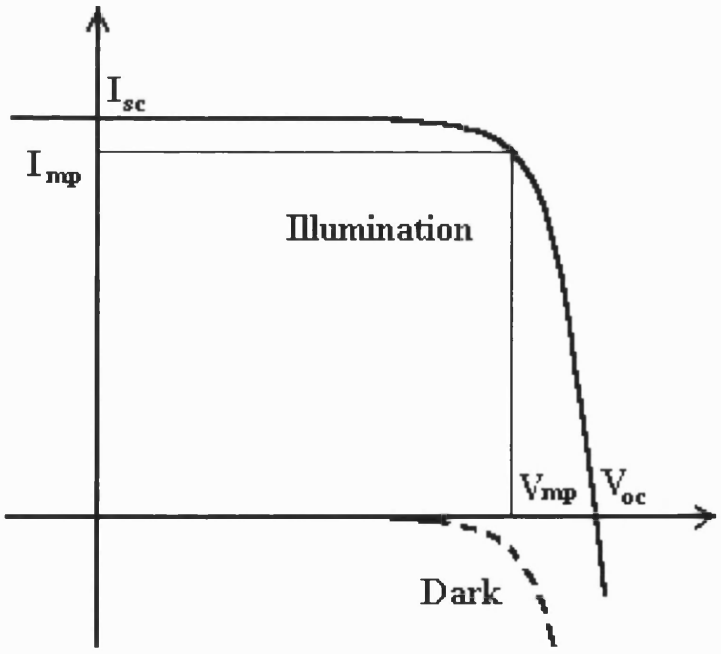

Figure 5.35 I – V characteristics for solar cells in the dark and under illumination

where m is the ideality factor or the junction perfection factor. If m is equal to 1, the junction is called an ideal junction, and V_{oc} obtains its highest value. I_0 is the junction saturation current density given as [132]

$$I_0 = A\left(\frac{qD_e n_i^2}{L_e N_A} + \frac{qD_p n_i^2}{L_h N_D}\right) \tag{5.115}$$

Here A is the junction area. An estimate of the magnitude of I_0 is given by

$$I_0 = 1.5\times 10^5 \exp\left(-\frac{Eg}{k_B T}\right) \qquad Acm^{-2} \tag{5.116}$$

This relationship ensures that the V_{oc} increases with increasing band gap, while the I_{sc} decreases with increasing band gap. For large values of m, I_0 is larger in such a way that V_{oc} is reduced. The value of m for solar cells in reality is between 1 and 2.

The light-to-electricity conversion efficiency (LECE), η, can be obtained as

$$\eta = \frac{I_{mp}V_{mp}}{P_{input}} = \frac{I_{sc}V_{oc}FF}{P_{input}} \tag{5.117}$$

where P_{input} is the total power in the light incident on the cell. Normally this is 100mW cm^{-2} for simulated solar illumination.

Solar cells generally have series and shunt resistances as shown in figure 5.36, the simplest equivalent circuit of a solar cell. A current generator represents the photocurrent, I_{ph}. The major contributions to the series resistance, R_s, are the bulk resistance of the semiconductor materials and the back contacts and interconnections. The shunt resistance, R_{sh}, is caused by leakage across the junction around the edge of

the cell and in nonperiphereal regions in the presence of defects and precipitates of impurities in the junction region.

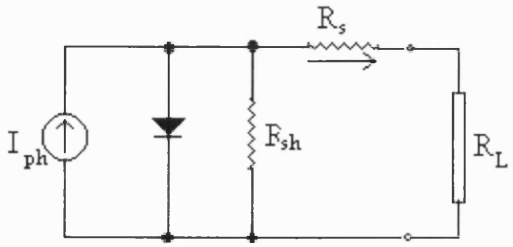

Figure 5.36 Equivalent circuit of a solar cell showing series and shunt resistances

Both types of resistances affect the performance of the cells. The effects of series and shunt resistances were illustrated in figures 5.37 and 5.38.

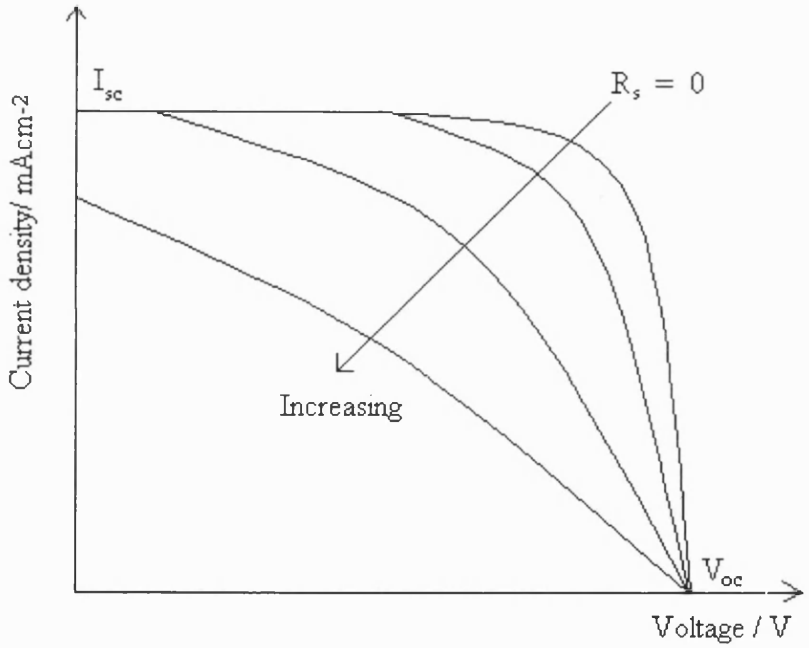

Figure 5.37 Effect of series resistance on the I-V characteristics of solar cells

It can be seen from figure 5.37 that the short circuit current decreases with increasing series resistance. The same is true for the fill factor. Numerical solutions also indicate that even small values of series resistance, say 0.5 ohm, are enough to

cause serious effects [133]. So the back contacts plays a key issue in fabrication of solar cells. Note that series resistance does not affect the open-circuit voltage.

It has shown in figure 5.38 that shunt resistance does affects the open-circuit voltage and does not affect the short-circuit current at all. The open-circuit voltage increases with increasing shunt resistance. The reduction of defects and impurities of the junction will increase the value of shunt resistance and improve the cell performance.

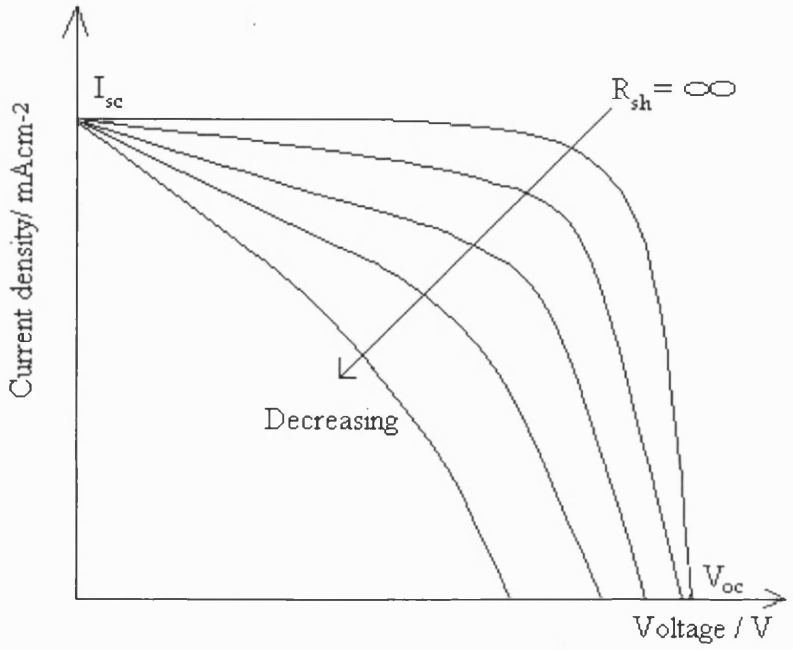

Figure 5.38 Effect of shunt resistance on the I-V characteristics of solar cells

In practical devices, the shunt resistance is normally large enough to be neglected at one sun intensity or above, but in the low intensities and temperatures the shunt resistance become important [134]. On the other hand, the series resistance becomes increasingly important at high intensities and high temperatures.

Figure 5.39 shows the maximum LECE as a function of band gap predicted theoretically [132].

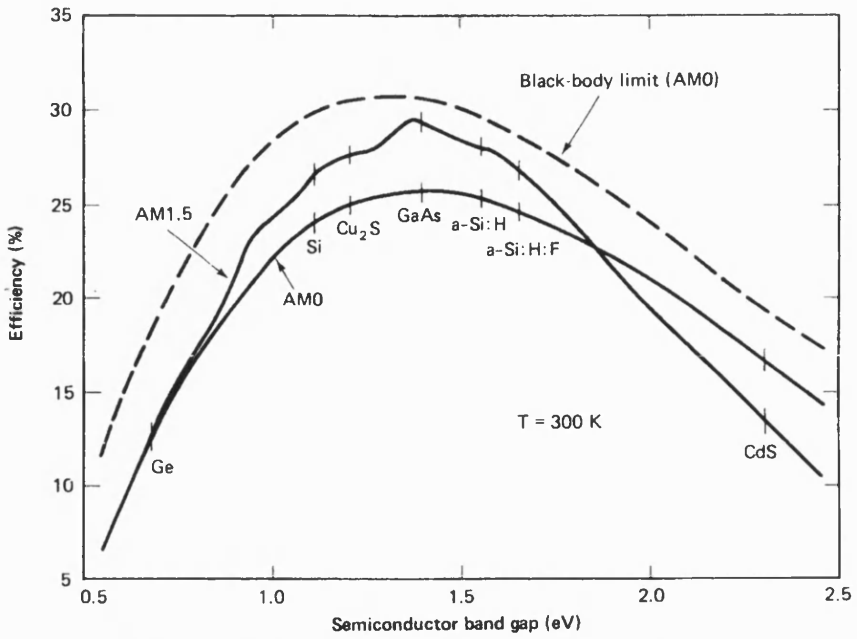

Figure 5.39 Theoretical prediction for maximums of solar cell efficiency as a function of the band gap of the cell material (taken from [132]).

References:

1. B. Ray, II-VI Compounds, Pregamon Press Ltd, New York (1969).
2. E. Shanthi, A. Banerjee, V. Dutta and K.L. Chopra, J. Appl. Phys., **53**, 1615 (1982).
3. E. Shanthi, A. Banerjee and K.L. Chopra, Thin Solid Films, **88**, 93(1982).
4. E. Shanthi, V. Dutta, A. Banerjee, and K.L. Chopra, J. Appl. Phys., **51**, 6243 (1981).
5. W. G. Haines and R. H. Bube, J. Appl. Phys., **49**, 304 (1978).
6. H. K. Muller, Phys. Stat. Sol., **27**, 723 (1968).
7. R. L. Weiher and R. P. Ley, J. Appl. Phys., **37**, 299 (1966).
8. Y. Ohhata, F. Shinoki and S. Yoshida, Thin Solid Films, **59**, 255 (1979).
9. J. Aranovich, A. Ortiz and R. H. Bube, J. Vac. Sci. Technol., **16**, 994 (1979).
10. S. Major, A. Banerjee and K. L. Chopra, Thin Solid Films, **108**, 33(1983).

11. R.A. Soref, H. W. Moos, J. Appl. Phys., **35**, 2152(1964).

12. M. Cardona, G. Harbeke, Phys. Rev. A **137**, 1467 (1965).

13. Landolt-Börnstein: Numerical Data and Fundamental Relationships in science and Technology, New Series, Ed. by K. H. Hellwege, Springer-Verlag Berli-Heidelberg, Vol. **17**, 103(1982).

14. M.E. Ozsan, D.R. Johnson, M. sadeghi, D. Sivapathasundaram, G. Goodlet, M. J. Furlong, L. M. Peter and A.A. Shingleton, J. Mat. Sci. Materals in Electronics, **7**, 119(1996).

15. E. Gutsche, J. Voigt, Proc. 7^{th} Int. Conf. II-VI Semiconducting Compounds, Providence, R.I., USA, W.A. Benjamin Inc., New York, 1967, 337.

16. A.R. Moore, R.W. Smith, Phys. Rev., **138**, A 1250 (1965).

17. M. Sze, Physics of Semiconductor Devices, 2d ed., John Wiley & Sons, New York, 1981.

18. I. Kaur, D. K. Pandya and K. L. Chopra, J. Electochem. Soc., **127**, 943 (1981).

19. D. Thesis, J. Phys. Chem. Solids, **38**, 1125(1977).

20. Y. S. Park, F.L. Chen, J. Appl. Phys., **36**, 800(1965).

21. M. Aven, B. Segall, Phys. Rev., **130**, 81(1963).

22. J. H. Haanstra, J. Dieleman, Ext. Abstr. Electrochem. Soc., **14**, 2(1965).

23. K.L. Chopra and S. R. Das, Thin Film Solar Cells, Plenum Press, New York, 1983.

24. M. Inoue, Jpn. J. Phys. Soc., **26**, 1186 (1969).

25. D. M. Heinz, E. Banks, J. Chem. Phys., **24**, 391(1956).

26. R .C. Kainthla, PhD. Thesis, Indian Institute of technology, Delhi (1980).

27. M. Cardona, D.L. Greenaway, Phys. Rev., **131**, 98(1963).

28. A.G. Fisher, J. N. Carides and J. Dresner, Solid State Commun., **2**, 157(1964).

29. S. Yamada, Jpn. J. Phys. Soc., **15**, 1940 (1960).

30. H. O. Finklea, Semiconductor Electrodes, Elsevier Science Publishers B.V., 1988.

31. J. S. Blakemore, Solid State Physics, Cambridge University Press, London, 1985.

32. N. Sato, Electrode Chemistry, **1**, 47, Japan Technical Information Service, Tokyo, 1993.

33. N.Sato, Electrochemistry at Metal and Semiconductor Electrodes,Elsevier Science B.V., Amsterdam, 1998.

34. J.R. Hook and H.E. Hall, Solid State Physics, 2nd ed, John Wiley & Sons, New York (1991).

35. W. Schockley, Electrons and Holes in Semiconductors, Van Nostrand, New York,(1950).

36. H. Gerischer, Electrochimica Acta, **35**, 1677(1990).

37. R.H. Bube, Photoelectronic Properties of Semiconductors, Cambridge University Press, 1992.

38. J. N. Hobstetter, in Semiconductors, ed. by N.B. Hannay, Reinhold, New York, (1959).

39. W.R. Beam, Electronics of Solid, McGraw-Hill, New York (1965).

40. S. Wang, Solid State Electronics, McGraw-Hill, New York (1966).

41. J. P. McKelvey, Solid State and Semiconductor Physics, Harer and Row, New York, (1966).

42. A. S. Grove, Physics and Technology of Semiconductor Devices, John Wiley, New York, (1967).

43. A. Many, Y. Goldstein and N. B. Grover, Semiconductor Surfaces, North-holland, Amsterdam, (1965).

44. R. Dalven, Introduction to Applied Solid State Physics, Plenum Press, (1990).

45. J. Van Laar and J .J. Scheer, Photoemission of Semiconductors, Philips Technical Review, **29**, 54 (1968).

46. H. K. Henisch, Semiconductor Contacts, Oxford University press, 29(1984).

47. R. L. Bell, Negative Electron Affinity Devices, Oxford University Press,17(1973).

48. S. G. Davison and J.D. Levine, in Solid State Physics, ed. by H. Ehrenreich, F.Seitz and D. Turnbull, Academic Press, New York, **25**, 1(1970).

49. L. M. Peter, Chem. Rev., 90, 753 (1990).

50. S.R. Morrison, Electrochemistry at Semiconductor and Oxidised Matel Electrodes, Plenum Press, (1980).

51. Yu. V. Pleskov and Yu. Ya. Gurevich, Semiconductor Photoelectrochemistry, Consultants Bureau, New York, (1986).

52. A. K. Vijh, Electrochemistry of Matels and Semiconductors, Marcel Dekker, Inc., New York, (1973).

53. Yu. V. Pleskov, Croat. Chem. Acta, **44**, 179 (1972).

54. W. Schottky, Z. Phys., **113**, 367 (1939); **118**, 539 (1942).

55. N. F. Mott, Proc. Roy. Soc., (London), **A171**, 27(1939).

56. J. F. Dewald, Bell System Tech., **34**, 615 (1960).

57. A. J. McEvoy, M. Etman and R. Memming, J. Electroanal. Interface Electrochem., **190**, 225(1985).

58. R. A. Marcus, J. Chem. Phys., **24**, 966(1956).

59. R. A. Marcus, Ann. Rev. Phys. Chem., **15**, 115(1964).

60. H. Gerischer, Z. Phys. Chem.N .F., **26**, 223(1960).

61. H. Gerischer, Z. Phys. Chem.N .F., **27**, 48(1961).

62. B. O. Seraphin, in Proc. 7^{th} Intern. Conf. Physics of Semiconductors, ed. M. Hulin, Paris, 165(1964).

63. B. O. Seraphin, J. Phys., **28**, C3(1967).

64. R. Ludeke and W. Paul, in II-VI Semiconducting Compounds, Intern. Conf., Providence, ed. D.G. Thomas, W.A. Benjamin, Inc., New York, 123(1967).

65. B. Batz, Solid State Comm., **4**, 21 (1966)

66. C. N. Berglund, J. Appl. Phys., **37**,3019(1966).

67. H. Lange and W. Henrion, Phys. Stat. Sol., **23**, K67(1967).

68. W. E. Engeler, H. Fritzsche, M.Garfinkel and J.J. Tieman, Phys. Rew. Letters, **14**, 1069(1965).

69. G. W. Gobell and E. O. Kane, Phys. Rew. Letters, **15**, 142 (1965).

70. M. Garfinkel, J. J. Tieman and W. E. Engeler, Phys. Rew., **148**, 695(1966).

71. B. Lax, in in Proc. 7^{th} Intern. Conf. Physics of Semiconductors, ed. M. Hulin, Paris, 123 (1964).

72. H. C. Praddaude, Phys. Rew., **140**, A1292(1965).

73. M. Reine, Q.H. F. Vrehen and B. Lax, Phys. Rew., **163**, 726(1967).

74. J. G. Mavroides, M. S. Dresselhaus, R.L. Aggarwal and G. F.Dresselhaus, Jpn. J. Phys. Soc., **21**, 184(1966).

75. D. E. Aspnes, Surface Science, **37**, 418(1973).

76. D. F. Blossey and P. H. Handler, in Semiconductor and Semimetals, ed. R.K. Wilardson and A. C. Beer, Academic Press, New York, **9**, 257(1972).

77. D. E. Aspnes in Handbook on Semiconductors, ed. M. Balanki, North Holland, New YorK, **2**, 109(1980).

78. M. Cardona, Modulation Spectroscopy, Academic Press, New York, (1969).

79. P. M. Raccah, J. W. Garland, Z. Zhang, U. Lee, S. Ugur, S. Mioc, S.K. Ghandi and I. Bhat, J. Appl. Phys., **57**, 2014 (19885).

80. F. H. Pollak and H. Shen, Superlattices and Microstructures, **6**(2), 203(1989).

81. F. H. Pollak and H. Shen, Mat. Sci. Eng. Reports, **R10**, 275 (1993).

82. B. O. Seraphin and N. Bottka, Phys. Rew., **139**, A560 (1965).

83. R. Williams, phys. Rew., **117**, 1487 (1960).

84. K. L. Shaklee, F. H. Pollak and M. Cardoda, Phys. Rew. Letters, **15**, 883(1965).

85. D. E. Aspnes and M. Cardona, Phys. Rew., **173**, 714(1968).

86. D. E. Aspnes and J. E. Rowe, Phys. Rew., B, **5**, 4022 (1972).

87. D. E. Aspnes and A. Frova, Solid State Commun., **7**, 155(1969)

88. H. Shen and F. H. Pollak, Phys. Rew. B, **42**, 7097(1990).

89. P.L. Jackson and E.G. Seebauer, J. Appl. Phys., **60**, 943(1991).

90. U. Behn and H. Roppisher, J. Phys. C: Solid State Phys., **21**, 5507(1988).

91. J. L. Birman, Phys. Rew., **114**(3), 1490(1959).

92. B. B. Snavely, Phys. Rev., **167**(3), 730(1960).

93. P. E. Vanier, F. H. Pollak, P. M. Raccah, Appl. Optics, **16**, 2858(1977).

94. P. Slvador, A. M. Chaparro, B. Coll and M. Gonzalez, Surface Science, **293**, 160 (1993).

95. R. K. Pandey, S. R. Kumar, A.J. N. Rooz, and S. Chandra, Thin Solid Films, **200**, 1 (1991).

96. R. P. Raffaelle, H. Forsell, E. M. Potdevin, R. Friendfeld, J. G. Mantovani, S. G. Bailey, S. M Hubbard, E. M. Gordon and A. F. Hepp, Solar Energy Mater. Solar Cells, **57**(2), 167 (1999).

97. O. A. Ileperuma, C. Vithana, K. Premaratne, S. N. Akuranthilaka, S. M. McGregor and I. M. Dharmadasa, J. Materials Science-Materials in Electronics, **9**(5), 367(1998).

98. D. Lincot and R. Ortega Borges, J. Electrochem. Soc., **139**, 1880 (1992).

99. K. D. Rogers, J. D. Painter, M. J. Healy, D. W. Lane and M. E. Ozsan, Thin Solid Films, **339**(1-2), 299(1999).

100. J. Touskova, D. Kindl and J. Tousek, Thin Solid Films, **293**(1-2), 272(1997).

101. S. Dennison, J. Materials Chemistry, **5**(11), 1885(1995).

102. A. K. Turner, J. M. Woodcock, M. E. Ozsan, J. G. Summers, J. Barker, S. Binns, K. Buchanan, C. Chai, S. Dennison, R. Hart, D. Johnson, R. Marshall, S. Oktik, M. Patterson, R. Perks, S. Roberts, M. Sadeghi, J. Sherbone, J.Szubert and S. Webster, Solar Energy Materials, **23**(2-4), 388(1991).

103. L. Thouin, S. Massaccesi, S. Sanchez and J. Vedel, J. Electroanal. Chem., **374** (1-2), 81(1994).

104. J. F. Guillemoles, A. Lusson, P. Cowache, S. Massaccesi and J. Vedel, Advanced Materials, **6**(5), 376(1994).

105. R. Jeyakumar, S. Ramamurthy, M. Jayachandran and M. J. Chockalingam, Materials Research Bulletin, **29**(2), 195(1994).

106. P. J. Sebastian, M. E. Calixto, R. N. Bhattachcharya and R. N. Noufi, J. Electrochem. Soc., **145** (10), 3613 (1998).

107. A. Saraby-Reintjes, L. M. Peter, M. E. Özsan, S. Dennison and S. Webster J. Electrochem. Soc., **140**,2880 (1993).

108. R. Schuhmann, J. Amer. Chem. Soc., **47**, 356(1925).

109. W. J. Danaher and L. E. Lyons, Aust. J. Chem., **37**, 689(1984).

110. P. R. Panicker, M. Knaster and F.A. Kroger, J. Electrochem. Soc., **125**(4), 566(1978).

111. P. R. Unwin and R. G. Compton in Comprehensive Chemical Kinetics Vol 29, Elsevier, Amsterdam, 173 (1989).

112. R. L. Wang, K. Y. Tam, R. G. Compton, Electroanalysis, **9**(4), 284(1997).

113. R. L. Wang, K. Y. Tam, R. G. Compton, J. Electroanal. Chem., **434**(1-2), 225(1997).

114. R. G. Compton, P. R.Unwin, J. Electroanal. Chem., **205**, 1(1986).

115. R. G. Compton, M. J. Day, M. E. Laing, R. J. Northing, J. I. Penman, A. M. Walker, J. Chem. Soc. Faraday Trans I **84**, 2013 (1988).

116. R. A. Batchelor, D. Phil. Thesis, University of Oxford, 1991.

117. J. I. Pankove, Optical Processes in Semiconductors, Englewood Cliffs, N.J.: Prentice-Hall, (1971).

118. W. W. Gärtner, Phys. Rew., **116**, 84 (1959).

119. M. A. Butler, J. Appl. Phys., **48**, 1914 (1977).

120. J. Reichman, Appl. Phys. Lett., **36**, 574 (1980).

121. J. Reichman and M. A. Russak, in Phtoefects at Semiconductor-Electrolyte Interfaces, ed. by A.J. Nozik, ACS Symposium Series No. 146, American Chemical Society, Washington D.C., 359 (1981).

122. F. El Guibaly, K. Colbow and B. L. Zfunt, J. Appl. Phys., **52**, 3480 (1981).

123. F. El Guibaly and K. Colbow, J. Appl. Phys., **53**, 1737 (1982).

124. W. J. Albery, P. N. Bartlett, A. Hamnett and M. P. Dare-Edwards, J. Electrochem. Soc., **128**, 1492 (1981).

125. L. M. Peter in Specialist Periodical Reports in Electrochemistry, Volume 9, Royal Society, London, 66, (1984).

126. A. Kampmann and D. Lincot, J. Electroanal. Chem., **418**, 73(1996).

127. W. J. Albery, J. Electrochem. Soc., **128**,1492 (1981).

128. A. Etcheberry, M. Etman, B. Fotouhi, J. Gautron, L. Sculfort and P. Lemasson, J. Appl. Phys., **53**, 8867 (1982).

129. J. F. McAleer and L. M. PeterFaraday Discuss. Chem. Soc., **70**, 67 (1981).

130. G. Horowitz, Appl. Phys.Lett., **40**, 409 (1982).

131. W. Shockley, Electrons and Holes in Semiconductors, Van Nostrand, New York, 313 (1950).

132. M. A. Green, Solar Cells Operation Principles, Technology, and System Applications, Prentice-Hall, Inc., Englewood Cliffs, N.J. 07632, 76(1982).

133. H. J. Hovel, Semiconductors and Semimetals, Vol. 11, Solar Cell, Academic Press, New York, 5 (1975).

134. R. Sahai and A.G. Milnes, Solid State Electron, 13, 1289 (1970).

CHAPTER SIX

EXPERIMENTAL

6.1 Chemicals and Solutions

All solutions were made up from ultrapure chemicals with at least 5 9s and high purity Milli-Q water which has very low concentrations of ionic, organic, and particulate contamination. The resistivity of the water was typically 18.2 MΩcm. Unless otherwise stated, solutions for both electrodeposition and characterisation were degassed by bubbling argon about 10 minutes before being using.

The deposition solution was 0.5 M cadmium sulphate (99.999%, Aldrich Gold Label), 5.0×10^{-4} M tellurium oxide (99.9995%, Aldrich). The pH of the solution was adjusted to 1.4 with sulphuric acid (99.999%, Aldrich). Cadmium chloride (99.99+%, Aldrich) was used to control the chloride ion concentration (typically 800ppm). The solutions were purified by adding cadmium power (99.999%, <200 mesh, Aldrich) and stirring for 48 hours before filtering. The solutions for characterisation were 0.1 M Na_2SO_3 with 10^{-3} M NaOH.

The depositions were made at 85°C, while all experiments for characterisation were performed at room temperature. All experiments were carried out in A Faraday Cage.

The etching solution for making contacts was freshly made from diaminoethance and Milli-Q water with 50:50 (volume).

6.2 Safety Measurements

Since all chemicals used in this part were highly toxic, gloves, mouth mask and white coat must be worn within the laboratory. Eating and drinking were strictly prohibited. Great care must be taken when weighing chemicals and making-up solutions. All the waste must be collected in the specifically labelled bottles. Due to the use of high deposition temperature (85°C) and flowing solution by a pump, double-layer tubes were used, and the connections were clamped tightly by the clamps.

6.3 Glassware

6.3.1 Cells for electrodeposition

A stirred cell was used for electrodeposition. It was designed to ensure that the deposited films were smooth, uniform and reproducible.

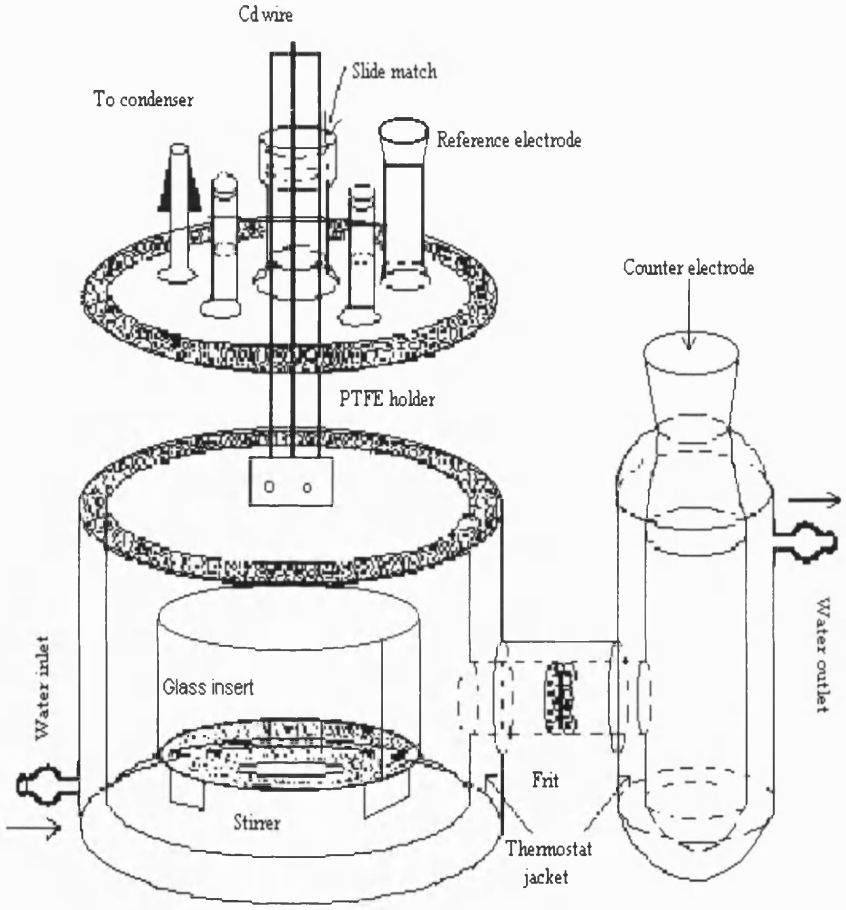

Figure 6.1 Stirred cell used for the cathodic electrodeposition of CdTe

It can be seen from figure 6.1 that a glass insert was designed to control movement of solution to form laminar flow on the sample surface and to avoid a direct stir underneath from the stirrer by using an appropriate size frit or membrane. The insert had a window of size of 25 × 30 mm opposite of the counter electrode to provide a uniform electric field. When the flowing solution passes through the window, the

laminar flow is produced. The counter electrode was placed to a separate compartment by a frit to prevent potential contamination from the counter electrode. The sample holder was made from PTFE with a Cadmium foil as a connection. The holder was closely matched with glass junction by two silicon rings. This design has two functions: 1) prevention of solution losses 2) reduction of the chance that toxic chemicals escape. There were other four precision joints on the lid. One of them was for the reference electrode compartment mounted in a glass tube with a frit. The second was connected with a water-cooled condenser to minimise evaporation losses. The other end of the condenser was linked to a collector with a frit to reduce the losses further. The rest were for solution filling and a thermometer. A PTFE coated magnetic stirrer bar was placed underneath the insert. There were outer glass lips for the lid and cell body for precise fitting. There was a silicon sheet between them. The two were sealed further in place with clamps. Water was circulated through the jacket to maintain the temperature constant at 85°C. The total volume for the cell was about 400 ml, but the solution volume (maximum) was 300 ml.

6.3.2 Cells for Characterisation

6.3.2.1 Cell for Photocurrent and Capacitance – Voltage Measurements

A cell with a single large quartz window that can be used to measure different positions of a sample was designed for photocurrent measurement. It consisted of three compartments. One was the reference compartment connected via a Luggin capillary to minimise iR drop between the reference and working electrodes. The counter electrode was placed in a compartment connected by a separate frit. The configuration is shown in figure 6.2.

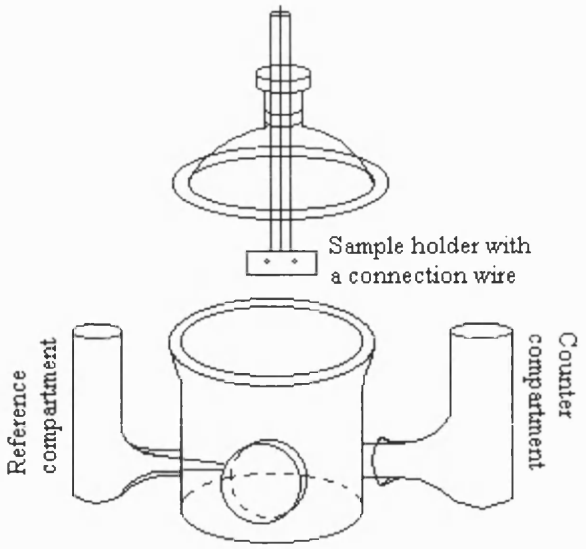

Figure 6.2 A single window glass cell with two side arms

6.3.2.2 Cell for Electrolyte Electroabsorbance (EEA) Measurements

A cell with two quartz windows was designed for EEA measurement. The two windows are of same size and are in parallel as shown in figure 6.3.

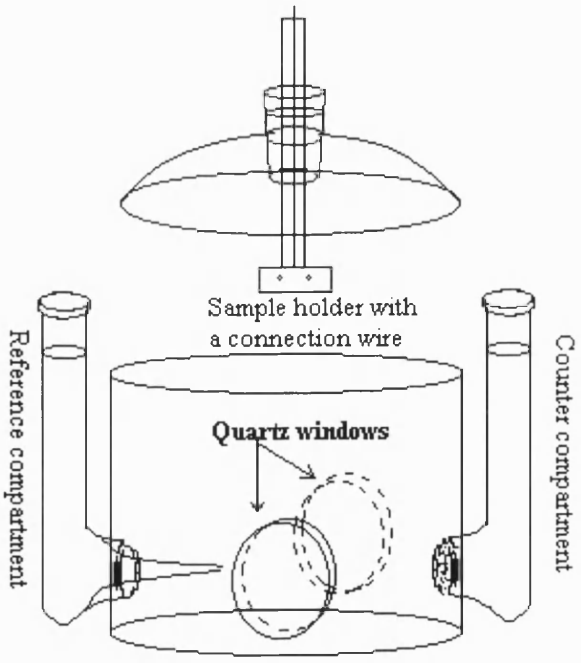

Figure 6.3 A two-window glass cell with two side arms

6.3.2.3 A Cell for Electrolyte Electroreflectance (EER) Measurements

A cell with three quartz windows was designed for EER measurement. The angle between the middle and side window was 60^{o}, so this cell had two choices for the angle of the reflection. One was 45^{o}, and the other was 60^{o}. The sample holder can be moved by rotation or vertical movements as shown in figure 6.4. If you want an angle of 60^{0} from an angle at 45^{0}, you can rotate the holder handle at angle of 15^{0}.

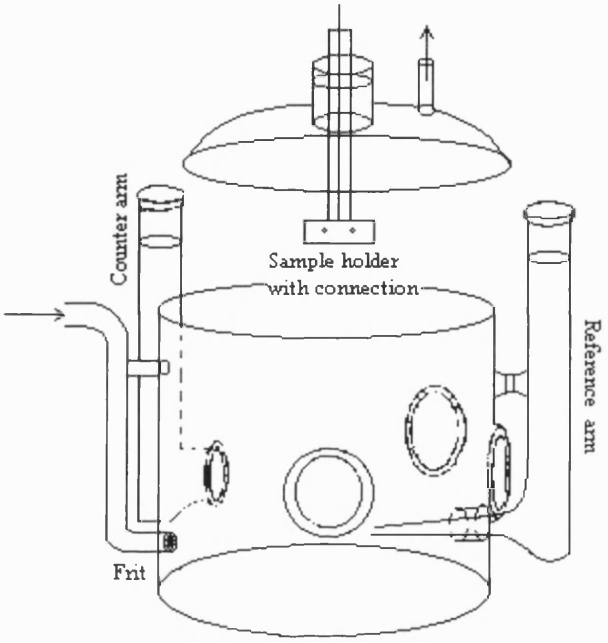

Figure 6.4 A cell with three quartz windows for EER

6.4 Channel Flow Cell for Electrodeposition

A channel flow cell was machined from PTFE. A smooth cadmium sheet was attached to wall of the channel and connected to a cadmium wire through the wall. The channel dimensions were 50 × 10 × 1 mm. The channel and transparent CdS coated glass were clamped together by a rectangular clamp made from Pyrex glass with three screws to hold the channel cell and the glass substrate tightly. The rectangular clamp had a long slot on the back that allowed the channel cell to slide freely in or out of the clamp without needed to dismantle it. The glass substrate was slightly longer than the

channel cell for convenient connection to the working electrode. The cell components are shown in figure 6.5.

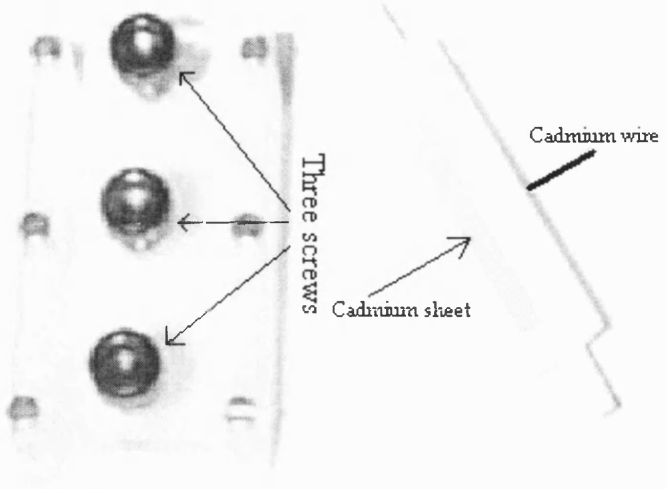

Figure 6.5 A channel flow cell with a rectangle clamp

6.5 Electrodes

6.5.1 Reference Electrodes

Several different types of reference electrodes were used. For all experiments for characterisation of CdTe, a saturated calomel ($Hg/HgCl_2/KCl_{(satd)}$) electrode (SCE) was used. Its potential is 0.241 V vs. a normal hydrogen electrode (NHE) [1] at room temperature. For all experiments involving CdTe electrodeposition, a Cd wire was placed in the tube contained a deposition solution and a frit to separate it from the deposition solution. This reference electrode is shown in figure 6.6. The potential of the Cd wire was stable unless the Cd wire was covered fully by CdTe. The potential of the Cd wire placed in 1 M $CdSO_4$ solution was – 0.675 V vs SCE [2]. When the Cd wire was covered fully by CdTe, the colour of the wire became dark. In this case it was cleared carefully. Contact with other metals was avoided in order to prevent contamination of the deposition solution.

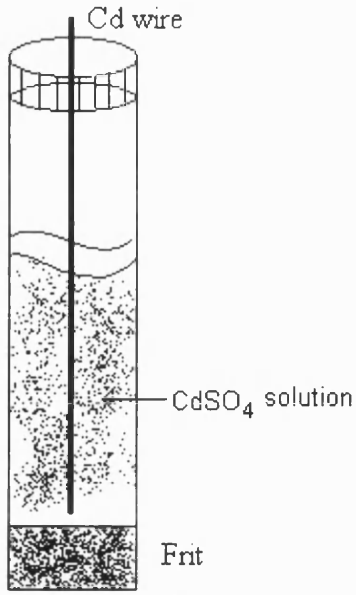

Figure 6.6 Cd wire reference electrode

6.5.2 Working Electrodes

The substrates used for all cathodically electrodeposited thin films were fluorine-doped tin oxide on glass (10 Ω/square) with a layer of 80nm CdS deposited by a chemical bath deposition (CBD). Samples for electrodeposition were cut to approximately 2.4 × 5.0 cm in the stirred cell and to 1.5 × 6.0 cm in the flow cell by using a diamond cutter from a 30 × 30 cm sheet of CdS provided by BP Solar. The working electrodes for electrodeposition were mounted in the stirred cell that using the sample holder made from PTFE as shown in figure 6.7. A sheet of Cd surrounded the holder walls to ensure the best contact with the CdS substrate. The substrate and Cd sheet were tightly held together by two screws on the holder. The working electrodes for electrodeposition in the flow cell and for all experiments involving characterisation were very simple. They consisted of a piece of CdS and an appropriate size crocodile clip connected with a copper wire and fixed on the end of the glass tube. This is shown in figure 6.8.

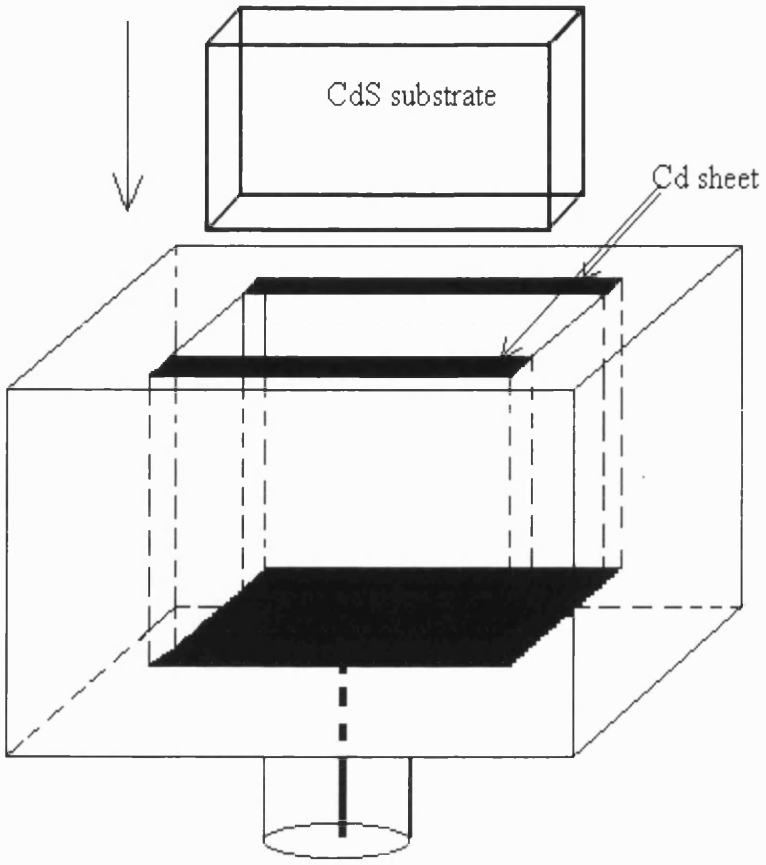

Figure 6.7 Working electrode holder for the stirred electrodeposition.

Two screws are not shown.

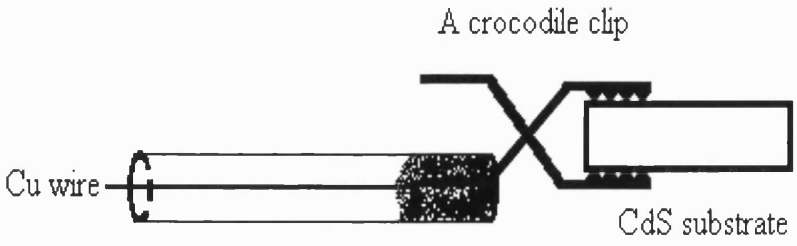

Figure 6.8 Working electrode holder used for the flow cell deposition and all experiments for characterisation of CdTe

6.5.3 Counter Electrodes

Three kinds of electrodes were used. The counter electrode in the stirred cell was a spectrographically pure carbon rod placed in a separate compartment as shown in figure 6.1. A Cd wire was used for external cell connection. The counter electrode in the flow cell experiments was a sheet of Cd located in parallel with and opposite to the working electrode. The use of Cd sheet was to avoid contamination from anodic reaction in the deposition solution, but CdTe also formed on the surface of Cd sheet due to Te displacement. Mechanical polishing was necessary to clean it periodically. The counter electrode used for all characterisation experiments was a platinum sheet or gauze a large area.

6.6 Preparation and Treatment of Samples

6.6.1 Preparation and Treatment of CdS Substrates

The end of the CdS coated substrates were dipped into 15% HCl for a few seconds to remove CdS in the contact region, then washed thoroughly with Milli-Q water and dried by nitrogen. The substrates were then heated in an oven with 430°C about 15 minutes. There as-deposited films are yellow, after annealing in air they became orange as shown in figure 6.9. After cooling down naturally to room temperature, the electrodes were immersed in glacial acetic acid (BDH Aristar grade) for not more than 2 minutes, washed with Milli-Q water and then sonicated twice in Milli-Q water for a few minutes. The samples were masked using polyimide tape to define the deposition area. The exposed area was typically 2.2 × 2.5 cm for the stirred cell deposition, and 0.8 × 2.5 cm for the channel cell deposition. Care was taken to avoid creases on the masks, since they cause leakage. The masks could be used only once. After the

masking, the sample was washed with Milli-Q water, and dried it again by nitrogen before placing it into the deposition cell.

Figure 6.9 Colour change caused by annealing of CdS plates

6.6.2 Treatments of CdTe

After deposition, the CdTe samples were rinsed thoroughly using warm Milli-Q water, dried in a stream of nitrogen, and then stored in a desiccator over silica gel for at least 48 hours before using. Thin film CdTe samples were annealed in air in an oven at 430°C for 15 minutes to type convert n-type CdTe to p-type CdTe. Samples were placed in the small glass cylinder shown in figure 6.10. The CdTe samples used for characterisation experiments were masked by PTFE tape with an area of 5 × 5 mm. The sample connection with a crocodile clip was treated by silver paint to make a good contact.

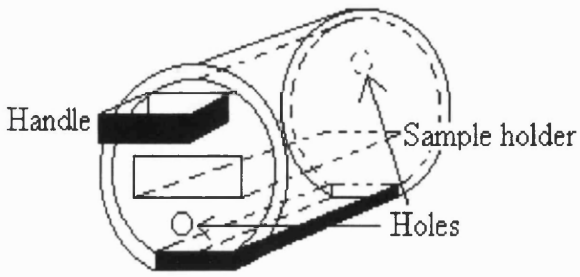

Figure 6.10 A diagram of a glass-made device for CdTe type conversion

6.7 CdTe Thin film Deposition

6.7.1 Electrodeposition in the Stirred Cell

Solution was carefully transferred into the stirred deposition cell, and all glassware was assembled. Great care was taken to check the system for leakage before switching on the circulation pump. The potential of the working (substrate) electrode was controlled with respect to the Cd^{2+}/Cd reference electrode via a potentiostat programmed by a waveform generator (Hi-Tek Instruments, PPR1) that provided step and pulse sequences for plating experiments. The deposition potentials varied from 0 to 50 mV positive to the $Cd2^{+}/Cd$ electrode. The deposition charge was measured by using a Wenking EV 180 electronic integrator interfaced to the potentiostat. The potentiostat was switched on immediately as the electrode was inserted into the solution. The time required to deposit a 2 μm CdTe film depended on potential and stirring conditions. Typically it was about 3 hours. The experimental setup is shown in figure 6.11.

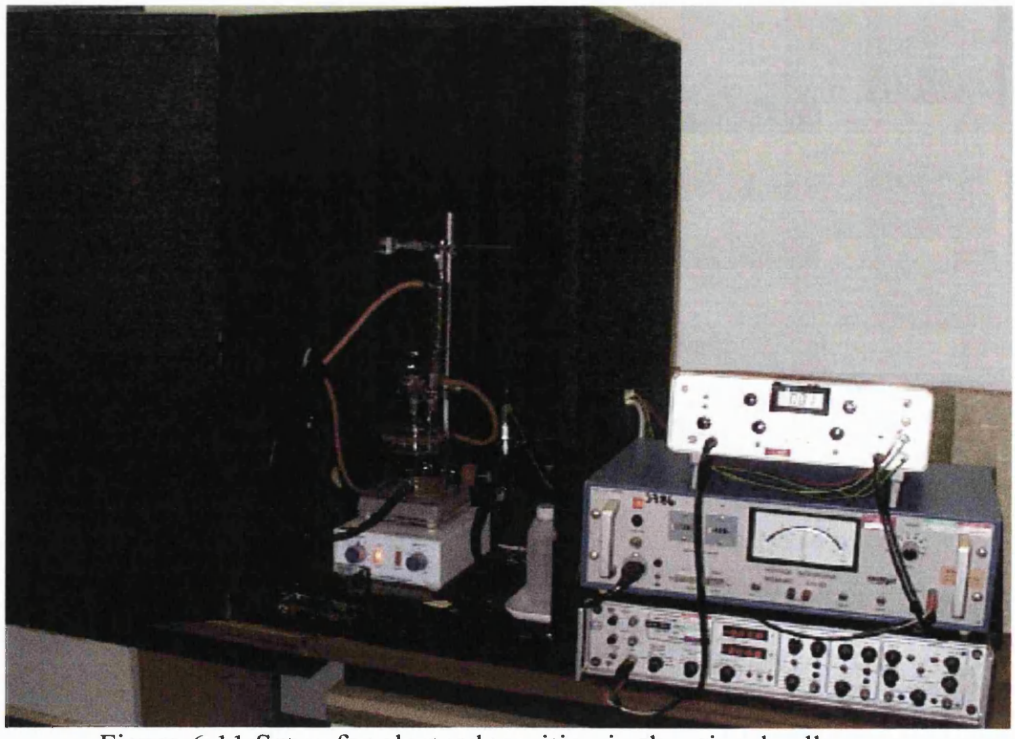

Figure 6.11 Setup for electrodeposition in the stirred cell

6.7.2 Electrodeposition in the Flow Cell

The substrate electrode were mounted flush in one side of the channel using a silicone rubber gasket. The reference electrode was a cadmium electrode mounted in a junction 2.5 cm upstream of the centre of the electrode. The system was pre-checked by using pure water instead of highly toxic cadmium solution for a few days to make sure that it was leak-free at 85°C. The solution was poured into the lower reservoir carefully and then was circulated by a PTFE-lined pump between the lower and upper reservoirs. The temperature of the electrolyte was controlled via a glass heat exchanger immersed in a thermostat- controlled water bath, and the upper reservoir was also jacketed. The flow rate was calibrated and was up to 10 cm^3s^{-1}. The channel electrode was connected into the circuit easily and safely by using a by-pass switch. The deposition potential was 30 mV versus Cd^{2+}/Cd. The experimental setup is shown in figure 6.12.

Figure 6.12 Setup for electrodeposition in the flow cell

The CdTe samples were stored in a desiccator over silica gel. They are shown in figure 6.13.

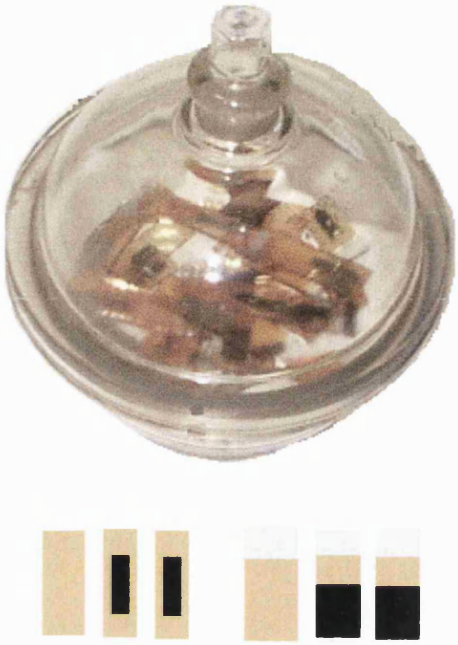

Figure 6.13 CdTe samples and the storing desiccator

6.8 Experimental Techniques

6.8.1 Calibration of Monochromator

Accurate wavelength values are essential for EEA/EER and photocurrent spectroscopy experiments. The monochromator calibration procedure was as follows:

1. Replace the tungsten lamp carefully by a He-Ne laser with a wavelength of 632.8nm;
2. Adjust widths of both the front and back slits to about 1 mm using a micrometer on the top of the slits;
3. Switch on the laser power, and then adjust wavelength dial until the laser spot is seen,adjust to maximise the transmitted laser intensity;
4. Set the wavelength dial to the correct reading corresponding to the He-Ne line. Place a diode in the output beam;

5. Check all connections and switch on the computer according to the diagram shown in figure 6.14. Set the width of the rear slit to half millimetre and the range of the scan wavelength ±5 nm away the reading by step 3. The photocurrent was recorded vs. wavelength to check the correct setting. Repeat and adjust until agreement in laser wavelength is obtained

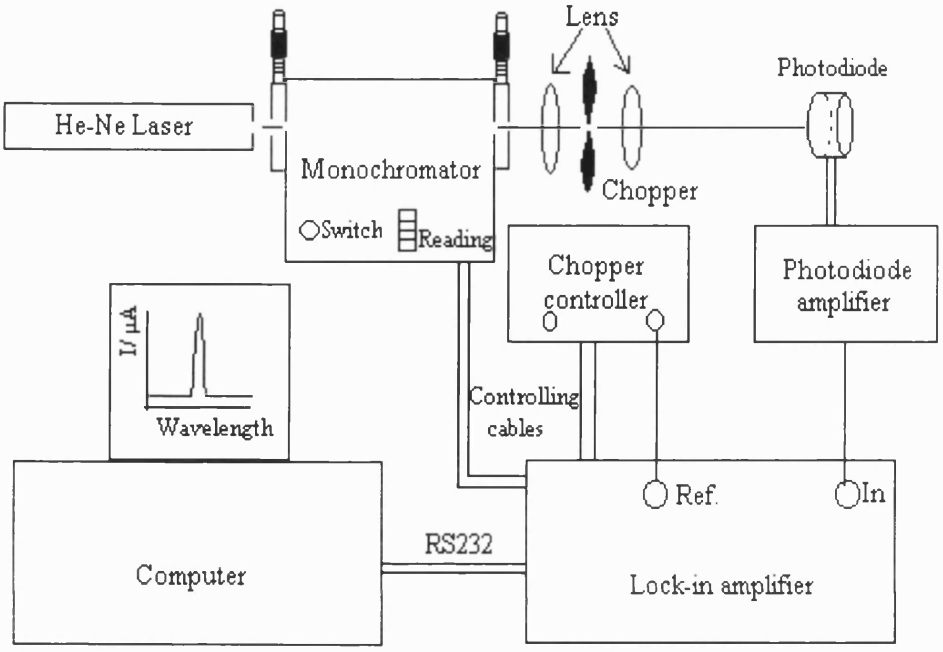

Figure 6.14 A experimental setup used for calibration of monochromator

6.8.2 Capacitance – Voltage Measurements

Capacitance voltage measurements for Mott-Schottky plots are widely used to characterise thin films to obtain doping density and flatband potentials. The experiments were based on using a phase sensitive detection technique. The experimental setup shown in figure 6.15 allows experiments to be carried out in the dark and under illumination.

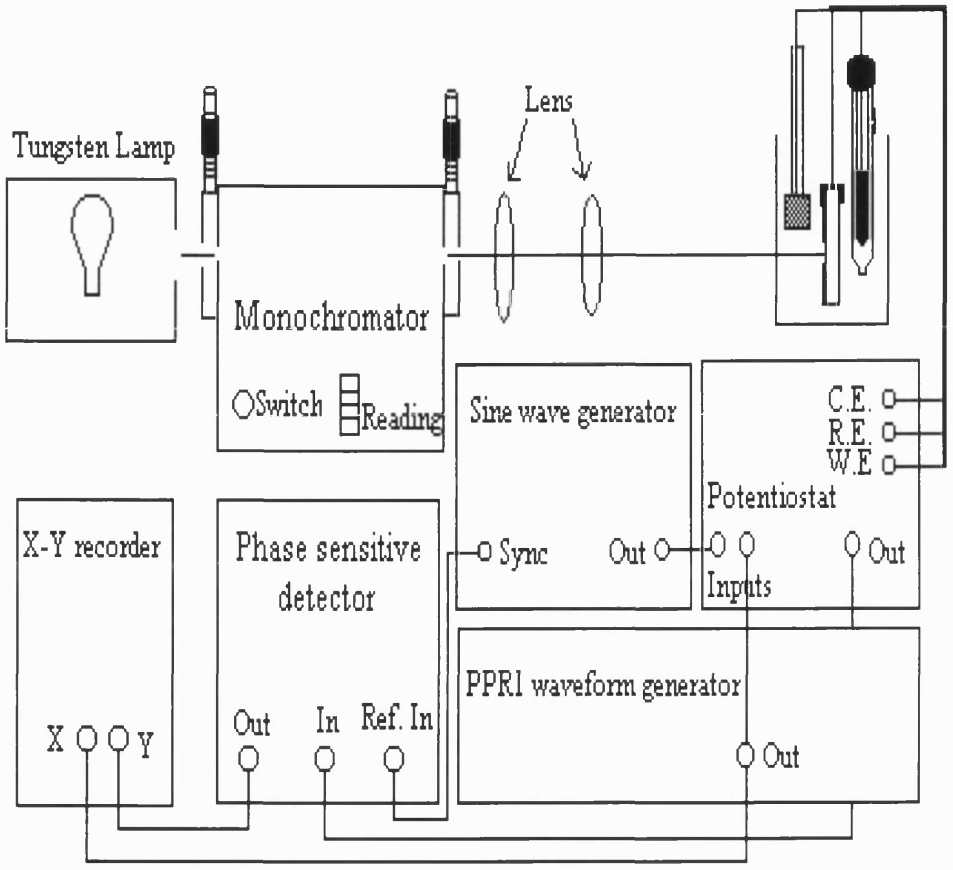

Figure 6.15 Experimental setup for capacitance voltage measurements

It can be seen from figure 6.15 that a sinusoidal modulated ac voltage generated by a sine waveform generator (Farnell LF1) was superimposed on the dc potential, which was scanned between the values of interest using a waveform generator (Hi-Tek Instruments, PPR1). The 90° component of the ac current, which is directly related to capacitance, was measured by the phase sensitive detector (9412, ORTEC Brookdeal) and recorded vs. potential by a chart recorder (Phillips PM8271). The system was calibrated using precision decade capacitance box (Time Electronics, 9000). The series resistance effects in the circuit were neglected.

6.8.3 Photocurrent Spectroscopy

The experimental arrangement for photocurrent spectroscopy is shown in figure 6.16. All data for photocurrent spectroscopy was collected using a PC computer with an RS 232 interface. This is linked to the monochromator stepper motor for automated wavelength scans. Light for a 120 W tungsten lamp (Bentham IL 1) passes through the front slit of the computer controlled monochromator (Applied Photophysics, f/3.4) interfaced to a stepper motor/driver (Applied Photophysics, 7602), and then the rear slit image was focused onto the thin film electrode by using lenses. A mechanical chopper (Bentham 218) was used to modulate the focused beam. The output of the potentiostat was connected to the lock-in amplifier (Stanford Research SRS 830) which synchronised to the frequency of the chopper. The total in phase photocurrent was measured and collected and averaged at each wavelength by the computer, which was connected to the SRS 830 by an RS 232 interface.

The photocurrent versus wavelength spectrum can be converted the IPCE spectrum for the samples measured using a calibrated Si photodiode (Macam Photometrics). The IPCE of the calibrated (standard) photodiode, Φ_{std}, may be calculated using equation [21,25]

$$\Phi_{std} = \frac{i_{std}}{P_{std}} \times \frac{hc}{\lambda q} = \frac{1240 i_{std}}{\lambda P_{std}} \qquad (6.1)$$

where i_{std} is the current measured from the standard photodiode in Am^{-2}, P_{std} is the power of the incident light in Wm^{-2}. λ is the wavelength of the incident light in nm. Normally the ration of i_{std} to P_{std} is termed "the absolute sensitivity of the photodiode". So the sample IPCE can be calculated from the simple relationship.

$$\Phi_{sample} = \frac{i_{sample}}{i_{std}} \times \Phi_{std} \qquad (6.2)$$

Where Φ_{sample} is the IPCE of the sample, i_{sample} is the current measured from the sample. A high IPCE means that the majority of the photon are being absorbed and converted to current, while a low IPCE indicates that the majority are being scattered or simply passing through the cell with no absorption.

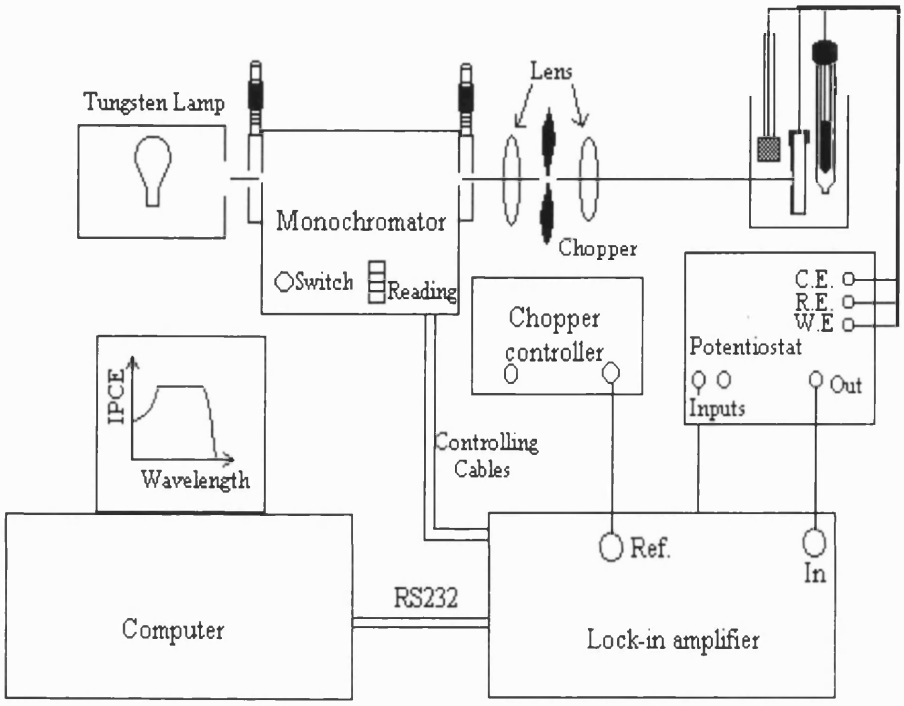

Figure 6.16 Diagram of the experimental setup used for photocurrent spectroscopy

6.8.4 Electrolyte Electroabsorbance/reflectance Spectroscopy

The setup diagram for electrolyte electroabsorbance spectroscopy (EEA) is illustrated in figure 6.17. A monochromatic light beam illuminated the thin film electrode perpendicularly. A 120 W tungsten lamp (Bentham IL 1) in combination with a diffraction grating monochromator (Bentham M 300, 1200 lines/mm) controlled by a computer was used to provide monochromatic illumination. The beam was focused on

the working electrode using a lens. After passing through the electrode in which the modulation of the electric field perturbs the optical constant of the thin film, the modulated beam was detected by a Si-photodiode (Macam Phtometrics) connected to a home-made current amplifier. The output of the amplifier was fed to a lock-in amplifier (Stanford SRS 830) interfaced to a computer via the RS 232 port. The computer also controlled the monochromator motor via the lock-in amplifier RS 232 port. The electrode dc and ac potentials were provided by the lock-in amplifier regulated by the computer as well. Typical values of frequency and amplitude of the modulation were 270 Hz and 100mV, respectively. The dc bias was typically zero versus SCE. The normalised $\Delta T/T$ against the wavelength was recorded, collected and stored by the computer.

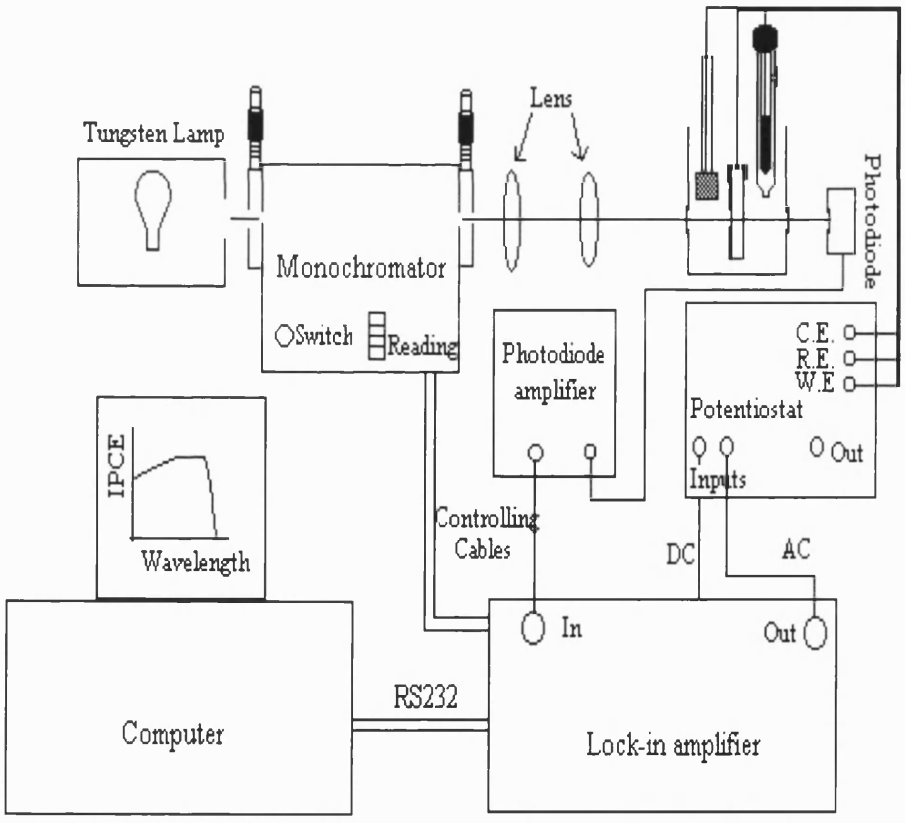

Figure 6.17 Diagram of the experimental setup used for electrolyte electroabsorbance spectroscopy

The experimental arrangement for electrolyte electroreflectance (EER) was similar to that for EEA. The angle of the incident light was slightly changed from 0^{o} to 45^{o}, the cell used was also changed from two-window to three-window cell. The detection photodiode was placed at an angle of 45^{o} to detect the reflected light. Dedicated software written by M. Bailes enabled communication between the computer and the lock-in amplifier, data acquisition and data processes to be performed through a series of simple operations on the screen menus.

6.8.5 Surface Analytical Techniques

There are several surface analytical techniques that were used in this study to characterise CdTe thin films. They are listed in the following table.

Name	Acronym	Model	Function	Literature
Atomic force Microscopy	AFM	Topometrix 2010 Discoverer	High resolution Surface morphology	[3]
Scanning electron microscopy	SEM	Jeol 6310 Jeol T330	Surface morphology	[4]*
X-ray diffraction	XRD	Phillips Diffractometer	Structural analysis	[5]
Wavelength Dispersive x-ray Analysis	WDX	Jeol Microprobe X-ray analyser	Deposit composition analysis	[4,5]*

* The Standard sample or crystal is needed for the reference.

** It was essential for cross-section images and WDX analysis to cut the samples properly. There were a few steps to do so. They are: 1) mark the sample in the right size with a marked pin; 2) scratch it with a diamond cutter very lightly in the one direction only; 3) put it in a plastic net, and dip into liquid nitrogen and then remove it away rapidly.

6.9 Back Contacts

Before fabrication of CdTe/CdS solar cells, the p-CdTe/n-CdS was etched in 50% diaminoethane (v : v) in water for 60 s to create a Te-rich surface, then gold was evaporated through a mask to form ohmic contacts. The size of spot was 2 × 2 mm. Figure 6.18 shows the gold contacts.

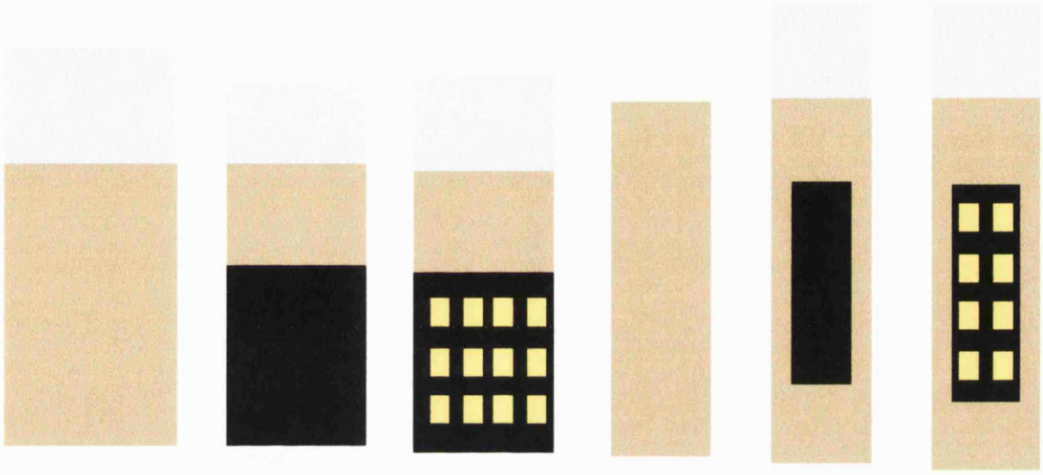

Figure 6.18 Back contacts of CdTe/CdS solar cells

6.10 Efficiency Measurements

It may seem a simple matter to measure solar cell efficiency by measuring the power in the incident sunlight using a pyranometer and the electrical power generated by the cell at the maximum power point. The difficulty in this method is that the performance of the cell measured in this way will depend on the solar spectrum, which varies with air mass, weather conditions, and so on. So it is very difficult to compare the performance of cell one with another. A standard reference solar simulator was used, which it consisted of a Xenon lamp with appropriate filters to give the intensity of the light of 1000 Wm^{-2} with a spectral distribution close to AM 1.5 (G). The experimental configuration used for efficiency measurements is shown in figure 6.19.

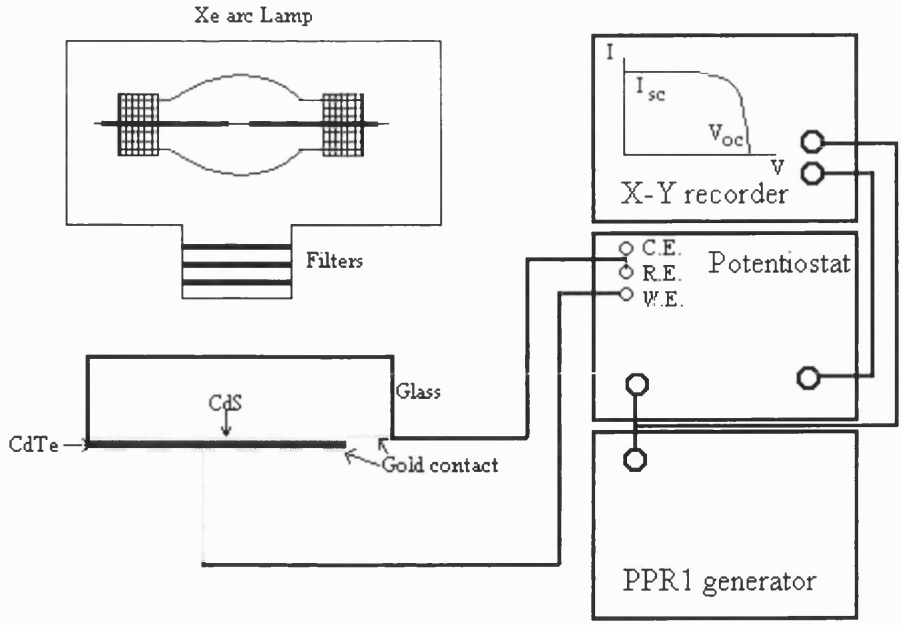

Figure 6.19 Diagram of the solar simulator system

It can be seen from figure 6.19 that the counter and reference electrodeconnections of the potentiostat were connected together, and then linked with SnO_2 conducting glass, the working electrode was contacted with the back contact via a moveable probe. The voltage was scanned from a low negative value to a higher positive one termed forward bias. The current follower output of the potentiostat and the potential applied were fed to an x-y chart recorder. The maximum power point was found from the product of the current photogenerated and the applied potential.

References:

1. A.J. Bard and L.R. Faulner, Electrochemical Methods, John Wiley & Sons, 1980.
2. A. Saraby-Reintjes, L.M. Peter, M.E. Özsan, S. Dennison and S. Webster J. Electrochem. Soc., **140**,2880 (1993).
3. Samual H. Cohen, Mona T. Bray and Marcia L. Lightbody, Atomic Force Microscopy/Scanning Tunneling Microscopy, New York: Plenum Press, c1994.
4. Joseph I. Goldstein, Scanning electron microscopy and X-ray microanalysis a text for biologists, materials scientists, and geologists, New York : Plenum Press, 1992
5. N.F.M. Henry, H. Lipson and W.A. Wooster, The interpretation of X-ray diffraction photographs, London : Macmillan, 1953

CHAPTER SEVEN

RESULTS AND DISCUSSIONS

OPTICAL AND ELECTRICAL CHARACTERISATION OF CdTe THIN FILMS GROWN BY A STIRRED CELL

7.1 Introduction

CdTe/CdS solar cells as well as cells fabricated from silicon and copper indium selenide (CIS) or copper indium gallium selenide (CIGS) are promising photovltaic devices for the huge demands of energy markets in the coming century, and they are being widely studied in many laboratories [1-20]. CdTe is one of the few II-VI compounds that can be doped as n- and p-type and is a direct-band-gap material. The band gap of crystal CdTe is 1.51 eV [21], which is close to the calculated optimum bandgap for AM 1.5 solar spectrum. The techniques for growth of CdTe thin films include 1) close-spaced sublimation (CSS) [7,14-15, 22-25], 2) metalorganic chemical vapour deposition [26-27], 3) molecular-beam epitaxy (MBE) [27-28], 4) sintering [29-30], 5) screen printing [31-32], 6) vacuum evaporation [33-34] and 7) and electrodeposition [1-6,8-12, 16,35]. CdS has a band gap energy of 2.45 eV, and transmits most of the visible spectrum. Vacuum deposition and spray pyrolysis have been more widely used to deposit CdS thin film than chemical deposition in the past decades. The reason for this is that subtle change in deposition temperature, reagent concentration, and substrate type were found to change the morphology and electrical properties of the chemical bath deposit. However, a greater understanding of the mechanisms of chemical bath film growth has been achieved and films with the same properties as deposited by those traditional routes can be grown reproducibly. The chemical bath deposition (CBD) process has been shown to be a low cost effective route to the production of uniform adherent films for large area (at least 30 × 30 cm) electrodeposited solar cells [11]. The thickness of the CdS film in CdTe/CdS solar cells plays an important role [36]. For example, the thickness of the CdS film in the highest

efficiency solar cells (16%) in the small area for CdTe/CdS was reduced from 80 nm to ~ 50 nm [7]. Research in the past has also managed to make large area devices (~7000 cm^2 modules [37]) with reasonable initial efficiency of ~9%. However, the use of these devices in terrestrial solar energy conversion requires at least 15% module efficiency with a lifetime of about 25 years [38]. The major problem for achieving these goals is the lack of understanding of the materials and of the complex interfaces in this device.

The aim of this work is to contribute towards the understanding of this complex device by conducting a series of experiments on materials and interfaces and combining the information with a new model to derive characteristic material parameters.

Capacitance voltage experiments are normally carried out to obtain the doping density and the flatband potential using Schottky barriers (metallic contacts) [39]. Few studies have been made using an electrolyte as a contact [40]. The main benefit of the electrolyte contact is that it avoids the risk of modifying the properties of the surface during the formation of the metallic contact layer.

Electrolyte electroabsorbance/reflectance (EEA/EER) spectroscopy has been used extensively to characterise single crystal and thin film semiconductors. A few studies on CdTe/CdS thin films by EER/EEA have been reported [6,12, 41-42]. Two parameters, the bandgap energy (Eg) and the broadening parameter (Γ), can be obtained by fitting a third-derivative spectrum using the fitting function discussed in chapter 5. Of particular importance is the broadening parameter which is linked with structural or compositional inhomogeneity. Larger values of Γ may indicate the existence of a high density of stacking faults in the crystal and thin film [40]. The diffusion of sulphur from the CdS into the CdTe film has been investigated recently by

Lane et al [17]. The shift in Eg measured from the EER spectrum of the annealed CdTe/CdS film has further confirmed that sulphur diffusion occurs [12].

7.2 Voltammogram and Definition of Deposition Conditions

Panicker et al [45] first grew CdTe thin films by electrodeposition and described the deposition conditions in detail. The range of CdTe deposition potential was from 0.143 to 0.824 V versus NHE at 25°C. The ratio of Cd to Te in the deposit was strongly dependent on the deposition potential.

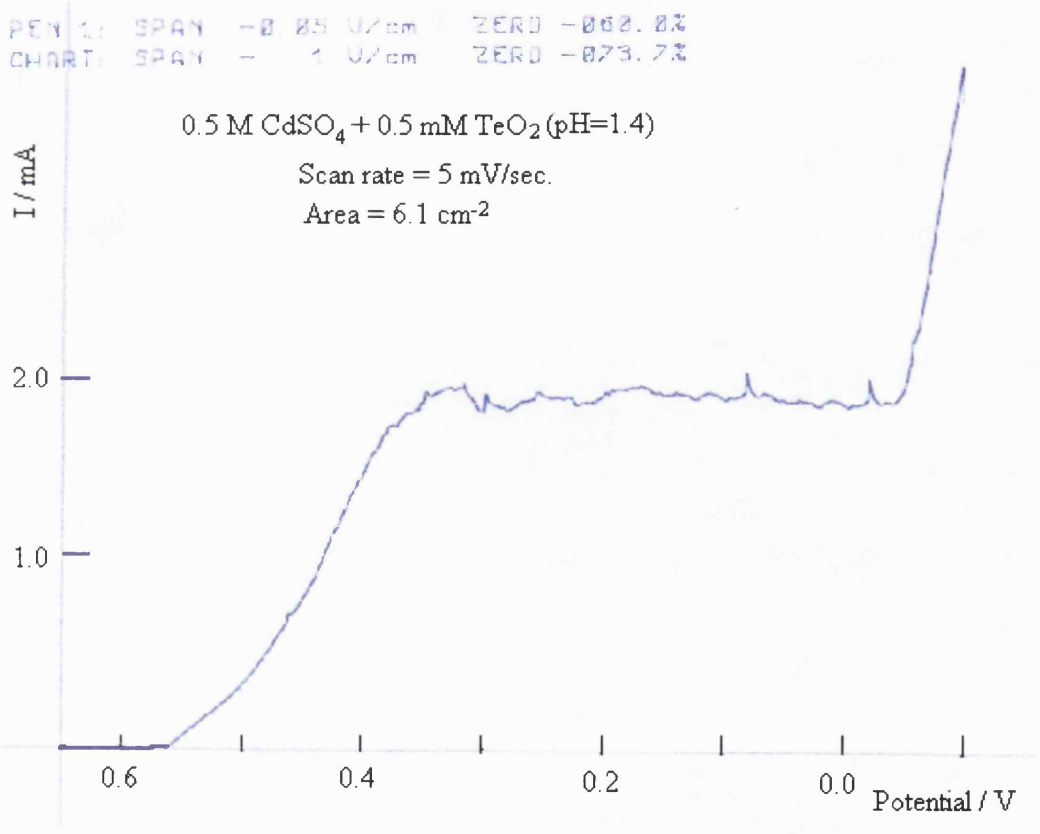

Figure 7.1 Linear sweep voltammogram for the deposition of CdTe from 0.5 M $CdSO_4$, 0.5 mM $HTeO_2^+$ (pH=1.4) onto a SnO_2 (F)/CdS surface at 85°C in stirred solution. Electrode area 6.1 cm^2, scan rate 5 mV s^{-1}.

Figure 7.1 shows an experimental current-voltage response for a transparent CdS/SnO_2 electrode with a masked area of 6.1 cm^2 at 85°C in the stirred solution. The figure shows an onset of deposition at ca. 0.56 V vs Cd^{2+}/Cd reference electrode, followed by a rise in the current to a plateau beginning at ca. 0.35 V up to ca. –0.05 V. After the plateau there is a steep rise due to Cd deposition. The process in the range of plateau appears to be diffusion controlled process because potential changes do not cause changes in current. The deposition current only varied with mass transport of the TeO_2 in the solution and was controlled by the speed of the stirring bar and solution temperature. The small oscillations on the plateau current are due to stirring. The shape of the linear sweep voltammogram is quite similar to that reported in the literature [10].

CdTe films were deposited from stirred solution at controlled potentials in the range +5 mV positive to Cd^{2+}/Cd reference electrode. +5 mV was suggested by Kampmann et al [46] as an ideal value for obtaining stoichiometric films. The electrodeposition current density was set at 0.30 ± 0.05 mA cm^2 by controlling the stirrer speed. A series of thicknesses of CdTe were deposited. Each thickness of CdTe sample was duplicated in case of failure or damage to the sample. Film thicknesses were determined from the deposition charge and were confirmed by SEM and profilometry (Talystep profilometer). The values agreed within 5%.

Figure 7.2 shows samples of as-deposited CdTe. The thick films are black. Thinner films are partially transparent. Charge and thickness data for samples electrodeposited in the stirred cell are listed in Table 7.1.

Figure 7.2 Pictures of some of the electrodeposition samples taken by digital camera.

Table 7.1 lists 8 samples of differing thickness electrodepositied in the stirred cell.

Table 7.1 Samples with the deposition parameters

Sample No	Charge/ C	Size/ cm	t/sec.	Thickness+	Colour
1	15.53	2.2 × 2.5	94150	2.0μm	Dark
2	15.53	2.2 × 2.5	94268	2.0μm	Dark
3	13.20	2.2 × 2.5	80000	1.7μm	Dark
4	13.20	2.2 × 2.5	79500	1.7μm	Dark
5	7.77	2.2 × 2.5	47070	1.0μm	Dark
6	7.77	2.2 × 2.5	47000	1.0μm	Dark
7	4.04	2.2 × 2.6	23540	0.5μm	Dark
8	4.04	2.2 × 2.5	25430	0.5μm	Dark
9	1.55	2.2 × 2.5	911	0.2μm	Grey*
10	1.55	2.2 × 2.5	900	0.2μm	Grey*
11	0.78	2.2 × 2.5	450	0.1μm	Grey*
12	0.78	2.2 × 2.5	456	0.1μm	Grey*
13	0.39	2.2 × 2.5	235	50nm	Grey*
14	0.39	2.2 × 2.5	228	50nm	Grey*
15	0.16	2.2 × 2.5	95	20nm	Slight blue
16	0.16	2.2 × 2.5	92	20nm	Slight blue

* slightly blue. + calculated from deposition charge using density of CdTe = 5.855 g cm^{-3} taken from [47]

All as-deposited samples were kept for at least 48 hours in a desiccator over silica gel before any further use or analysis. If this step was omitted, the films peeled off or

photocorroded easily during measurements or produced pinholes during thermal treatment.

In order to compare results, the samples were cut in half. One was kept as n-type, the other was annealed at 430°C in air for 15 minutes to convert the n-CdTe to p-type.

7.3 Absorption Measurements

Absorption experiments were carried out in a UV/vis spectrometer (Lambda 10, Perkin-Elmer) with an annealed CdS film as a reference. The absorption coefficients were obtained using Beer's Law, and equation 5.59 was used to obtain the band gap of CdTe using exterpolation of the linear part. It can be seen from figure 7.3 that the band gap was 1.52 – 1.54 eV for as-deposited films, and 1.50 –1.52 eV for annealed films. The line slopes in the annealed plot are steeper. This suggests that structural disorder in the as-deposited films is removed by annealing. The absorption data for thin samples were more difficult to analyse due to problems with interference effects.

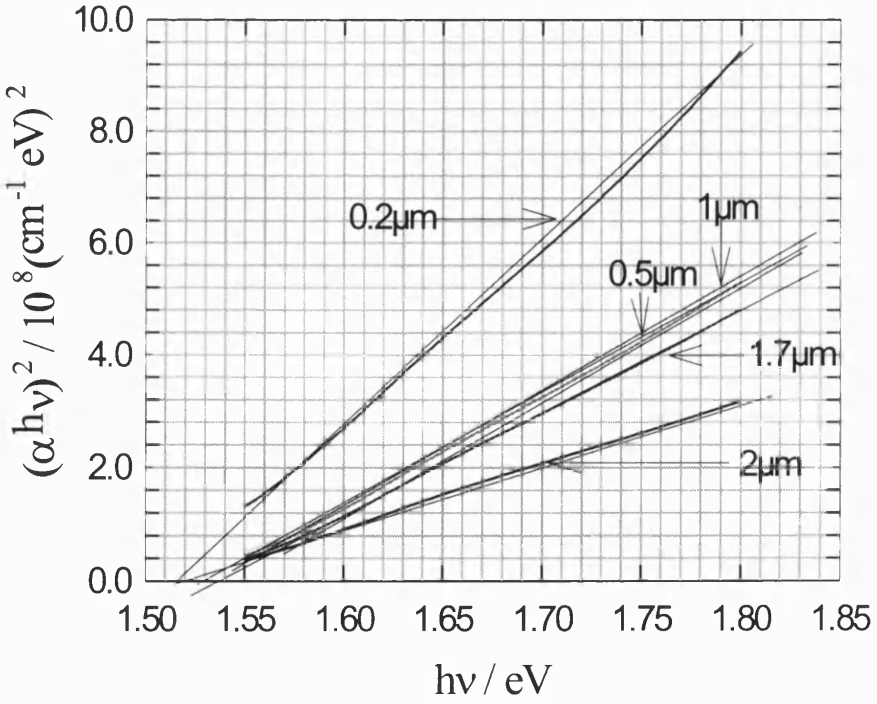

Figure 7.3a Plots to obtain Eg for as-deposited films

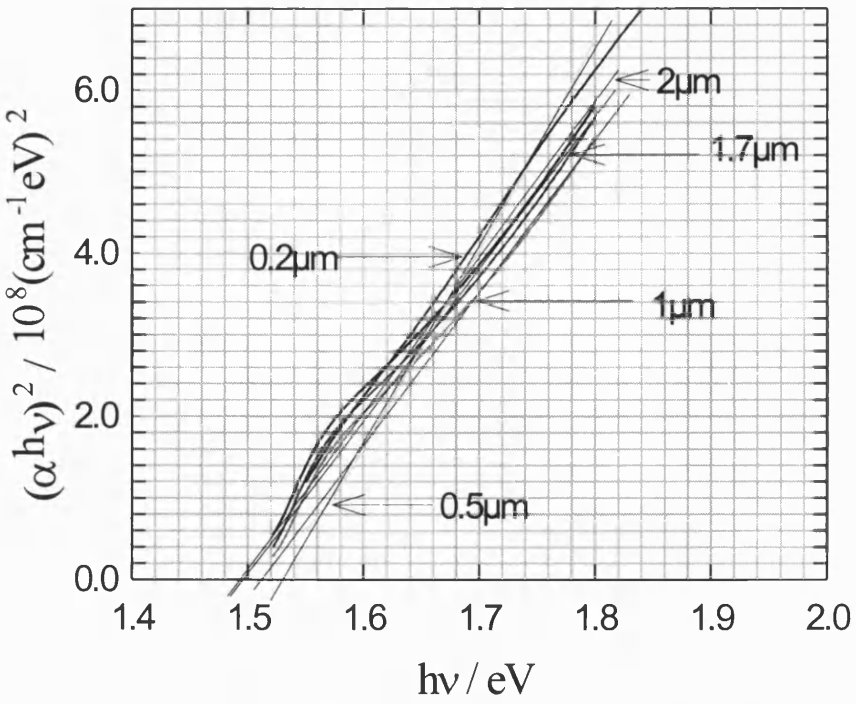

Figure 7.3b Plots to obtain Eg for annealed films

7.4 WDX and XRD

The results for WDX experiments showed that ratio of Cd to Te for all CdTe samples (as-deposited and annealed) was within a range of 1 ± 0.01.

The XRD spectra of Cd sheet (99.999%) and CdS coated SnO_2 conducting glass XRD are shown in figures 7.4 and 7.5, respectively.

The as-deposited CdTe films were uniform and strongly adherent, and they exhibited pronounced <111> preferential orientation in the XRD spectra as shown in figure 7.6a. Thermal treatment does not result in significant recrystallisation in those samples as shown in figure 7.6b. Although the peak <111> intensity decreases significantly, the other peaks like <220>, <311> and <400> come out only with very weak intensities. The ratio of the <220> intensity to the <111> intensity is introduced to quantify texture of the CdTe films. It has been reported that the ratio of the <220> to the <111> was 1.25 [44]. The ratio of the peak intensities, RPI, was normalised by that of a random bulk CdTe power. Details ware given in chapter 8.

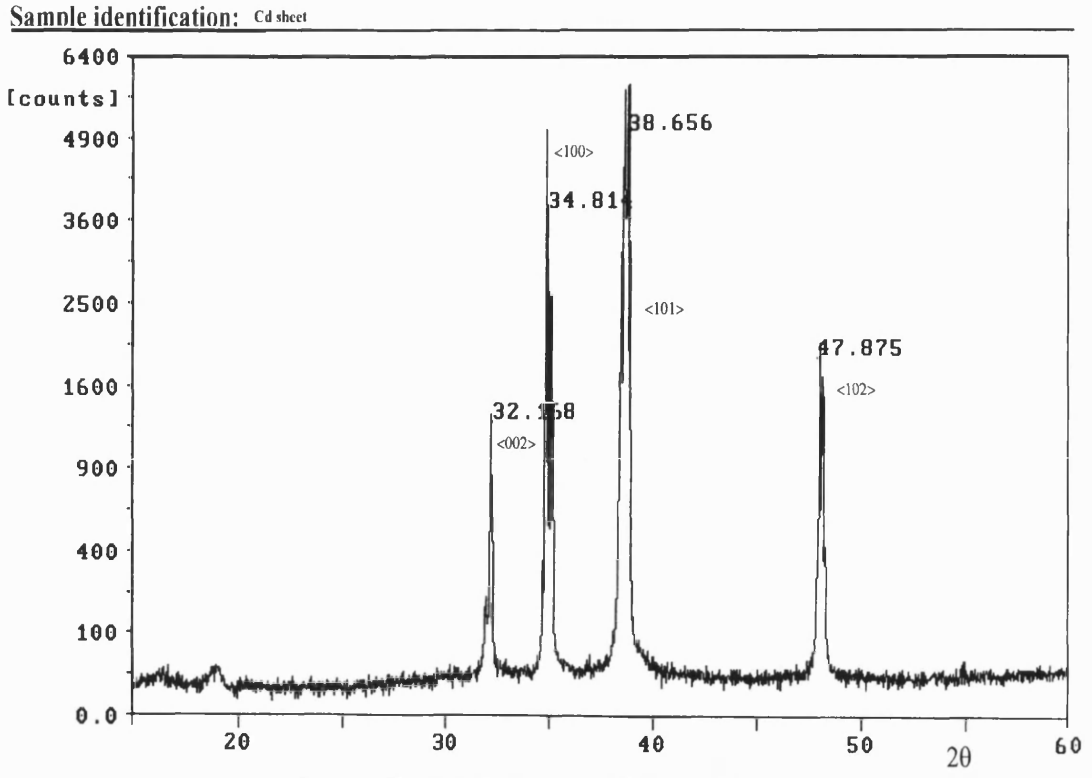

Figure 7.4 XRD pattern of Cd sheet.

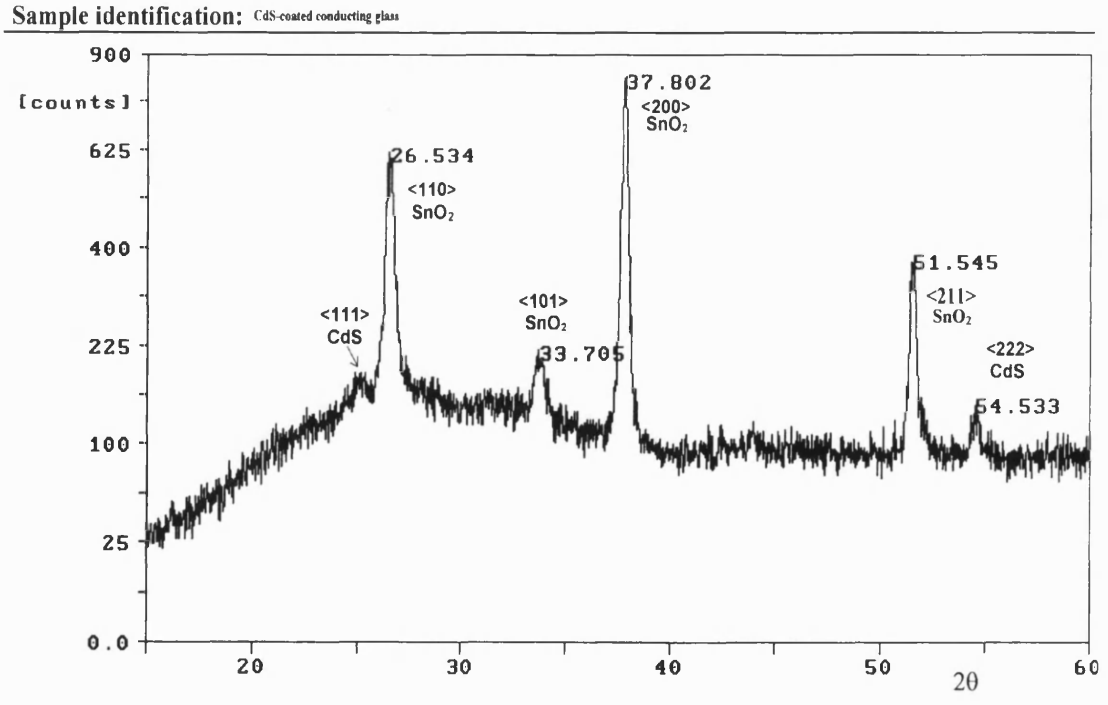

Figure 7.5 XRD pattern of CdS coated SnO_2 conducting glass (annealed).

Most of these peaks can be observed in all CdTe/CdS thin films.

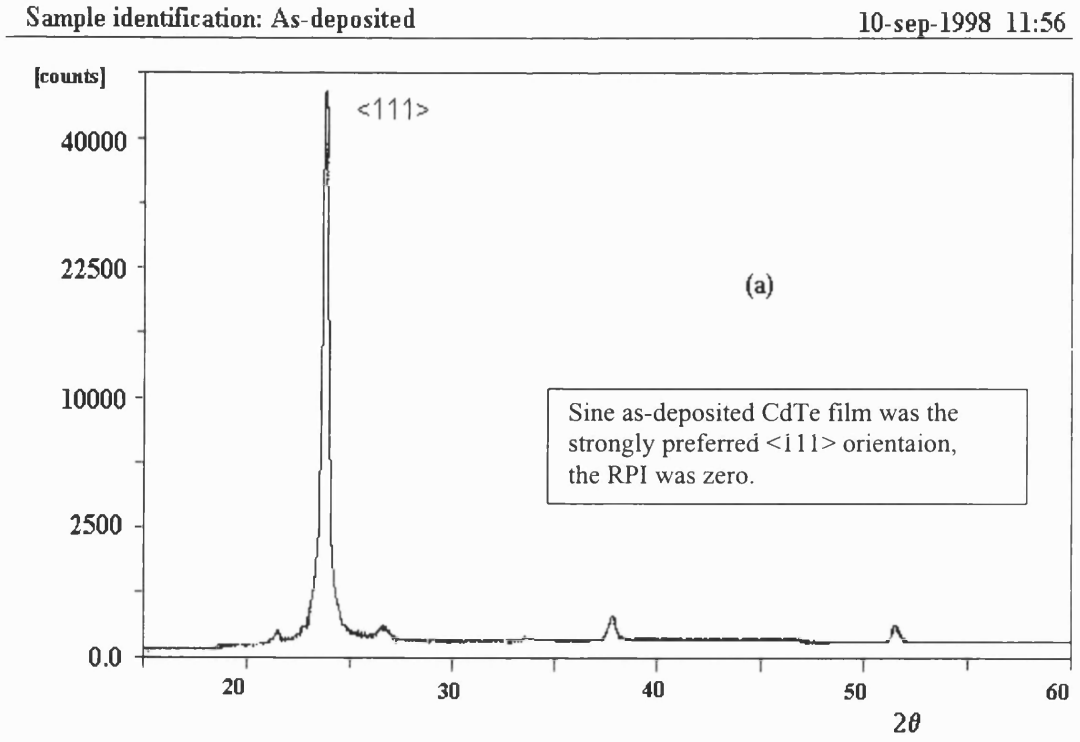

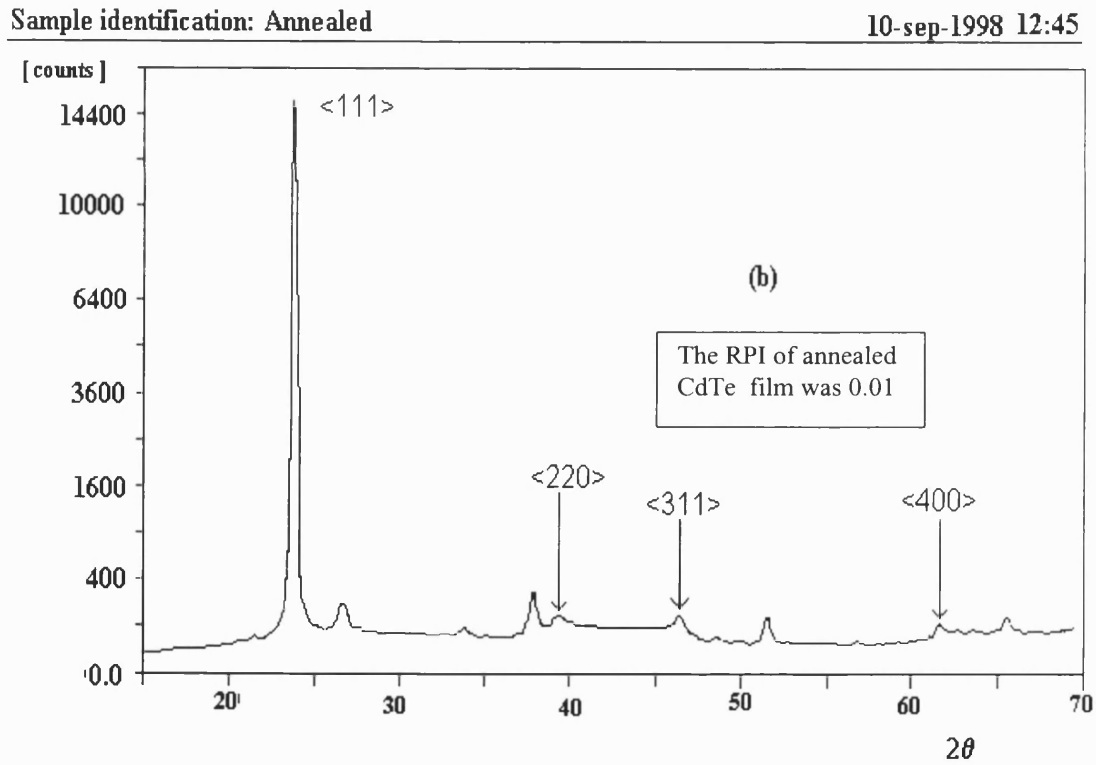

Figure 7.6 XRD spectra of as-deposited and annealed CdTe film prepared in the stirred cell. (a) as – deposited and (b) annealed

7.5 AFM and SEM Images

AFM and SEM were carried out on as-deposited and annealed CdTe samples. The images showed that the grain size of as-deposited samples was less than 100 nm, and the grain size significantly increased after annealing. Figure 7.7 shows AFM images of as–deposited and annealed CdTe samples.

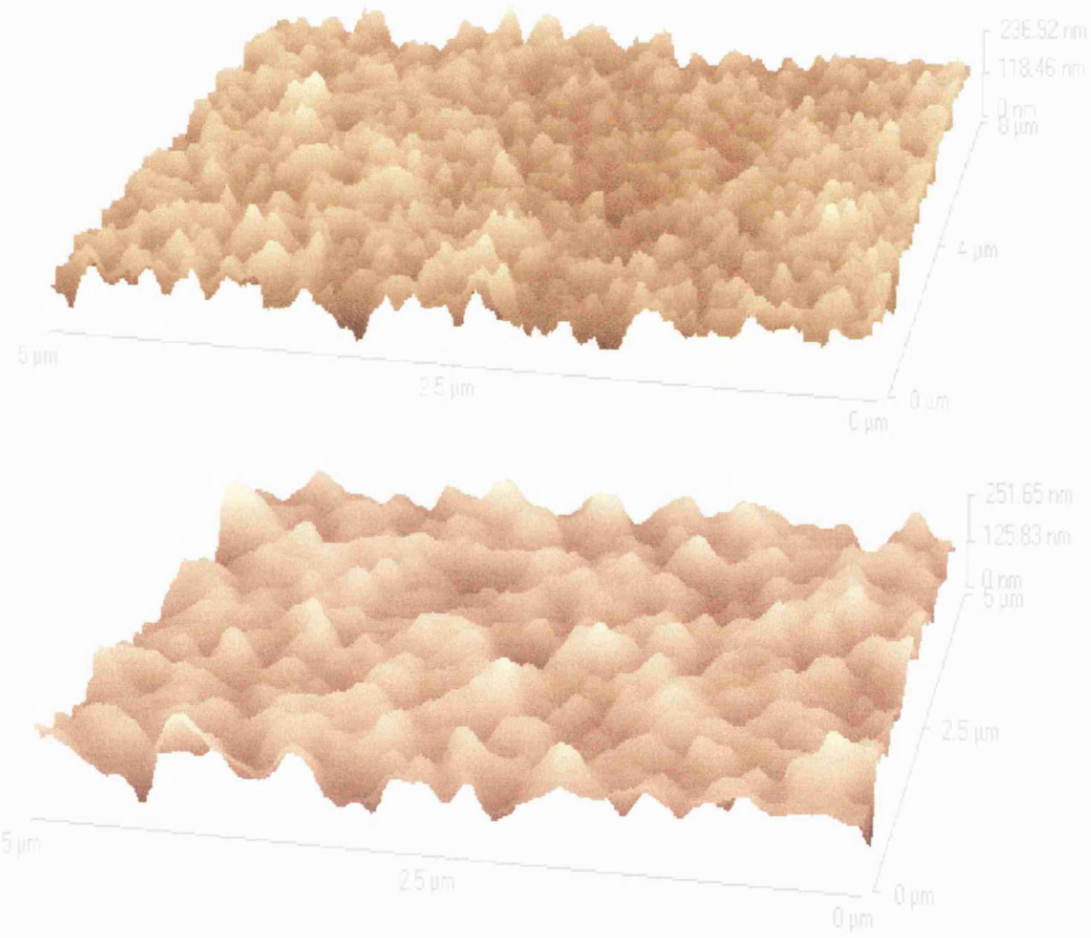

Figure 7.7 AFM images of as-deposited and annealed CdTe films (2µm)

—— upper image: as-deposited, lower image: annealed.

The increase in the grain size was also confirmed by SEM images as shown in figure 7.8.

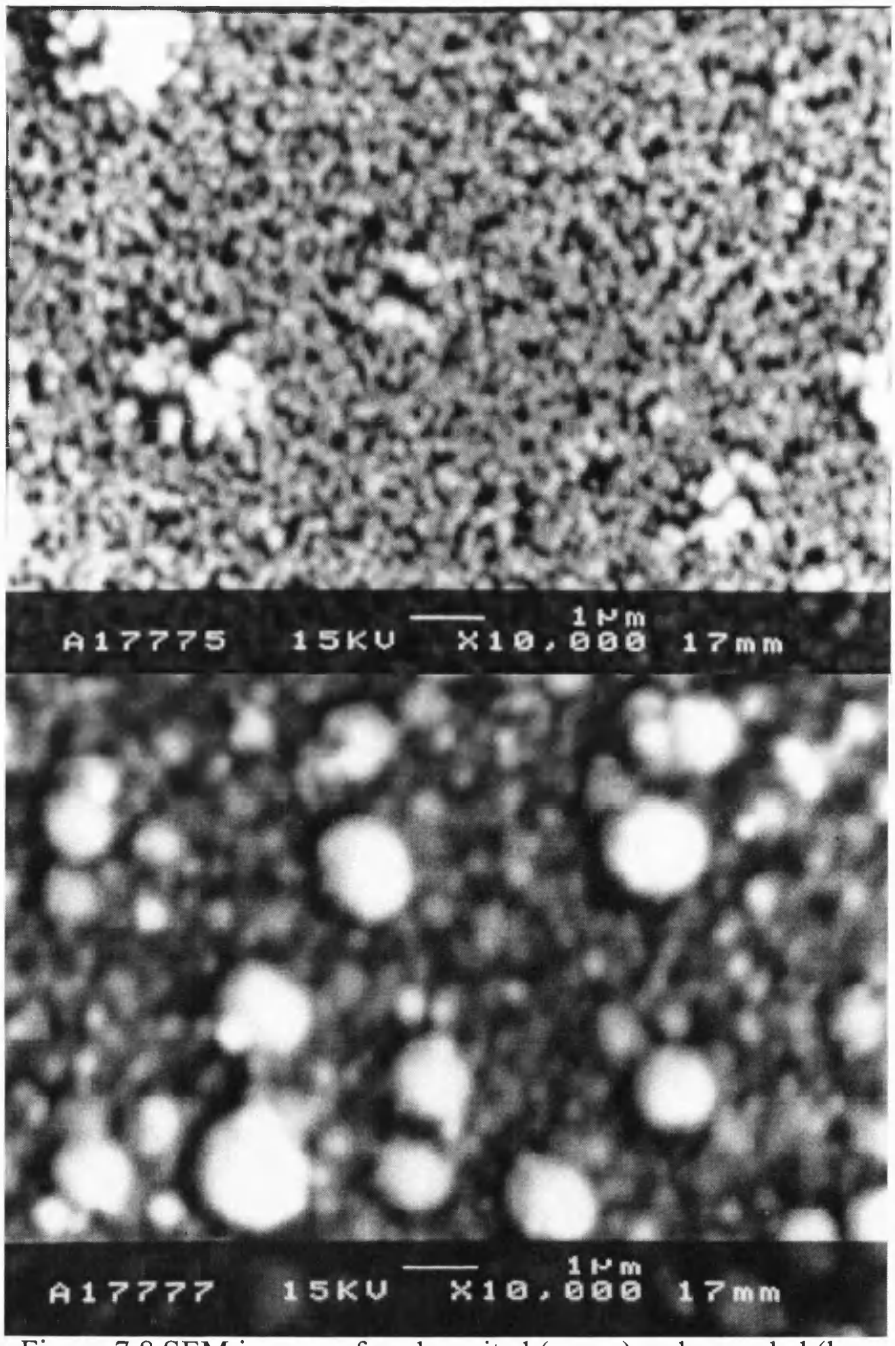

Figure 7.8 SEM images of as-deposited (upper) and annealed (lower) CdTe films (samples were the same as in figure 7.7).

SEM also was used to confirm the thickness of the samples by the images of the cross-section of the samples. Figure 7.9 shows a cross-section image of a 2μm annealed CdTe film.

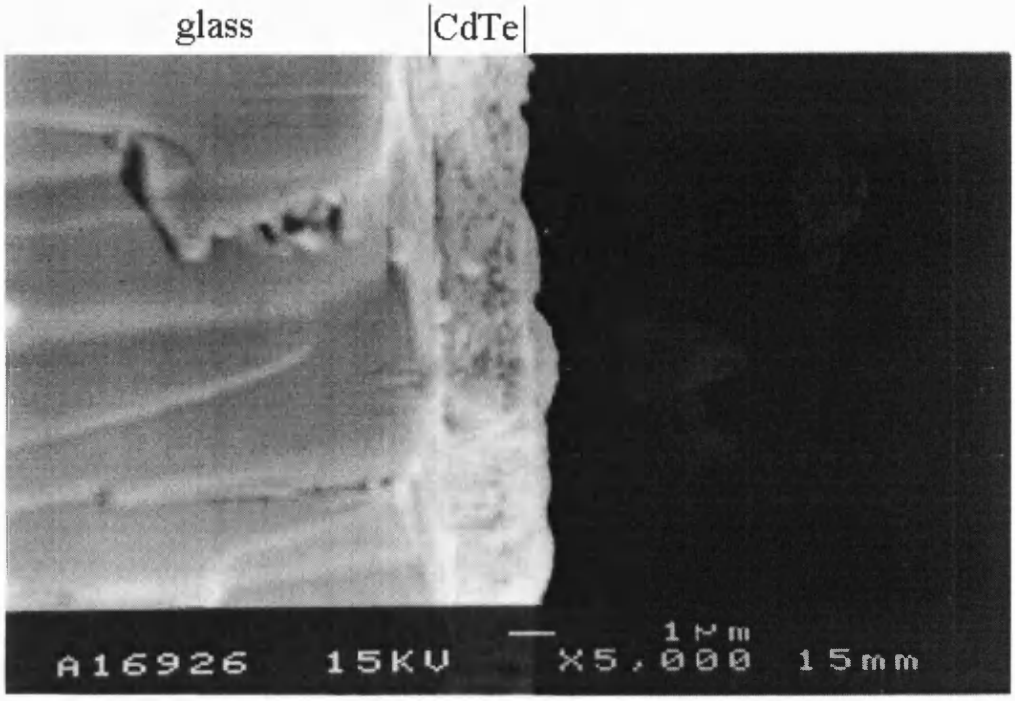

Figure 7.9 A cross-section image of a 2 µm annealed film.

Note that the film is not very uniform

7.6 Capacitance-Voltage Measurements

Capacitance-voltage measurements using solid contacts are commonly used to characterise the dopant densities in semiconductors. An electrolyte contact was used for the measurements reported here. The experiments for both as-deposited and annealed samples were made in the dark and under illumination (650nm). Since the Mott-Schottky plots for as-deposited and annealed films are similar, it might be concluded that type conversion does not occur. However the photocurrent spectra for electrolyte and glass side illumination show clearly that the annealed films are p-type. The apparent similarity in the Mott-Schottky plots arises from a Schottky junction at the as-deposited CdTe/electrolyte interface, whereas the annealed films have an internal n-p junction between the n-CdS and the p-CdTe [48]. The Mott-Schottky plots for both junction are similar. Mott-Schottky plots for a 2 µm CdTe film are shown in figure 7.10.

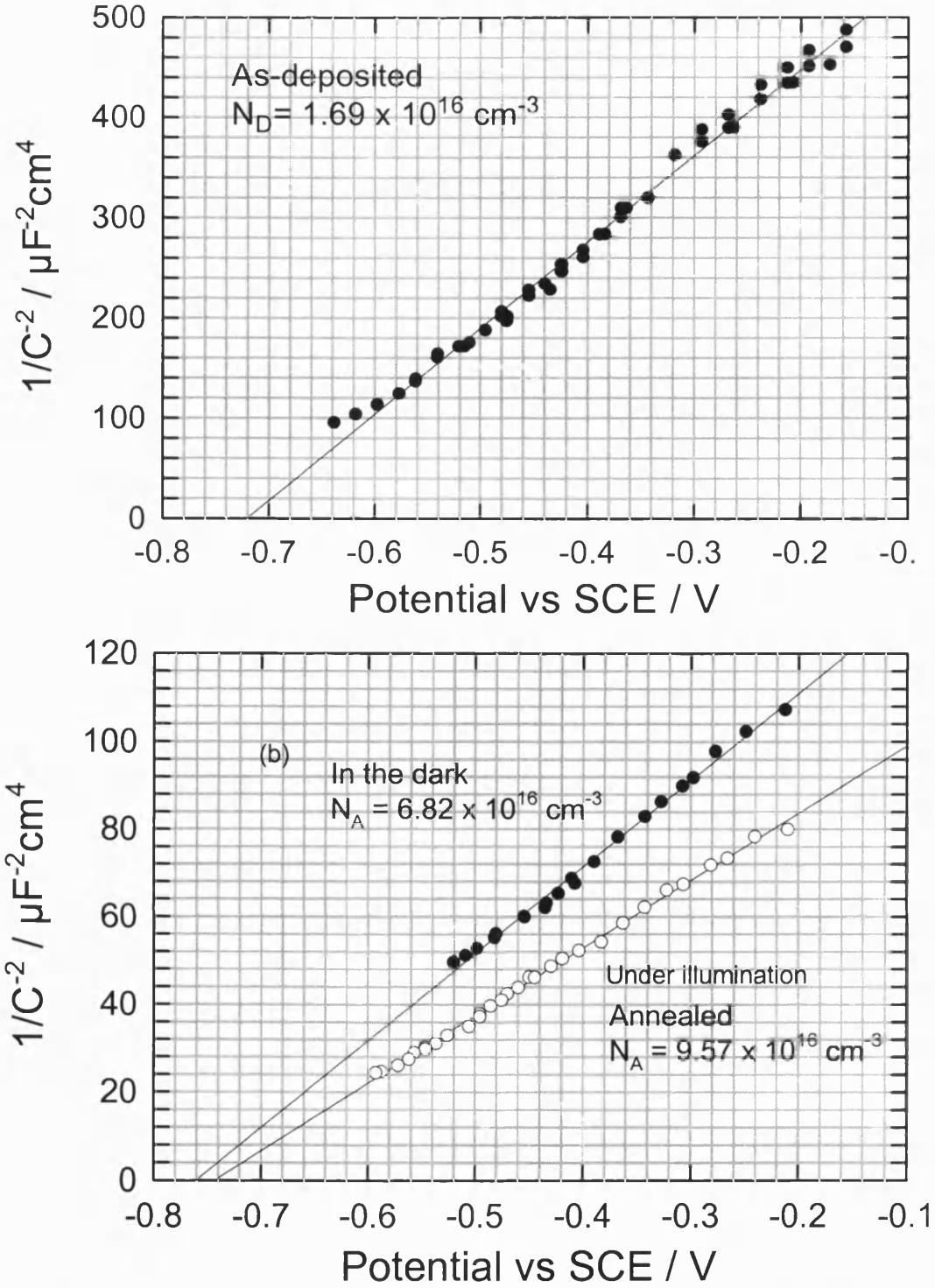

Figure 7.10 Mott-Schottky plots for as-deposited and annealed CdTe films (2μm) measured in 1 M Na_2SO_3 solution. The experimental conditions were: a 8mV (p-to p) and 10KHz ac, 650nm monochromatic light for illumination. There were no significant differences in the flatband potential for in the dark and under illumination.

(a) as-deposited (n-CdTe/electrolyte junction)

(b) annealed (n-CdS/p-CdTe)

The structures of the junctions in the as-deposited and annealed samples are shown schematically in figure 7.11.

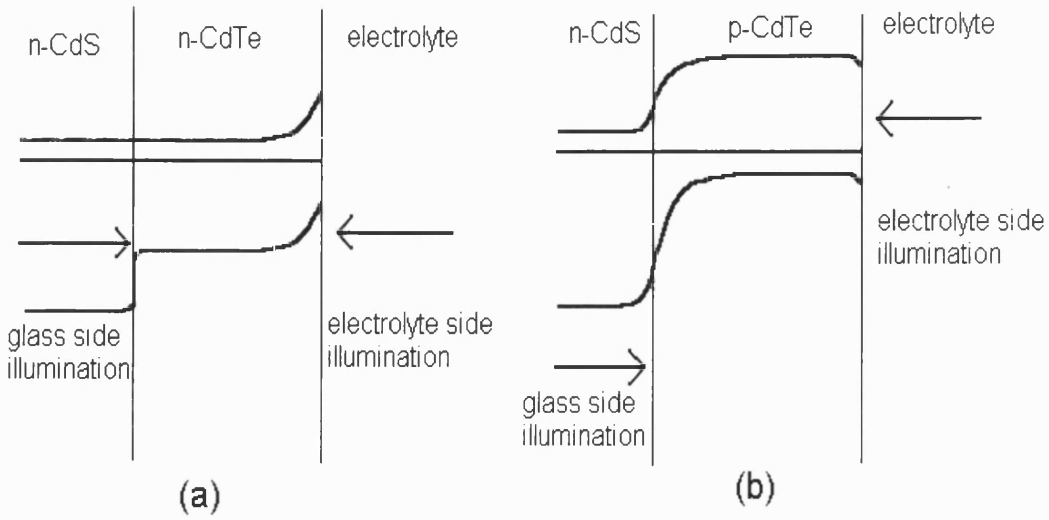

Figure 7.11 Qualitative band bending structures of CdTe/CdS thin films.
An electrolyte as a contact. Illumination was 650nm monochromatic light.
(a) as-deposited and (b) annealed

Since a high concentration of the electrolyte was used in both cases, the Helmholtz capacitance, C_H, and the diffuse layer capacitance, C_d, were bigger than C_{SC}. According to equation 5.32, the measured capacitance was the space charge layer capacitance. So the Mott-Schottky plot can be used to obtain the doping density and the flatband potential V_{fb}. It can be seen from figure 7.10 that monochromatic light did not affect the slope and the intercept for as-deposited films, while the flatband potential changed slightly to more positive values for annealed films. The shift in the flatband potential under illumination for the annealed films is small, indicating that surface charging is minimal when Na_2SO_3 is used as a hole scavenger. In the case of the type converted film, the meaning of the 'flatband potential' is not clear since the junction is internal.

For the as-deposited films, the slope in the Mott-Schottky plot is linked to the doping density of the film (seen equation 5.34) and the intercept is the flatband potential. For the annealed films, the slope of the Mott-Schottky plot can still be used to obtain the doping density of the p-CdTe if it is assumed that the n-CdS is highly doped so that the total space charge capacitance is determined largely by the doping density of the p-CdTe. The width of the space charge region under certain applied potentials can be then calculated by equation 5.110. The results for thicker films are listed in Table 7.2. The applied potential for calculating the width of the space charge region was zero vs. SCE. The capacitance-voltage experiments for thin films failed due to photocorrosion. The values of the flatband potential for as-deposited CdTe are in agreement with the literature [49-50] which is – 0.8 V vs SCE independent of pH 4.8 – 12.8 measured at 1KHz. The doping density for annealed films is higher than that for as-deposited ones.

Table 7.2 V_{fb} and doping densities for different thicknesses of the CdTe films

Thickness/μm	*Type of films*	*V_{fb} vs. SCE*	*Doping density/cm^{-3}*	*W W^0/μm*
2.0	As-deposited	~ - 0.72	1.68×10^{16}	0.22
2.0	Annealed	~ - 0.76	9.57×10^{16}	0.10
1.7	As-deposited	~ - 0.75	2.24×10^{16}	0.19
1.7	Annealed	~ - 0.84	6.27×10^{16}	0.13
1.0	As-deposited	~ - 0.80	2.43×10^{16}	0.18
1.0	Annealed	~ - 0.82	9.87×10^{16}	0.11
0.5	As-deposited	~ - 0.70	6.90×10^{15}	0.33
0.5	Annealed	~ - 0.75	3.34×10^{16}	0.16

Lincot et al [46] have fitted the one-side-illumination spectral response using the Gärtner equation [51] and their analysis gave the doping density for as-deposited CdTe films deposited at +5mV vs. Cd^{2+}/Cd as 1.9×10^{16} cm^{-3}. The corresponding width of the space charge region was 0.32 μm at 0.5V vs. a saturated K_2SO_4 mercury sulfate electrode (+0.65V vs.SHE). In the present work the doping densities for the annealed CdTe films were in a range of 2.4 to 9.6×10^{16} cm^{-3} which is in agreement with the value of 5×10^{16} cm^{-3} in literature [52] which was determined by Mott-Schottky plots with solid contacts. It was assumed for calculating the width of the space charge region for the annealed films that $\Delta\phi_{sc}$ = 1V. The width of the space charge region for $\Delta\phi_{sc}$ = 1V is termed W^0.

7.7 Photocurrent Spectroscopy

The photocurrent voltage characteristics of 2μm CdTe/CdS films are shown in figure 7.12. It can be seen from the figure that the as-deposited film does not exhibit a well-defined photocurrent plateau. Instead the current continues to increase with increasing reverse bias. This means that hole trapping occurs and that the films have high defect densities. This is supported by the fact that the EER/A spectra of the films are very broad (see section 7.9). By contrast, type converted films exhibit a well-defined photocurrent plateau and much narrower EER/A.

Since an electrolyte was used as a contact, photocurrent spectra for illumination from the glass (G) and electrolyte (E) sides for both as-deposited and annealed samples were obtained. The spectra give information not only on the incident-to-photocurrent-conversion-efficiency (IPCE), but also on the band gap of the films. G and E photocurrent spectra may also provide information on the width of the space charge region and the diffusion length of the minority carriers if theoretical treatments are introduced. Figure 7.13 shows photocurrent spectra of thicker as-deposited CdTe

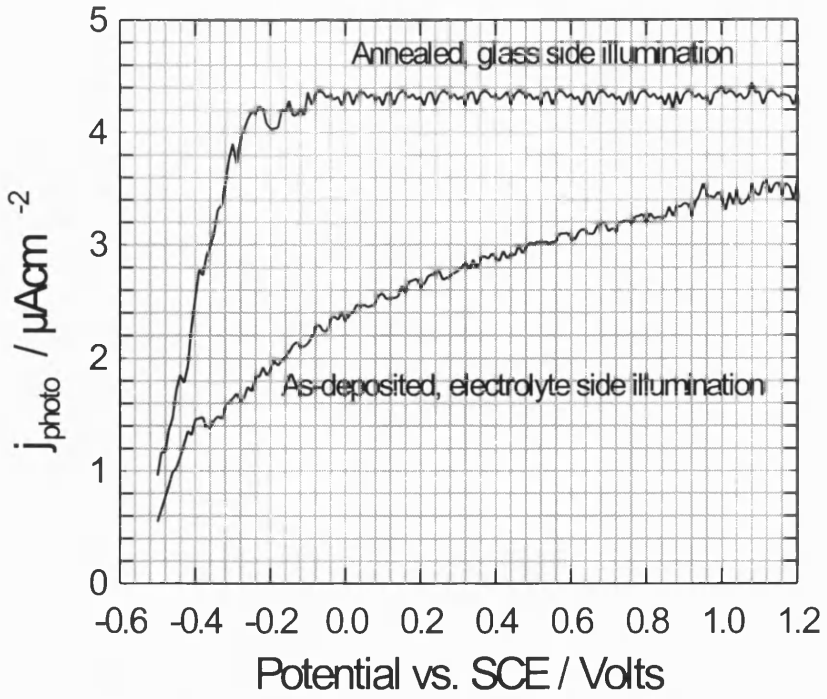

Figure 7.12 Photocurrent of 2μm CdTe films against voltage under illumination with 700 nm light.

samples, and figure 7.14 shows the photocurrent spectra of thinner films. It can be seen from figure 7.13 that 1) a higher photocurrent response is observed when illumination is from the electrolyte side (E), indicating that the junction is located in the electrolyte/n-CdTe interface; 2) a low photocurrent response is observed when light passes through the glass side (G) because most of light is absorbed by CdTe before it reaches the junction except close to band edge. Figure 7.14 indicates that the photocurrent responses of the thinner films (less than 200nm thick) for both G and E illumination geometries overlap. This is because the film thickness is not greater than the width of the space charge region, and the absorbed light within the space charge region converts photons that are collected by external circuit.

Heat treatment resulted in type conversion of the CdTe and substantial changes in the photocurrent spectra. The spectra of the thicker annealed CdTe films illuminated from the glass substrate and electrolyte sides are shown in figure 7.15.

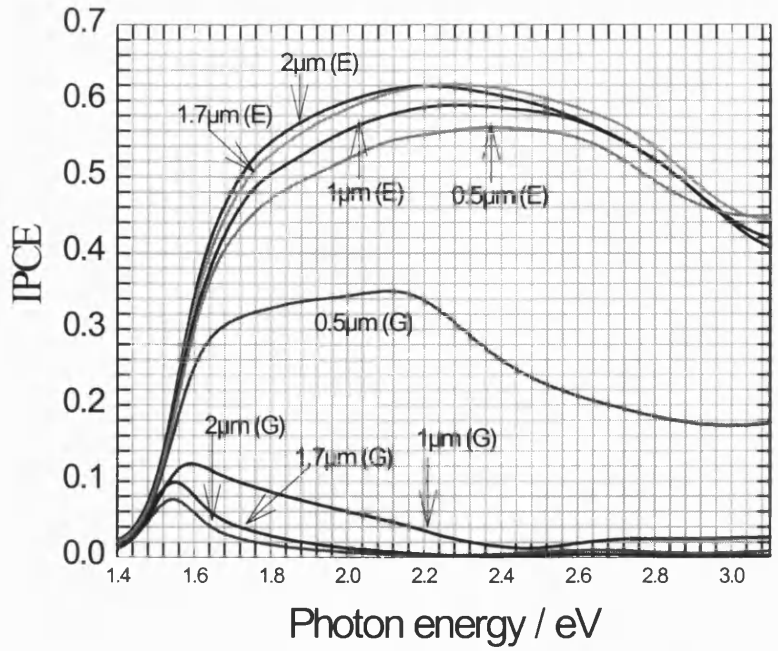

Figure 7.13 Normalised photocurrent spectra (uncorrected for reflection losses) for thicker as-deposited CdTe films from stirred solution. Electrolyte: 0.1 M Na_2SO_3. CdTe film thicknesses as shown. Illumination either from the electrolyte side (E) or through the glass side (G).

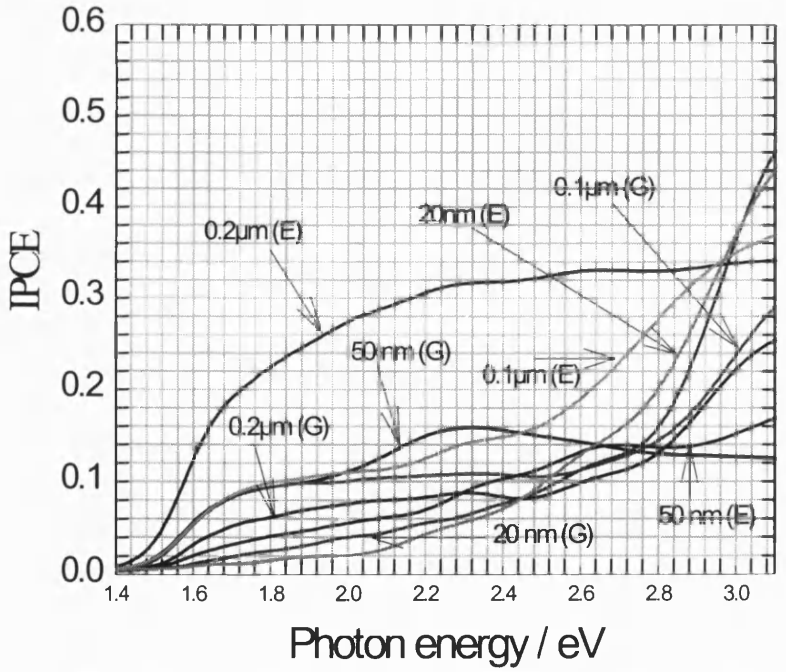

Figure 7.14 Normalised photocurrent spectra (uncorrected for reflection losses) for thinner as-deposited CdTe films from stirred solution. Electrolyte: 0.1 M Na_2SO_3. CdTe film thicknesses as shown. Illumination either from the electrolyte side (E) or through the glass side (G).

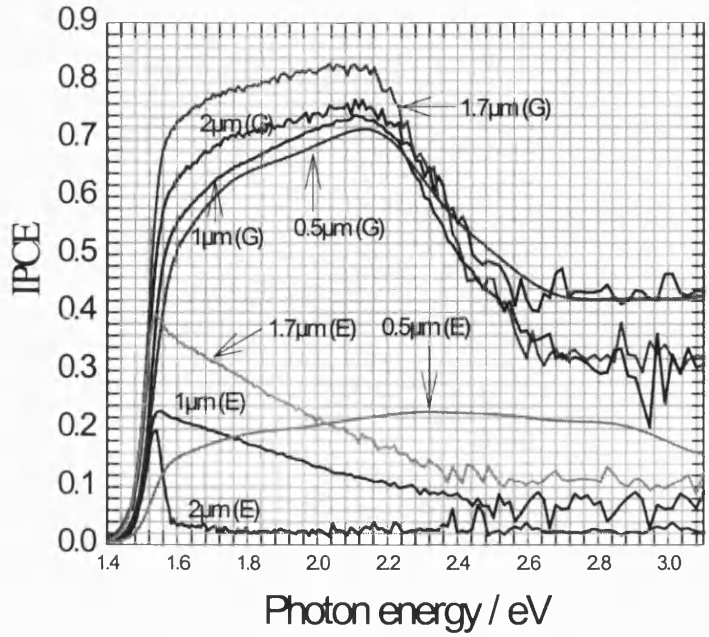

Figure 7.15 Normalised photocurrent spectra (uncorrected for reflection losses) for thicker annealed CdTe films from stirred solution. Electrolyte: 0.1 M Na_2SO_3. CdTe film thicknesses as shown. Illumination either from the electrolyte side (E) or through the glass side (G).

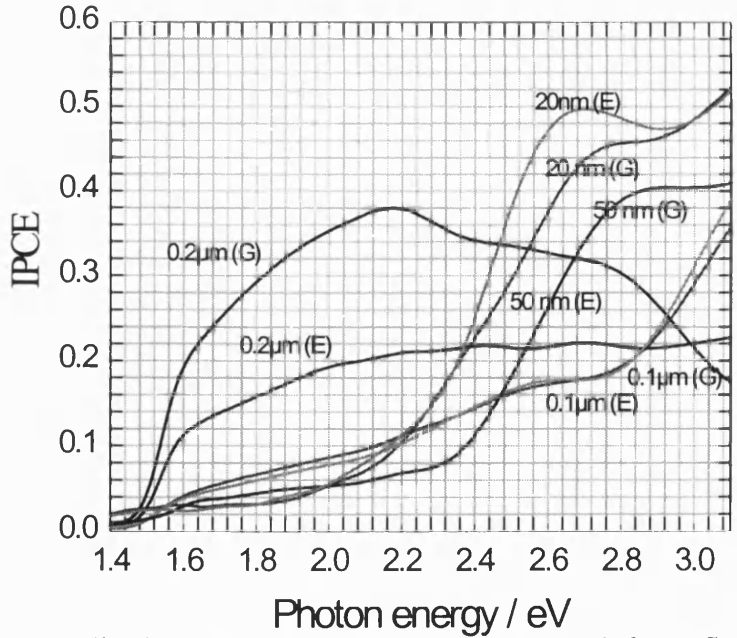

Figure 7.16 Normalised photocurrent spectra (uncorrected for reflection losses) for thinner annealed CdTe samples deposited from stirred solution. Electrolyte: 0.1 M Na_2SO_3. CdTe film thicknesses as shown. Illumination either from the electrolyte side (E) or through the glass side (G).

Comparison with figure 7.13 indicates that the larger response is observed for the glass side illumination. This is because type conversion creates an n-CdS/p-CdTe junction, and light entering through the glass side is absorbed in the space charge region and the photogenerated carriers are collected. By contrast, light entering through the electrolyte is mainly absorbed in the bulk of the CdTe film. Only a small part of light can reach to the p-n junction. Since photogenerated carriers in the neutral region of the CdTe diffuse to reach the junction to be collected, so that the response is small except for at the band edge, increasing the electron lifetime will improve the photocurrent response in higher energy region E illumination. Photocurrent spectra for thinner annealed CdTe films are shown in figure 7.16.

7.8 Results for a two-side-fitting Model

W and L are two key factors to characterise solar cell devices. W can be obtained using equation 5.109 or 5.111 if the doping density and the flatband potential are known from Mott-Schottky plots. By contrast, to obtain L is more complicated. Details have been given in the literature [53]. An alternative way to obtain both W and L simultaneously is to fit the photocurrent response using the Gärtner equation [51]. This equation is applicable only to bulk semiconductors or to thick films, but it is invalid for thin film solar cells since the semi-infinite boundary condition no longer applies. A called two-side-fitting model has therefore been developed in section 5.12. The following assumptions were made for this model: 1) the junction is planar and doping is uniform; 2) the space charge region is recombination-free; and 3) the rate of recombination at CdTe/electrolyte interface is infinitive. This model is only valid for the photocurrent spectral response for annealed films in both illumination geometries because in the case of as-deposited films the junction is located at the CdTe/electrolyte

interface. The assumption of infinite recombination rate at the CdTe/electrolyte interface is reasonable for low values of band bending since the polycrystalline material is likely to have a very high density of surface states that promote recombination near flatband conditions where the density of majority carriers (holes) is high.

Equations 5.98 and 5.100 were used to fit experimental results. The procedures for two-side-fitting are as follows: The first step is to correct for reflection losses. The E and G illumination geometries are shown in figure 7.17.

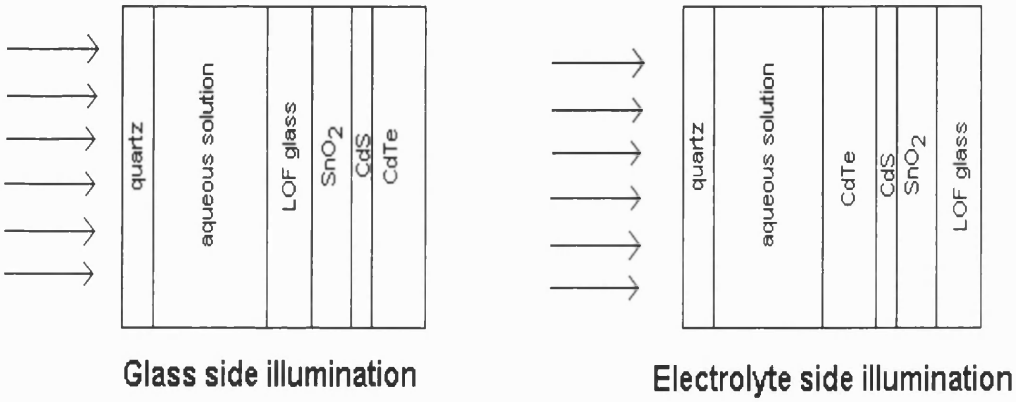

Figure 7.17 G and E illumination geometries for correction of reflection losses

The correction for G illumination before reaching the CdTe layer was obtained as

$$T_{CdS}^{G} = \left(1-\left(\frac{N_{air}-N_{quartz}}{N_{air}+N_{quartz}}\right)^2\right)\times\left(1-\left(\frac{N_{water}-N_{quartz}}{N_{water}+N_{quartz}}\right)^2\right)\times\left(1-\left(\frac{N_{water}-N_{LOF}}{N_{water}+N_{LOF}}\right)^2\right)$$
$$\times\left(1-\left(\frac{N_{SnO_2}-N_{LOF}}{N_{SnO_2}+N_{LOF}}\right)^2\right)\times\left(1-\left(\frac{N_{SnO_2}-N_{CdS}}{N_{SnO_2}+N_{CdS}}\right)^2\right) \quad (7.1)$$

where N represents the refractive index, the subscripts indicate materials, LOF stands for Libby Owns Ford fluorine doped tin oxide glass.

After passing through the CdS layer the correction for G illumination becomes

$$T_{CdTe}^{G} = T_{CdS}^{G} \times \exp(-\alpha_{CdS} * d_{CdS}) * \left(1 - \left(\frac{N_{CdTe} - N_{CdS}}{N_{CdTe} + N_{CdS}}\right)^2\right) \quad (7.2)$$

where d_{CdS} is the thickness of CdS layer (80nm), and T_{CdS}^{G} and T_{CdTe}^{G} are transmittance of the CdS and CdTe layers, respectively, and α_{CdS} is the absorption coefficient of CdS.

The correction for E illumination is given by

$$T_{CdTe}^{E} = \left(1 - \left(\frac{N_{air} - N_{quartz}}{N_{air} + N_{quartz}}\right)^2\right) \times \left(1 - \left(\frac{N_{water} - N_{quartz}}{N_{water} + N_{quartz}}\right)^2\right) \times \left(1 - \left(\frac{N_{water} - N_{CdTe}}{N_{water} + N_{CdTe}}\right)^2\right) \quad (7.3)$$

The intensity of light entering the CdTe layer after reflection and absorption corrections was obtained and is shown in figure 7.18.

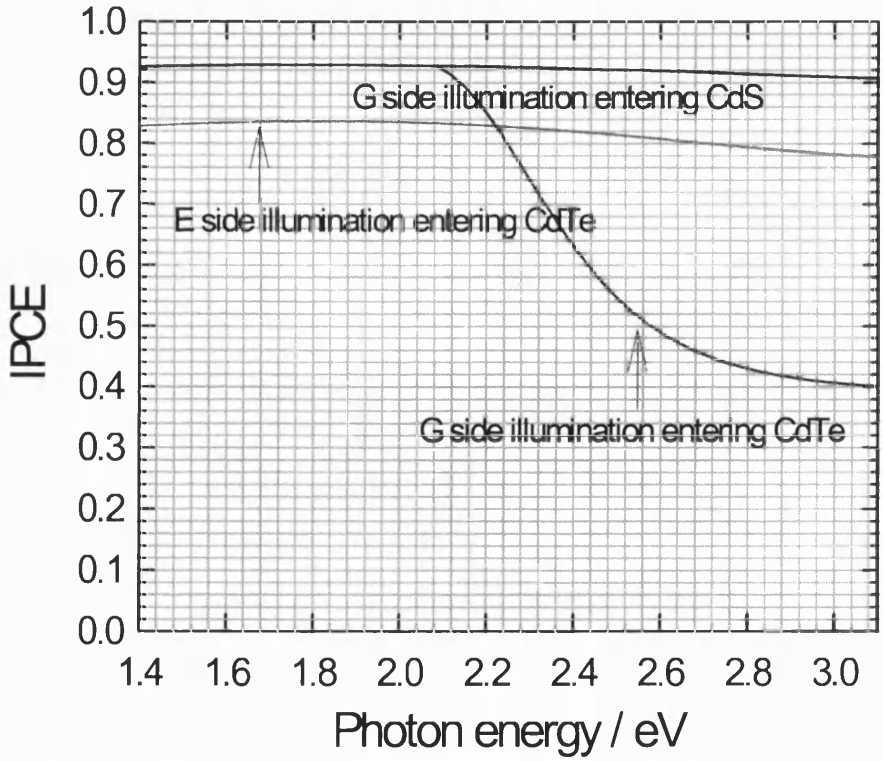

Figure 7.18 Calculating the reflection losses for both electrolyte and glass illumination geometries.
(Multiple reflection were not considered)

It can be seen from figure 7.18 that these calculations predict that the maximum experimental IPCEs (uncorrected for reflection loss) should be around 0.84 and 0.93 for the E and G geometries, respectively. The calculated IPCE values for the CdTe layer are also shown in figure 7.18 when it is assumed that the CdS layer acts only as an absorber without contributing the photocurrent.

The next step was to fit the experimental results using equations 5.98 and 5.100 by a non linear least square regressions. The fitting processes were conducted by using SigmaPlot 5.02. The fitting conditions were: tolerance = 0.0001, stepsize=10, and iterations = 300.

The absorption coefficient of CdTe, α_{CdTe}, was taken from literature data [4] for a recrystallised electrodeposited CdTe film. The absorption coefficient of CdS, α_{CdS}, was obtained from transmission measurements of heat treated CdS films. The refractive index of CdS, N_{CdS}, was taken from the [54], the refractive index of CdTe, N_{CdTe}, from [55], the refractive index of SnO_2, N_{SnO2}, from [56] and the refractive index of LOF glass, $N_{LOF,}$ from [57]. The refractive indeces of water and quartz, N_{water} and N_{quartz} are 1.333 and 1.524, respectively.

CdS is the window material of CdTe solar cells. The bandgap energy for the CdS is 2.45 eV, and the CdS layer absorbs higher energy light as shown in figure 7.18 for G geometry illumination. In principle, the CdS layer might contribute photocurrent over the absorption region, but in practice in all experiments the CdS layer appeared to act as a 'dead layer'. There are several possible reasons for the absence of a photoresponse from the CdS layer. Before fabrication of the junction, the CdS is certainly photoactive [40]. After annealing, however, the layer may become so highly doped that the space charge region is very thin, and holes are not collected efficiently. Alternatively the heat treatment may introduce a very high density of recombination centres. A third

possibility is that the junction is not actually formed between CdS and CdTe but within the CdTe layer as the result of sulphur diffusion.

The best fitting of the photocurrent spectra for both illumination geometries gave the width of the space charge region, W_{CdTe}, and the diffusion length, L_n.

Figure 7.19 shows a best fitting of the photocurrent spectra for a 2μm annealed CdTe. Figure 7.20 shows another best fitting of the spectra for a 1μm annealed films.

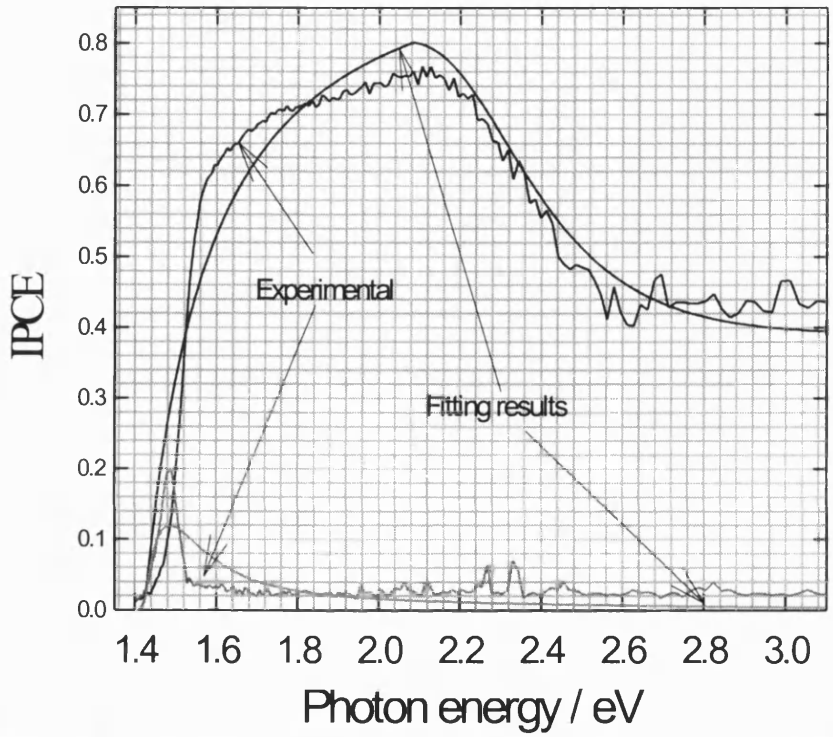

Figure 7.19 A best fit of the photocurrent spectra for a 2 μm annealed CdTe film using equations 5.98 and 5.100. W_{CdTe}= 0.1μm, L_n= 0.5μm and W_{CdS}= 0 nm. Reflection losses have been taken into account.

The fit in higher energy region for the G side illumination geometry is much better in figure 7.19 but the E side fit is poor. By contrast, the fit to the E geometry is better in figure 7.20 (1μm film). In both cases the CdS layer does not contribute to the photocurrent at all. The experimental spectra for the G geometry exhibit a much

sharper onset at the bandgap that is predicted from the model using the absorption coefficient data given in [4]. The reason for this is not clear at present, but it may indicate that the degree of recrystallisation and sulphur/tellurium fiddusion is diffenert in the films prepared in the current work. It is also interesting to note that the experimental spectra also show an abrupt change in slope at around 1.6 eV that is not predicated by the absorption coefficient data. More accurate fitting would require better α_{CdTe} data.

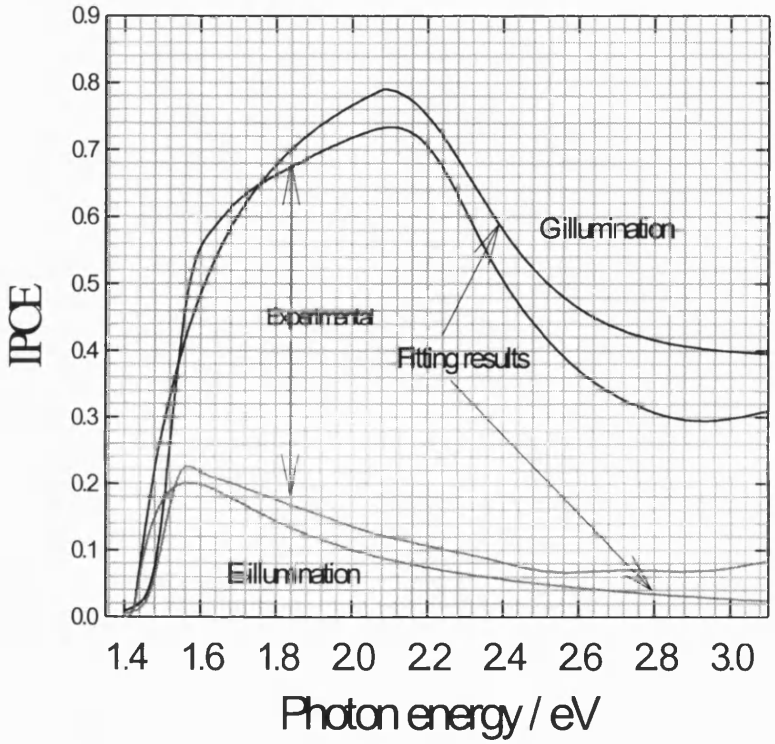

Figure 7.20 Best fit of the photocurrent spectra for a 1μm annealed CdTe film using equations 5.98 and 5.100. W_{CdTe}= 0.12μm, L_n= 0.45μm and W_{CdS}= 0 nm. Reflection losses have been taken into account.

Figure 7.21 shows α_{CdTe} data taken from literature [2,4,72-73]. Marple and Ehrenreich [72] measured the UV-vis spectrum by spectroscopic ellipsometry in the 5 to1.75 eV region. Samples were high-resistivity single crystals with cleavage surfaces. Myers et al. [73] measured n and k for both single crystals and polycrystalline film samples in the range 0.45 –1.9μm. The films were made by sublimation of the

compound with deposition on heated fused-quartz substrates. Both Basol et al. [2] and Lincot et al [4] measured absorption coefficient of p-CdTe thin films prepared by electrodeposition. The discrepancy in the α_{CdTe} in Lincot's and Basol's arises from the fact that these films were probably not fure CdTe but instead $CdTe_{1-x}S_x$ with different x. Details are discussed in chapter 8. All data near bandgap were less accurate and the differences between them were the order of 3 (see [72-73]). They are not shown in figure 7.21. As seen in figure 7.21, Lincot's data is between Basol's and the single crystal data. In this thesis, Lincot's data are used to fit experimental data.

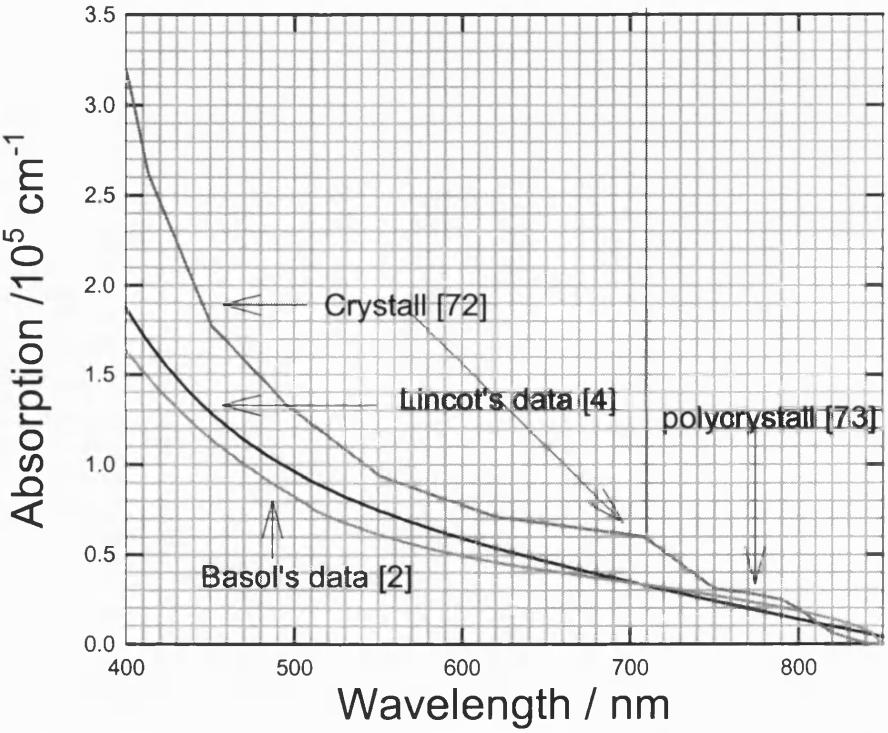

Figure 7.21 Absorption coefficient of p-CdTe taken from literatures [2,4,72-73]. Note that the onset of absorption occurs at longer wavelengths for the data of Basol and lincot. This is good evidence of sulphur diffusion

2222

The results obtained by fitting the spectra for the 1.7μm annealed CdTe films were W_{CdTe}= 0.15μm, L_n= 1.0 μm and W_{CdS}= 0 nm , and W_{CdTe}= 0.10μm, L_n= 0.40μm and W_{CdS}= 0 nm for the 0.5 μm annealed CdTe films. The fitting shows that CdS layer acts as a dead layer and that the width of the space charge were almost a constant for all the

four samples. This shows that the electrodeposition process was reproducible. It was noted that the 1.7μm sample reproducibly gave the highest value of L_n. The reason is unknown so far. The results are listed in table 7.3.

Table 7.3 Summary of the WCdTe and Ln from the fitting

Thickness/ μm	W_{CdTe} /μm	L_n/ μm	W_{CdS}/ μm
2.0	0.10	0.50	0
1.7	0.15	1.0	0
1.0	0.12	0.45	0
0.5	0.10	0.40	0

7.9 EEA and EER Spectroscopy

The electrodeposited CdTe samples were further characterised by using EER or EEA spectroscopy. The degree of perfection of the CdTe (and CdS) films was linked directly with the broadening parameter obtained by fitting to the generalised line function proposed by Aspnes [43]. Figure 7.22 shows EER spectra of as-deposited and annealed CdTe films (2μm). The as-deposited CdTe sample gives Eg = 1.54 eV and Γ = 100 meV. The larger value of Γ probably indicates a high degree of structural imperfection or strain in the film [58]. The type-converted CdTe film gave Eg = 1.51 eV and Γ = 50 meV. The bandgap value corresponds exactly to that of pure single-crysatl CdTe. The decrease in Γ indicates that strain in the film has been removed or structural perfection of the film has improved. It appears that sulphur diffusion during annealing is unlikely to occur in this case. According to Ohata's study [17], the relationship between the bandgap of the $CdTe_{1-x}S_x$ and sulphur content, x, was given by

$$Eg = 1.51 - 1.010x + 1.74x^2 \qquad (7.4)$$

Since no appreciable reduction in Eg was observed, it can be calculated that x is very small. This behaviour contrast markedly with that observed for films prepared by pulse deposition using a flow cell. In these cases sulphur diffusion clearly occurred since Eg was reduced by the annealing process (see chapter 8).

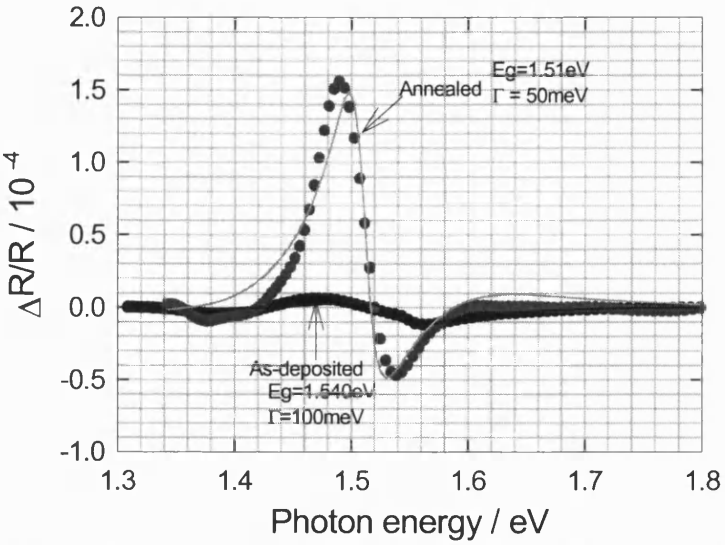

Figure 7.22 EER spectra of as-deposited and annealed CdTe films (2μm).
lines – fit to generalised line function

Figure 7.23 shows EER spectra of the 0.5μm CdTe films. The bandgap energy and the broadening parameter are shown in the figure.

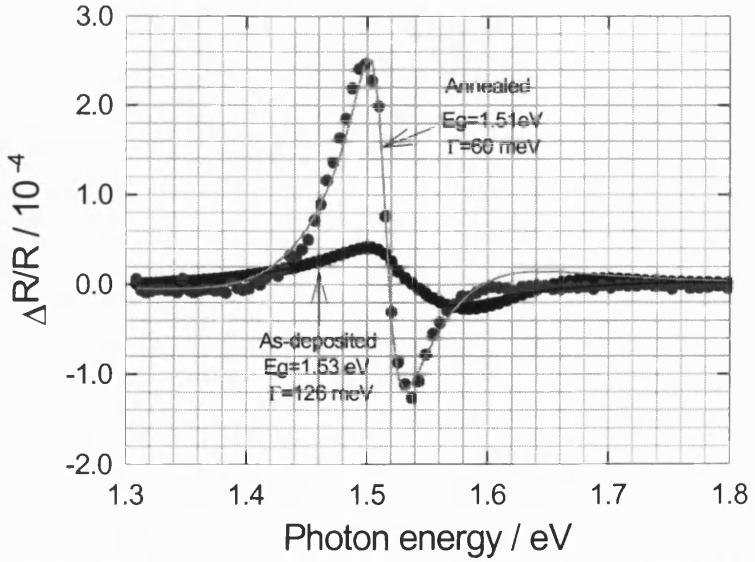

Figure 7.23 EER spectra of as-deposited and annealed CdTe films (0.5μm).
lines – fit to generalised line function

The EER spectra of thicker films only provide information about the CdTe. For thinner films, the EER spectra give information not only about the CdTe but also about the CdS (substrate). Figure 7.24 shows the EER spectra of a 200 nm CdTe film. The fitting to the lineshape equation gives the values of Eg and Γ of the CdTe films shown in the figure. For the annealed films, the EER spectra also exhibit a response in the CdS region. The values of Eg and Γ of the CdS film are shown in the figure and are in good agreement with reports in the literature [40]. The large Γ values indicate that the films have high stacking fault densities.

Figure 7.25 shows an example of the EER spectra obtained for very thin CdTe films. It is interesting to note that a clear CdTe response is still obtained even though the film is very thin. They are almost same as in the figure 7.25.

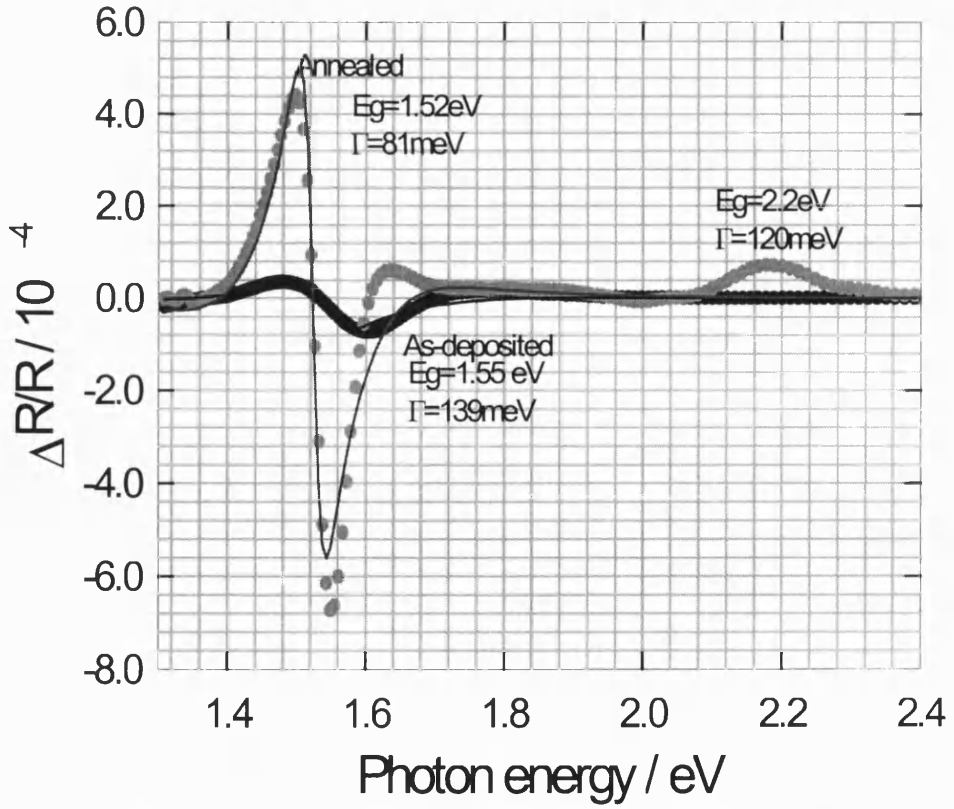

Figure 7.24 EER spectra of as-deposited and annealed CdTe films (200nm). lines – fit to generalised line function

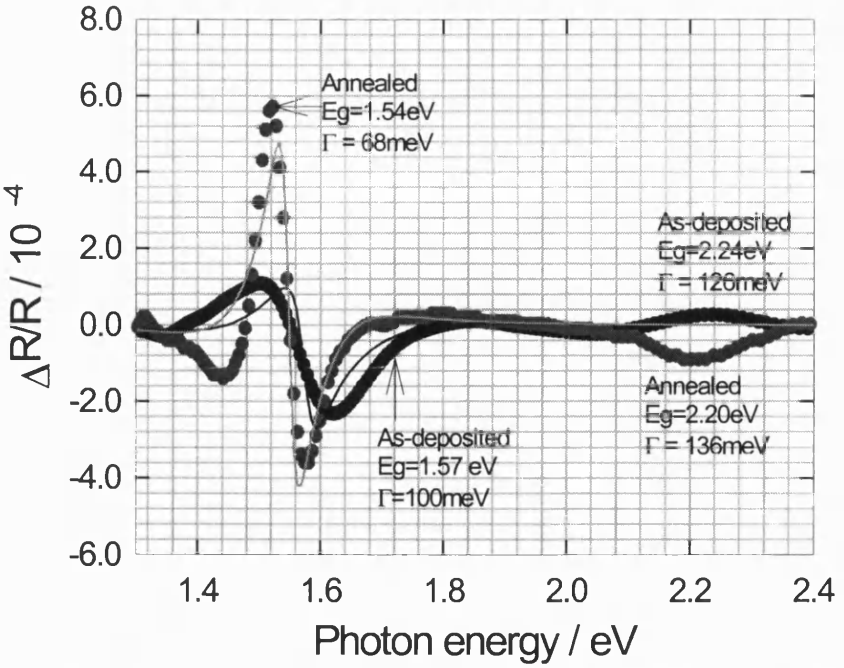

Figure 7.25 EER spectra of as-deposited and annealed CdTe films (50 nm).

lines – fit to generalised line function

For the thinner films, EEA spectroscopy is alternative way to characterise the properties of the CdTe. Figure 7.25 shows EEA spectra of a 0.5μm film. The values of Eg and Γ are shown in the figure. Figure 7.26 shows EEA spectra of very thin CdTe films (50nm).

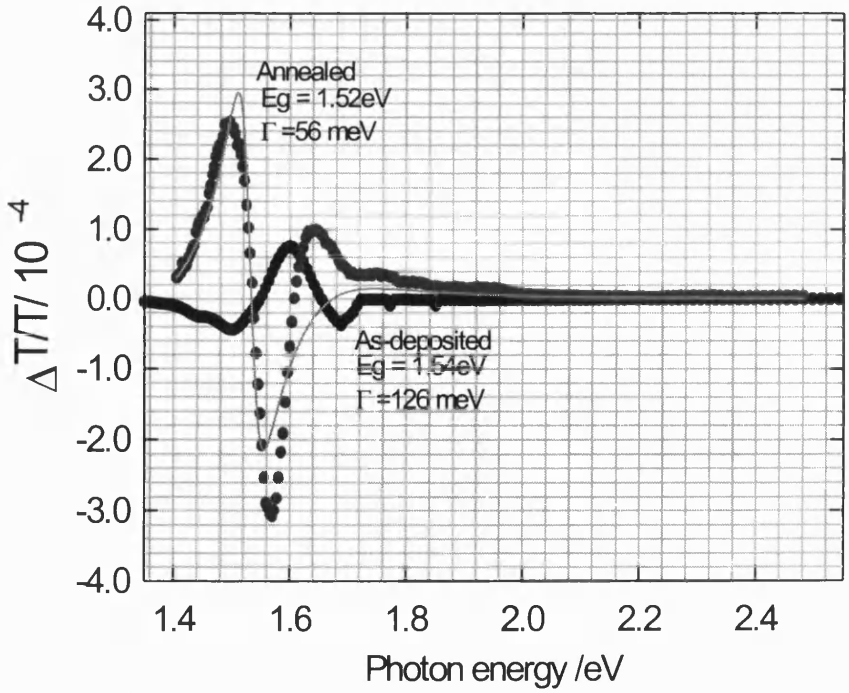

Figure 7.26 EEA spectra of as-deposited and annealed CdTe films (0.5μm).

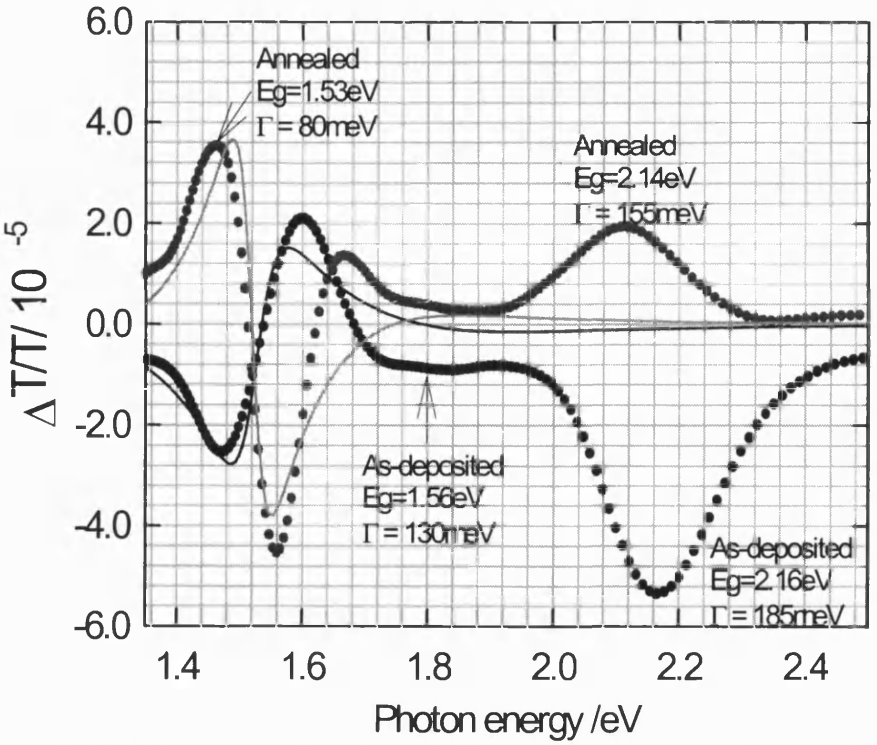

Figure 7.27 EEA spectra of as-deposited and annealed CdTe films (50 nm).

It is clear that EEA spectrum is better for studies of thinner films because light is transmitted through whole CdTe/CdS films and has much larger CdS response than EER one, compared figure 7.25 with figure 7.27. The values of Eg and Γ for the CdS from 50 nm CdTe samples for both EEA and EER are summarised in the Table 7.4.

Table 7.4 Summary of the values of Eg and Γ of the CdS from fitting.

	As-deposited		Annealed	
EER	Eg=2.24eV	Γ=136meV	Eg=2.20eV	Γ=126meV
EEA	Eg=2.16eV	Γ=185meV	Eg=2.14eV	Γ=155meV

It has been shown that Eg is decreased by thermal annealing. The Eg is lower than that of as-deposited CBD CdS films. This observation is in agreement with the literature

[40]. It is important to note that there is no CdS response in the EEA/R spectra at all for all thick annealed CdTe films (over 0.5μm). That indicates that there is no CdS region existing in those thicker films because the electroreflectance effect needs a field. While a big response in the CdS region in the EEA/R spectra is observed in the 50 nm film. This agrees nicely with the photocurrent results — CdS response is only seen for very thin films.

Table 7.5 gives details of parameters obtained by fitting EER or EEA spectra to the lineshape equation for different thicknesses.

Table 7.5 Summary of values of the bandgap Eg and the broadening parameter Γ.

Thickness	EEA(as-dep)	EEA(annealed)	EER(as-dep)	EER(annealed)
2μm			Eg=1.54 eV Γ =100meV	Eg=1.51 eV Γ =50meV
1.7μm			Eg=1.54 eV Γ = 94meV	Eg=1.50 eV Γ =61meV
1μm			Eg=1.53 eV Γ = 94meV	Eg=1.50 eV Γ =56meV
0.5μm	Eg=1.54 eV Γ =126meV	Eg=1.52 eV Γ =56meV	Eg=1.53 eV Γ =126meV	Eg=1.51 eV Γ =50meV
200nm	Eg=1.53 eV Γ =170meV	Eg=1.52eV Γ = 63meV	Eg=1.55 eV Γ =139meV	Eg=1.52 eV Γ =71meV
100 nm	Eg=1.55 eV Γ =170meV	Eg=1.52 eV Γ = 76meV	Eg=1.56 eV Γ =127meV	Eg=1.53 eV Γ = 68meV
5 0 nm	Eg=1.56 eV Γ =130meV	Eg=1.53 eV Γ = 80meV	Eg=1.57 eV Γ =100meV	Eg=1.55 eV Γ = 68meV

* as-dep = as-deposited

7.10 Fabrication and Testing of Photovoltaic Cells.

A 2μm annealed CdTe/CdS sample was fabricated into solar cells. Gold contacts to CdTe (4 mm^2) were prepared after etching the CdTe surface in 50%(V/V) diaminoethane for less than 1 minute and rinsing with Milli-Q water. The samples were dried in flowing nitrogen and then placed in the vacuum chamber of an Edwards coating unit. 100 nm gold was evaporated through 4 mm^2 holes in a mask. Under AM 1.5 (G) the open-circuit voltage was ~ 680mV, the short-circuit current was 16mAcm^{-2}. This gave a 6% efficient cell. The W and power are shown in figure 7.28.

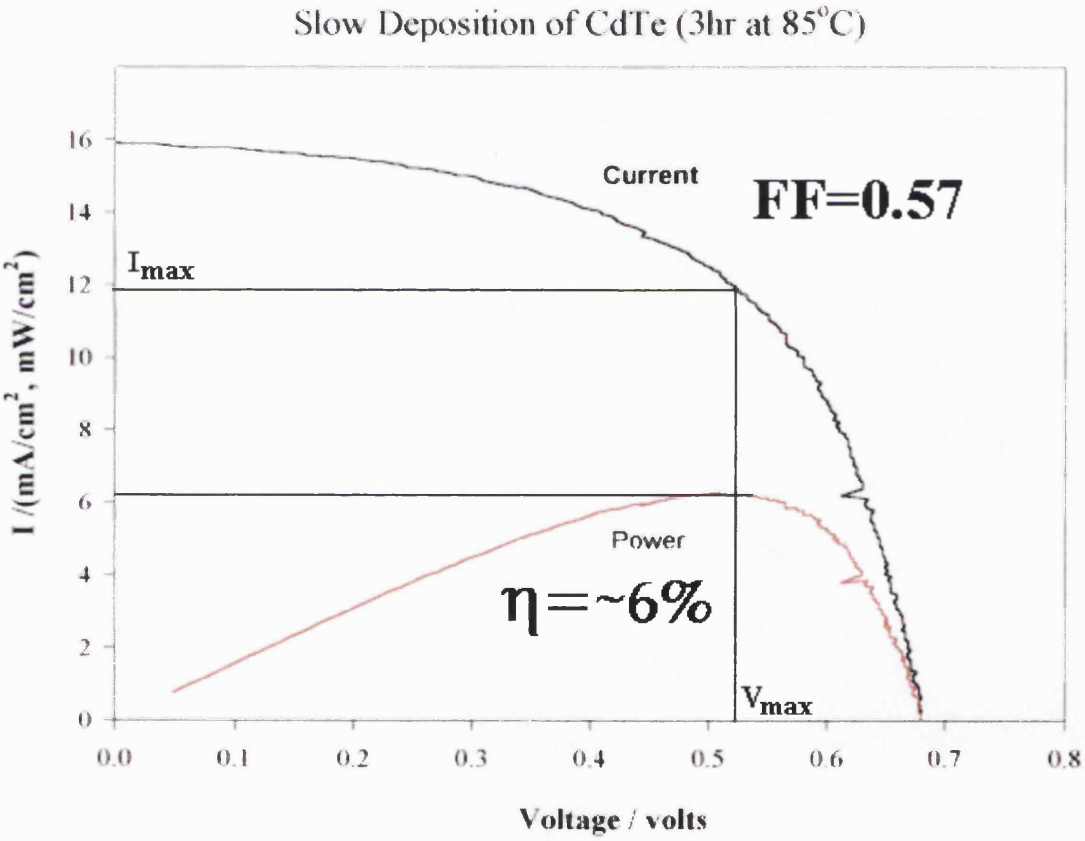

Figure 7.28 I-V curve measured under AM1.5 (G). The cell area was 0.04cm^2.

As mentioned in Chapter 5, the series resistance can give rise to a decrease in the short-circuit current. This may be the case in our solar cells. That is also shown in

figure 7.28. CdTe films are highly resistive with a dark resistivity of greater than 10^6 Ωcm [59]. Bad back contacts result in higher series resistance and reduce the performance of the solar cells. To achieve a high efficiency for the CdTe/CdS solar cells, the formation of ohmic contacts to high resistivity CdTe films is important [60]. This issue has been studied extensively [61-62]. Uda et al [62] used Cu_2Te-Au contacts to the CdTe films and improved the conversion efficiency. The conversion efficiency for the CdTe/CdS cells fabricated with Te-Au contact increased gradually with increasing temperature of annealing Te-Au contact until 400°C. The maximum efficiency was around 4%. While the cell efficiency reached over 10% for the same cells with Cu_2Te-Au contact. McCandless et al. [67] studied the effects of the back contact on the cell conversion efficiency. Back contacts with Cu/Au were made to the CdTe/CdS films deposited by PVD. The conversion efficiency was less than 4% (V_{OC} was less 400 mV and J_{SC} was less than 10 mA cm^{-2}) when the contacts were not annealed. When the contacts were heat treated at 150°C in air followed by immersion in Br_2-CH_3OH solution for 5 s, the efficiency increaed to 9.6% with V_{OC} = 729 mV, J_{SC} = 19 mA cm^{-2}, and FF = 69%. Recently Dharmadasa [63] has published a review on back contacts of the CdTe solar cells.

7.11 Conclusions

CdTe/CdS solar cells prepared by CSS reached the highest conversion efficiency (16%). The CSS CdTe films are post treated with $CdCl_2$ to promote recrystallisation and type conversion. Post treatment with $CdCl_2$ is not normally used for electrodeposition. Instead chloride is deliberately added to the deposition bath with the intention of incorporating chloride with the films. Dennison [65] studied the effects of chloride concentrations in the deposition bath on the cell conversion efficiency. The

cell conversion efficiency increased from 5% in the Cl-free deposition bath to over 10% in the 300ppm Cl deposition bath. In the present work, films were annealed in air without the presence of $CdCl_2$ and recrystallisation was not observed in spite of the fact that a high Cl^- concentration was used in the bath. Touškovà et al [66] have reported that recrystallisation of CdTe is associated with structure changes in CdS films and higher content of the chloride ions in CdTe layers. The function of the $CdCl_2$ treatment includes: grain growth, reduction in the density of defects and formation of an interfacial $CdTe_{1-x}S_x$ layer which is believed to reduce the interfacial stress caused by the lattice mismatch between CdS and CdTe [67-70]. The bandgap energy shifted to lower energy (less than 1.51 eV which is the value for pure CdTe crystal) is directly linked with the sulphur diffusion which reported in the CSS films [42,67,74], in the ED films [12,19], in the PVD cells [75] and in the stacked elemental layer films [70]. The values of the CdTe bandgap for annealed films deposited at +5mV vs. Cd^{2+}/Cd in our experiments were around 1.51 eV. There is less evidence of S diffusion. Different results were obtained for pulse and flow cell films (see chapter 8). CdTe films grown near the Cd^{2+}/Cd potential had good properties [4], but they failed to recrystallise during annealing. It appears to be essential for fabricating an efficient solar cell to have Te-rich CdTe films [12]. Films deposited at more positive potential to the Cd^{2+}/Cd in the stirred cell were also studied, and annealing in this case led to recrystallisation. More detailed discussion of recrystallisation is present in chapter 8.

Good quality CdTe/CdS films were obtained by electrodeposition in the stirred cell. The present studies have demostartes that a combination of spectrioscopic and structural techniques gives useful information about electrodeposited CdTe/CdS. A proposed two-side-fitting model for photocurrent spectra is established and provided evidence for quality of the films. More accurate fitting would require better α_{CdTe} data.

References:

1. B. M. Basol, E. S. Tseng and R. L. Rod, U. S. Patent No. 4,388,483 (1983).
2. S. S. Ou, O. M. Stafsudd and B. M. Basol, J. Appl. Phys. **55**(10), 3769 (1984).
3. J.M. Woodcock, M.E. Özsan, A.K. Turnerm, D.W. Cunningham, D. R. Johnson, R. J. Marsahll, Mason, S. Oktik, M.H. Patterson, S. J. Ransome, S. Robertts, M. Sadeghi, J. M. Sherborne, D. Sivapathasundaram and I. A. Walls, Proc. 12th E. C. Photovoltaic Solar Energy Conf. Amsterdam, H. S. Stephens & Associates, 1995, p.2043.
4. A. Kampmann and D. Lincot, J. Electroanal. Chem., **418**, 73 (1996).
5. S. K. Das and G. C. Morris, Solar Energy Materials and Solar Cells, **30**,107 (1993).
6. N. W. Duffy, D. Lane, M. E. Ozsan, L. M. Peter, K. D. Rogers and R. L. Wang, Thin Solid Films, in press.
7. T. Aramoto, S. Kumazawa, H. Higuchi, T. Arita, S. Shibutani, T. Nishio, J. Nakajima, M. Tsuji, A. Hanafusa, T. Hibino, K. Omura, H. Ohyama and M. Murozono, Jpn. J. Appl. Phys., **36**, 6304(1997).
8. D. Lincot, B. Mokili, M. Froment, R. Cortès, M.C. Bernard, C. Witz and J. Lafait, J. Phys. Chem. B, **101**, 2174 (1997).
9. A. M. Hermann, R. Westfall and R. Wind, Solar Energy Mater. Solar Cells, **52**,355(1998).
10. S. Dennison, J. Materials Chemistry, **5**(11), 1885 (1995).
11. J. M. Woodcock, A.K. Turner, M. E. Özsan and J.G. Summers, In Proceedings of the 22nd IEEE Photovoltaic Solar Energy Conference, Las Vegas, April 1991 (IEEE, New York, 1991), p72.
12. L. M. Peter and R. L. Wang, Electrochemistry Communication, **1**,554 (1999).

13. P. M. Raccah, U. Lee, S. Ugar, D. Z. Xue, L. L. Abeles and J. W. Garland, J. Vac. Sci. Technol., **13**, 13 (1985).

14. T. L. Chu, S. S. Chu, C. Ferekides, C. Q. Wu, J. Britt and C. Wang, J. Appl. Phys., **70**, 7608(1991).

15. J. Britt and C. Ferekides, Appl. Phys. Lett. **62**(22), 2851(1993).

16. S. K. Das and G. C. Morris, Solar Energy Mater. & Solar Cells, **30**, 107(1993).

17. D. W. Lane, G. J. Conibeer, D. A. Wood, K. D. Rogers, P. Capper, S. Romani and S. hearne, J. Cryst Growth, **197**, 743 (1999)

18. K. Ohata, J. Saraie and T. Tanaka, Jpn. J. Appl. Phys., **12**, 1641 (1973).

19. K. D. Rogers, J. D. Painter, M. J. Healy, D. W. Lane and M. E. Özsan, Thin Solid Films **339**,299 (1999).

20. D. P. Halliday, J. M. Eggleston, K. Durose, J. Cryst. Growth, **186**, 543 (1998).

21. S. M. Sze, Semiconductor Devices: Physics and Technology, John Wiley & Sons, New York, (1985).

22. Y. S. Tyan and E. A. Perez-Albulerne, Proc. 16th IEEE Photovoltaic Specialists' Conf., San Diego, CA (IEEE, New York), 794 (1982)

23. K.W. Mitchell, C. Eberspacher, F. Cohen, J. Avery, G. Duran and W. Bottenberg, Proc. 18th IEEE Photovoltaic Specialists' Conf., Las Vegas, NV (IEEE, New York), 1359 (1985).

24. Y. S. Tyan, Eastman Kodak Company, U.S. Patent No. 4,207,119, June 10 (1980).

25. T. L. Chu, S. S. Chu, S. T. Ang, K. D. Han, Y. Z. Liu, K. Zweibel and H. S. Ullal, Proc. 19th IEEE Photovoltaic Specialists' Conf., New Oreans, LA (IEEE, New York), 1466 (1987).

26. A. Rohatgi, Proc. 2989 Polycrystalline Thin Film Program Review Meeting, 45 (1989).

27. H.C. Chou, A. Rohatgi, N. M. Jokerst, S. Kamra, S. R. Stock, S. L. Lowrie, R. K. Ahrenkiel and D. H. Levi, Mater. Chem. And Physics, **43**, 178 (1996).

28. S. A. Ringel, A.W. Smith, M. H. Macdougal and A. Rohatgi, J. Appl. Phys. **70**, 881(1991).

29. Y. K. Jun and H. B. Im, J. Electrochem. Soc., **135**, 1658 (1988).

30. H. Matsumoto, A. Nakano, Y. Komatsu, K. Kuribayashi and S. Ikegami, Jpn. J. Appl. Phys., **22**, 367 (1984).

31. H. Matsumoto, K. Kuribayashi, H. Uda, Y. Komatsu, A. Nakano and S. Ikegami, Solar Cells, **11**, 367 (1988).

32. S. Ikegami, Solar Cells, **23**, 89 (1988).

33. G. C. Morris, A. Tottszer and S. K. Das, Mater. Forum, **15**, 164 (1991).

34. R. W. Birkmire, B. E. McCandless and W. N. Shafarmas, Solar Cells **23**, 115(1988).

35. B. M. Basol, Solar Cells, **23**, 69 (1989).

36. D. M. Oman, K. M. Dugan, J. L. Killian, V. Ceekala, C. S. Ferekides and D.L. Morel, Solar. Energy Mater. & Solar Cells, **58**, 361 (1999).

37. T. Nishio, K. Omura, A. Hanafusa, T. Arita, H. Higuchi, T. Aramoto, S. Shibutani, S. Kumazawa and M. Murozono, 25th IEEE PVSC, 953 (1996).

38. S. M. McGregor, I. M. Dharmadasa, I. Wadsworth and C. M. Care, Optical Materials, **6**, 75 (1996).

39. P. K. Nair, J. Campos and M. T. S. Nair, Semicond. Sci. Technol., **3**, 134 (1988).

40. M. E. Özsan, D. R. Johnson, M. Sadeghi, D. Sivapathasundaram, G. Goodlet, M.J. Furlong, L. M. Peter and A. A. shingleton, J. Mat. Sci.: Materials in Electronics **7**, 110 (1996).

41. W. S. Enloe, J. C. Parker, J. Vespoli and T. H. Myers, J. Appl. Phys., **61**(5), 2005 (1987).

42. T. Toyama, T. Yamamoto and H. Okamoto, Solar Energy Mater. & Solar Cells, **49**, 213 (1997).

43. D.E. Aspnes, Surface Sci., **37**, 418(1973).

44. J. Liabrés and V. Delmas, J. Electrochem. Soc., **133**(12). 2580 (1980).

45. M. P. R. Panicker, M Knaster and F. A. Kroger, J. Electrochem. Soc., **125**(4), 566(1978).

46. A. Kampmann, P. Cowache, J. Vedel and D. Lincot, J. Electroanal. Chem., **387**, 53 (1995).

47. P. Cowache, D. Lincot and J. Vedel, J. Electrochem. Soc., **136**(6), 146(1989).

48. M. E. Özsan, D. R. Johnson, M. Sadeghi, D. Sivapathasundaram, L. M. Peter, M.J. Furlong, G. Goodlet, A. A. shingleton, D. incot, B. Mokili and J. Vedel, Proc. 1st World Conf. On Photoviltaic Energy Conversion, Hawaii, 1994, IEEE Editions, p327

49. H. D. Finklea, Semiconductor Electrodes, Elsevier Science Publishers B.V., Amsterdam, 282 (1988).

50. D. Lincot and J. Vedel, J. Cryst. Growth., **72**, 426(1985).

51. W.W. Gartner, Phys. Rev., **116**, 84 (1959).

52. M. E. Özsan, D. R. Johnson, S. Oktik, M. H. Patterson, D. Sivapathasundaram and J. M. Woodcock, 12th European Photovoltaic Solar Energy Conference, 1994, Amsterdam, p1604

53. L. M. Peter Chem. Rev. **90**, 753 (1990).

54. E. Khawaja and S.G. Tomlin, J. Phys. D: Appl. Phys., **8**, 581 (1975).

55. E. D. Palik, Handbook of Optical Constants of Solids, Academic Press, London, 1991

56. A.E. Rakhshani, Y. Makdisi and H. A. Ramazaniyan, J. Appl. Phys., **83**(2), 1049 (1998).

57. http://www.pilkington.com/sites/lof/tecprop.html

58. D.W. Lane, G. J. Conibeer, D.A. Wood, K. D. Rogers, P. Capper, S. Romani and S. Hearne, J. Cryst. Growth, **197**,743 (1999).

59. H. Uda, S. Ikegami, H. Sonomura, Jpn. J. Appl. Phys., **29**, 2003 (1990).

60. A. L. Fahrenbruch, solar Cells, **21**, 399 (1987).

61. N. Stratieva, R. Stefanov, G. Pchelarov, M. Stoev, A. Katerski, A. N. Tiwari and M. Igalson, 2nd World Conf. And exhibition on Photovoltaic Solar Energy Conversion, Vienna, Austria, 1036 (1998).

62. H. Uda, S. Ikegami, H. Sonomura, Solar Energy Mat. Solar Cells, **50**, 141 (1998).

63. I. M. Hdarmadasa, Prog. Crystal Growth and Charact. **36**(4), 249 (1998).

64. N. Romeo, A. Bosio and V. Canevari and T. A. Kuku, 12th European Photovoltaic Solar Energy Conference, Amsterdam, 662 (1994).

65. S. Dennison, J. Mater. Chem., **4**(1), 41 (1994).

66. J. Toušková, D. Kindl, L. Dobiášová and J. Toušek, Solar Energy Mater. And Solar Cells, **53**, 177 (1998).

67. B. E. McCandless and R. W. Birkmire, Solar Cells, **31**, 527 (1991).

68. H. R. Moutinho, F. S. Hasoon, F. Abufotuh, L. L. Kazmerski, J. Vac. Sci. Technol. A **13**(6), 2877 (1995).

69. A. Rohatgi, R. Sudharsanan, S. A. Ringel, m. H. MacDougal, Solar Cells, **30**, 109 (1991).

70. L. R. Cruz, L. L. Kazmerski, H. R. Moutinho, F. Hasoon, R. G. Dhere and R deAvillez, Thin Solid Films, **350**, 44 (1999).

71. K. Ohata, J. Saraie and T. Tanaka, Jpn. J. Appl. Phys., **12**, 1641 (1973).

72. D.T. F. Marple and H. Ehrenreich, Phys. Rev. Lett. **8**, 87 (1962).

73. T.H. Myers, S. W. Edwards and J. F. Schetzina, J. Appl. Phys. **52**, 4231 (1981).

74. D. H. Levi, H. R. Moutinho, F. S. Hasoon, B. M. Keyes, D. K. Ahrenkiel, M. Al-Jassim, L. L. Kazmerski and R. W. Birkmire, Solar Energy Mater. And Solar Cells, **41/42**,381 (1996).

75. K. D. Rogers, J. D. Painter, D. W. Lane and M. J. Healy, J. Electronic Materials, **28**(2), 112 (1999).

CHAPTER EIGHT

RESULTS AND DISCUSSION

Optical and Characterisation of CdTe Films

Prepared in a Channel Flow Cell

8.1 Introduction

Cost is the key factor that limits large-scale application of solar cells. Thin film CdTe/CdS photovoltaic devices are one of most promising alternatives to conventional silicon solar cells. Although the close-spaced sublimation (CSS) technique has produced the highest solar cell efficiency (16%) [1-3] so far, films grown by electrodeposition [4-13] have also been investigated extensively since the growth technique is low-cost and commercial exploitation is feasible. The commonly used acidic deposition solution contains high concentrations of less-expensive cadmium and low concentrations of high-cost tellurium. The low concentrations of tellurium are limited by the solubility of TeO_2, rather than by cost. The rate of film deposition is determined mainly by the concentrations of the components used in the solution. Since a very high ratio of Cd^{2+} to TeO_2 concentration exists in the solution, the rate of film growth is determined predominantly by mass transport of the tellurium component. As the solubility of the TeO_2 increases with decreasing pH [14], the pH of the bath (near 1.4) is a compromise between maximising the TeO_2 concentration and avoiding dissolution of the CdS. To grow high quality (uniform and adherent) films in the stirred solution, the time for depositing a 2μm CdTe film is several hours as shown in chapter 7.

The possibility of reducing the deposition time has become a very interesting issue. The rotating disk electrode (RDE) has been used to study the influence of mass transport, and values of the diffusion coefficient of $HTeO_2^+$ over a range of temperatures have been obtained [15]. However, the RDE is not good way to deposit films for solar applications. As an alternative, a channel flow cell, which has been widely used to study the reactions of the electrode surface (Compton et al [16]), may be the best choice to control the rate of mass transport of $HTeO_2^+$ and to achieve a substantial reduction of the deposition time. The present work has demonstrated that is

possible to deposit a 2μm CdTe film in less than 20 min [8]. This chapter presents results obtained for films prepared in the flow cell. The properties of CdTe/CdS film structures have been assessed by the methods described in the chapter 7.

8.2 Deposition Current Densities and Linear Sweep Voltammogram

A well-defined channel flow cell gives a laminar flow, and the electrode current density, j_L, within the channel under diffusion controlled processes is given by [16]

$$j_L = 0.925nFC\left(\frac{v_f D^2}{h^2 x_e d}\right)^{1/3} \qquad (8.1)$$

Here n is the number (6) of electrons transferred in the reaction, F is the Faraday constant, v_f is the volume flow rate ($cm^3\ s^{-1}$), C is the bulk concentration of the $HTeO_2^+$ (mol cm^{-3}), D is the diffusion coefficient of $HTeO_2^+$ ($cm^2\ s^{-1}$), h is the half height of the channel (cm), d (cm) is the channel width and x_e is the length of the electrode (cm). Extrapolation of data for the diffusion coefficient of $HTeO_2^+$ as a function of the temperature to 85°C gives $D_{HTeO_2^+} = 1.13\times10^{-5}$ cm^2s^{-1} at 85°C [15]. This value was used to calculate the dependence of j_L on volume flow rate and the corresponding deposition time for a 2 micron CdTe film as shown in figure 5.21. It should clearly be possible to reduce the deposition time to 25 minutes at a volume flow rate of 10 $cm^3\ s^{-1}$.

Figure 8.1 shows voltammograms for different flow rates at 85°C in the channel flow cell.

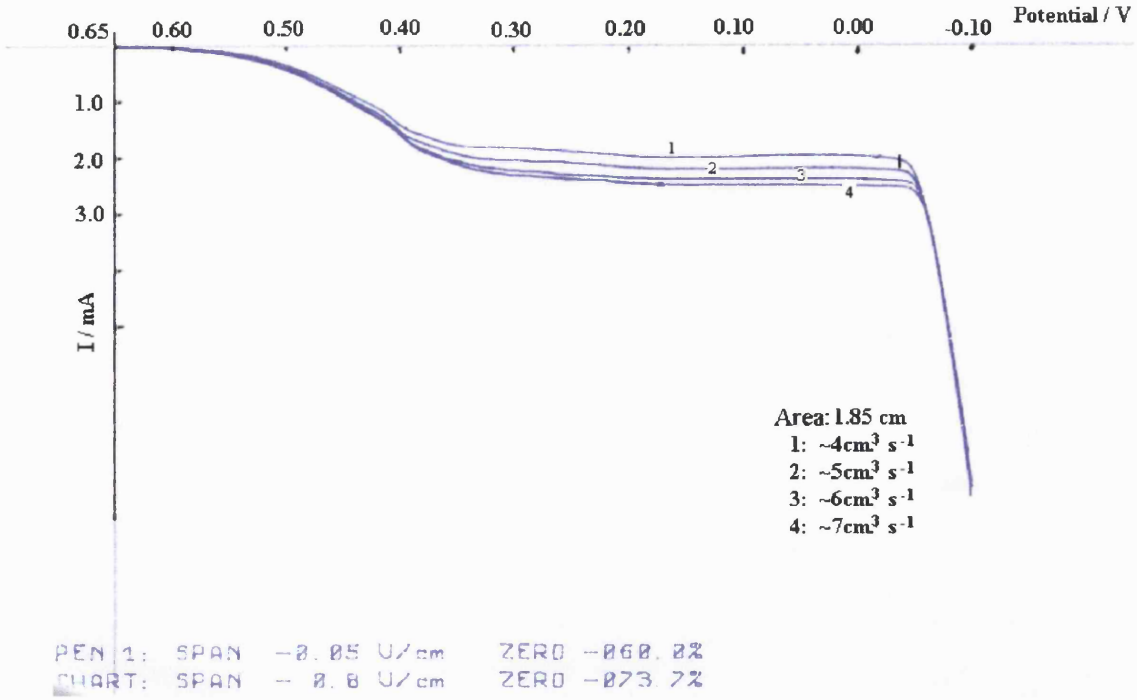

Figure 8.1 Voltammograms for different flow rates in a channel flow cell for the deposition of CdTe from 0.5 M $CdSO_4$, 0.5 mM $HTeO_2^+$ (pH=1.4) onto a CdS-coated conducting glass at 85°C. Electrode size 2.3 × 0.8 cm. Scan rate = 10 mV s^{-1}. The channel dimensions were 50 × 10 × 1 mm. The flow rates are shown in the figure.

Compared with figure 7.1, the current-voltage curves are much smoother. The limiting deposition current density in the channel cell is several times higher than in the stirred solution at the same temperature. The deposition films in the channel cell should be more uniform if the flow was laminar. This also confirmed that the deposition process in the range of the plateau is diffusion controlled. The small oscillations observed on the curve in stirred solution disappeared because laminar flow was achieved, ensuring uniform mass transport of $HTeO_2^+$ to the electrode surface.

8.3 Preparation of CdTe Thin Films by Different Methods

Careful attention was given to the preparation of the CdS-coated conducting glass substrate because it is difficult to mask the smaller electrode size. Re-masking a masked sample was found to lead to a non-uniform deposit. It was found advantageous to flush the assembled electrode with warm Milli-Q water (the washing bottle was placed in the thermostated bath) and to wait for a few seconds to start deposition when the assembled electrode was placed into the circulated solution. It was also essential to check whether the junctions of the assembled channel electrode were leak-free before inserting them into the circulated circuit. This was done using a clean plastic syringe.

Two deposition temperatures were used: room temperature and 85°C. Films were grown at a range of deposition potentials from zero mV to +50 mV versus the Cd^{2+}/Cd. Pulse deposition technique was also used in the channel cell. The preferred deposition conditions for pulsed electrodeposition were: V_1= 10 mV, t_1= 1 s, V_2 = +175 mV, t_2 = 0.1s in flowing solution with 0.5 M $CdSO_4$, 0.5 mM $HTeO_2^+$, 800 ppm $CdCl_2$ and a pH of 1.4. The pulse deposition waveform is depicted in figure 8.2.

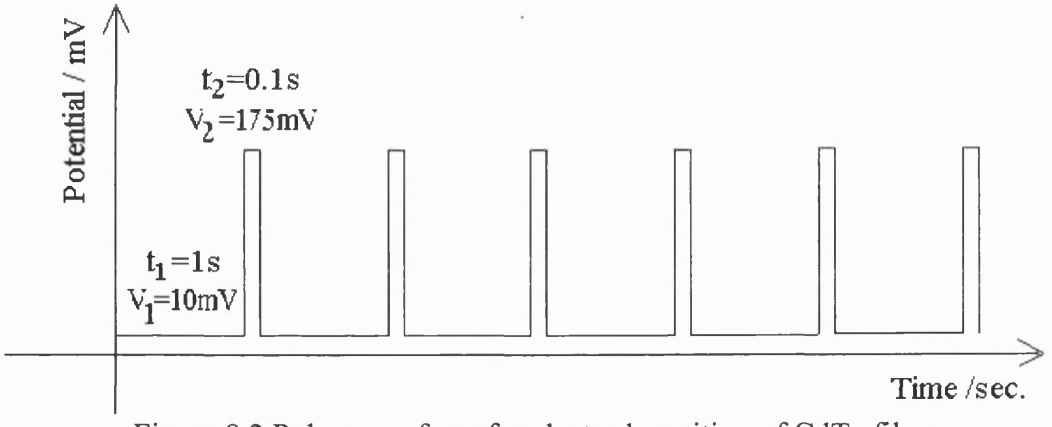

Figure 8.2 Pulse waveform for electrodeposition of CdTe films

Deposition of a 2μm film at room temperature at the flow rate of ~ 6 cm^3s^{-1} takes about 1h. The reasons why the deposition time was increased to near two times of the deposition at 85°C are: 1) the diffusion coefficient of the $HTeO_2^+$ at room temperature,

~6 $\times 10^{-6}$ cm^2s^{-1}, is only half of that at 85°C, and 2) the lower flow rate, compared with 10 cm^3s^{-1}. The deposition potential was fixed +5mV positive to the Cd^{2+}/Cd reference electrode.

If the deposition potential was far from the Cd^{2+}/Cd potential, the composition of the deposit was not stoichiometric and the film properties were poor. Since films deposited by the pulsed deposition encountered problems like pinholes and poor adhesion after annealing, a two-step deposition method was used. The first step is to deposit a film with a thickness of a few hundreds nm at +20mV vs. the Cd^{2+}/Cd potential. The next step is then to grow the film with the pulsed deposition. The final thicknesses of the samples were 1.8μm, unless otherwise stated.

Figure 8.3 shows as-deposited samples with the flow direction in the channel cell.

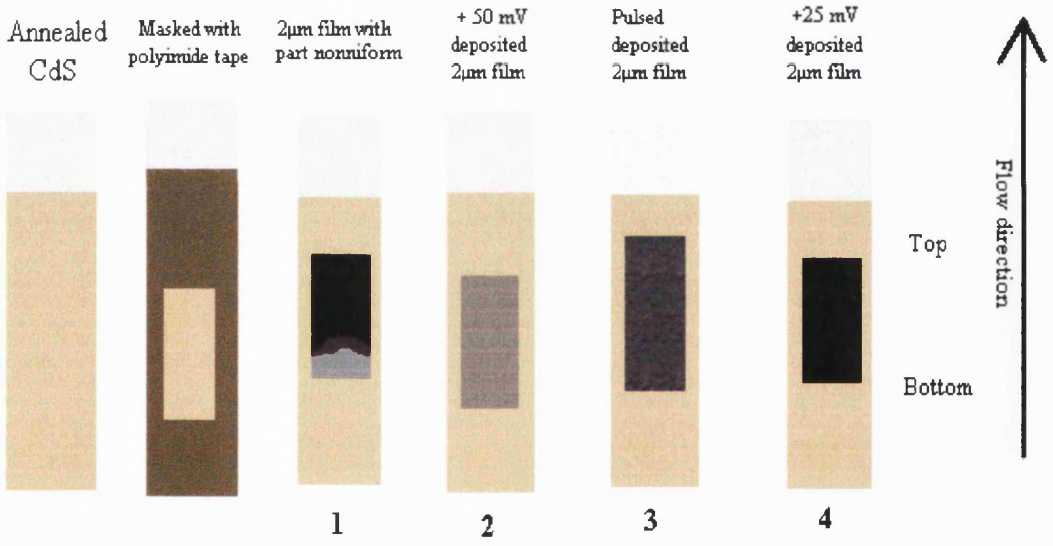

Figure 8.3 Samples of as-deposited films prepared in the channel flow cell showing the flow direction during deposition processes and positions in the films. No 1 is a non-uniform sample typical for room temperature deposition.

Possible reasons why non-uniform films are formed on the top (upstream) side are that the part was placed within the entry length (see figure 1.10) or there may be creases in the polyimide masking tape on the upstream side that cause turbulence.

The different colours of samples are due to different thickness and composition in the deposits. The deposition potentials are also shown about samples. Details are discussed in the next sections.

Table 8.1 gives a summary of charge, deposition temperature and time for films deposited in the channel cell. The film thickness was confirmed by SEM cross-section image and the films were 1.8 μm thick.

Table 8.1 Films with deposition parameters

Sample Code	Charge / C	Method	t/sec	Size / cm	Temperature
RT1	5.18	+5 mV	~4208	2.3×0.8	25°C
RT2	4.94	+5mV	~4010	2.2×0.8	25°C
RT3	5.04	+5mV	~4080	2.2×0.8	25°C
HT1	4.94	+5mV	~1506	2.3×0.8	85°C
HT2	4.94	+15mV	~1230	2.2×0.8	85°C
HT3	4.94	+30mV	~1170	2.1×0.8	85°C
HT4	4.94	+50mV	~1246	2.2×0.8	85°C
HT5	4.94	Puled	~1056	2.2×0.8	85°C
HT6	4.94	Two-step	~1105	2.2×0.8	85°C

* RT- deposited at room temperature, HT- deposited at 85°C.

8.4 XRD and WDX

XRD and WDX were used to study the composition and structures of the electrodeposited CdTe films.

Figure 8.4 shows an XRD spectrum of a typical as-deposited CdTe film. It exhibits a strongly preferential <111>orientation.

Figure 8.5 shows an XRD spectrum of a 1.8 μm annealed CdTe film. The annealed film was partially recrystallised. The intensity of the <111> peak for the film decreased from 52500 to 19800, and the initial preferential orientation was partially lost as shown by the appearance of <220> and <311> peaks. Recently Painter [17] has used the ratio of the <220> peak area to the <111> peak area to quantify texture of the CdTe films. The ratio of the peak areas was normalised with reference to that of a random bulk powder. As mentioned in chapter 7, for the sake of simplicity the ratio of the <220> intensity to the <111> was introduced to quantify texture of the CdTe films in this thesis. The ratio of the <220> intensity to <111> for powder CdTe was 1.25 [18]. The ratio of the peak intensities was normalised (RPI) with reference to that of a random bulk powder. If the values of the RPI are less than 0.01, annealed CdTe films have a strongly preferred <111> orientation and are not recrystallised which is termed non recrystallisation. If the values of the RPI are greater than 0.8, the annealed CdTe films are randomly orientated and fully recrystallised. When the RPI values are between these values, the annealed films are partially recrystallised during annealing. Those films were termed partial recrystallisation to different extent.

It is important to note that recrystallisation was not observed for annealed films deposited in the stirred solution for the same deposition potential and post treatment.

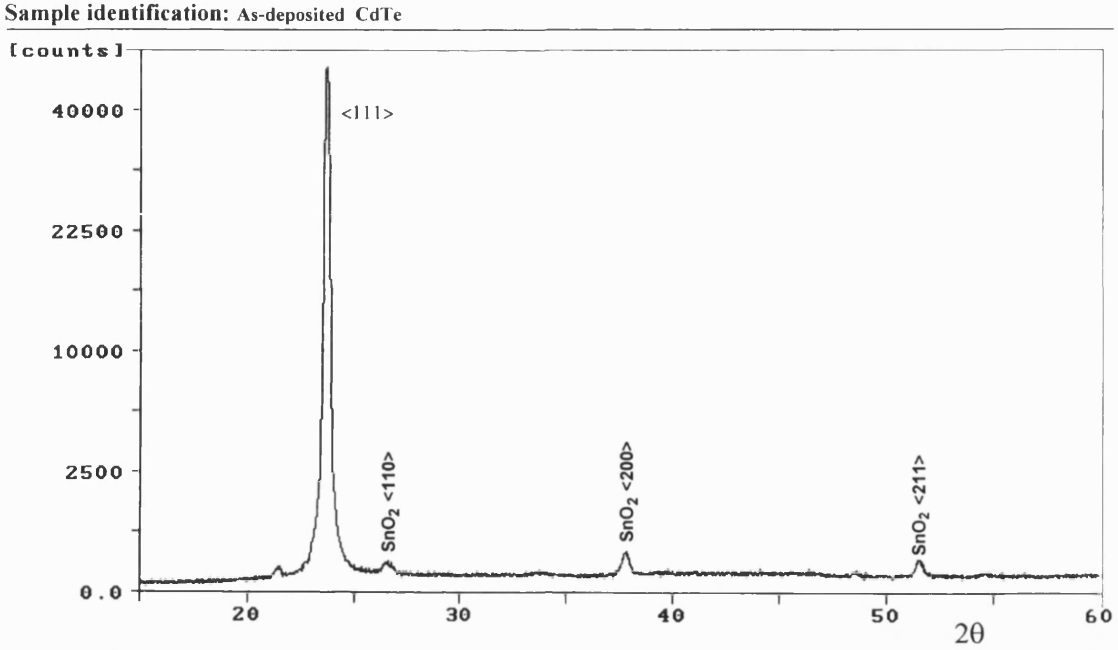

Figure 8.4 XRD pattern of as-deposited 1.8μm CdTe film prepared in the channel cell.

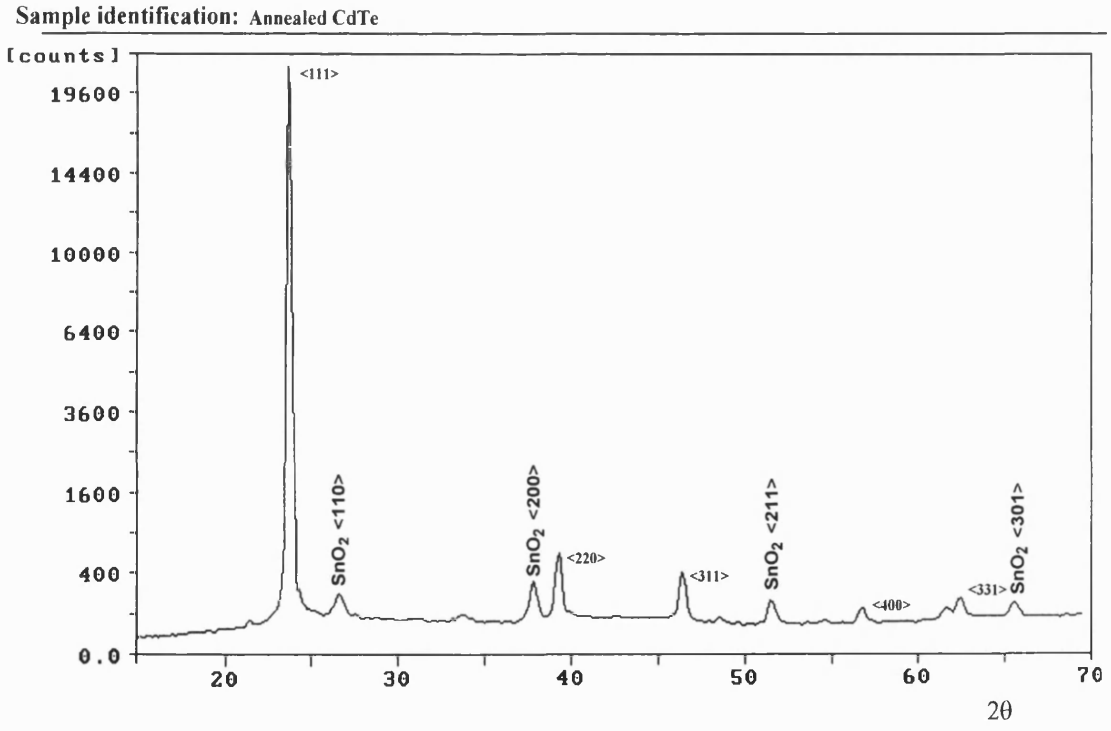

Figure 8.5 XRD pattern of an annealed 1.8μm CdTe film prepared in the channel cell.

The deposition potential was + 5mV at room temperature. RPI = 0.03.

The XRD pattern of an annealed 1.8μm CdTe film deposited at 85°C at + 20 mV vs. Cd^{2+}/Cd is shown in figure 8.6. The value of the RPI is increased from 0.03 in figure 8.6 to 0.17. This indicates the extent of recrystallisation of the film is greater. The WDX analysis indicate that the more positive the deposition potential, the more Te the deposited films contain. The films deposited potentials within a range of + 20 to + 80 mV vs. Cd^{2+}/Cd in the channel cell can lead to recrystallisation.

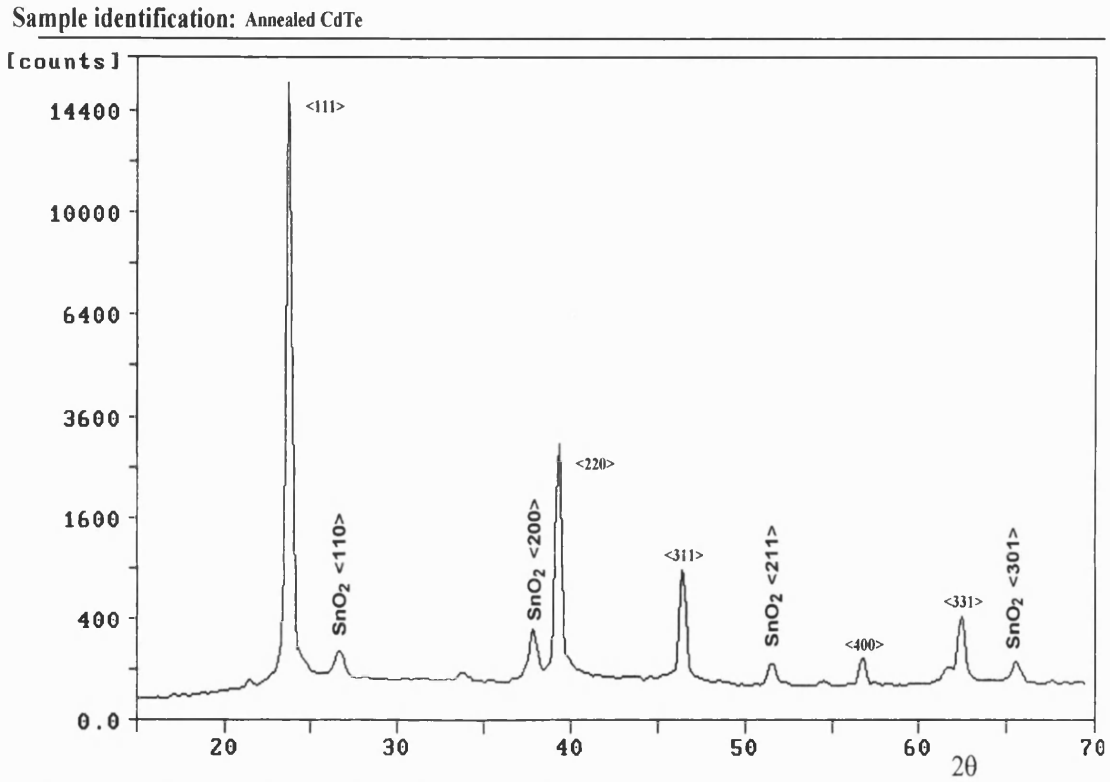

Figure 8.6 XRD pattern of a 1.8μm annealed CdTe film prepared in the channel cell. The deposition potential was + 40 mV Cd^{2+}/Cd at 85°C. RPI = 0.17

Pulsed deposition was used to deposit CdTe thin films. In this case the annealed films were found to be recrystallised to a high extent, and this technique seems to be reproducible. Figure 8.7 shows an XRD pattern of the pulsed deposition film with full recrystallisation. The deposition conditions were –90 mV, 1s, then 160 mV, 0.1s. Deposition of 1.8 μm film took 28 min.

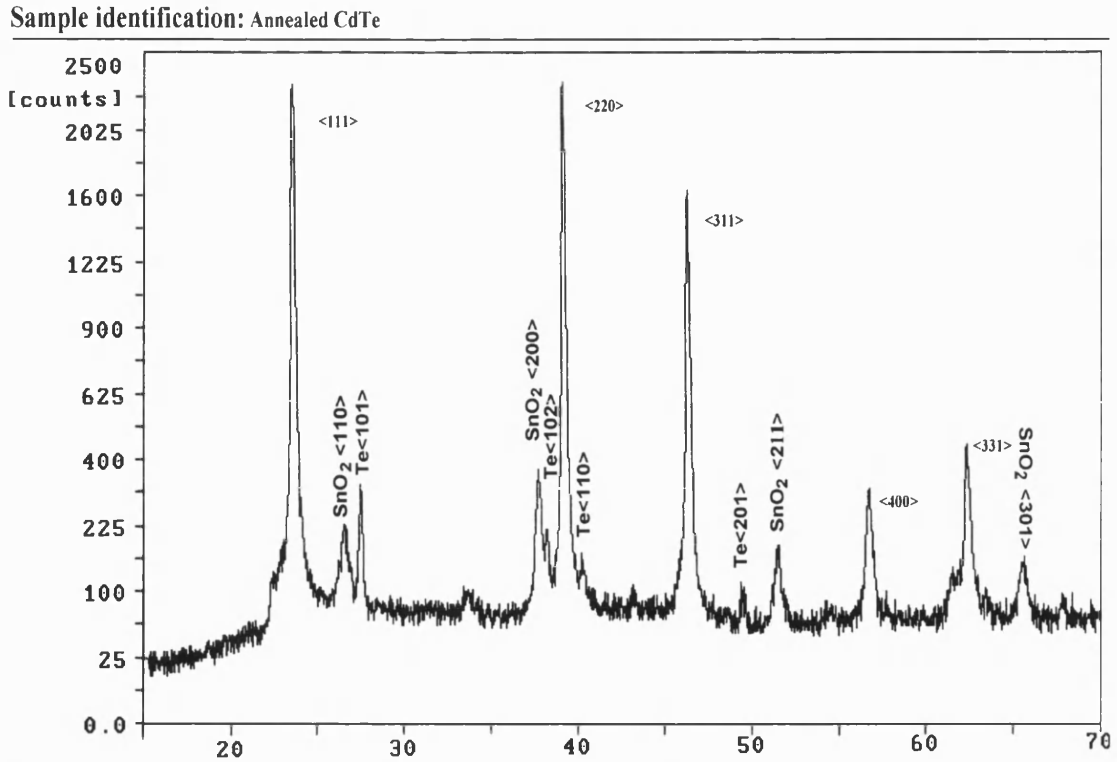

Figure 8.7 XRD pattern of an annealed 1.8μm CdTe film prepared by the pulsed deposition in the channel cell at 85°C. Depositition conditions: -90mV, 1s and +160mV, 0.1S. Deposition time 28 min. RPI = 0.82.

It can be seen from figure 8.7 that the intensity of the <111> peak decreases from 40000 to 2300, and the intensity of the <220> peak increases to 2300. The remaining peaks increase as well. The value of the RPI further increased to 0.82. The spectrum indicates that full recrystallisation has taken place during annealing, and the CdTe films lose their preferential orientation. The XRD pattern is the same as that of CdTe powder [18]. The important thing is that tellurium crystal peaks appear in the XRD pattern. This XRD pattern is similar with literature [19] in which about 12% conversion efficiency CdTe/CdS (fully recrystallised) cells were etched by HNO_3-H_3PO_4-H_2O agent and the etching left the Te-rich surface. The WDX results confirm that the film was slightly Te excess.

Fully recrystallised films often have pinholes. In this case adhesion to the CdS may be a problem. In order to tackle this problem, constant potential deposition was used to form a thin compact CdTe layer on the CdS surface, and then the pulse deposition was conducted. Generally the quality of films was improved, although a few pinholes were still observed in the film after annealing. A film was fabricated into test solar cells. Its XRD pattern is shown in figure 8.8. The film thickness was 1.8μm, and the deposition time was 26 min. The value of The RPI was 0.40.

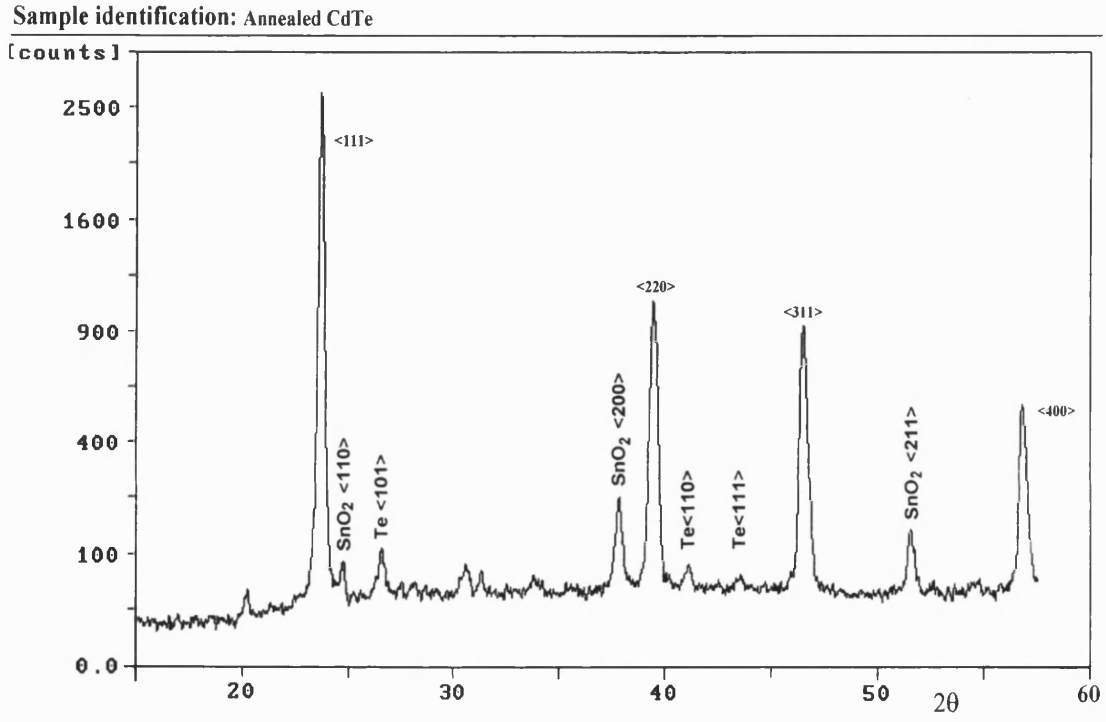

Figure 8.8 XRD pattern of an annealed 1.8μm CdTe film prepared by two-step deposition in the channel cell at 85°C. The first 200 nm was formed by normal deposition at +20mV vs. Cd^{2+}/Cd, then pulsed deposition was used to grow the remainder of the CdTe film. The pulsed deposition conditions were the same as described above. RPI = 0.40.

This film was also slightly Te-rich. It seems probable that the Te excess in as-deposited films enhances the recrystallisation during annealing.

In order to examine the composition in different parts of a sample, positions were defined as shown in figure 8.9 for WDX analysis. The composition values were obtained using at-least-3-point average within the different locations.

Table 8.2 summarises the results for three different CdTe films deposited at room temperature, each of which was cut into two with one half annealed. The samples are chosen as examples of recrystallisation where did not occur (sample B), occurred only partly (sample A, non-uniform and sample C). They were annealed in air at 430°C for 15 min (the same conditions were used in chapter 7). Four results for films deposited at 85°C are given in Table 8.3. Three of them were deposited in our laboratory. They were cut into two with one annealed. They were marked as D (not recrystallised), E (partly recrystallised), and F (fully recrystallised). Sample G was provided by BP solar. The annealing process was the same as described above.

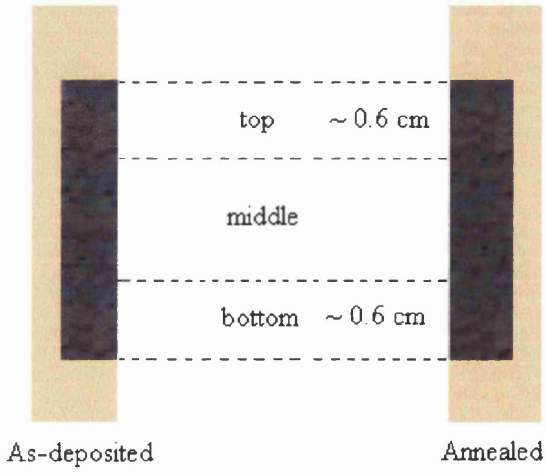

Figure 8.9 Positions mapped for WDX analysis

Table 8.2 Results of WDX analysis for films deposited at room temperature

Name	Position	Cd(%)	Te(%)	Annealed	Position	Cd(%)	Te(%)
A	Bottom	40.6	59.4	A′	Bottom	42.0	58.0
As-	Middle	50.3	49.7	Partial	Middle	50.6	49.4
deposited	Top	50.2	49.8	Recrystal.	Top	50.2	49.7
B	Bottom	50.0	50.0	B′	Bottom	50.1	49.8
As-	Middle	50.3	49.7	Non	Middle	50.3	49.7
deposited	Top	50.2	49.8	Recrystal.	Top	50.3	49.7
C	Bottom	50.2	49.8	C′	Bottom	50.2	49.8
As-	Middle	50.0	50.0	Partial	Middle	50.0	50.0
deposited	Top	50.1	49.9	Recrystal.	Top	50.1	49.9

*Samples A and B were deposited at + 5mV vs. Cd^{2+}/Cd and sample C was deposited at +20mV. RPI (A′) = 0.03, RPI (B′) < 0.01, and RPI (C′) = 0.04.

Fully recrystallised films were deposited at more positive potentials or pulsed deposition or using a combination of both methods at 85°C. However, recrystallisation only seems to be reproducible for films deposited by the pulsed deposition at 85°C.

It is clear from Tables 8.2 and 8.3 that the content of Te in the films seems to decrease after annealing, possibly due to evaporation, The films with a slight Te excess appeared to recrystallise fully.

Table 8.3 Results of WDX analysis for films deposited at 85°C

Name	Position	Cd(%)	Te(%)	Annealed	Position	Cd(%)	Te(%)
D	Bottom	50.3	49.7	D′	Bottom	50.4	49.6
As-	Middle	50.3	49.7	Non	Middle	50.3	49.7
deposited	Top	50.2	49.8	Recrystal.	Top	50.3	49.7
E	Bottom	50.0	50.0	E′	Bottom	50.1	49.8
As-	Middle	50.0	50.0	Partial	Middle	50.1	49.9
deposited	Top	49.6	50.4	Recrystal.	Top	50.0	50.0
F	Bottom	49.9	50.1	F′	Bottom	50.1	49.9
As-	Middle	50.0	50.0	Full	Middle	50.1	49.9
deposited	Top	49.8	50.2	Recrystal.	Top	50.0	50.0
G	Bottom	50.1	49.9	G′	Bottom	50.2	49.8
As-	Middle	50.2	49.8	Non	Middle	50.6	49.4
deposited	Top	50.3	49.7	Recrystal.	Top	50.3	49.7

Note: The extent of recrstallisation is defined by the value of the RPI in the XRD pattern for annealed films. RPI (D′) < 0.01, RPI (E′) = 0.4, RPI (F′) = 0.82 and RPI (′) < 0.01.

8.5 AFM and SEM Images

AFM and SEM were used to study the CdTe film structures. Generally the images of as-deposited films were same as those of images deposited in the stirred solution and the grain size of as-deposited films was not greater than 100 nm, whereas the grain size for annealed films increased significantly after annealing. Figure 8.10 shows AFM images of the 1.8μm CdTe samples. An increase in the grain size is also evident of the SEM images shown in figures 8.11 and 8.12.

Images of the film cross-section were used to obtain the film thickness. The mean thickness obtained from SEM images was about 90% of that calculated from the deposition charge. This indicates the current efficiency for deposition was ~90%. The reason for the current loss may be the oxygen reduction at the electrode surface.

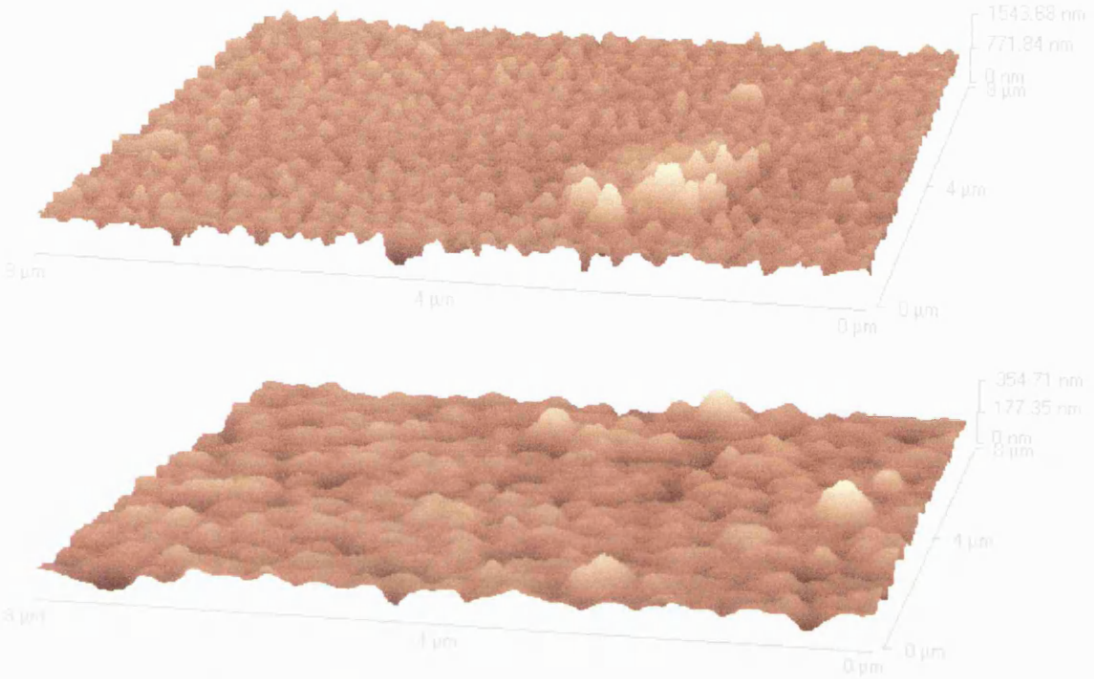

Figure 8.10 AFM images of as-deposited (upper) and annealed 1.8 μm CdTe films (lower) deposited in the flow cell (sample F).

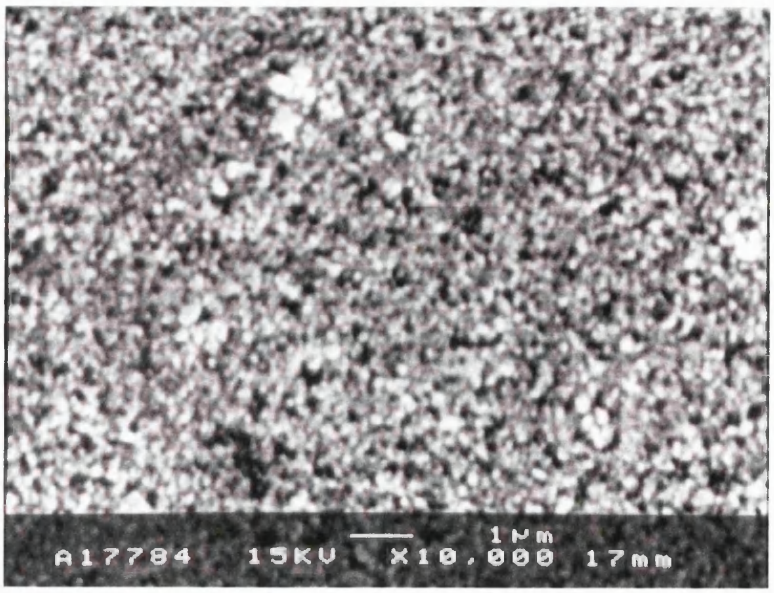

Figure 8.11 A SEM image of as-deposited 1.8μm CdTe film (F) grown in the flow cell

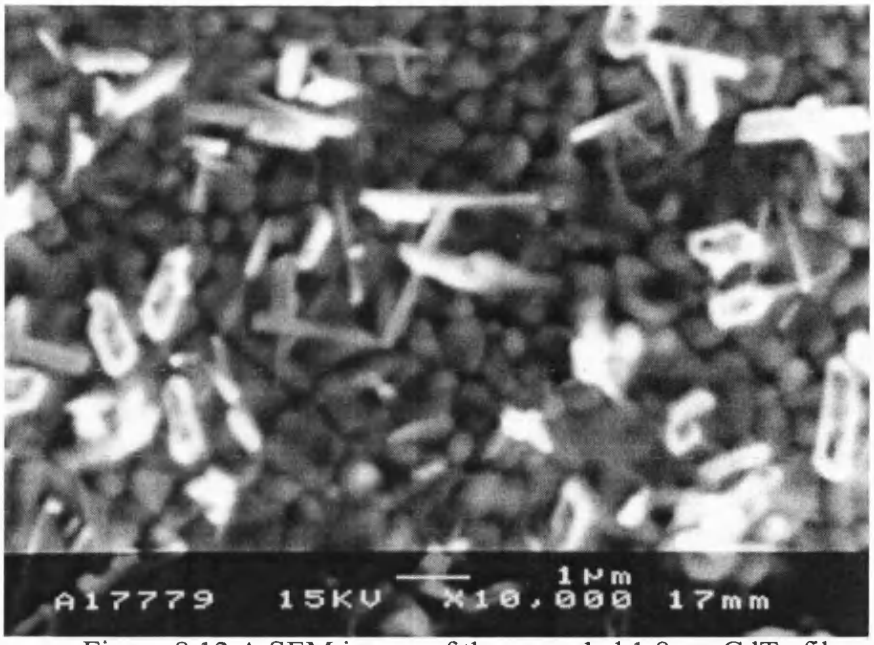

Figure 8.12 A SEM image of the annealed 1.8μm CdTe film prepared in the flow cell at 85oC (sample F).

8.6 Photocurrent Spectroscopy

As shown in chapter 7, photocurrent spectroscopy with electrolyte contacts is a powerful technique. Illumination can pass through either the glass substrate (G) or through the electrolyte (E) sides for both as-deposited and annealed films. Analysis of the photocurrent spectra for G and E illumination geometries can provide not only information about the location of the interface but also values of doping density and minority carrier diffusion length.

Figure 8.13 shows photocurrent spectra of as-deposited and annealed films deposited at room temperature. The annealed film (B′) was partially recrystallised and uniform, and the thickness was 1.8μm (measured by SEM). The E side photocurrent response of the as-deposited flow cell film is less ideal than that of the corresponding slowly grown film. The photocurrent rises slowly over the whole energy range rather than displaying a sharp onset at the CdTe band-edge (1.51 eV). This non-ideal

behaviour is consistent with a high density of defects. Annealing the as-deposited film not only effects the film type conversion to p-type but also reduces the defect density significantly as shown by the G spectrum. The E side photocurrent response in the higher energy range indicates that CdS may be formed at the CdTe surface due to annealing (the same oven was used to anneal CdS sheets).

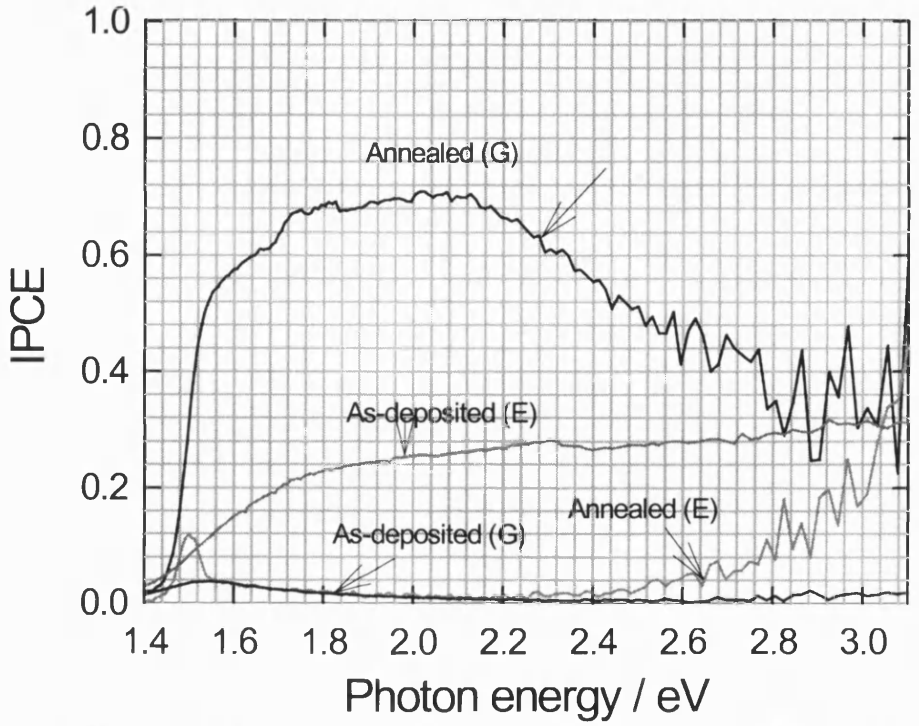

Figure 8.13 Photocurrent spectra of as-deposited and annealed CdTe films deposited in the channel cell at room temperature. E: illumination through electrolyte side. G: illumination through glass side. The annealed film was partially recrystallised.

Non-uniform films were often obtained by deposition at room temperature. Composition analysis of the films was made by WDX, and the results were shown in Table 8.2. Photocurrent spectroscopy was also used to analyse the films. The results are shown in figures 8.14 and 8.15. The locations were divided into three parts as shown in figure 8.3. T, M and B present the top, middle and bottom of the film, respectively.

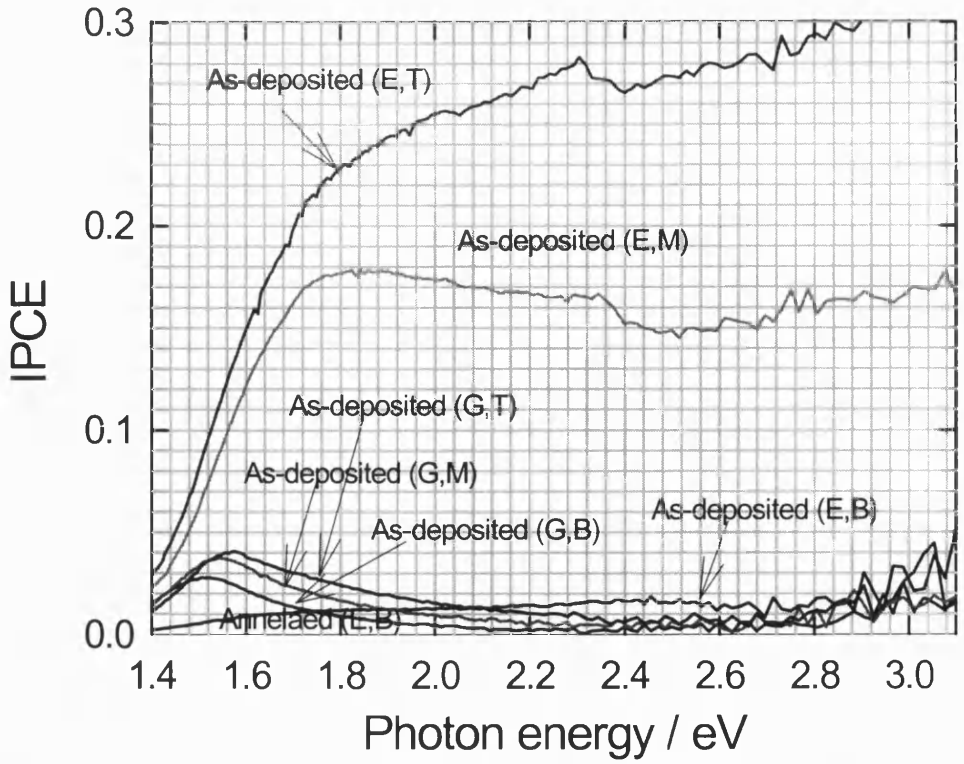

Figure 8.14 Photocurrent spectra of as-deposited CdTe film grown at room temperature. The thickness of the film was 1.8μm. Illumination geometry and position as shown.

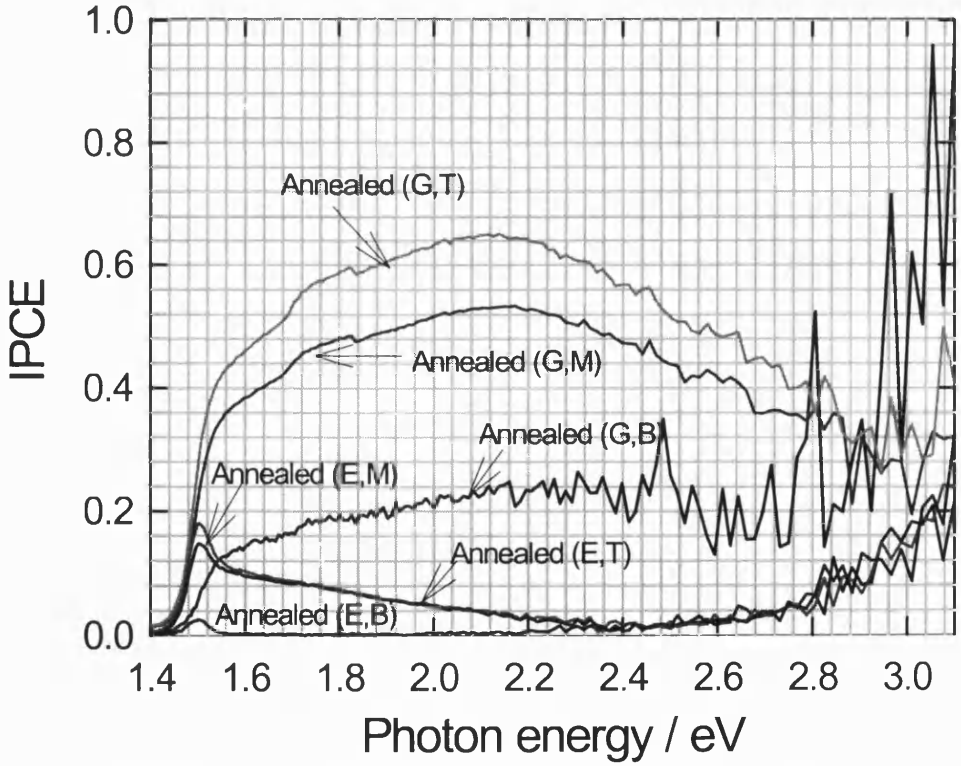

Figure 8.15 Photocurrent spectra of annealed CdTe film grown at room temperature. The thickness of the film was 1.8μm. Illumination geometry and position as shown.

The bottom of the film was quite reflective, and its composition as determined by WDX indicated the presence of excess Te. The as-deposited film does not give a good photocurrent response for the E side, while the annealed film gives 20% IPCE for the G side. The top of the film (normally dark) gave good photocurrent responses as the usual uniform films deposited in the channel cell. In this case, the quality of the film in different parts seems to vary with the flow direction, and the top (downstream) deposits usually have the highest quality.

Figure 8.16 compares the photocurrent spectra of as-deposited and annealed films prepared in the flow channel cell (F) at 85°C with the photocurrent spectra of an annealed film deposited in the stirred cell (S). The films had identical thicknesses. The annealed F film was fully recrystallised as confirmed by XRD (figure 8.7) and type converted, while the annealed S film did not recrystallised, although type conversion was satisfactory.

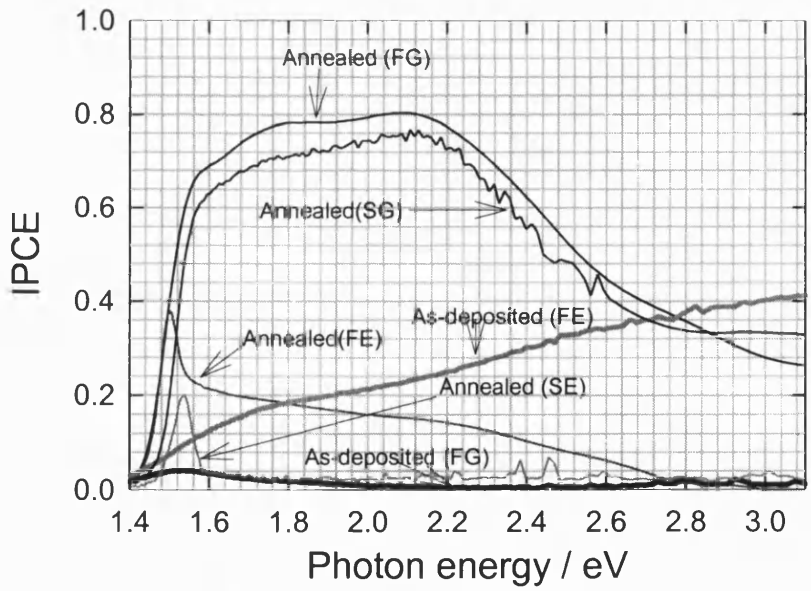

Figure 8.16 Photocurrent spectra for as-deposited and annealed films prepared in the channel cell (F) and type converted film deposited in stirred cell (S). Note that the high photocurrent efficiency in the E geometry for the annealed F film indicates a longer electron diffusion length. Note also the shift of the phocurrent onset to lower energies in the case of the F film, which indicates junction alloying.

The as-deposited film gives a non-ideal photocurrent response, and annealing has a profound effect on the photocurrent spectra. The annealed F films exhibit a good photocurrent performance that is better than those for films deposited from stirred solution. The higher photocurrent is now observed for the G side illumination due to the formation of an internal junction. The change in the spectra therefore provides direct proof of type-conversion. In the G side illumination, the photocurrent onset difference between the annealed F and S films is 30 meV, and the F one is lower. When illumination was from the E side for the F films, a substantial photocurrent was measured, whereas the photocurrent for the S films was much smaller in this E geometry. The explanation for this result is straightforward. Current is observed in the E geometry only if electrons generated near the CdTe/electrolyte interface can be collected at the internal junction. The shorter the electron lifetime, the lower is the probability that the electron will be collected. The large photocurrent observed for the E geometry here means that the annealed F films have a longer electron lifetime, or a longer diffusion length, $L_n = (D_n\tau_n)^{1/2}$, where D_n is the electron diffusion coefficient and τ_n is the electron lifetime, and so have higher IPCE efficiencies than the S films deposited in the stirred cell.

Figure 8.17 also shows photocurrent spectra of as-deposited and annealed films prepared in the channel cell at 85°C. The annealed film was only partially recrystallised as indicated by the XRD spectrum shown in figure 8.8. The film thickness was 1.8μm. Note that the photocurrent efficiency within the energy range of 2.1 to 3.1eV in the G geometry for the as-deposited film indicates that CdS layer may contribute the photocurrent.

Comparison of the photocurrent spectra of the fully recrystallised CdTe film with that of the partially recrystallised CdTe film indicates that the former has a higher IPCE, but the values of the bandgap are similar (~1.48eV).

The bandgap energy of annealed films including those deposited at both room temperature and 85°C obtained from the onset of the photocurrent spectra was less 1.49eV, while no bandgap value could be obtained for the as-deposited films due to their non-ideal photocurrent behaviour.

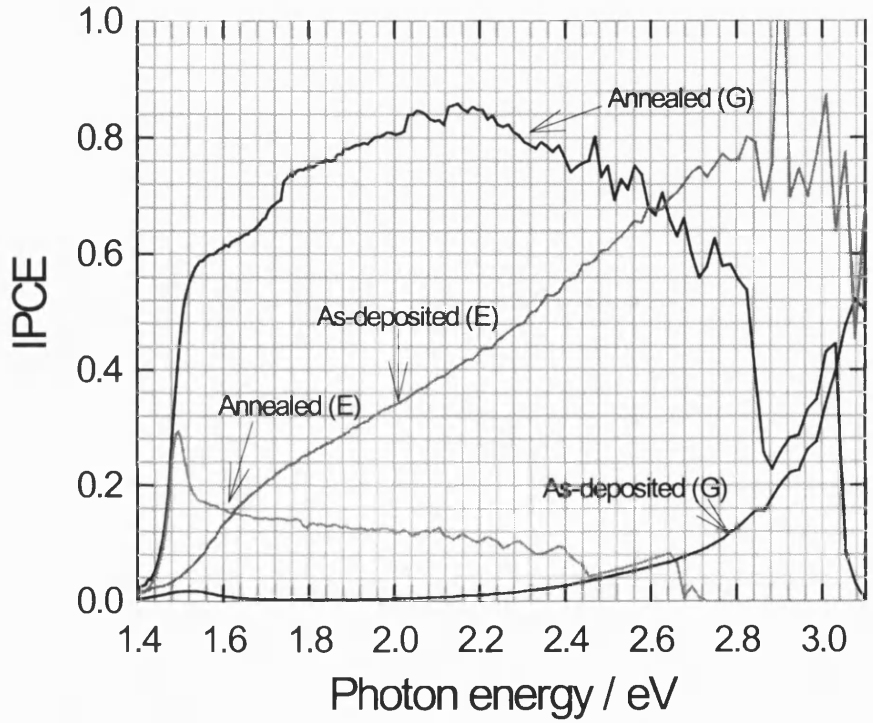

Figure 8.17 Photocurrent spectra for as-deposited and annealed films prepared in the channel cell. Note that the photocurrent efficiency within the energy range of 2.1 to 3.1eV in the G geometry for the as-deposited film indicates that CdS layer may contribute the photocurrent. Film thickness 1.8μm.

8.7 Results for the two-side-fitting Model

The two-side-fitting model was used to fit photocurrent spectra of films deposited in the channel cell. The detailed fitting procedures are described in chapter 7. Again it was assumed that n-CdS was heavily doped and that the hole lifetime in CdS was very short,

so that essentially no holes are collected by the space charge region. So the width of the space charge region in the n-CdS can be ignored (seen equation 5.109), and it was assumed that the rest of CdS does not contribute to the photocurrent, i.e. the whole CdS layer acts as a "deal layer".

Figure 8.18 shows a best fit of the photocurrent spectra for a 1.8μm annealed CdTe film deposited at room temperature at +5mV vs. Cd^{2+}/Cd. This particular annealed film was not recrystallised.

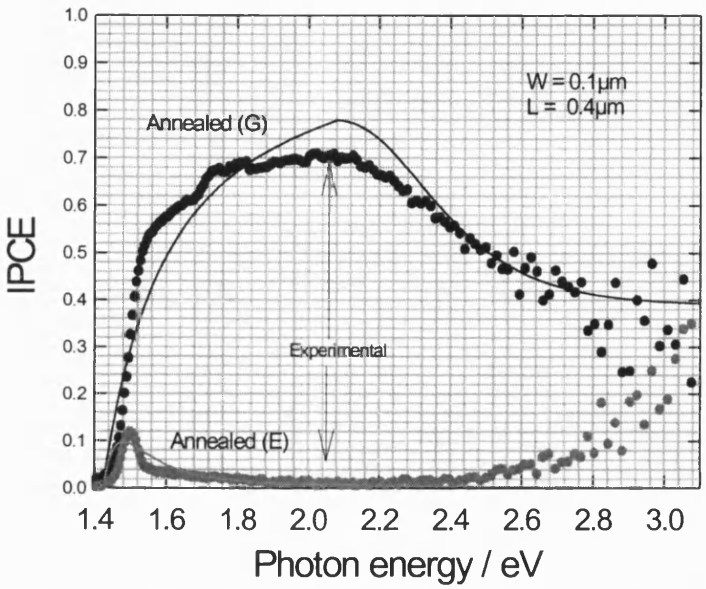

Figure 8.18 A best fit of the photocurrent spectra for a 1.8μm annealed CdTe film deposited at room temperature using equations 5.98 and 5.100. Reflection losses have been taken into account. The fitting results as shown.

Figure 8.19 shows a best fit of the photocurrent spectra for a 1.8μm annealed film prepared at 85°C. This film was partially recrystallised as confirmed by the XRD spectrum shown in figure 8.8.

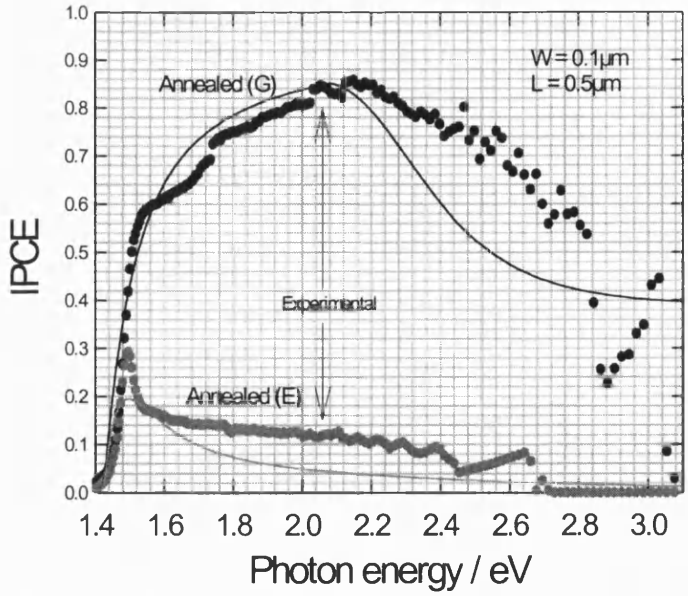

Figure 8.19 A best fit of the photocurrent spectra for a 1.8μm annealed CdTe film deposited at 85°C using equations 5.98 and 5.100. Reflection losses have been taken into account. The fitting results as shown. The film was partially recrystallised.

Figure 8.20 shows a best fit of the photocurrent spectra for a 1.8μm annealed film prepared at 85°C. This film was fully recrystallised as confirmed by the XRD spectrum shown in figure 8.7.

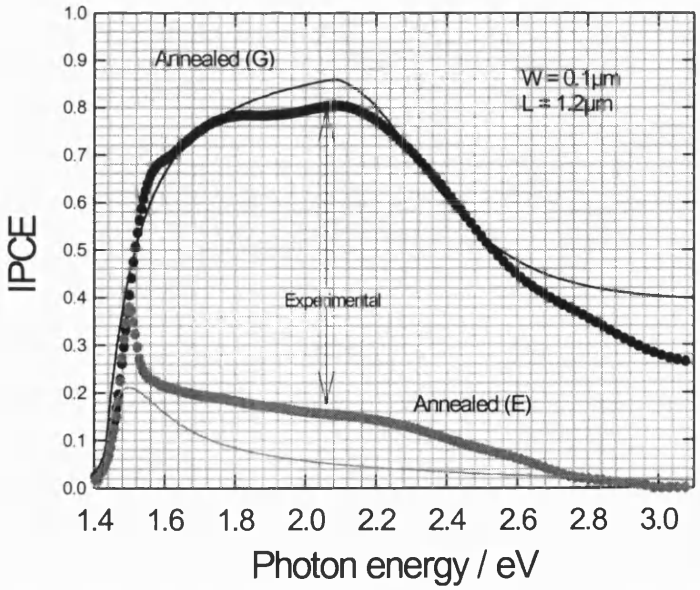

Figure 8.20 A best fit of the photocurrent spectra for a 1.8μm annealed CdTe film deposited at 85°C using equations 5.98 and 5.100. Reflection losses have been taken into account. The fitting results as shown. The film was fully recrysatllised.

Comparison of the fitting results from figure 8.20 with those from figures 8.18 and 8.19 indicates that the longest electron diffusion length is observed for fully recrystallised films. The fitting results seem to be a good fit to the spectrum in the G geometry illumination for the recrystallised films. It is clear now that the α_{CdTe} taken from Kampmann & Lincot [4] must correspond to a fully recrystallised CdTe film containing 5% sulphur which is proved by the EER/EEA spectra in the next section.

Generally speaking, the width of the space charge region obtained by fitting spectra for all non- or partially recrystallised films was ~0.1 μm and reproducible, while the electron diffusion length was between 0.3 μm and 0.7 μm. The fully recrystallised films give the longest diffusion length (1.2μm).

The fitting results also prove that the assumptions of a CdS 'dead layer' for the fitting model is correct. Otherwise the experimental results in the CdS absorption region should have higher IPCE efficiencies than the fit predicted for the G geometry. The fit was less satisfactory for the E geometry. The fit for the E geometry illumination cannot be improved by increasing the diffusion length L because the fit to the G geometry then becomes poor. The model proposed is appropriate for a single crystal because the junction is homogeneous and uniform. However the CdTe/CdS films are both polycrystalline. In the as-grown state, vapour deposited CdTe layers are found by TEM to be typically columnar for lower growth temperatures [20]. Electrodeposited CdTe films have been shown to grow with a characteristic columnar structure [21]. So the structure of the p-CdTe may be as shown in figure 8.21. The p-CdTe film is non-uniform. The crystal size of fully recrystallised films was up to 1μm. For the E illumination, if it is assumed that half of light beam goes through the thick part of the CdTe film and the other passes through the thin part of the sample, and the non-uniformity of the CdTe films was ±15%, the fit for figure 8.20 with the present

parameters W_{CdTe} = 0.1μm and L_n =1.2 μm was much better within errors of ±5%. This non-uniform structure has less effect on the photocurrent spectrum for the G illumination since the film is thick.

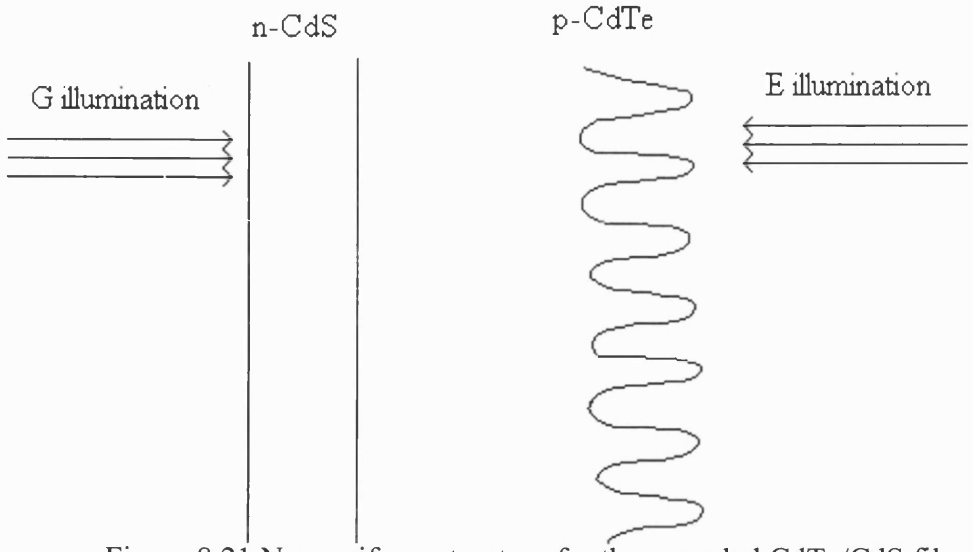

Figure 8.21 Non-uniform structure for the annealed CdTe/CdS films.

Due to shortage of time, capacitance voltage measurements were not carried out, so the doping density of the CdTe films was not obtained. However, if it is assumed that the junction potential is of the order of 1 V, the doping density can be worked out using equation 5.110 to be 8×10^{16} cm^{-3}. This is in reasonable agreement with the value of $5 \times 10^{16} cm^{-3}$ for electrodeposited p-CdTe given by Özsan et al. [22]. It is an order of magnitude higher than the value of 5.8×10^{15} cm^{-3} for electrodeposited p-CdTe film electrodeposited at +5mV vs. Cd^{2+}/Cd reported by Kampmann and Lincot [23], who fitted photocurrent spectra for G side illumination using the Gärtner equation. It has been reported that the doping densities of the p-CdTe increase with increasing deposition potentials up to 8.5×10^{17} cm^{-3} [24]. Since the Te concentration in the films increased with increasing deposition potential, this suggests that excess Te may acts as an acceptor state.

8.8 Electrolyte Electroreflectance (EER) Spectroscopy

The optical properties of the CdTe/CdS films were studied by electrolyte electroreflectance (EER). In this technique, an ac potential perturbation is applied to the thin film based on a transparent electrolyte contact under a constant electric field. The modulation of the electric field perturbs the optical constant of the solid, resulting in a synchronous modulation ΔR of the reflected light intensity. This normalised $\Delta R/R$ spectrum exhibits third derivative structure at critical points in the band structure. Details are given in chapter 5.

The EER spectra were fitted using the generalised line function (equation 5.50) to provide values of E_g and Γ. Figure 8.22 shows EER spectra of as-deposited and annealed CdTe films grown at room temperature in the flow cell.

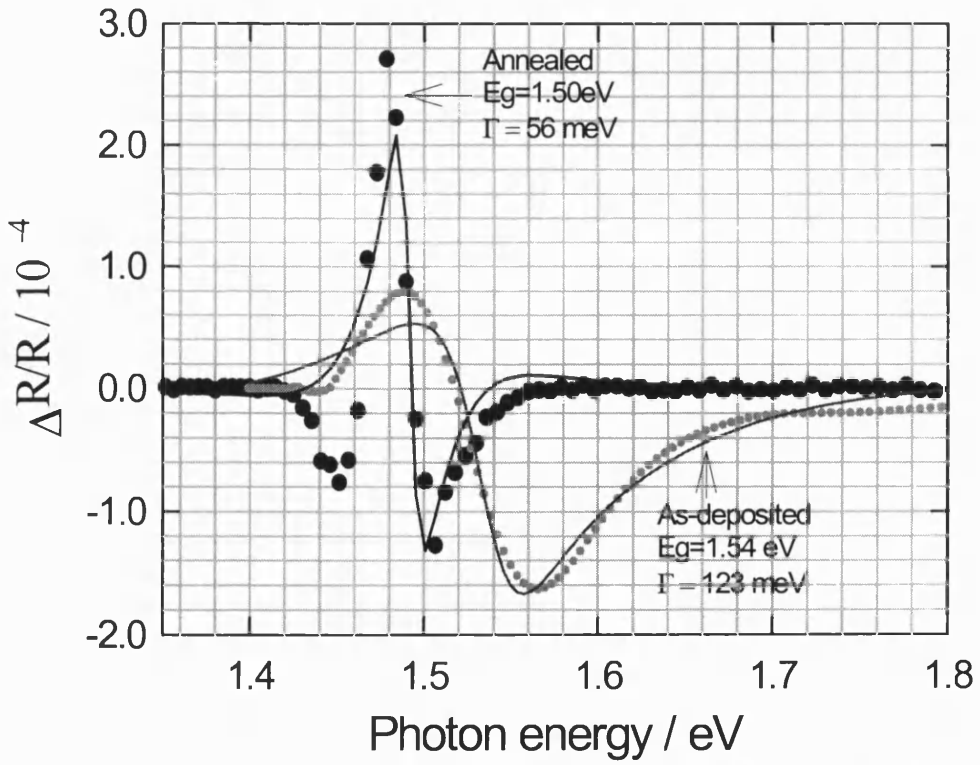

Figure 8.22 EER spectra of as-deposited and annealed CdTe films deposited at room temperature in the channel cell. (1.8μm). This annealed film is partially recrystallised Lines - fit to generalised line function.

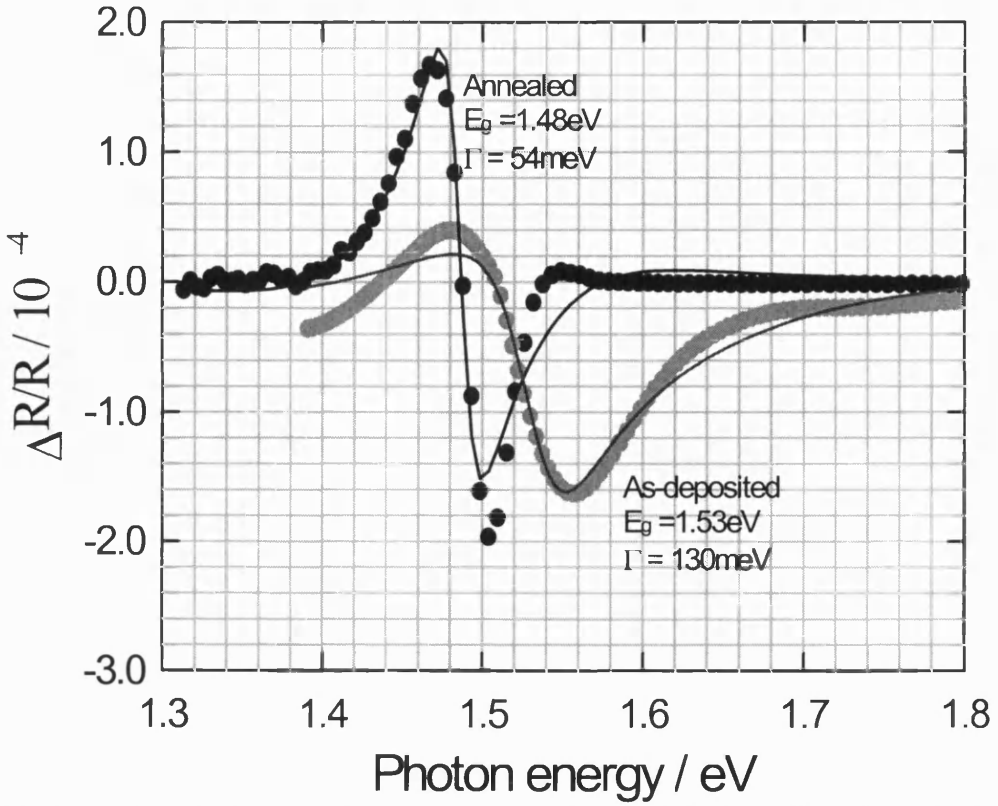

Figure 8.23 EER spectra of as-deposited and annealed CdTe films deposited at 85°C in the channel cell. (1.8μm). The annealed film was partially recrystallised. Lines - fit to generalised line function. The fitting results as shown.

Figure 8.23 shows EER spectra of as-deposited and annealed films deposited in the channel cell at 85°C. The annealed film was partially recrystallised. The thickness of the film was 1.8μm. The large values of Γ in the as-deposited films can arise from structural disorder, stress or compositional imhomogeneity. After annealing, structural disorder or strain was removed from the films and the CdTe grain size was increased. The EER spectra of the type-converted structure (measured in the G geometry) are much sharper. The value of Γ for samples deposited at room temperature decreased from 123 to 56 meV, and for films deposited at 85°C from 130 to 54 meV.

Figure 8.24 illustrates the substantial changes in the EER spectrum that result from annealing and type-conversion of the films grown in the channel cell by the pulsed potential technique. The annealed films were fully recrystallised. The as-deposited film measured in the G geometry gives Eg = 1.51 eV and Γ = 91 meV. The large value of Γ indicates a high degree of structural imperfection or strain or compositional imhomogeneity in the film.

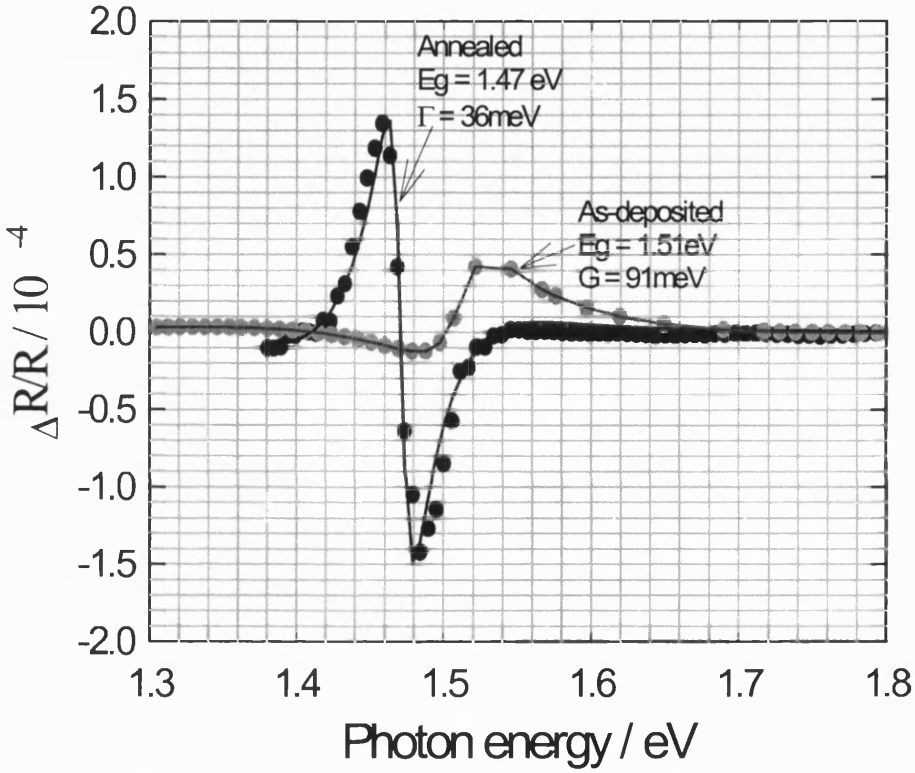

Figure 8.24 EER spectra of as-deposited and annealed CdTe films deposited at 85°C in the channel cell. (1.8μm). The annealed film was fully recrystallised. Lines - fit to generalised line function. The fitting results as shown.

After annealing, the bandgap value shifts towards lower energy (from 1.51 eV to 1.47 eV). The value of Γ is reduced from 91 to 36 meV. This very low Γ value indicates that the film in the space charge region is free of structural imperfections and is homogeneous in its composition.

The shift in Eg on annealing is consistent with sulphur and tellurium diffusion. The diffusion of sulphur from the CdS layer into the CdTe film to form $CdTe_{1-x}S_x$ and the diffusion of tellurium from the CdTe layer into the CdS to form $CdS_{1-z}Te_z$ were first studied by Ohata et al. [25] who have established the following relationship between the bandgap of the $CdTe_{1-x}S_x$ and sulphur content

$$Eg = 1.51 - 1.010x + 1.74x^2 \quad (8.2)$$

Toyama et al. [26] used EER to study CdTe/CdS films prepared by closed space sublimation (CSS). These workers compared the EER spectra of a CSS cell using Au contacts, and found the bandgap of the CdTe in the CSS cell was shifted toward lower energies by 40meV relative to Eg for the pure monocrystalline CdTe in the Schottky CSS cell. From the shift in Eg they calculated that the composition of the active layer in the annealed cell was $CdTe_{0.95}S_{0.05}$. Rogers et al. [27] have confirmed the relationship of Ohata et al. and have reported that x reaches 0.05 after annealing a PVD cell. Using the fitting value of Eg obtained from the generalised line function, it was found in the present study that x = 0.01, 0.03 and 0.05 for non, partial and full recrystallisation, respectively.

Table 8.4 lists the properties of three types of annealed CdTe films deposited in the flow cell by methods described above.

Table 8.4 Summary of the properties of three kinds of annealed CdTe films

Recrystallisation	Photocurrent	EER	W/μm	L/μm
Non	Eg =1.50eV	Eg=1.50eV,Γ=56meV	0.1	0.4μ
Partial	Eg =1.48eV	Eg=1.48eV,Γ=54meV	0.1	0.5μ
Full	Eg =1.47eV	Eg=1.47eV,Γ=36meV	0.1	1.2μ

8.9 Fabricating and Testing of Phtovoltaic Cells

A partially recrystallised CdTe/CdS film deposited at 85°C was fabricated into solar cells by evaporating gold on the CdTe surface through a mask (4 mm^2). Under AM 1.5 (G), the open-circuit voltage was ~800mV, and the short-circuit current was 14 mA cm^{-2}. The cell efficiency was 5%. The IV and power response are shown in figure 8.25.

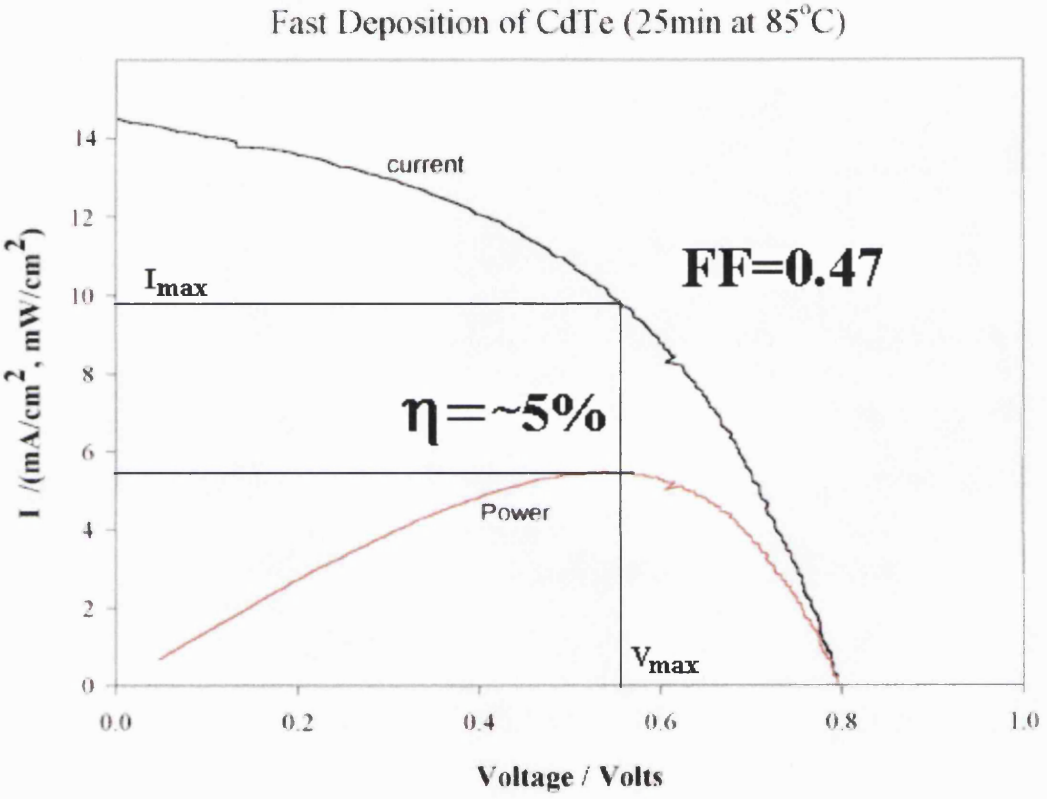

Figure 8.25 I-V curve measured under AM 1.5 (G). The Cell area was 0.04cm^2.

Comparison of figure 8.25 with figure 7.27 indicates that solar cells made from films deposited in the channel cell have higher open-circuit voltage (~800mV, greater by 100mV) with a slightly lower short-circuit current than those grown in stirred solution. The lower fill factor (FF) may be due in part to a poor contact to the CdTe [28]. The shunt resistance may be a major problem in the CdTe/CdS solar cells

deposited in the flow cell due to pinholes which cause a lower shunt resistance. By contrast, for those solar cells made from the films prepared slowly in the conventional stirred cell the series resistance plays an important role in which back contacts are the major source of the series resistance.

8.10 Conclusions

Type conversion for the CdTe/CdS films obtained in the conventional stirred cell was satisfactory, but they did not recrystallise. It is believed that $CdCl_2$ acts as a recrystallising agent [28]. It has been reported that CSS CdTe/CdS solar cells made without $CdCl_2$ treatment have a lower conversion efficiency (not more than 6%) [29], while the efficiency in the cells made from molecular-beam epitaxy (MBE) with $CdCl_2$ treatment dramatically increased from 1.3% to 8.6% [30]. There was a significant reduction in the series resistance that increases the short-circuit current. It has been reported that the type conversion anneal causes interdiffusion of S and Te between the two layers (CdS and CdTe deposited by PVD) which has significant consequences for the cell efficiency [31] and confirmed by Rogers et al. [32] to electrodeposited CdTe films provided by BP solar. Recently Rogers et al. [33] have extensively studied the diffusion processes after annealing of the PVD CdTe/CdS films. Diffusion of sulphur into CdTe and tellurium into CdS took place after annealing for only 2 min with grain growth and/or stress reduction in the CdTe. However recrystallisation of the CdTe/CdS film did not occur at this early stage. After 5 min annealing there were further, more significant changes to the structures of both CdTe and CdS layers. Partial recrystallisation occurred, and the initial preferred <111> orientation was lost. Both layers became closer to a random orientaion distribution. A 15 min anneal is sufficient to cause complete recrystallisation and the disappearance of stoichiometric CdTe.

$CdS_{0.93}Te_{0.07}$ was formed in the CdS region within the first 2 min annealing and did not change with further annealing. $CdTe_{1-x}S_x$ formed in the CdTe region of the structure, and x decreased with increasing annealing time. Interdiffusion of S and Te at the CdTe/CdS interface changes the optical absorption in the structure as a result of the band gap changes associated with alloy formation. S interdiffusion into CdTe to form $CdTe_{1-x}S_x$ decreases bandgap of the CdTe for $x \leq 0.290$ and Te interdiffusion to CdS to form $CdS_{1-z}Te_z$ diminishs bandgap of the CdS for $z \leq 0.290$ as well. The minimum bandgap for $CdTe_{0.71}S_{0.29}$ is 1.363 eV. The alloying appears to lead to reduced lattice mismatch or a gradual transition from CdS to CdTe with fewer interface states [34]. The interdiffusion is often accompanied by recrystallisation. As seen in chapter 7, CdTe films grown near the Cd^{2+}/Cd potential in the stirred cell retain preferential <111> orientation on annealing and show less evidence of sulphur diffusion. Fast deposition of CdTe films by constant and pulsed potential deposition methods has been successfully carried out in the channel flow cell. 1.8μm films have been deposited in less than 20 min. The properties of the films differ from those of films grown by conventional electrodeposition from stirred solution. The as-deposited films are structurally more disordered, but after annealing and type-conversion they become of sufficiently high-quality to make them suitable for the fabrication of efficient solar cells. Those films deposited in the flow cell recrystallise and show evidence of sulphur diffusion. CdTe films containing excess Te recrystallised during annealing.

The two-side-fitting model for photocurrent spectra can be used to obtain the minority diffusion length and the doping density. However, its application and validity are limited by many factors such as the accuracy of absorption coefficients and refractive index, and the film thicknesses, and information about the interfaces. Since

the model is only applicable to the uniform junction, problems may arise if the films are non-uniform or if the junction in non-planar.

References:

1. T. L. Chu, S. S. Chu, C. Ferekides, C. Q. Wu, J. Britt and C. Wang, J. Appl. Phys., **70**, 7608(1991).
2. J. Britt and C. Ferekides, Appl. Phys. Lett. **62**(22), 2851(1993).
3. T. Aramoto, S. Kumazawa, H. Higuchi, T. Arita, S. Shibutani, T. Nishio, J. Nakajima, M. Tsuji, A. Hanafusa, T. Hibino, K. Omura, H. Ohyama and M. Murozono, Jpn. J. Appl. Phys., **36**, 6304(1997).
4. D. Lincot, B. Mokili, M. Froment, R. Cortès, M.C. Bernard, C. Witz and J. Lafait, J. Phys. Chem. B, **101**, 2174 (1997).
5. A. M. Hermann, R. Westfall and R. Wind, Solar Energy Mater. Solar Cells, **52**,355(1998).
6. S. Dennison, J. Materials Chemistry, **5**(11), 1885 (1995).
7. J.M. Woodcock, A.K. Turner, M. E. Özsan and J.G. Summers, In Proceedings of the 22nd IEEE Photovoltaic Solar Energy Conference, Las Vegas, April 1991 (IEEE, New York, 1991), p72.
8. L. M. Peter and R. L. Wang, Electrochemistry Communication, **1**,554 (1999).
9. B. M. Basol, E.S. Tseng and R.L Rod, U.S. Patent No. 4,383,483 (1983).
10. S. K. Das and G.C. Morris, J. Appl. Phys., **73**, 782 (1993).
11. S. K. Das and G. C. Morris, Solar Energy Mat. And Solar Cells, **28**, 305 (1993).
12. S. Dennison and S. Webseter, J. Electroanal. Chem., **333**, 287 (1992).
13. B. M. Basol, Solar Cells, **23**, 69 (1989).
14. R. Schuhmann, J. Am. Chem. Soc., **47**, 356 (1925).

15. A. Saraby-Reintjes, L.M. Peter, M.E. Özsan, S. Dennison and S. Webster J. Electrochem. Soc., **140**, 2880 (1993).

16. P.R. Unwin and R.G. Compton in *Comprehensive Chemical Kinetics* Vol 29, p 173 Elsevier, Amsterdam (1989).

17. J. D. Painter, PhD thesis, Cranfield University, Department of Materials and Medical Sciences, (1999).

18. J. Liabrés and V. Delmas, J. Electrochem. Soc., **133**(12), 2580 (1986).

19. J. Sarlund, M. Ritala, M. Leskelä, E. Siponmaa and R. Zilliacus, Solar Energy Materials and Solar Cells, **44**, 177(1996).

20. R. W. Birkmire, E. Eser, Annu. Rew. Mater. Sci., **27**, 625(1997).

21. J. Barker, S. P. Pinns, D. R. Johnson, R. J. Marshall, S. Oktik, M. E. Özsan, M. H. Patterson, S. J. Ransome, S. Roberts, M. Sadeghi, J. Sherborne, A. K. Turner and J. M. Woodcock, Int. J. Solar Energy, **12**, 79 (1992).

22. M. E. Özsan, D. R. Johnson, S. Oktik and M. H. Patterson, 12th European Photovoltaiv Solar Energy Conference, 1994, Amsterdam, p1604.

23. A. Kampmann and D. Lincot, J. Electroanal. Chem., **418**, 73 (1996).

24. A. Kampmann, P. Cowache, J. Vedel and D. Lincot, J. Electroanal. Chem., **387**, 53 (1995).

25. K. Ohata, J. Saraie, T. Tanka, Jpn. J. Appl. Phys., **12**, 1641(1973).

26. T. Toyama, T. Yamamoto and H. Okamoto, Solar Energy Mater. Solar Cells, **49**, 213 (1997).

27. D. W. Lane, G. J. Conibeer, D. A. Wood, K. D. Rogers, P. Capper, S. Romani, S. Hearne, J. Cryst. Growth **197**, 743 (1999).

28. B. E. McCandless and R. W. Birkmire, Solar Cells, **31**, 527(1991).

29. T. Okamoto, Y. Matsuzaki, N. Amin, A. Yamada and M. Konagai, Jpan. J. Appl. Phys. Vol., **37**, 3894 (1998).

30. S. A. Ringel, A. W. Smith, M. H. MacDougal and A. Rohatgi, J. Appl. Phys., **70**(2), 881 (1991).

31. R. W. Birkmire, B. E. McCandless, S. S. Hegedus, Int. J. Solar Energy **12**, 145 (1992).

32. K. D. Rogers, J. D. Painter, M. J. Healy, D. W. Lane and M. E. Özsan, Thin Solid Flms, **339**, 299(1999).

33. K. D. Rogers, J. D. Painter, D. W. Lane and M. J. Healy, J. Electronic Materials, **28**(2), 112(1999).

34. H. C. Chou, A. Rohatgi, N. M. Jokerst, S. Kamra, S. R. Stock, S. L. Lowrie, R. K. Ahrenkiel and D. H. Levi, Materials Chemistry and Physics, **43**, 178 (1996).

Summary and Outlook for Future Work

Slow and fast deposition of CdTe films has been successfully conducted in a stirred cell and in a channel flow cell, respectively. The time requested to deposit a 2μm film has been reduced from 2-3h in the stirred cell to less than 20 min in the channel cell. The films prepared by fast deposition were found to recrystallise during annealing, and they were sufficiently high-quality to make them suitable for fabrication of efficient solar cells. Electrodeposited CdTe films with Te excess were found to recrystallise during annealing. The pulsed deposition method in stirred solution and fast deposition in the flow cell are promising methods for deposition of CdTe films that can be used to make efficient solar cells. Further work needs to be done to correlate the CdTe composition with recrystallisation and to improve the CdTe adhesion to the CdS and back contacts. The following areas deserve further study:

1) Deposition at more positive constant potentials and pulsed deposition in the stirred cell. A more detailed study of the influence of CdTe composition in subsequent recrystallisation needs to be undertaken. Further WDX and XRD studies could be used to determine the variation in the composition and the extent of recrystallisation. The CdTe/CdS interface plays an important role for solar cell applications. Etching samples through to the interface would be useful to understand what happens to the CdTe/CdS interface after annealing. XRD and EER/A analysis could be used to study these etched samples.
2) More high resolution STM and SEM should be used to study the structure of the CdTe/CdS interface. Also more accurate absorption coefficient data for the intermixing should be obtained, and the two-side-fitting modelling should be developed further.

3) Further studies are essential for full characterisation of the films deposited in the flow cell. In particular, improvement of the film uniformity and adhesion are required. Further XRD and EER analysis would be useful to enhance understanding of interdiffusion of S and Te.
4) Back contacts seem to be a major problem limiting solar cell performance, and further work is needed in this area.
5) It would be interesting to study using $CdCl_2$ to enhance recrystallisation as an alternative to using Te excess. The grain size in the polycrystalline solar cell clearly plays an important role in performance, and further study of grain growth is needed.
6) Only a few solar cells were tested in the present work. Further characterisation of large area cells would be very desirable.